

# IL NUOVO CIMENTO

ORGANO DELLA SOCIETÀ ITALIANA DI FISICA  
SOTTO GLI AUSPICI DEL CONSIGLIO NAZIONALE DELLE RICERCHE  
E DEL COMITATO NAZIONALE PER L'ENERGIA NUCLEARE

VOL. XXII, N. 3

Serie decima

1° Novembre 1961

## Equations for Alpha-Disintegration Energies.

Y. P. VARSHNI (\*) and R. N. BHARGAVA (\*\*)

*Department of Physics, Allahabad University, Allahabad*

(ricevuto il 10 Marzo 1961)

**Summary.** — For nuclei with  $Z \geq 84$  and  $N \geq 128$ , it has been shown that  $(Q - 0.625 Z)$  is a smooth function of the mass number  $A$ , where  $Q$  is the  $\alpha$ -disintegration energy. This has been utilized to develop two equations for  $Q$ . Results by these two equations are compared with those given by Roger's equation.

### 1. - Introduction.

One of the important applications of the Weizsäcker-Bethe semi-empirical mass equation has been in the calculation of  $\alpha$ -decay energies. Such calculations have been made by a number of workers.

Following PERLMAN and RASMUSSEN <sup>(1)</sup>, we shall denote the  $\alpha$ -disintegration energy (*i.e.* the energy of the  $\alpha$  group leading to the ground state plus the recoil energy of the nucleus) by  $Q$ .

PRYCE <sup>(2)</sup> made a detailed comparison of the calculated  $\alpha$ -decay energies from the Weizsäcker-Bethe (W-B) equation with the observed ones. He found that the difference between the two values for the nuclei with  $Z \geq 84$ ,  $N \geq 128$  decreases reasonably smoothly with increasing mass number and, by making

(\*) Now at the Division of Pure Physics, National Research Council, Ottawa 2, Canada.

(\*\*) Now at the Department of Physics, Columbia University, New York, N.Y., U.S.A.

(1) I. PERLMAN and J. O. RASMUSSEN: *Handb. d. Phys.*, vol. 42, (Berlin, 1957) p. 109.

(2) M. H. L. PRYCE: *Proc. Phys. Soc.*, **63**, 692 (1950).

certain simplifying assumption, deduced that

$$(1) \quad Q(\text{obs.}) - Q(\text{calc.}) = 4\varepsilon - 4a(A - 210.5),$$

where  $\varepsilon$  and  $a$  are constants and  $A$  is the mass number. In other words the difference is nearly linear with  $A$ . Calculated values of  $\alpha$ -decay energy were also reported by DAS<sup>(3)</sup>.

The inadequacy of the W-B mass equation to yield the correct  $\alpha$ -decay energies is a consequence of the fact, first shown by STERN<sup>(4)</sup>, that in the heavy mass region the observed masses show considerable departures from the calculated ones. STERN<sup>(4)</sup> showed that if a correction term

$$(2) \quad + 0.01270 - 0.02340 \exp[-18x]$$

(where  $x = (A - 208)/208$ ) is added to the W-B mass equation, it gives good results for nuclei with  $A \geq 208$ . JHA and DUBE<sup>(5)</sup> calculated  $Q$  by the W-B equation with Stern correction term for isotopes of  $Z = 83, 84$  and  $85$  and found satisfactory results. DUBE and SINGH<sup>(6)</sup> have suggested other types of correction terms to the mass equation to remedy for the differences in calculated and observed  $Q$  values.

Besides these, equations have also been proposed for the  $\alpha$ -disintegration energy in terms of the atomic number  $Z$  and neutron number  $N$ .

ROGER<sup>(7)</sup> has suggested

$$(3) \quad Q(\text{in MeV}) = 9 - \frac{N - 128}{6} \cdot \frac{102 - Z}{6},$$

for nuclei beyond  $Z = 84$  and  $N = 128$ .

VARSHNI<sup>(8)</sup> proposed

$$(4) \quad Q(\text{MeV}) = 0.4Z - 1.795(N - 132)^{\frac{1}{2}} - 26.208$$

for nuclei having  $N > 132$ . SUD<sup>(9)</sup> has found slightly improved results with slightly different values of the constants in the above equation.

A similar equation for  $\alpha$ -disintegration energy in the region of rare earth nuclei has been investigated by RAMASWAMY<sup>(10)</sup>:

$$(5) \quad Q = 0.36Z - 1.19(N - 82)^{\frac{1}{2}} - 17.89$$

(3) R. K. DAS: *Ind. Journ. Phys.*, **24**, 523 (1950).

(4) M. O. STERN: *Rev. Mod. Phys.*, **21**, 312 (1949).

(5) S. JHA and G. P. DUBE: *Ind. Journ. Phys.*, **26**, 15 (1952).

(6) G. P. DUBE and L. S. SINGH: *Curr. Sci.*, **23**, 84 (1954); *Ind. Journ. Phys.*, **28**, 177 (1954); *Proc. Ind. Acad. Sci.*, A **40**, 37 (1954).

(7) F. ROGER: *Compt. Rend. Acad. Sci.*, **240**, 858 (1955).

(8) Y. P. VARSHNI: *Nuovo Cimento*, **3**, 1148 (1956).

(9) L. V. SUD: private communication.

(10) M. K. RAMASWAMY: *Nuovo Cimento*, **4**, 1570 (1956).



( $N > 82$ ,  $Z < 82$ ). Good results were obtained for the 15  $\alpha$ -emitters in this region.

Systematics of  $\alpha$ -disintegration energy (<sup>11</sup>) are known to show a sharp break and a change of trend at the shell closures  $Z=82$  and  $N=126$ . In the presented paper we have confined ourselves to nuclei having  $Z \geq 84$  and  $N \geq 128$ .

It has been found that the function  $(Q - 0.625Z)$  is a smooth function of the mass number  $A$ , and from this we have developed two equations for  $Q$ .  $Q$  is taken in MeV.

Fig. 1 shows  $(Q - 0.625Z)$  plotted against  $A$ . Data have been taken from

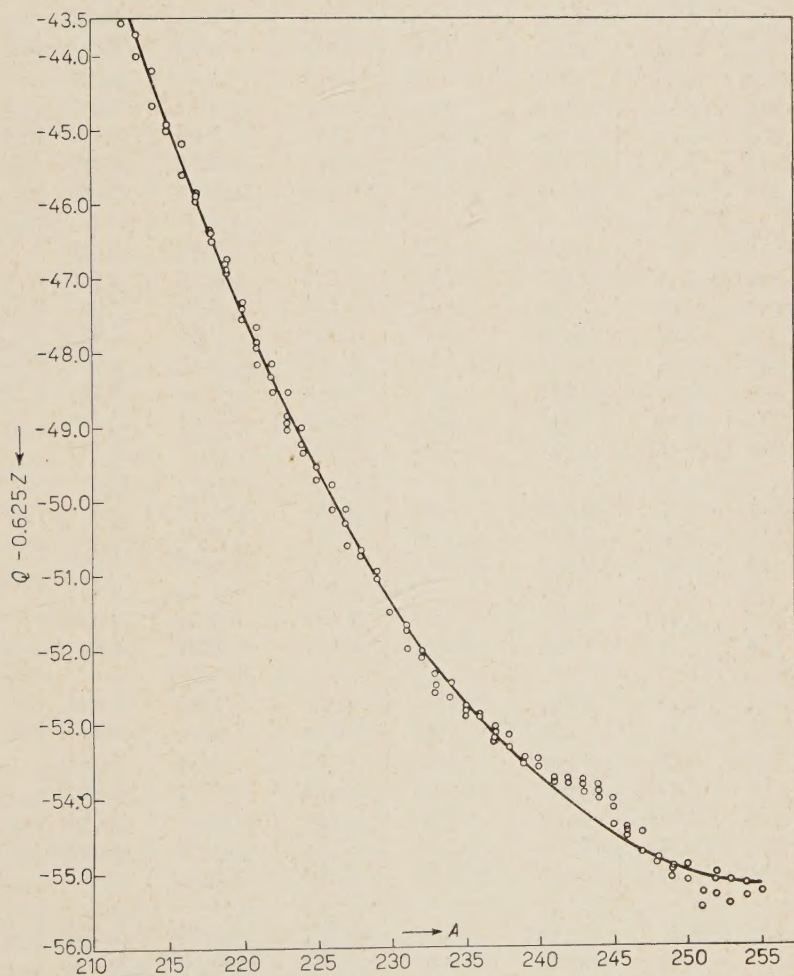


Fig. 1. — The function  $(Q - 0.625Z)$  vs. the mass number  $A$ . The curve represents eq. (6).

(<sup>11</sup>) I. PERLMAN, A. GHIORSO and G. T. SEABORG: *Phys. Rev.*, **77**, 26 (1950).

TABLE I ( $Q$  values are in MeV).

$Z$	$A$	$Q$ obs.	$Q$ calc. eq. (6)	% Error	$Q$ calc. eq. (7)	% Error	$Q$ calc. Roger eq. (3)	% Error
84	212	8.949	9.373	+ 4.73	8.986	+ 0.41	9.000	+ 0.57
	213	8.51	8.756	+ 2.89	8.459	- 0.60	8.500	- 0.12
	214	7.827	8.172	+ 4.40	7.934	+ 1.36	8.000	+ 2.21
	215	7.50	7.600	+ 1.33	7.422	- 1.04	7.500	0
	216	6.903	7.047	+ 2.08	6.923	+ 0.29	7.000	+ 1.41
	217	6.66	6.514	- 2.19	6.436	- 3.36	6.500	- 2.40
	218	6.110	6.000	- 1.80	5.962	- 2.42	6.000	- 1.80
85	213	9.4	9.381	- 0.20	9.084	- 3.36	9.000	- 4.26
	214	8.95	8.797	- 1.70	8.559	- 4.37	8.528	- 4.72
	215	8.15	8.225	+ 0.92	8.047	- 1.26	8.056	- 1.15
	216	7.94	7.672	- 3.37	7.548	- 4.94	7.583	- 4.50
	217	7.18	7.139	- 0.57	7.061	1.66	7.111	- 0.96
	218	6.75	6.625	- 1.85	6.587	- 3.90	6.639	- 1.64
	219	6.39	6.127	- 4.11	6.126	- 2.57	6.167	- 3.49
86	215	8.8	8.850	+ 0.57	8.672	- 1.45	8.556	- 2.77
	216	8.16	8.297	- 1.67	8.173	+ 0.16	8.112	- 0.59
	217	7.89	7.764	- 1.59	7.686	- 2.59	7.667	- 2.83
	218	7.26	7.250	- 0.13	7.212	- 0.66	7.222	- 0.52
	219	6.94	6.752	- 2.70	6.751	- 2.72	6.778	- 2.33
	220	6.398	6.272	- 1.96	6.302	- 1.50	6.333	- 1.02
	221	6.10	5.810	- 4.75	5.866	- 3.84	5.889	- 3.46
	222	5.587	5.367	- 3.94	5.447	- 2.50	5.444	- 2.56
87	217	8.50	8.389	- 1.30	8.311	- 2.22	8.167	- 3.92
	218	8.00	7.875	- 1.56	7.837	- 2.04	7.75	- 3.12
	219	7.44	7.377	- 0.85	7.476	+ 0.48	7.333	- 1.44
	220	6.81	6.897	+ 1.40	6.927	+ 1.72	6.917	+ 1.57
	221	6.449	6.435	- 0.21	6.491	+ 0.65	6.500	+ 0.79
	223	5.44	5.561	+ 2.22	5.657	+ 3.99	5.667	+ 4.17
88	219	8.10	8.002	- 1.20	8.001	- 1.22	7.833	- 3.30
	220	7.57	7.522	- 0.63	7.552	- 0.24	7.444	- 1.66
	221	6.83	7.060	+ 3.36	7.116	+ 4.19	7.056	+ 3.31
	222	6.671	6.617	- 0.80	6.692	+ 0.31	6.667	- 0.06
	223	5.974	6.186	+ 3.55	6.285	+ 5.16	6.278	+ 5.09
	224	5.784	5.775	- 0.15	5.884	+ 1.73	5.889	+ 1.82
	226	4.863	5.000	+ 2.81	5.124	+ 5.18	5.111	+ 5.10
89	221	7.7	7.685	- 0.19	7.741	+ 0.53	7.556	- 1.87
	222	7.09	7.042	- 0.67	7.317	+ 3.20	7.194	+ 1.47
	223	6.76	6.811	+ 0.75	6.903	+ 2.18	6.833	+ 1.08
	224	6.28	6.400	+ 1.91	6.59	+ 3.65	6.472	+ 3.06
	225	5.923	6.003	+ 1.35	6.103	+ 3.04	6.111	+ 3.17
	227	5.031	5.260	+ 4.55	5.39	+ 7.14	5.389	+ 7.12



TABLE I (*continued*).

Z	A	Q obs.	Q calc. eq. (6)	% Error	Q calc. eq. (7)	% Error	Q calc. Roger eq. (3)	% Error
90	223	7.69	7.436	— 3.30	7.532	— 2.05	7.333	— 4.64
	224	7.26	7.025	— 3.23	7.134	— 1.74	7.000	— 3.58
	225	6.69	6.628	— 0.92	6.748	+ 0.87	6.667	— 0.34
	226	6.444	6.250	— 3.01	6.475	— 0.48	6.333	— 1.72
	227	6.144	5.885	— 4.21	6.015	+ 2.10	6.000	— 2.34
	228	5.52	5.535	+ 0.27	5.668	+ 3.04	5.667	+ 2.66
	229	5.11	5.202	+ 1.80	5.333	+ 4.36	5.333	+ 4.36
	230	4.765	4.883	+ 2.47	5.011	+ 5.16	5.000	+ 4.93
	232	4.077	4.287	+ 5.15	4.414	+ 8.27	4.333	+ 6.28
91	226	6.93	6.875	— 0.79	7.000	+ 1.01	6.861	— 1.00
	227	6.58	6.510	— 1.06	6.640	+ 0.91	6.556	— 0.36
	228	6.20	6.160	— 0.64	6.293	+ 1.53	6.25	+ 0.81
	229	5.79	5.827	+ 0.63	5.958	+ 2.90	5.944	+ 2.66
	231	5.138	5.202	+ 1.24	5.326	+ 3.62	5.333	+ 3.80
92	227	6.90	7.135	+ 3.46	7.265	+ 5.29	7.056	+ 2.26
	228	6.79	6.785	— 0.07	6.918	+ 1.90	6.778	— 0.18
	229	6.53	6.452	— 1.19	6.583	+ 0.51	6.5	— 0.46
	230	5.988	6.133	+ 2.42	6.261	+ 4.56	6.222	+ 3.91
	231	5.5	5.826	+ 5.92	5.951	+ 8.20	5.944	+ 8.07
	232	5.411	5.537	+ 2.32	5.664	+ 4.68	5.667	+ 4.73
	233	4.900	5.262	+ 7.38	5.370	+ 9.59	5.389	+ 9.98
	234	4.851	4.999	+ 3.05	5.099	+ 5.11	5.111	+ 5.36
	235	4.66	4.750	+ 1.93	4.84	+ 3.86	4.833	+ 3.71
	236	4.577	4.514	— 1.37	4.593	+ 0.35	4.556	— 0.46
	238	4.267	4.082	— 4.33	4.139	— 3.00	4.000	— 6.26
93	231	6.39	6.451	+ 0.95	6.576	+ 2.91	6.500	+ 1.72
	233	5.63	5.881	+ 4.45	5.995	+ 6.48	6.000	+ 6.57
	235	5.23	5.375	+ 2.77	5.465	+ 0.24	5.500	+ 5.16
	237	4.950	4.917	— 0.66	4.985	+ 0.71	5.000	+ 1.01
94	232	6.70	6.787	+ 1.30	7.014	+ 4.69	6.778	+ 1.16
	233	6.41	6.512	+ 1.59	6.720	+ 4.84	6.556	+ 2.27
	234	6.30	6.249	— 0.80	6.449	+ 2.37	6.333	+ 0.52
	235	5.95	6.000	+ 0.84	6.190	+ 4.03	6.111	+ 2.71
	236	5.862	5.764	— 1.67	5.943	+ 1.38	5.889	+ 0.46
	237	5.75	5.542	— 3.61	5.610	— 2.43	5.667	— 1.44
	238	5.589	5.332	— 4.59	5.489	— 1.79	5.444	— 2.59
	239	5.235	5.235	— 0.00	5.281	+ 0.88	5.222	— 0.25
	240	5.246	5.051	— 3.71	5.085	— 3.07	5.000	— 4.69
	241	4.976	4.779	— 3.96	4.802	— 2.94	4.778	— 3.98
	242	4.980	4.719	— 5.24	4.732	— 4.98	4.556	— 8.51

TABLE I (continued).

Z	A	Q obs.	Q calc. eq. (6)	% Error	Q calc. eq. (7)	% Error	Q calc. Roger eq. (3)	% Error
95	237	6.110	6.167	+ 0.93	6.235	+ 2.05	6.278	+ 2.75
	239	5.90	5.860	- 0.67	5.806	- 1.59	5.889	- 0.19
	241	5.628	5.504	- 2.20	5.427	- 3.57	5.500	- 2.27
	243	5.428	5.096	- 6.11	5.101	- 6.06	5.111	- 5.84
96	238	6.63	6.582	- 0.72	6.639	+ 0.14	6.667	+ 0.56
	240	6.38	6.301	- 1.23	6.235	- 2.27	6.333	- 0.74
	241	6.20	6.129	- 1.14	6.152	- 0.77	6.167	- 0.53
	242	6.213	5.969	- 3.92	5.882	- 5.33	6.000	- 3.43
	243	6.159	5.721	- 7.11	5.734	- 6.90	5.833	- 5.29
	244	5.895	5.584	- 5.27	5.579	- 5.36	5.667	- 3.87
	245	5.62	5.459	- 2.68	5.449	- 3.08	5.500	- 2.14
	246	5.46	5.346	- 7.08	5.327	- 5.44	5.333	- 2.33
	248	5.14	5.151	+ 0.21	5.126	- 0.27	5.000	- 2.72
97	243	6.83	6.346	- 7.08	6.349	- 7.04	6.500	- 4.83
	244	6.78	6.209	- 8.41	6.204	- 8.50	6.361	- 6.18
	245	6.48	6.084	- 6.11	6.075	- 6.25	6.222	- 3.98
	247	5.85	5.867	+ 0.29	5.845	- 0.09	5.944	+ 1.61
	249	5.53	5.694	+ 2.96	5.669	+ 2.51	5.667	+ 2.48
98	244	7.29	6.834	- 6.25	6.829	- 6.32	7.000	- 3.98
	245	7.23	6.709	- 7.21	6.697	- 7.51	6.889	- 4.72
	246	6.865	6.596	- 3.91	6.577	- 4.20	6.778	- 1.27
	248	6.36	6.401	+ 0.64	6.376	+ 2.51	6.556	+ 3.08
	249	6.29	6.319	+ 0.46	6.294	+ 0.06	6.444	+ 2.45
	250	6.122	6.250	+ 2.09	6.225	+ 1.68	6.333	+ 3.45
	252	6.211	6.139	- 1.15	6.106	- 1.69	6.111	- 1.61
99	246	7.4	7.221	- 2.41	7.202	- 2.68	7.417	+ 0.23
	247	7.4	7.117	- 3.82	7.095	- 4.12	7.333	- 0.91
	248	6.98	7.026	+ 0.65	7.001	+ 0.19	7.250	+ 3.87
	249	6.87	6.944	+ 1.07	6.919	+ 0.71	7.167	+ 4.32
	251	6.58	6.814	+ 3.55	6.794	+ 3.25	7.000	+ 6.38
	252	6.750	6.764	+ 0.20	6.731	- 0.28	6.917	+ 2.47
	253	6.74	6.725	+ 0.22	6.719	- 0.31	6.833	+ 1.38
	254	6.52	6.697	+ 2.71	6.701	+ 2.77	6.750	+ 3.53
100	250	7.55	7.500	- 0.66	7.475	- 0.99	7.778	+ 3.02
	251	7.00	7.439	+ 6.27	7.419	+ 5.98	7.722	+ 10.31
	252	7.16	7.389	+ 3.18	7.356	+ 4.13	7.667	+ 7.08
	253	7.05	7.350	+ 4.25	7.344	+ 4.17	7.611	+ 7.96
	254	7.32	7.322	+ 0.02	7.324	+ 0.08	7.556	+ 3.22
	255	7.20	7.300	+ 1.38	7.320	+ 1.67	7.500	+ 4.17
Average percent errors				2.45		2.89		2.98



ASARO and PERLMAN <sup>(12)</sup>. The points are seen to lie on a regular curve which is a function of  $A$  alone. From this we are led to assume that the factor  $0.625Z$  eliminates the  $Z$  dependent effects *i.e.* the Coulomb energy and the symmetry energy in the semi-empirical mass equation.

The Coulomb energy term is  $+a_3Z^2/A^{\frac{1}{2}}$ , where  $a_3$  is a constant. From this it is readily seen that its contribution to  $Q$  will be  $+4a_3(Z-1)/A^{\frac{1}{2}}$  nearly. (As  $A$  appears in the cube root, the variations in the denominator will be small.) With  $A \sim 230$ , this will be  $\sim 4a_3Z/6.13$ . Recently GREEN <sup>(13)</sup> has determined  $a_3 = 0.71$  MeV; using this value for  $a_3$ , the effect comes out to be  $\sim +0.46Z$  MeV.

Besides the Coulomb energy, the symmetry energy is also  $Z$  dependent. It is put as  $a_4(N-Z)^2/4A$ , where  $a_4$  is a constant. Its contribution to the disintegration energy will be approximately  $-a_4(N-Z)^2/A^2$  or  $-a_4(1-2Z/A)^2$ . In this case it is not possible to separate out the effect of  $Z$ .

Two different equations were found to give a reasonable representation of the behaviour of the points:

$$(6) \quad Q - 0.625Z = -364.1233 + 0.802594A + 6779630/A^2$$

and

$$(7) \quad Q - 0.625Z = -36.0684 - 0.695557(A-200) + 6.3286 \cdot 10^{-3}(A-200)^2.$$

In eq. (7) the constant 200 is merely for computational convenience. The curve shown in Fig. 1 represents eq. (6).

The calculated values of  $Q$  from eq. (6), (7) and the Roger equation (3), together with the observed values are recorded in Table I. Calculations were also carried out with eq. (4). The results were satisfactory at low  $Z$ , but at high  $Z$  the errors were large and hence these results have not been reproduced. All  $Q$  values are in MeV.

## 2. - Discussion.

It will be observed from Table I that the average percent errors by all the three equations, *viz.* eq. (6), (7) and the Roger equation (3), are in the neighbourhood of 3%. The average percent error by eq. (6) is the lowest (2.45) and that by eq. (3) the highest (2.98).

<sup>(12)</sup> F. ASARO and I. PERLMAN: *Rev. Mod. Phys.*, **26**, 456 (1954); **29**, 831 (1957).

<sup>(13)</sup> A. E. S. GREEN: *Phys. Rev.*, **95**, 1006 (1954).

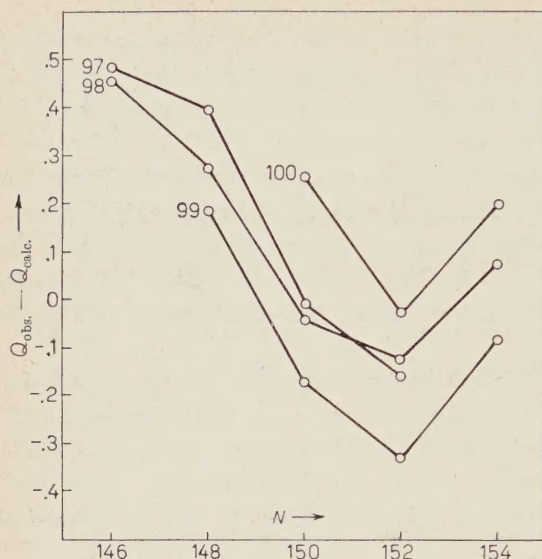


Fig. 2. —  $Q$  (obs.) —  $Q$  (calc. by eq. (6)) shown against the neutron number  $N$ . The figures by the side of the curves denote atomic numbers. To avoid overlapping, the points for  $Z=99$  have been shifted down by 0.1 MeV and those for  $Z=100$  shifted up by 0.2 MeV. The discontinuity at  $N=152$  corresponds to the subshell at this neutron number, suggested by GHIORSO *et al.* <sup>(14)</sup>.

Being related to the gradient of the «mass surface» (or «energy surface»), the  $\alpha$ -disintegration energy is better suited than the mass surface itself for exhibiting irregularities which point to structural features in nuclei. Eq. (6) defines a smooth  $Q$  curve. Any systematic deviation from this may be the consequence of subshells or other structural changes in the nuclei in this region.

GHIORSO *et al.* <sup>(14)</sup> have suggested a subshell at  $N=152$  on the basis of the systematics of  $\alpha$ -particle energy in this region. Fig. 2 shows a plot of  $Q$  (obs.) —  $Q$  (calc. by eq. (6)) *vs.*  $N$ . As expected there is a definite break at  $N=152$ .

Another interesting feature may be noted in Fig. 1. Between mass numbers 240 and 245 the points are seen to lie appreciably above the curve and there is a sort of a hump. This flimsy evidence is suggestive of some structural change at  $A \sim 242$ .

<sup>(14)</sup> A. GHIORSO, S. G. THOMPSON, G. H. HIGGINS, B. G. HARVEY and G. T. SEABORG: *Phys. Rev.*, **95**, 293 (1954).

# RIASSUNTO (\*)

È stato dimostrato che  $(Q - 0.625 Z)$ , per nuclei aventi  $Z \geq 84$  ed  $N \geq 128$ , è una funzione continua del numero di massa  $A$ , in cui  $Q$  è l'energia della disintegrazione  $\alpha$ . Utilizziamo questa proprietà per costruire due equazioni per  $Q$ . Confrontiamo i risultati di queste due equazioni con quelli dati dall'equazione di Roger.

(\*) Traduzione a cura della Redazione.



## On Magnetic and Luminescent Centres Induced in the Crystal of Lithium Fluoride by X-Ray Irradiation (\*)

A. CHOUDHURY

*Physics Department, Jadavpur University, Calcutta*

(ricevuto il 19 Maggio 1961)

**Summary.** — The diamagnetic susceptibility of LiF decreases on irradiation with X-rays. The difference in diamagnetic susceptibility of the sample before and after colouration obeys the Curie law. This is due to the paramagnetism of induced colour centres, predominantly  $F$  centres. On complete thermal bleaching the diamagnetic susceptibility recovers its original value. The changes in magnetic susceptibilities which occur at different stages of thermal bleaching are found to have close correspondence with the integrated intensity of thermoluminescence emission. It has been concluded from the results that the destruction of  $F$  centres alone cannot account for the intensity of thermoluminescence emission or magnetic changes.

### 1. — Introduction.

Alkali halides are transparent over a wide range of wave-lengths from 200 nm to 15  $\mu\text{m}$ . New absorption bands or colour centres, as they are termed, can be created by irradiation with ionizing radiations. Of the various colour centres, the  $F$  centre is the simplest. It is formed by the trapping of an electron in an anion vacancy of the crystal. Similarly trapping of positive holes at cation vacancies produces  $V$ -type centres. A variety of other centres, e.g.,  $R_1$ ,  $R_2$ ,  $M$  or  $V_2$ ,  $V_3$ ,  $V_4$ , etc., are also known to occur under suitable conditions.

The magnetic measurements with coloured alkali halides have shown that the  $F$ -centres are paramagnetic <sup>(1)</sup> and their contribution to susceptibility

(\*) The work was carried out in the Indian Institute of Technology, Kharagpur.

(1) P. JENSEN: *Ann. d. Phys.*, **34**, 161 (1939); A. B. SCOTT, H. J. HROSTWISKI and L. B. BUPP: *Phys. Rev.*, **79**, 346 (1950).

follows the Curie law. The paramagnetic resonance experiments on  $F$  centres give a « $g$ » value which is approximately the same as that for the free electron.

The luminescence and the thermoluminescence of alkali halides irradiated by X-rays and cathode rays have been reported by several authors <sup>(2)</sup>. Irradiated at low temperatures, alkali halides get coloured and store up energy; on subsequent heating they emit light showing peaks at characteristic temperatures. The peaks in the thermoluminescence curve are associated with the trapping stages of holes or electrons. The investigations of YUSTER, SHARMA and MAURER <sup>(3)</sup> show that the colour centres are intimately related to the glow peaks. HEER and BATE <sup>(4)</sup> have also shown that the magnetic susceptibility of the coloured crystal can well be explained by the concentration of  $F$  centres alone. It is therefore expected that the magnetic changes that occur in coloured alkali halide crystals during thermal bleaching should have a close correspondence with the thermoluminescence data.

## 2. - Experiments and results.

The thermoluminescence and magnetic measurements have been carried out with single crystals of lithium fluoride irradiated by X-rays at room tem-

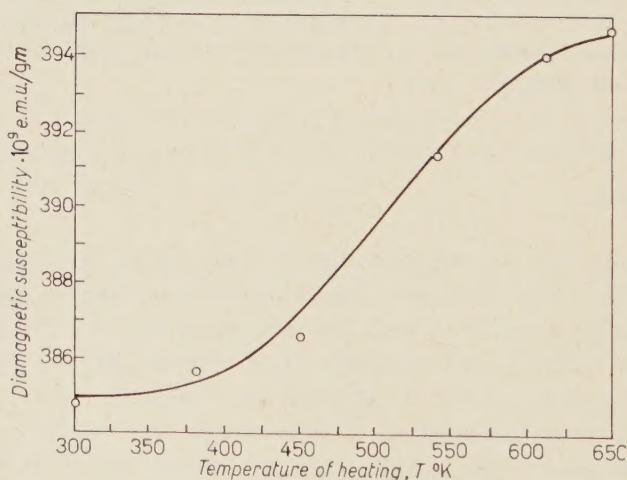


Fig. 1. - The magnetic susceptibility of X-ray ( $7 \cdot 10^5$  R.U.) coloured LiF after thermal bleaching at elevated temperatures.

<sup>(2)</sup> J. SHARMA: *Phys. Rev.*, **87**, 535 (1952); A. HALPERIN and A. BRAUER: *Phys. Rev.*, **108**, 928 (1957).

<sup>(3)</sup> P. PRINGSHEIM and R. YUSTER: *Phys. Rev.*, **78**, 293 (1950); D. DUTTON and R. MAURER: *Phys. Rev.*, **90**, 126 (1953); J. SHARMA: private communication.

<sup>(4)</sup> C. V. HEER and R. T. BATE: *Journ. Phys. Chem. Solids*, **7**, 14 (1958).



perature (27°C). The single crystals were obtained from Harshaw Chemical Company; they were coloured by 30 kV (unfiltered) X-rays from a tungsten target. The dosage of the radiation was measured by a dosimeter (Baldwin

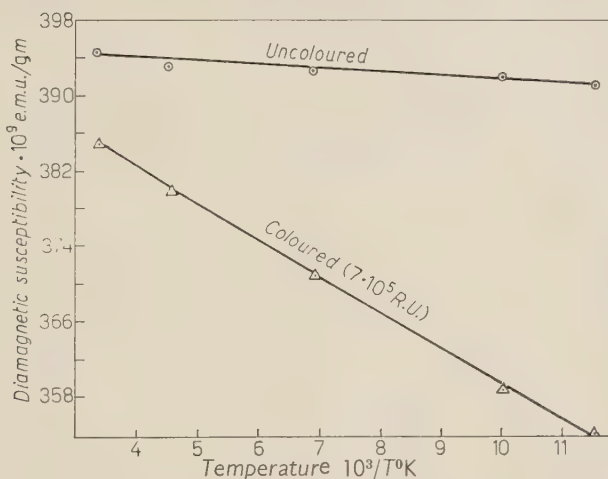


Fig. 2. — The variation of magnetic susceptibility of coloured and uncoloured LiF with the reciprocal of temperature.

Ionex M.K.3). The thickness of the crystals, and the dosage of radiation received by the crystals were approximately the same in all the cases of measurements.

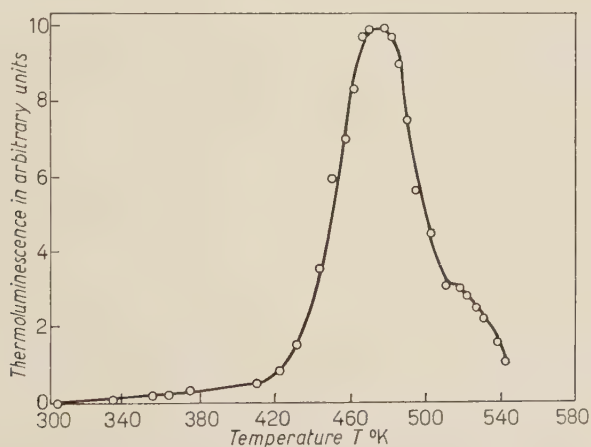


Fig. 3. — The thermoluminescence of LiF irradiated with X-rays ( $7 \cdot 10^5$  R.U.).

The magnetic susceptibility of LiF before and after coloration has been measured at room temperature. The magnetic susceptibilities have also been

measured for samples partially bleached by heating to different temperatures; all measurements have been made after quenching the samples to room temperature. The changes in magnetic susceptibility are shown in Fig. 1. The temperature variation of the magnetic susceptibility of LiF before and after coloration has also been measured between 87°K and 300°K and the results are shown in Fig. 2.

The thermoluminescence of X-ray-irradiated LiF has been measured by the method of Bose<sup>(5)</sup> which is shown in Fig. 3. The change in area of the thermoluminescence curve corresponding to different temperatures has been measured by a planimeter.

### 3. - Discussion.

The decrease in diamagnetic susceptibility due to irradiation *i.e.*  $\Delta\chi$  is a measure of the number of paramagnetic centres created in the process. As expected,  $\Delta\chi$  obeys the Curie law (Fig. 2). Thermal bleaching of colour centres

is attended by thermoluminescence emission. Thus whatever may be the emission mechanism during thermoluminescence the area under the glow curve should be a measure of the number of luminescent centres. In Fig. 4 are shown the changes in area under the glow curve as the temperature of the coloured sample is increased; also the corresponding variation in  $\Delta\chi$  at different stages of bleaching. It is seen (Fig. 4) that there is a similarity between the two corresponding curves. The differences in the behaviour of  $\Delta\chi$  and  $\Delta A$  curves are more pronounced at temperatures well below that of the glow peak. But it is to be remembered that the magnetic data are obtained from the quenched samples at different

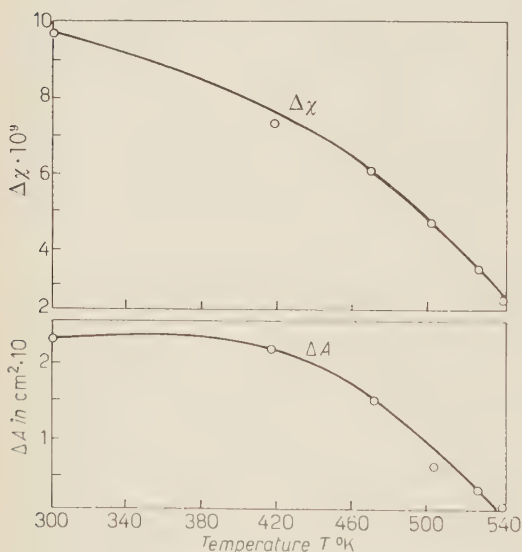


Fig. 4. -  $\Delta\chi$  and  $\Delta A$  as functions of temperature for LiF coloured with X-rays.  $\Delta\chi$  is the change in magnetic susceptibility after the coloured crystals were heat-treated at a particular temperature and  $\Delta A$  is the corresponding change in area of the thermoluminescence curve.

(5) H. N. BOSE and J. SHARMA: *Proc. Nat. Inst. Sci. Ind.*, **26**, 47 (1950); *Proc. Phys. Soc. (London)*, B **66**, 371 (1953).



stages of bleaching, while the thermoluminescence curve is a continuous record of the emission; so that an exact correspondence can not be expected. It has been shown <sup>(3)</sup> that the intensity of the thermoluminescence emission is not controlled only by the number of  $F$  centres destroyed. So it seems, that the magnetic changes are also not due to destruction of  $F$  centres only.

The number of paramagnetic centres has been calculated from the relation  $\Delta K = n\mu^2/kT$  or from the slope of the curve (Fig. 2). The corresponding number of  $F$  centres has been estimated using Smakula's equation. The number of  $F$  centres ( $N_F$ ) is found to be  $9.5 \cdot 10^{17}/\text{cm}^3$  and the corresponding number of magnetic centres ( $N_M$ ) is  $9.2 \cdot 10^{18}/\text{cm}^3$ .

On comparing the values of  $N_F$  and  $N_M$  it is found that the change in magnetic susceptibility cannot be due to  $F$  centres only. One may consider the number of  $F$  centres to be of the same order as the number of  $V$ -type centres. Assuming all such centres to be magnetically equivalent, the number of magnetic centres can be taken as double the number of  $F$  centres. But the discrepancy between the two concentrations is too large to be explained in this manner. The natural conclusion is either the colour centres have magnetic moments higher than the Bohr magneton or X-ray irradiation produces additional paramagnetic centres. The second alternative is indirectly supported by the fact that plastic deformation in these crystals produces considerable decrease in diamagnetic susceptibility. Also it has been reported that large changes in mechanical properties <sup>(6)</sup> of alkali halides are produced by irradiation. So the present result implies that some of the lattice defects other than  $F$  centres produced by X-rays are paramagnetic.

\* \* \*

The author is greatly indebted to Prof. H. N. BOSE of the Indian Institute of Technology, Kharagpur, for his valuable guidance throughout the work and to Prof. S. D. CHATTERJEE for his kind interest in the work.

<sup>(6)</sup> D. R. FRANKL and T. A. READ: *Phys. Rev.*, **89**, 663 (1953).

#### RIASSUNTO (\*)

La suscettività diamagnetica del LiF decresce per irradiazione con raggi X. La differenza di suscettività magnetica del campione prima e dopo la colorazione obbedisce alla legge di Curie. Questo fenomeno è dovuto al paramagnetismo dei centri di colore indotti, in predominanza centri  $F$ . Dopo un completo imbianchimento termico la suscettività diamagnetica riprende il suo valore originario. Si trova che le variazioni della suscettività magnetica, che hanno luogo in stadi diversi dell'imbianchimento termico, corrispondono approssimativamente all'intensità integrata della emissione per termoluminescenza. Dai risultati si conclude che la distruzione dei centri  $F$  non può dar conto della intensità della emissione per termoluminescenza o delle variazioni magnetiche.

(\*) Traduzione a cura della Redazione.

Sul decadimento per cattura elettronica del  $^{37}\text{A}$ .

C. MANDUCHI e G. ZANNONI

*Istituto di Fisica dell'Università - Padova*  
*Istituto Nazionale di Fisica Nucleare - Sezione di Padova*

(ricevuto il 15 Giugno 1961)

**Riassunto.** — Si descrive un'esperienza sul rapporto delle probabilità di decadimento per cattura di elettroni dell'orbita  $L$  e dell'orbita  $K$  relativo al  $^{37}\text{A}$ . Il dispositivo impiegato consiste in due contatori proporzionali coassiali connessi in anticoincidenza. Il rapporto di cattura, dedotto da una serie di dieci misure, risulta in valor medio  $0.0971 \pm 0.0005$ . L'energia corrispondente al picco  $L$  risulta  $(254 \pm 2)$  eV.

## 1. — Introduzione.

Il rapporto delle probabilità di decadimento per cattura di elettroni dell'orbita  $L$  e dell'orbita  $K$  è stato determinato sperimentalmente da diversi autori per vari nuclidi: il disaccordo fra i risultati rende tuttavia incerta la verifica delle previsioni teoriche <sup>(1)</sup>.

In questo articolo si riportano i primi risultati di una serie di misure che ci si propone di svolgere in modo sistematico e, per quanto possibile, esauriente. I risultati qui esposti si riferiscono al  $^{37}\text{A}$ , che decade secondo lo schema:



la transizione è di tipo « permesso ». Il rapporto di cattura  $L_1/K$ , calcolato in base alla teoria di BRYSK e ROSE <sup>(2)</sup>, risulterebbe prossimo a 0.08; introducendo le correzioni proposte da ODIOT e DAUDEL <sup>(3)</sup>, che tengono conto del-

<sup>(1)</sup> B. L. ROBINSON e R. W. FINK: *Rev. Mod. Phys.*, **27**, 424 (1955); **32**, 117 (1960).

<sup>(2)</sup> H. BRYSK e M. E. ROSE: *Rev. Mod. Phys.*, **30**, 1169 (1959).

<sup>(3)</sup> S. ODIOT e R. DAUDEL: *Journ. Phys. et Rad.*, **17**, 60 (1956).



l'effetto di correlazione fra le posizioni degli elettroni, il rapporto si approssima a 0.10, quando si considerino soltanto le correzioni di Pauli, e probabilmente assume un valore anche maggiore se si introducono tutte le correzioni pertinenti. Il contributo al rapporto di cattura  $L/K$  relativo ai sottostrati  $L_{II}$  e  $L_{III}$  è molto piccolo e può essere trascurato.

Le precedenti determinazioni del rapporto di cattura  $L/K$  per il  $^{37}\text{A}$  sono state effettuate con contatori proporzionali. L'interpretazione dei risultati è complicata dal fatto che, per la limitata efficienza del dispositivo, vi è una probabilità non trascurabile di fuga di radiazione. Indichiamo con  $K$  ed  $L$  rispettivamente le probabilità di cattura elettronica dai livelli  $K$  ed  $L$ ; con  $\omega_K$  il rendimento di fluorescenza per raggi X della serie  $K$  del  $^{37}\text{Cl}$  e con  $P$  la probabilità di fuga dal contatore per questi raggi; con  $k$  la percentuale della componente  $K_\alpha$  nella radiazione  $K$  emessa. Ogni evento di cattura  $K$  può dar luogo ad un impulso corrispondente nel contatore: 1) attraverso l'emissione di un fotone della serie  $K$ , che viene assorbito nel gas del contatore, con l'intensità relativa  $K\omega_K(1-P)$ ; 2) attraverso l'emissione di un elettrone Auger, accompagnato a sua volta da raggi X di bassa energia, entrambi assorbiti integralmente nel contatore, con l'intensità relativa  $K(1-\omega_K)$ . Per la cattura  $L$  si hanno analoghe possibilità, con la differenza che la probabilità di fuga per i fotoni  $L$  è trascurabile: l'intensità relativa degli impulsi corrispondenti si può perciò esprimere senz'altro con  $L$ . A questi impulsi si aggiungono però degli impulsi spuri originati dai fotoni  $L$  che accompagnano quei fotoni  $K_\alpha$  che non vengono rivelati dal contatore: l'intensità relativa di questi è data da  $K\omega_K Pk$ . Il rapporto delle aree definite dagli spettri  $L$  e  $K$  risulta pertanto:

$$\frac{N_L}{N_K} = \frac{L/K + \omega_K k P}{1 - \omega_K P}.$$

PONTECORVO *et al.* <sup>(4)</sup> impiegarono un contatore contenente Xe, che per l'alto numero atomico dovrebbe rendere trascurabile la fuga dei fotoni  $K$  e quindi l'intensità relativa degli spettri  $L$  e  $K$  determinerebbe direttamente il rapporto di cattura  $L/K$ : essi trovano un valore compreso fra 0.08 e 0.09; LANGEVIN e RADVANYI <sup>(5)</sup>, usando un metodo analogo, hanno ottenuto  $0.092^{+0.010}_{-0.005}$ . SANTOS-OCAMPO e CONWAY <sup>(6)</sup>, applicando il sistema ad anti-coincidenza descritto da CURRAN *et al.* <sup>(7)</sup>, ottengono, sempre per il  $^{37}\text{A}$ , il valore  $0.103 \pm 0.003$ , che confermerebbe il risultato teorico calcolato in base alle

<sup>(4)</sup> B. PONTECORVO, D. H. W. KIRKWOOD e G. C. HANNA: *Phys. Rev.*, **75**, 982, 985 (1949).

<sup>(5)</sup> M. LANGEVIN e P. RADVANYI: *Compt. Rend.*, **241**, 33 (1955).

<sup>(6)</sup> A. G. SANTOS-OCAMPO e D. C. CONWAY: *Phys. Rev.*, **120**, 2196 (1960).

<sup>(7)</sup> R. W. P. DREVER, A. MOLJK e S. C. CURRAN: *Nucl. Instr.*, **1**, 41 (1957).

correlazioni di Pauli. Gli errori di queste misure vengono ricondotti principalmente: 1) all'incertezza nell'estrapolazione a energia zero dello spettro  $L$ ; 2) alla valutazione della linea di base dello spettro.

Per le nostre misure è stato impiegato un dispositivo analogo, in linea di principio, a quello proposto da CURRAN *et al.* (<sup>7</sup>). Esso consiste in due contatori proporzionali coassiali, connessi in anticoincidenza: il catodo del contatore centrale è costituito da un insieme di fili che ne definiscono il volume sensibile; un altro sistema di fili suddivide il volume circostante in otto contatori proporzionali in parallelo, i quali equivalgono ad un unico contatore coassiale col primo. Il dispositivo registra gli impulsi del contatore centrale, che non coincidono con impulsi di ampiezza corrispondente al livello  $K$  nel

contatore periferico. Eliminati gli impulsi spuri coll'anticoincidenza, gli impulsi  $L$  residui si possono tutti attribuire ad eventi reali di cattura  $L$ ; l'intensità dello spettro  $K$  a sua volta deriva in parte dai fotoni di cattura  $K$  assorbiti nel contatore centrale, e in parte da fotoni  $K_\alpha$  di origine esterna, che compensano con buona approssimazione gli eventi  $K$  non rivelati.

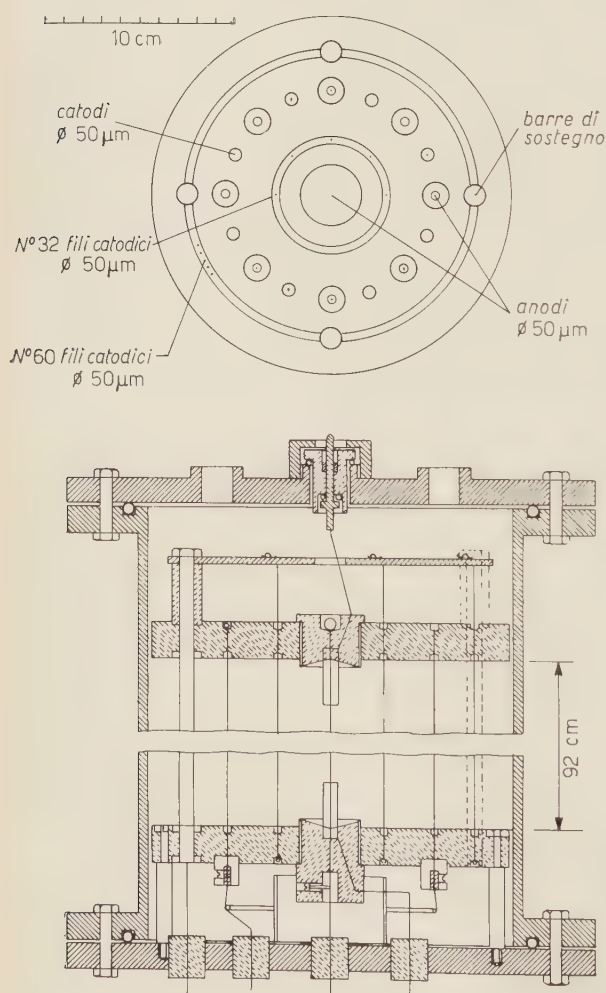


Fig. 1. - Dispositivo sperimentale.

## 2. - Dispositivo sperimentale.

Il sistema di contatori proporzionali impiegato nelle nostre misure è illustrato in Fig. 1. Le piastre terminali, di plexiglas, sono distanziate da barrette metalliche; l'anodo del contatore centrale è costituito da un filo teso fra terminali di teflon, ai quali sono fissati i tubi di campo. Il catodo di questo



contatore è formato da 32 fili distribuiti su una circonferenza di 27.5 mm di raggio: il numero di questi è sufficiente ad eliminare gli effetti inerenti all'accoppiamento induttivo fra il contatore centrale e i contatori periferici. Gli anodi di questi ultimi sono distribuiti su una circonferenza di 55 mm di raggio; essi sono intercalati con altri fili che assieme al catodo del contatore centrale e alla rete di fili più esterna costituiscono i catodi degli otto contatori periferici collegati in parallelo. I fili più esterni, di acciaio armonico di 0.1 mm, sono distribuiti su una circonferenza di 76.5 mm di raggio; tutti gli altri fili sono di tungsteno di 0.05 mm. Sia i catodi che gli anodi del contatore sono isolati dall'involucro; i contatori periferici possono essere alimentati colla stessa tensione del contatore centrale. La lunghezza utile del sistema è di 88 cm; la pressione massima ammissibile per il gas è di 10 atmosfere.

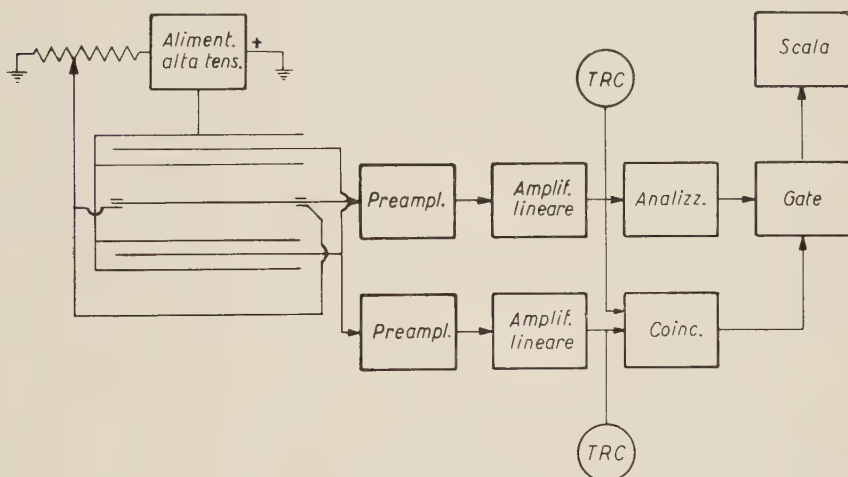


Fig. 2. — Schema funzionale del dispositivo di misura.

In Fig. 2 è riportato lo schema funzionale del dispositivo di misura. Gli impulsi del contatore centrale sono adattati ed amplificati mediante un amplificatore lineare non sovraccaricabile ed inviati ad un analizzatore monocanale. Gli impulsi dei contatori periferici, amplificati con sistema analogo, e gli impulsi amplificati del contatore centrale, sono inviati tramite discriminatori di ampiezza ad un circuito di coincidenza. I segnali dell'analizzatore sono applicati ad un contatore di impulsi tramite un circuito di anticoincidenza: questo risponde solo se l'impulso dell'analizzatore non è accompagnato da un segnale del discriminatore connesso all'uscita del circuito di coincidenza. I tempi di risoluzione delle coincidenze possono variare da 0.5 a 5  $\mu\text{s}$ ; al fine di evitare un eccessivo affollamento di impulsi al sistema di conteggio, è stato predisposto un circuito selettore in grado di anticoincidere gli impulsi con ampiezza supe-

riore ad una soglia prefissata: con questo accorgimento, le correzioni di tempo morto risultano trascurabili.

Il dispositivo di misura è stato tarato con un impulsatore di precisione, i cui transienti hanno caratteristiche analoghe a quelle degli impulsi prodotti dal contatore.

### 3. - Procedimento sperimentale.

Misure preliminari sono state effettuate mediante due sistemi di contatori analoghi a quelli descritti, ma con diverse caratteristiche costruttive, in particolare per il rapporto fra i volumi sensibili dei contatori centrale e periferico, e per il numero dei fili catodici e degli anodi periferici <sup>(8)</sup>. I risultati ottenuti



Fig. 3. - Spettro dei raggi X conseguenti a cattura  $K$  del  $^{37}\text{A}$ , relativo ai contatori periferici.

<sup>(8)</sup> C. MANDUCHI e G. ZANNONI: *Nuclear Electronics* (A.I.E.A., Vienna, 1961).



non differiscono sensibilmente da quelli riportati nel seguito per il contatore impiegato in questa misura, il quale permette peraltro una migliore definizione della linea di base.

Il gas impiegato per il riempimento del contatore è una miscela di argon con  $(8 \div 10)\%$  di metano, depurata su Ca a  $300^\circ\text{C}$  e introdotta in una bombola attraverso un refrigeratore ad azoto liquido. In Fig. 3 è riportato lo spettro  $K$  relativo al contatore periferico: la risoluzione del picco essendo migliore del  $24\%$ , la frazione di eventi  $K$  assorbiti ed esclusi dal discriminatore connesso al circuito di coincidenza è certamente molto piccola.

#### 4. - Risultati.

In Fig. 4 è riportato lo spettro dei raggi X, conseguenti a decadimento del  $^{37}\text{A}$ , relativo al contatore centrale, in anticoincidenza con il contatore peri-

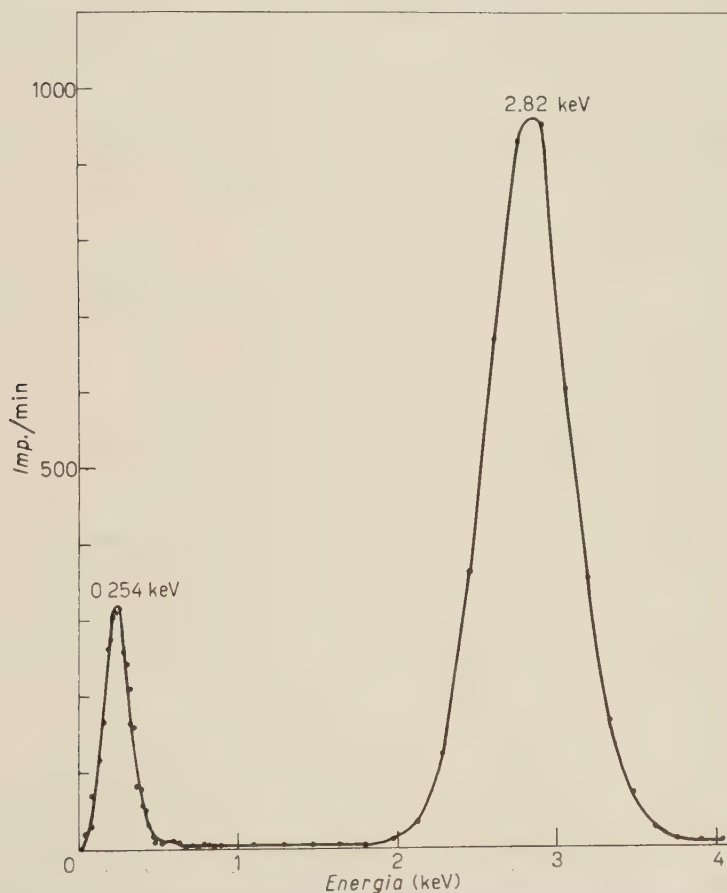


Fig. 4. - Spettro dei raggi X conseguenti a decadimento del  $^{37}\text{A}$ , relativo al contatore centrale in anticoincidenza con i contatori periferici.

ferico; la risoluzione del picco  $K$  risulta migliore del 22%. Il picco  $L$  è mostrato in particolare nella Fig. 5: il fondo naturale, non sottratto allo spettro, è indicato con linea tratteggiata. L'attività presente tra i due picchi sembra doversi attribuire a degradazione della radiazione conseguente a cattura: complessivamente essa non raggiunge il 2% degli eventi  $K$ . Nella valutazione dello spettro  $L$  si è supposto che questa « linea di base » si prolunghi sotto tutto il picco.

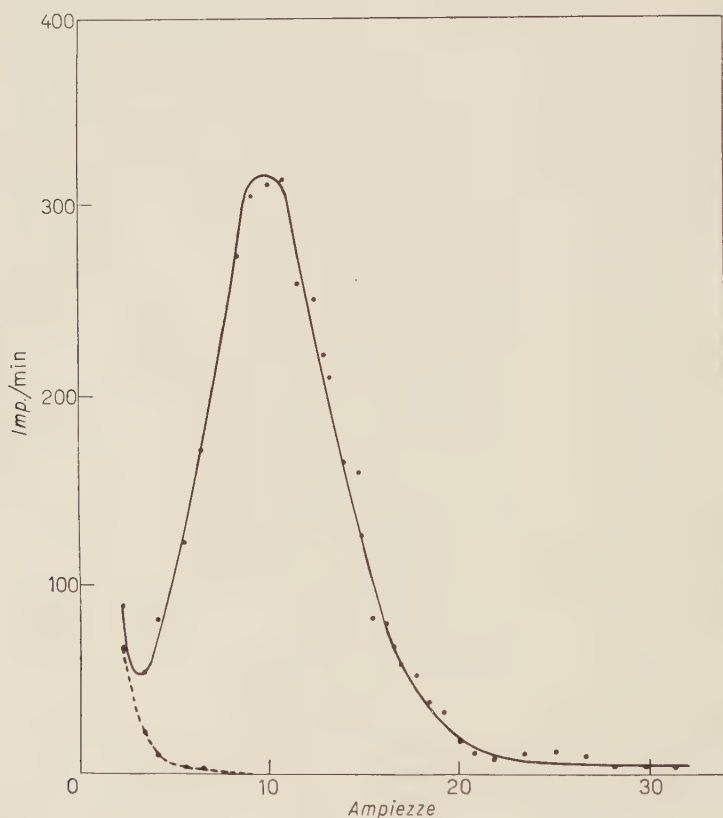


Fig. 5. — Spettro dei raggi X conseguenti a cattura  $L$ , relativo al contatore centrale in anticoincidenza con i contatori periferici. Il fondo naturale, indicato con linea tratteggiata, non è sottratto.

L'intensità degli eventi  $L$  è stata determinata sottraendo al conteggio integrale il fondo naturale e la linea di base, ed aggiungendo l'attività relativa alla zona di bassa energia ( $0 \div 40$ ) eV valutata per estrapolazione grafica. Il contributo inerente a questa estrapolazione si aggira intorno allo 0,5% dell'attività  $L$  totale, e pertanto un errore nella valutazione di esso non influenza sensibilmente il valore del rapporto  $L/K$ .



L'intensità degli eventi  $K$  è stata determinata sottraendo al conteggio integrale il fondo naturale.

Per la valutazione del rapporto di cattura  $L/K$  dalle intensità  $N_L$  e  $N_K$  degli eventi  $L$  e  $K$ , determinate sperimentalmente, è stata applicata la relazione:

$$\frac{L}{K} = \frac{N_L}{N_K} [1 - (P_2 + P_4)\omega_K] - (P_1 + P_2 + P_3)\omega_K k,$$

dove  $P_1$  è la probabilità di fuga dei fotoni  $K$  dalle estremità del contatore centrale,  $P_2$  la probabilità che essi incontrino i fili catodici,  $P_3$  la probabilità che essi attraversino il contatore periferico senza esserne rivelati,  $P_4$  la probabilità che essi raggiungano l'involucro metallico.

Questa relazione differisce da quella proposta da DREVER e MOLJK <sup>(9)</sup> in quanto il nostro dispositivo presenta una zona di gas che isola il sistema di contatori dall'involucro a potenziale zero. La presenza di questa zona comporta una diminuzione della probabilità di fuga dal contatore e migliora la risoluzione del contatore periferico.

I valori delle probabilità  $P_i$  alle diverse pressioni sono stati calcolati secondo PRICE *et al.* <sup>(10)</sup>; in particolare, per la pressione di 3 atmosfere si ottiene  $P_1 = 4.00 \cdot 10^{-3}$ ;  $P_2 = 1.23 \cdot 10^{-3}$ ;  $P_3 = 1.00 \cdot 10^{-5}$ ;  $P_4 = 4.80 \cdot 10^{-7}$ . Per il rendimento di fluorescenza  $\omega_K$  è stato assunto il valore di 0.093 <sup>(11)</sup>, mentre l'ab-

TABELLA I.

Pressione (atm)	Attività (imp/min)	$N_L/N_K$	$L/K$	$E_L$ (eV)
2	26.185	0.0973	0.0965	250
2	26.239	0.0969	0.0961	257
2	30.134	0.0956	0.0948	256
3	25.074	0.0967	0.0961	248
3	17.134	0.0966	0.0960	256
3	23.027	0.0964	0.0958	253
3	27.388	0.0986	0.0980	255
3	17.367	0.0986	0.0980	250
4	19.310	0.1004	0.1000	268
4	19.604	0.0999	0.0995	252
$L/K$ media		$0.0971 \pm 0.0005$		
$E_L$ media		254	$\pm 2$ eV	

<sup>(9)</sup> R. W. P. DREVER e A. MOLJK: *Phil. Mag.*, **2**, 427 (1957).

<sup>(10)</sup> B. T. PRICE, C. C. HORTON e K. T. SPINNEY: *Radiation Shielding* (Londra, 1957), cap. V.

<sup>(11)</sup> F. BERTRAND, G. CHARPAK e F. SUZOR: *Journ. Phys. et Rad.*, **20**, 956 (1959).

bondanza relativa  $k$  dei fotoni  $K_{\alpha}$  nella serie  $K$  è stata considerata prossima all'unità.

I risultati delle misure sono esposti in Tabella I. Il rapporto di cattura  $L/K$  per il  $^{37}\text{A}$  risulta in valor medio 0.0971 con errore standard di 0.0005.

In Tabella I sono riportate, nell'ultima colonna, le energie corrispondenti al massimo del picco  $L$ , ottenute attribuendo al livello  $K$  l'energia di 2.819 keV <sup>(12)</sup>: il valor medio di 254 eV, con errore standard di 2 eV, è maggiore di quello di 238 eV che si ricava per interpolazione dai dati spettroscopici <sup>(13)</sup>.

\* \* \*

Ringraziamo il Prof. A. ROSTAGNI per le utili discussioni sull'argomento del presente lavoro.

---

<sup>(12)</sup> Y. CAUCHOIS: *Journ. Phys. et Rad.*, **16**, 253 (1955).

<sup>(13)</sup> R. D. HILL in K. SIEGBAHN: *Beta- and Gamma-Ray Spectroscopy* (Amsterdam, 1955), pp. 914-919.

---

## SUMMARY

The  $L$  and  $K$  X-radiations of  $^{37}\text{Cl}$  resulting from orbital-electron capture have been studied using a special multiwire proportional counter system. The  $L/K$ -capture ratio of  $^{37}\text{A}$  has been determined to be  $0.0971 \pm 0.0005$ . The average energy of the  $L$  peak was found to be  $(254 \pm 2)$  eV.



## The Angle of Divergence of Pairs Produced by Photons in a Crystal.

A. LEVI

*Istituto di Fisica dell'Università - Genova*

(ricevuto il 24 Luglio 1961)

**Summary.** — The distribution of the angle of divergence of pairs produced by high-energy photons in a crystal differs in many features from the usual one-atom distribution. This difference is calculated by taking into account the number of reciprocal points corresponding to the various angles. The result is, that, if the photon beam incides on the crystal normally to a lattice plane, although the total cross-section is less than the one-atom cross-section, there are some angles where large constructive interferences occur. If, on the other hand, the photon beam makes a small but finite angle  $\theta$  with the normal to a lattice plane, the crystal distribution oscillates around the one-atom distribution. Numerical calculations have been performed by means of an « IBM 650 » computer.

### Introduction.

The total cross-section for pair production by photons in a crystal has been studied by ÜBERALL <sup>(1)</sup>. I evaluate here by similar methods the effects of the crystal structure on the distribution of the angle of divergence of the pair, which in the following will be termed simply the pair angle. Natural units are chosen ( $\hbar = c = m = 1$ ).

The essential quantity which defines the interference properties of the crystal is, in the Born approximation <sup>(1)</sup>

$$(1) \quad NF = \left| \sum_{\mathbf{L}} \exp [i\mathbf{q} \cdot \mathbf{L}] \right|^2,$$

where  $\mathbf{q}$  is the momentum transfer,  $\mathbf{L}$  is any lattice vector, and  $N$  is the total

<sup>(1)</sup> H. ÜBERALL: *Phys. Rev.*, **103**, 1055 (1956).

number of atoms in the crystal.  $F$  is called the (perfect) lattice structure factor and it can receive a simple geometrical meaning, as we shall see later. The net effect of the crystalline structure on the differential cross-section is multiplication by the factor

$$(2) \quad F' = \exp[-Aq^2](F - 1) + 1,$$

$F'$  is the « real lattice structure factor ».  $A$  is a function of temperature, depending on the crystal properties, and representing approximately the mean square reticular vibration. It can be calculated in Einstein's approximation, in Debye's approximation as ÜBERALL does, or in a better approximation as in Schiff's paper <sup>(2)</sup>, but its exact value is not really important (besides the order of magnitude) as long as it is small enough, and in any case can affect only the numerical values but not the mean features of the phenomenon.

Both  $F$  and  $F'$  are functions of  $\mathbf{q}$  which, as it is easy to see, by referring to a representation in the reciprocal lattice, become improper in the limit of an infinite crystal, and in practice for macroscopic crystals. In fact if we define the cell structure factor

$$(3) \quad nf = \left| \sum_1^n \exp[i\mathbf{q} \cdot \mathbf{l}] \right|^2,$$

where the sum runs over the atoms contained in the cell, we find

$$(4) \quad F = \frac{n}{N} f \prod_{i=1}^3 \frac{\sin^2 \pi N_i q_i}{\sin^2 \pi q_i} \left( \mathbf{q} = \sum_{i=1}^3 q_i \mathbf{b}_i; \quad \mathbf{a}_k \cdot \mathbf{b}_i = 2\pi \delta_{ik} \right).$$

So  $F$  is negligible unless all the  $q_i$ 's are integers, in which case it is equal to  $n^{-1}Nf$ , that is, very large. Only the reciprocal lattice vectors contribute.

On the other hand, it is easy to see that the function  $f - 1$  (which needs to be considered only for integer  $q_i$ 's) is an oscillating function, and we can say that its mean value is small over a region in  $q$ -space whose smallest size is larger than the inverse of all the distances between the atoms in the cell. The mean value of  $f$ , and therefore of  $F$ , over such a region is close to 1.

The mean  $\bar{F}$  of  $F$  is equal to the sum of the  $f$ 's corresponding to the points contained in the region divided by the volume of the region measured in cells of the reciprocal lattice.

If now so small a region is considered, that the electrodynamical cross-section, written as a function of  $\mathbf{q}$ , be approximately constant in it and equal to  $d\sigma/dS$ , and if the measure of the region is called simply  $\delta S$ , that region will

<sup>(2)</sup> L. I. SCHIFF: *Phys. Rev.*, **117**, 1394 (1960).

contribute to the total cross-section, in the amorphous case, the amount

$$(5) \quad \sigma_{am}(\delta S) = \frac{d\sigma}{dS} \delta S.$$

In the crystalline case, if also the factor  $\exp[-Aq^2]$  can be considered approximately constant in  $\delta S$ , the same region will contribute instead the amount

$$(6) \quad \sigma_{cr}(\delta S) = \bar{F}' \sigma_{am}(\delta S) = \sigma_{am}(\delta S) + \exp[-Aq^2](\bar{F}' - 1) \frac{d\sigma}{dS} \delta S,$$

If we are interested in the contribution to the cross-section of a large region  $S$  of the  $q$ -space we merely have to break it down into smaller regions  $\delta S_i$ :

$$(7) \quad \sigma_{cr}(S) - \sigma_{am}(S) = \sigma'(S) - \sigma''(S)$$

having called

$$(8) \quad \sigma'(S) = \sum_i \exp[-Aq_i^2] \bar{F}(\delta S_i) \left( \frac{d\sigma}{dS} \right)_i \delta S_i$$

$$(8') \quad \sigma''(S) = \int_S \exp[-Aq^2] \frac{d\sigma}{dS} dS.$$

It is possible to write  $\sigma''$  as an integral, but not  $\sigma'$  because of the ensemble function  $\bar{F}$ . However, even to calculate  $\sigma'$ , a passage to the limit is necessary (we shall make the largest diameter of the small regions tend to zero) which will have to be made in a way depending on the special problem to be discussed.

I call  $\sigma'$  the interference correction and  $\sigma''$  the vibration correction. Both contain the factor  $\exp[-Aq^2]$  which, decreasing rapidly as  $q$  increases ( $A$  is at least of order 100), will allow drastic approximations, and it will be possible consequently to write  $\sigma'$  and  $\sigma''$  in closed form.

## 1. - The pair angle and its representation.

The pair angle  $\omega$  is connected with the total momentum of the pair  $\mathbf{p}_+ + \mathbf{p}_- = \boldsymbol{\eta}$ , by means of the following relation:

$$(9) \quad p_+^2 + p_-^2 + 2p_+ p_- \cos \omega = \eta^2.$$



On the other hand as the photon momentum  $k$  and  $y = \varepsilon_+/k$  are kept fixed,  $p_+$  and  $p_-$  remain fixed too, because of the energy relations  $(\varepsilon_+ + \varepsilon_- = k)$ :

$$(10) \quad p_+^2 + 1 = \varepsilon_+^2 = k^2 y^2,$$

$$(10') \quad p_-^2 + 1 = \varepsilon_-^2 = k^2(1 - y)^2.$$

I neglect Schiff's correction <sup>(2)</sup>, because for pair production any long range effect of the crystal potential  $V_{cr}$  cannot affect appreciably the electron waves as long as  $k$  is small compared with  $1/V_{cr}$  which is of the order 100 GeV.

So we have a one-to-one correspondence between  $\eta$  and  $\omega$ : as  $\omega$  varies from 0 to  $\pi$ ,  $\eta$  decreases monotonically, from  $p_+ + p_-$  to  $|p_+ - p_-|$ . On the other hand, momentum conservation gives

$$(11) \quad \mathbf{k} = \mathbf{q} + \boldsymbol{\eta}$$

and consequently, as  $\eta$  is fixed, the distance between the varying point in  $q$ -space and the end of  $\mathbf{k}$  is fixed, that is any surface  $\eta = \text{const}$  in  $q$ -space is a sphere, having the end of  $\mathbf{k}$  as its centre and  $\eta$  as radius, and it is at the same time a surface  $\omega = \text{constant}$ . As  $\eta$  is less than  $k$ , these spheres do not contain the origin, but pass near it.

But since we are now interested only in the interference and vibration corrections, which become substantially small for  $q \gtrsim 1/\sqrt{A}$ , we are allowed to consider not all the surface of these spheres, but just the small area near the origin of  $q$ -space and contained in a sphere having the origin as its centre and  $\sim 1/\sqrt{A}$  as radius; that area does not exist unless the minimum value of  $q$  (which is approximately  $2/k$ ) becomes small enough, that is  $k$  must be far away from threshold. But when  $k$  is large enough, so is  $\eta$  compared with  $q$  and the solid angle becomes so small that the area can be approximated with a plane. In fact the maximum value reached by the solid angle is approximately  $\pi/16A^2$ , that is extremely small for all solids, even at 0 °K. Thus we can consider approximately plane circles.

The calculation of  $\sigma''$  presents no difficulties: we merely have to integrate the differential cross-section, multiplied by  $\exp[-Aq^2]$ , over these circles or over the whole planes, which is about the same thing because of the exponential factor. But to calculate  $\sigma'$ , it is necessary to consider the position of the vector  $\mathbf{k}$  with respect to the reciprocal lattice. We can introduce here Überall's hypothesis: that a crystal plane exists, being almost perpendicular to the vector  $\mathbf{k}$ . Corresponding to this, there is in the reciprocal lattice a crystal axis (which henceforth will be termed simply the axis) forming with  $\mathbf{k}$  a small angle  $\theta$ , the crystal angle. Otherwise, as we shall see, the difference between  $\sigma'$  and  $\sigma''$ , that is between the crystal cross-section and the amorphous one,

is small. The hypothesis allows us to overcome the bulk of the difficulties arising from crystal structure. Like ÜBERALL, we shall approximate all crystal planes normal to the axis with continuous planes and so reduce the crystal to a succession of planes.

In this case we shall be able to say that  $\bar{F}$  is just the ratio between the sum of the  $f$ 's referring to the various planes times the areas of those planes contained in the region, and the volume of the region divided by  $2\pi/a$ ; the last quantity is the distance between the neighbouring planes, if  $a$  is the lattice constant in the direction conjugate to the axis. The axis must have a direction bearing a simple relation to the crystal structure, but may not have one of the principal directions: for instance in the cubic structure, all we said is true even if we chose the diagonal in place of the side of the cube.

The crystal behaves now as an unidimensional lattice, and  $f$  can be reduced to a succession of numbers  $f_h$ , where  $h$  is the order number of the plane starting from the origin, (we use Überall's notation here) in the form:

$$(12) \quad f_h = \frac{2}{\eta} \sum_1^n_{k < k'} \cos 2\pi h d_{kk'} + 1,$$

where  $d_{kk'}$  is the component of the distance between the  $k$ -th and the  $k'$ -th atom in the cell in the direction conjugate to the axis.

## 2. - The electro-dynamical cross-section.

It is possible to write the Bethe-Heitler differential cross-section, in the case of exponential screening, in the following form:

$$(13) \quad d\sigma = \sigma_0 \frac{1}{2\pi\eta} \frac{\bar{W}}{(q^2 + q_0^2)^2} dS,$$

where  $d\sigma$  is cross-section in  $q$ -space, and we have put

$$(14) \quad \bar{W} = W_1 + W_2 + W_3 + 4,$$

where

$$(14') \quad W_1 = [k^2(1 + x^2) - \lambda^2 - \xi^2](A_+ R_+^{-\frac{3}{2}} + A_- R_-^{-\frac{3}{2}}),$$

$$(14'') \quad W_2 = -2k^2 x (A_+ R_+^{-\frac{3}{2}} - A_- R_-^{-\frac{3}{2}}),$$

$$(14''') \quad W_3 = - \left\{ \frac{2k^2(1 - x^2) + (\lambda^2 + \xi^2)[2 - 2k\lambda + \lambda^2 - k^2(1 + x^2)]}{k\lambda + \frac{1}{2}\xi^2} + 2k\lambda + \xi^2 \right\} (R_+^{-\frac{1}{2}} + R_-^{-\frac{1}{2}}),$$

and

$$A_{\pm} = B \pm \times C; \quad R_{\pm} = S \pm xT + x^2U, \quad B = \frac{1}{2}k\lambda + \frac{1}{4}\xi^2;$$

$$C = \frac{1}{2}k^2 \frac{\frac{1}{2}\xi^2 - \lambda(k - \lambda)}{(k - \lambda)^2}; \quad S = \lambda^2 + \xi^2 + \frac{1}{4} \frac{k^2 - 4}{(k - \lambda)^2} \left[ \lambda(k - \lambda) - \frac{1}{2}\xi^2 \right];$$

$$T = \frac{1}{2} \frac{k^2}{(k - \lambda)^2} \left[ \frac{1}{4}\xi^4 - \lambda^2 \left( k^2 - k\lambda + \frac{1}{2}\xi^2 \right) \right]; \quad U = \frac{1}{4} \frac{k^2}{(k - \lambda)^2} \left( k\lambda + \frac{1}{2}\xi^2 \right).$$

We have put in all these formulas:

$$x = 2y - 1; \quad \lambda = k - \eta; \quad \xi = \sqrt{q^2 - \lambda^2};$$

besides

$$\sigma_0 = \alpha^3 Z^2 = 3.8585 \cdot 10^{-7} Z^2; \quad q_0 = 9.01 \cdot 10^{-4} Z^{-\frac{1}{2}}.$$

These expressions have been obtained by BORSELLINO (private communication) and appear only slightly transformed here. Now I shall introduce the notations:

$$s = \frac{1}{1 - x^2}; \quad z = \frac{1}{k\lambda}; \quad u = \frac{1}{2}z\xi^2.$$

The maximum value of  $z$  is approximately  $(2/s) > 2$ ; and we can take  $\xi^2$  smaller than  $A^{-1}$ . As a consequence  $u$  is of order  $10^{-2}$  or less and it is possible to neglect its square. Besides we shall suppose that the energy is large ( $k \gg m$ ). These approximations give, in the first order in  $u$ ,

$$(15) \quad \bar{W} \approx 8k^2 z [(1 + x^2)s + 4sz(1 - 2sz)]u,$$

or

$$(16) \quad \bar{W} \approx 4\tau \frac{\xi^2}{\lambda^2},$$

having put

$$(17) \quad \tau = 2s - 1 + 2t - 2t^2; \quad t = \frac{1}{1 + \left( \frac{\omega}{\omega_0} \right)^2}; \quad \omega_0 = 4 \frac{s}{k},$$

where  $\omega_0$  is the characteristic angle of the pair. Substituting (16) into (13)



we find

$$(18) \quad d\sigma \approx \frac{\sigma_0}{2\pi k \lambda^2} \frac{4\tau \xi^2}{(q^2 + q_0^2)^2} dS.$$

On the other hand, we have

$$dS = dq_x dq_y dq_z \approx d\xi_x d\xi_y d\lambda = d\xi_x d\xi_y \left| \frac{d\lambda}{d\omega} \right| d\omega \approx \frac{\omega}{\omega_0} d\xi_x d\xi_y d\omega,$$

and finally we find

$$(19) \quad \frac{d\sigma}{d\omega} \approx \frac{\sigma_0}{2\pi k \lambda^2} \frac{\omega}{\omega_0} \frac{4\tau \xi^2}{(q^2 + q_0^2)^2} d\xi_x d\xi_y.$$

Now we are ready to evaluate the interference and vibration corrections. We shall begin with the former, which depends on the crystal angle  $\theta$ . It is necessary to consider separately the case  $\theta = 0$ , as it presents singularities in the cross-section. For the moment, we shall suppose  $\theta \neq 0$ .

### 3. - Interference correction: $\theta \neq 0$ .

When  $\theta$  is different from zero, the sphere, corresponding to  $\omega$  fixed, cuts a large number of lattice planes. Such planes can be given the label  $h$ , an integer from  $-\infty$  to  $+\infty$ , in such a way that the vector  $\mathbf{k}$  points towards the positive  $h$ 's. The interference correction is a series whose terms refer to the various harmonics in the Fourier expansion of the potential in the direction conjugate to the axis.

To calculate any term of the series it is necessary to study the behaviour of the mean perfect lattice structure factor  $\bar{F}$ . We shall begin by choosing our region, over which to average. If the sphere  $\omega = \text{const}$  (which will be approximated with a plane as usual) is given a small thickness  $b$ , the  $h$ -th plane will cut it along two straight lines, which define a long rectangular stick whose short sides are  $b$  and  $b \operatorname{ctg} \theta$ . Following our definition, we find

$$(20) \quad \bar{F} = \frac{2\pi}{a} f_h \frac{\frac{b}{\sin \theta}}{b^2 \operatorname{ctg} \theta} = \frac{2\pi f_h}{ab \cos \theta}.$$

Now the  $x$ -axis is taken in the plane of  $\mathbf{k}$  and its projection on the  $h$ -plane, the  $y$ -axis in the  $h$ -plane, and the  $z$ -axis in the direction of  $\mathbf{k}$ . If we divide the stick into small slices  $\delta S_i$  of length  $\delta q_{yi}$ , the mean  $\bar{F}$  in each slice will be

the same, and we shall have

$$(21) \quad \bar{F}(\delta S_i) \delta S_i = \frac{2\pi f_h}{ab \cos \theta} b^2 \operatorname{ctg} \theta \delta q_{yi} = \frac{2\pi b}{a \sin \theta} f_h \delta q_{yi}.$$

It is possible to put  $\delta q_{yi} = \delta \xi_{yi}$ ; and  $b = \delta \lambda = (\omega/\omega_0) d\omega$ . Thus we find

$$\frac{d\sigma'_h}{d\omega} = \sum_i \exp[-Aq_{hi}^2] \frac{2\pi}{a \sin \theta} f_h \left( \frac{d\sigma}{dS} \right)_{hi} \frac{\omega}{\omega_0} \delta \xi_y,$$

and taking the limit  $\delta \xi_{yi} \rightarrow 0$  we obtain

$$(22) \quad \frac{d\sigma'_h}{d\omega} = 2 \frac{\sigma_0 \tau' \omega}{a \sin \theta \lambda^2} f_h \int_0^\infty \exp[-Aq_h^2] \frac{\xi_h^2}{(q_h^2 + q_0^2)^2} d\xi_y,$$

having put

$$\tau = s\tau'; \quad q_h^2 = \lambda^2 + \xi_h^2; \quad \xi_h^2 = \xi_y^2 + r_h^2; \quad r_h = \lambda \operatorname{ctg} \theta - \frac{2\pi h}{a \sin \theta}.$$

For sake of simplicity we shall now introduce new notations:

$$A = A\lambda^2; \quad Q_0 = Aq_0^2; \quad R_h = Ar_h^2; \quad Y_h = Q_0 + R_h + A.$$

The integration can be performed and gives

$$(23) \quad \left\{ \begin{array}{l} \frac{d\sigma'}{d\omega} = \sum_{-\infty}^{+\infty} \frac{d\sigma'_h}{d\omega}, \\ \frac{d\sigma'_h}{d\omega} = \frac{\sigma_0 \tau' \omega}{a \sin \theta} A^{\frac{3}{2}} \frac{\exp[Q_0]}{A} f_h C_h, \\ C_h = \pi \left[ 1 - (1 + Q_0) \left( \frac{1}{2Y_h} - 1 \right) \right] Y_h^{-\frac{1}{2}} \operatorname{erfc} Y_h^{-\frac{1}{2}} - \sqrt{\pi} (1 + Q_0) Y_h^{-1} \exp[-Y_h], \end{array} \right.$$

(erfc is the complement to the usual error integral).

#### 4. - Interference correction: $\theta = 0$ .

When  $\theta$  is equal to zero, in general there is no interference, since the sphere  $\omega = \text{const}$  cuts the reciprocal lattice planes far outside the region surrounding the origin in which the reticular vibrations do not cancel the whole effect. Only for

such values of  $\omega$ , that the sphere  $\omega = \text{const}$  be approximately tangent to one of the  $h$ -planes, is the interference possible and even extremely strong. I shall call  $\omega_h$  those exceptional values of  $\omega$ : clearly,  $h$  can be only positive in this case.

Now the interference correction to the distribution of the pair angle is a kind of «line spectrum», and we are interested not so much in the shape of the lines as in their position and intensity (*i.e.* the total interference correction corresponding to the line of order  $h$ ).

The position of the line is found without any difficulties. It is defined by the condition that  $\lambda$  be equal to an integer  $h$  times the reciprocal reticular parameter  $2\pi/a$ ; on the other hand we have approximately

$$(24) \quad \lambda = 2 \frac{s}{k} + \frac{1}{8} \frac{k}{s} \omega^2,$$

and so we find

$$(25) \quad \omega_h \approx 4 \sqrt{\frac{h\pi s}{ka} - \frac{s^2}{k^2}}.$$

Hence we see that the line of order  $h$  exists only if  $k/s$  is greater than  $a/h\pi$ ; thus, as the photon energy increases, the line of order 1, which afterwards will be the strongest of all, appears last.

To calculate the intensity there are two equivalent possible methods. The direct method is the integration of  $d\sigma'_h$  over all pair angles before taking the limit  $\theta \rightarrow 0$ .

But it is much easier to relate the intensity of a line to the vibration correction, to be calculated in the next section. In fact we have

$$\begin{aligned} (26) \quad \sigma'_h(0) &= \lim_{\theta \rightarrow 0} \int_0^\infty \frac{d\sigma'_h}{d\omega} d\omega = \lim_{\varepsilon \rightarrow 0} \lim_{\theta \rightarrow 0} \int_{\omega_h - \varepsilon}^{\omega_h + \varepsilon} \frac{d\sigma'}{d\omega} d\omega = \lim_{\delta \rightarrow 0} \lim_{\theta \rightarrow 0} \int_{2\pi h/a - \delta}^{2\pi h/a + \delta} \frac{d\sigma'}{d\lambda} d\lambda = \\ &= \lim_{\delta \rightarrow 0} \lim_{\theta \rightarrow 0} \bar{F}\left(\theta, \frac{2\pi h}{a}, \delta\right) \int_{2\pi h/a - \delta}^{2\pi h/a + \delta} \frac{d\sigma''}{d\lambda} d\lambda = \lim_{\delta \rightarrow 0} \bar{F}\left(0, \frac{2\pi h}{a}, \delta\right) \left(\frac{d\sigma''}{d\lambda}\right)_{\lambda = 2\pi h/a} 2\delta = \\ &= \left(\frac{d\sigma''}{d\lambda}\right)_{\lambda = 2\pi h/a} \lim_{\delta \rightarrow 0} \frac{(2\pi/a)f_h}{2\delta} 2\delta = \frac{2\pi}{a} \frac{(d\sigma''/d\omega)_{\omega = \omega_h}}{(d\lambda/d\omega)_{\omega = \omega_h}} f_h, \end{aligned}$$

and so we are allowed to obtain the intensity of the line from the vibration correction calculated at the line. The direct calculation gives the same result, of course.



Now we shall say something about the «natural breadth» of such a line. To evaluate it we can reason as follows; the sphere  $\omega = \omega_h$  does not really coincide with the  $h$ -plane, it is only tangent to it, and the plane, in a region far apart from the axis, will go through larger spheres, *i.e.* smaller  $\omega$ 's. But because of the factor  $\exp[-Aq^2]$  of which the significant part refers to the component of  $\mathbf{q}$  perpendicular to the axis, the broadening is very small. In fact we have

$$q_{\perp}^2 = \eta_{\perp}^2 = \eta^2 - \eta_{\parallel}^2 = 2p_+p_- (\cos \omega - \cos \omega_h) \approx \frac{1}{2} \frac{k^2}{s} \omega_h (\omega_h - \omega).$$

So we can say that the line has a natural breadth of order

$$(27) \quad \delta_h = \frac{2s}{k^2 A \omega_h}.$$

In practical cases  $\delta_h$  may be some  $10^{-7}$  rad at 1 GeV.

## 5. - The vibration correction.

Taking polar co-ordinates in the  $\xi$ -plane we have

$$dS \approx \left| \frac{d\lambda}{d\omega} \right| \xi d\omega d\xi d\varphi,$$

and therefore

$$\frac{d\sigma''}{d\omega} \approx \left| \frac{d\lambda}{d\omega} \right| \int_0^{2\pi} d\varphi \int_0^{\infty} \exp[-Aq^2] \frac{d\sigma}{dS} \xi d\xi,$$

where the spheres  $\omega = \text{const}$  have been approximated with planes as usual. On the other hand, as

$$\frac{d\sigma}{dS} = \frac{\sigma}{2\pi k \lambda^2} 4\tau \frac{\xi^2}{(\xi^2 + \lambda^2 + q_0^2)^2},$$

does not depend on  $q$ , the factor  $2\pi$  at the denominator cancels, and we have

$$(28) \quad \begin{aligned} \frac{d\sigma''}{d\omega} &= \left| \frac{d\lambda}{d\omega} \right| \exp[-A\lambda^2] \frac{\sigma_0}{k\lambda^2} 4\tau \int_0^{\infty} \exp[-A\xi^2] \frac{\xi^2}{(\xi^2 + \lambda^2 + q_0^2)^2} \xi d\xi = \\ &= \frac{1}{2} \sigma_0 \omega \tau' \left[ - \left( \frac{1+Q_0}{A} + 1 \right) \exp[Q_0] E_i(-A-Q_0) - \frac{\exp[-A]}{A} \right]. \end{aligned}$$

The calculation of the correction (due to the crystal) to the distribution of the pair angles is now complete. Of course the distribution itself is not very well known even in amorphous substances, and so the formulas are more suitable for a comparison between the pair production at various  $\theta$ 's than for a direct quantitative measurement.

Finally we have to show that, if  $\theta$  is not rather small,  $\sigma'$  does not differ much from  $\sigma''$ , and therefore the total correction is small. This corresponds simply to show that for large  $\theta$  the sum

$$\frac{2\pi}{a \sin \theta} \sum_{-\infty}^{+\infty} f_h \frac{r_h^2 + q_y^2}{(r_h^2 + q_y^2 + \lambda^2 + q_0^2)^2} \exp[-A(r_h^2 + q_y^2 + \lambda^2)],$$

can be approximated with the integral

$$\int_{-\infty}^{+\infty} \frac{q_x^2 + q_y^2}{(q_x^2 + q_y^2 + \lambda^2 + q_0^2)^2} \exp[-A(q_x^2 + q_y^2 + \lambda^2)] dq_x.$$

In fact  $r_h$  is the  $q_x$  corresponding to a given  $h$ -plane, and we have  $|r_{h+1} - r_h| = 2\pi/a \sin \theta$ . Besides the average of  $f_h$  is 1. We have merely to show that the difference between the integrand  $\Omega$  calculated at the plane  $h$  and the same integrand at the plane  $h+1$  is negligible: we have the condition

$$\frac{2\pi}{a \sin \theta} \left| \frac{d\Omega}{dq_x} \right| \ll \Omega,$$

whence we draw

$$(29) \quad \sin \theta \gg \frac{2\pi}{a} \left| \frac{d}{dq_x} \ln \Omega \right| = \frac{4\pi q_x}{a} \left( \frac{1}{q_x^2 + q_y^2} - \frac{2}{q_x^2 + q_y^2 + \lambda^2 + q_0^2} - A \right) \left| \approx \frac{4\pi |q_x| A}{a} \approx \frac{4\pi \sqrt{A}}{a} \right|,$$

(taking into account the fact that  $|q_x|$  is of order  $1/\sqrt{A}$ ). In the case of diamond, at absolute zero, this would be equivalent to  $\theta \gg 8^\circ$ . So the condition is very stringent, and in fact the correction may not be negligible even at fairly large crystal angles. In this case, however, the full symmetry of the crystal must be taken into account. Our treatment, as well as Überall's, is valid only for small  $\theta$ 's.

## 6. — Results.

The numerical calculations have been performed by means of the digital computer IBM 650 of the «Centro di Calcolo Numerico dell'Università di Genova». The series appearing in (23) converges rapidly.

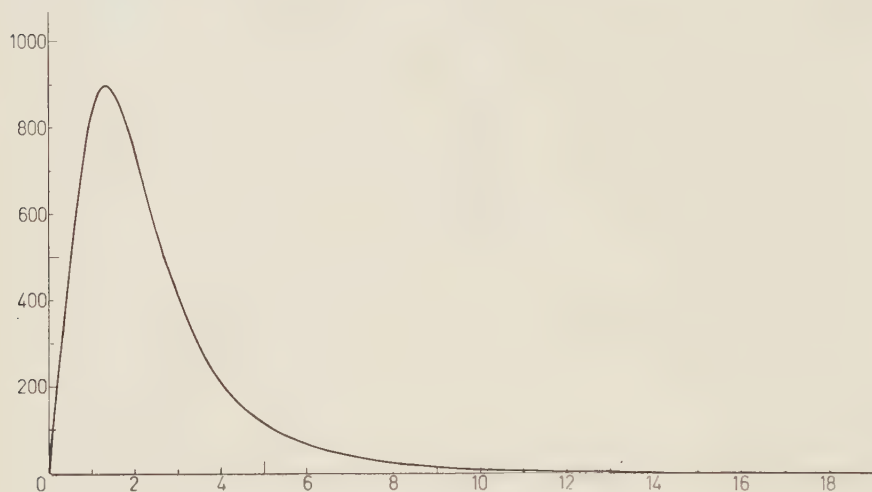


Fig. 1. — Vibration correction in diamond along a principal axis at room temperature.

The behaviour of the net correction has been plotted *vs.*  $\omega$  for various values of  $\theta$ . Diamond was chosen for numerical computation, as it presents large Überall effect even at room temperature, because of its high Debye temperature. For sake of simplicity, the side of the cube was chosen as the axis. The photon energy was taken to be equal to 1 GeV, and  $\gamma$  to be  $\frac{1}{2}$  (equipartition).

TABLE I. — Numerical values of  $\omega_h$  and  $\sigma_h$ .

$h$	$\omega$	$\sigma_h/\sigma_0$
1	0.004867	0.353437
2	0.007180	0.066715
3	0.008911	0.022449
4	0.010358	0.009507
5	0.011625	0.004566
6	0.012767	0.002374
7	0.013816	0.001303
8	0.014790	0.000743
9	0.015703	0.000463
10	0.016567	0.000261



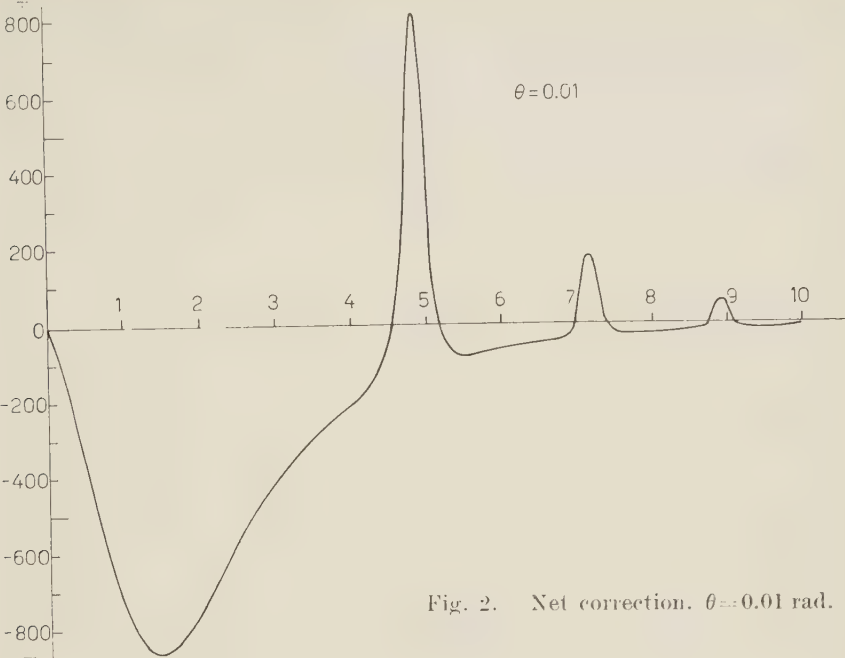


Fig. 2. Net correction.  $\theta=0.01$  rad.

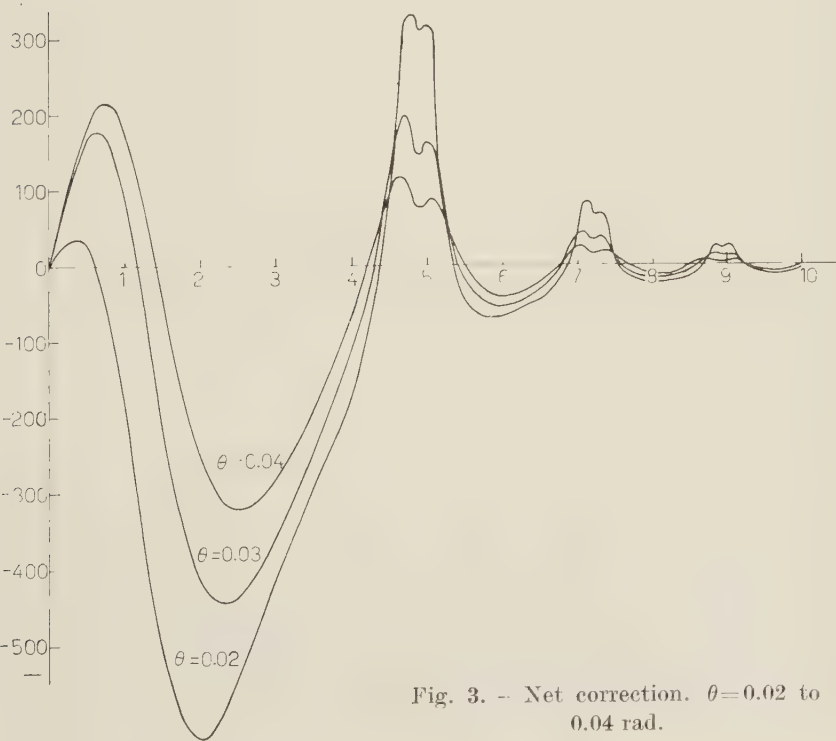


Fig. 3. - Net correction.  $\theta=0.02$  to  $0.04$  rad.

In the case  $\theta = 0$ , apart from the lines, we see just the vibration correction, which is a net negative correction with a minimum in the region of the small  $\omega$ 's (around 1.35 millirad), and falling exponentially to zero beyond say 10 millirad. So the small angle region is affected negatively by the crystal, and the mean pair angle is thereby increased. The lines are found rather in the large angle region. Their intensity and position are given in Table I.

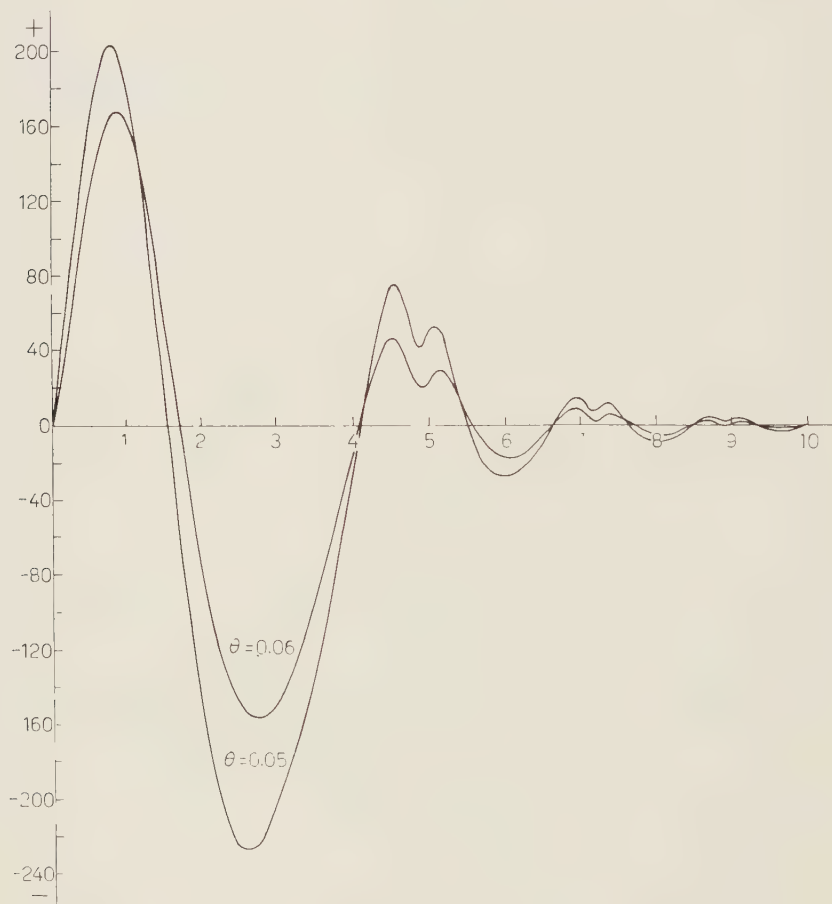


Fig. 4. — Net correction.  $\theta = 0.05$  and  $0.06$  rad.

The intensity is to be compared with the total intensity of symmetric pair production, which, in the same units, is 12.19 (for amorphous carbon at the high energy limit). So the first line gives a corrections of about 3% of all symmetric pairs. Increasing  $\theta$ , the lines begin to broaden and at the same time the principal minimum becomes weaker. Near  $\theta = 20$  millirad two new facts appear: the net correction in the region of very small  $\omega$ 's becomes posi-

tive (the plane  $h=0$  contributes more and more) and the maxima appear doubled. The last fact was unexpected. Then, as  $\theta$  increases, the maximum corresponding to  $h=0$  grows, while the principal minimum diminishes and

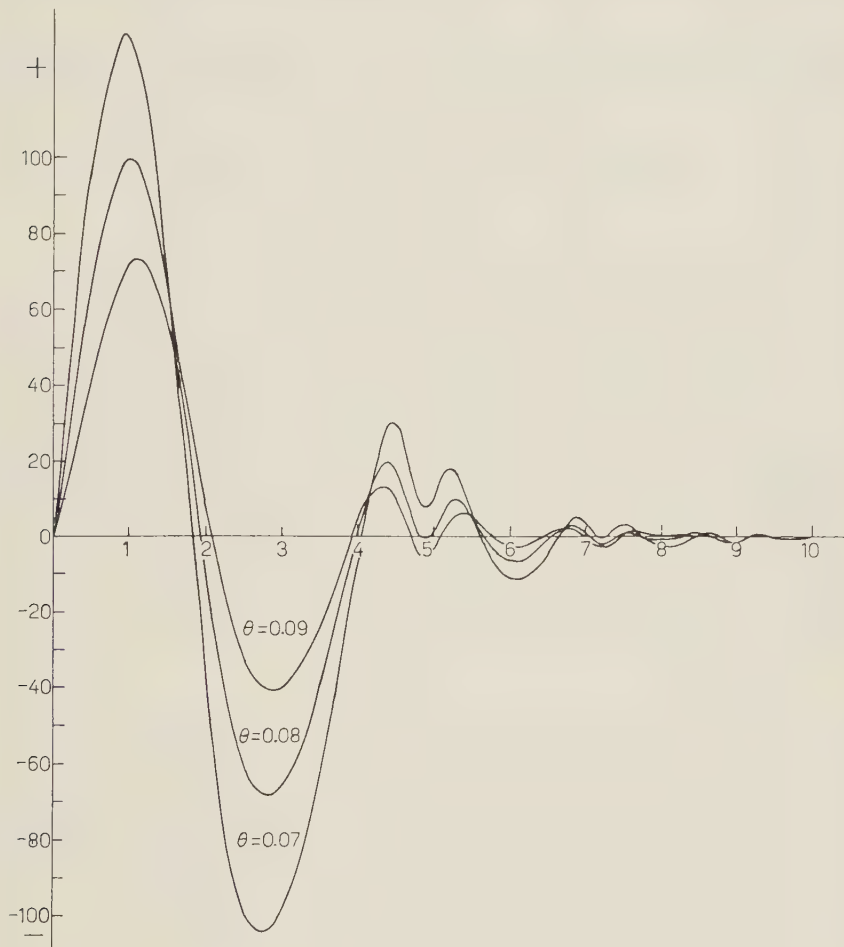


Fig. 5. — Net correction.  $\theta=0.07$  to  $0.09$  rad.

the other maxima appear broadened and more and more doubled. The situation in the neighbourhood of  $\theta = 90$  millirad is almost reversed compared to the neighbourhood of  $\theta = 10$  millirad. In place of the peaks there are minima (which are even negative) coming from the saddle-shaped tops of the peaks; the minima lying between two peaks have disappeared or become much weaker and are going to be substituted by new maxima arising from the union of the second part of the foregoing peak with the first part of the following one; the principal minimum is weak now and also much narrower than before; but

the peak of order zero, which did not even exist at  $\theta = 10$  millirad, is now already decreasing, and somewhere, near  $\theta = 120$  millirad it will be separated from the origin by a new negative region, that is, the net correction for very small pair angles will become negative again. In fact in the  $(\theta, \omega)$  plane we have: many negative regions along the  $\omega$ -axis, which form the principal minimum and all the minima which lie between the lines; then a snake-shaped positive region, which touches the  $\omega$ -axis at the lines, and the  $\theta$ -axis in a large band going from  $\theta \approx 18$  millirad to  $\theta \approx 120$  millirad; all the rest of the plane, *i.e.* the region of large  $\theta$ 's, is a slightly negative region (but this last feature is not very significant, since our approximations are not valid in this region).

The statement made by ÜBERALL, that the average over all  $\theta$ 's of the correction must be zero, because it refers to so large a region in  $q$ -space that (in our notation)  $\bar{F}$  cannot differ significantly from 1, seems to be approximately true for any fixed  $\omega$ . Of course, much less credit can be given to the other statement, following which the correction should tend quickly to zero with increasing  $\theta$ . We have already seen that it is not so, and indeed the first and the second statement do not agree with each other. The large slightly negative region seems to be necessary to balance the strong maxima of the snake-shaped region, and it would be very difficult to think that at large  $\theta$ 's the correction is really zero. If a larger  $A$  is chosen as suggested by SCHIFF<sup>(2)</sup>, the large pair angles are less affected by the crystal structure: and accordingly the lines are weaker.

\* \* \*

I wish to thank before all Prof. A. BORSELLINO, who suggested the problem and without whom it would have been impossible to do the work. Useful discussion has been provided by Dr. G. DIAMBRINI-PALAZZI and his collaborators BARBIELINI, BOLOGNA, MURTAS. Finally I thank Dr. C. BAFFICO and Dr. M. G. JANNUZZI for programming the numerical calculations.

#### RIASSUNTO

La distribuzione delle coppie prodotte da fotoni di grande energia in un cristallo rispetto all'angolo di apertura differisce in diversi aspetti dalla distribuzione consueta nel caso amorfo. Questa differenza è calcolata contando i punti reciproci corrispondenti ai vari angoli. Il risultato è che, se il fascio di fotoni incide sul cristallo normalmente a un piano reticolare, mentre la sezione d'urto totale è minore di quella di un atomo isolato, in corrispondenza di certi angoli ha luogo una fortissima interferenza costruttiva. Se invece il fascio fa un angolo  $\theta$ , piccolo ma non nullo, con la normale a un piano reticolare, la distribuzione nel cristallo oscilla intorno a quella del caso amorfo. I calcoli numerici sono stati fatti per mezzo di una calcolatrice « IBM 650 ».



## Thermomagnetic Study of Metals by Electron Diffraction.

S. YAMAGUCHI

*Institute of Physical and Chemical Research - Tokyo*

(ricevuto il 25 Luglio 1961)

**Summary.** — The temperature of the object bombarded with an electron beam (150 kV, 0.1 mA) is measured with the magnetic method. Invar (Ni: 36%, Fe: 64% by weight) with the known Curie point (250 °C) and nickel with the known saturation induction in the function of temperature served as the reference objects for the experiment. The Lorentz effect observable in the diffraction pattern obtained from the magnetic substance was applied to the present thermomagnetic analysis. The two temperatures 40° and 300 °C were controlled for the objects under the given conditions. The thermomagnetic anisotropy found in the hexagonal lattice of cobalt was revealed by the present electronic processes. The [110] induction in this crystal increased about 200 G when its temperature rose from 40° to 300 °C at  $H = 5\,000$  Oe.

### 1. — Introduction.

In the present study, an electron beam with a certain wavelength was utilized for heating the object by the electronic bombardment, for its crystallographic orientation by the diffraction procedure, and for its magnetic analysis by the aid of the Lorentz effect. The electron beam here used is characterized as follows:

wavelength:  $0.03\text{ \AA}$  (about 150 kV),  
electronic current: 0.1 mA, and  
cross-section of the electronic flux: 0.1 mm.

### 2. — Magnetic measurement of temperature.

**2.1. Preliminary process with invar.** — Powder of invar, whose Curie point was about 250 °C, was employed as a reference specimen for measuring the

temperature of the specimen bombarded by the electrons. The particles of this alloy were attracted at the sharp edge of a magnetized razor blade (remance: about 5 000 gauss). In this way the particles of the specimen were kept in a given magnetiza-

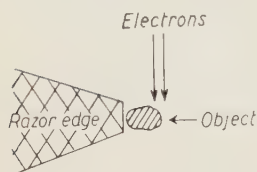


Fig. 1. — Arrangement for the experiment.

tion. An electron beam grazed these magnetized particles not only to preheat them, but also to give rise to a diffraction pattern subjected to the Lorentz effect. The experimental arrangement is illustrated in Fig. 1.

The Lorentz effect in the function of temperature was observed in the following process. Fig. 2 is a double diagram consisting of the diffraction pattern from the cold state of the specimen and that of its hot state. The pattern was first photographed from the specimen kept as cold as possible. Here the specimen was irradiated with the electrons only for 0.5 s.

The pattern from the hot specimen, which had been preheated by the electronic irradiation for two minutes, was superimposed upon the former pattern. The position of the specimen, that of the photographic plate, and the wavelength and the current of the incident beam were all kept constant in these processes. The double diagram thus obtained is shown in Fig. 2.

It is noticeable in Fig. 2 that the diffraction rings from the cold and the hot specimens are eccentric from each other. This means that the magnetization of the former specimen is different from that of the latter. This ring eccentricity  $\Delta Z$  leads to the estimation of

the induction change  $\Delta I$  caused by the temperature elevation. We have a relation between  $\Delta Z$  and  $\Delta I$  in the present arrangement:

$$\Delta Z = \frac{e\lambda L \bar{l}}{h} \cdot 4\pi \Delta I,$$

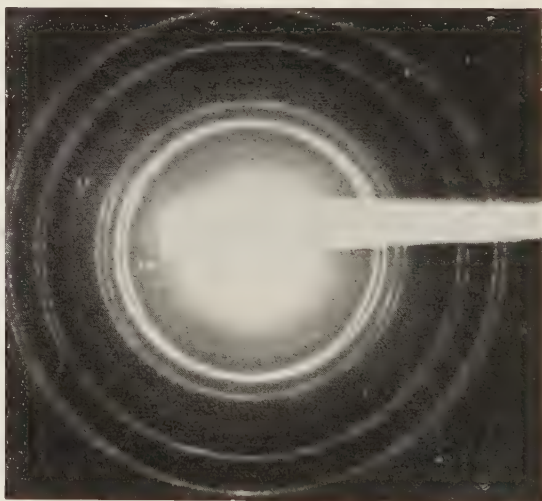


Fig. 2. Double diagram. The diffraction pattern from the cold specimen of Invar (40 °C) and that from its hot state (300 °C) are superimposed. Ring eccentricity means the difference of the Lorentz effect between these two states. Wavelength: 0.0299 Å. Camera length: 495 mm. Positive enlarged 2.3 times.

(1)

where  $e$  means the electron charge ( $1.6 \cdot 10^{-20}$  e.m.u.),  $\lambda$  the wavelength of the electrons ( $0.0299 \text{ \AA}$ ),  $L$  the camera length (495 mm),  $h$  the Planck's constant ( $6.6 \cdot 10^{-27}$  erg·s), and  $\bar{l}$  the effective magnetic path traversed by the electrons (\*). We obtain  $\Delta I = 300 \text{ G}$  if  $\bar{l} = 3 \text{ \mu m}$  is assumed here. This  $\Delta I$ -value agrees approximately with the known saturation induction of invar at room temperature<sup>(1)</sup>. This drastic change of the induction suggests that the temperature of the specimen exceeds its Curie point ( $250^\circ\text{C}$ ) under the hot condition in Fig. 2.

It was observed in the experiment, as a matter of fact, that some particles of the specimen left the razor edge in Fig. 1 when they were strongly irradiated with the electrons. This means that the Invar specimen has exceeded its Curie point so that it has behaved paramagnetic. There are found the diffraction rings characteristic of  $\text{Fe}_3\text{O}_4$  (magnetite), which is the inclusion in the Invar specimen. This ferromagnetic substance with high Curie point ( $575^\circ\text{C}$ ) held the Invar particles attracted at the razor edge even after their temperature had exceeded  $250^\circ\text{C}$ . This verifies that the temperature of the specimen remained always below  $575^\circ\text{C}$  under the present conditions.

Fig. 3 is a double diagram, in which the pattern from the specimen irradiated with the electron beam for two minutes is superimposed upon that from the specimen irradiated for four minutes. There is found no ring eccentricity here. This means that the specimen was always paramagnetic in these circumstances.

It was already demonstrated that the temperature of the cold specimen

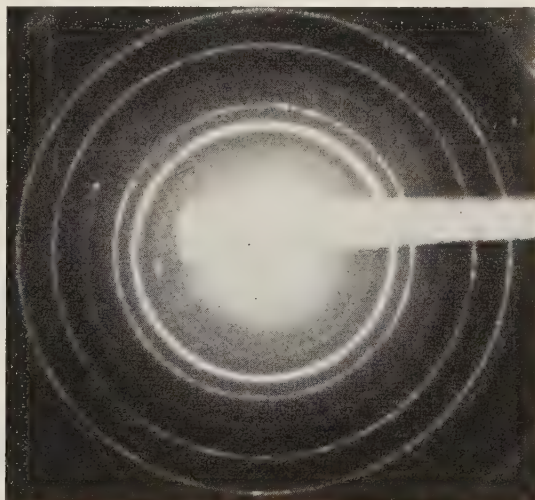
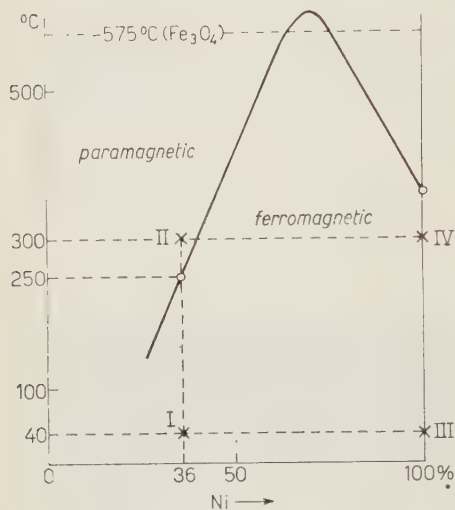


Fig. 3. — Double diagram. The two patterns from the specimen whose temperature has already exceeded its Curie point ( $250^\circ\text{C}$ ) are superimposed. No ring eccentricity.

(\*) It is difficult to determine precisely this effective magnetic path  $\bar{l}$ . The present circumstance is more complicated than that formulated by eq. (1). This formulation could be completed by assuming  $\bar{l}$  empirically.  $\bar{l} \simeq 3 \text{ \mu m}$  and  $2 \text{ \mu m}$  were assumed for Figs. 2 and 5 and for Fig. 6, respectively. These  $\bar{l}$ -values are a little larger than the grain size of the specimen.

(1) R. M. Bozorth: *Ferromagnetism* (Princeton, 1956), pp. 446 and 723.

in Fig. 2 remained about 40 °C (room temperature: about 20 °C) <sup>(2)</sup>. A crystalline diffraction pattern was, as a matter of fact, observable from paraffin (melting point: 45 °C) under the same conditions as for the cold specimen in Fig. 2.



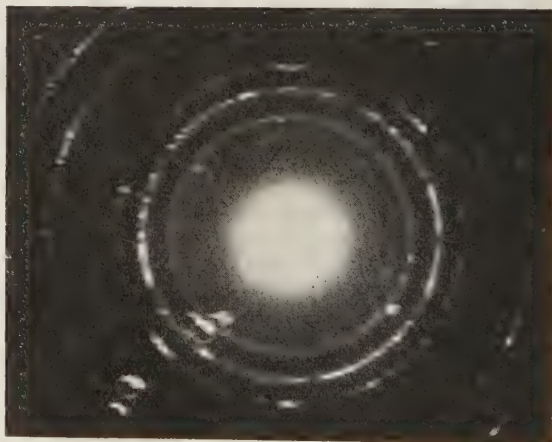
The magnetic transition curve of the Fe-Ni system is shown in Fig. 4 <sup>(1)</sup>. The points I and II on this diagram correspond to the low temperature specimen in Fig. 2 and to the high temperature specimens in Fig. 2 and 3, respectively.

Fig. 4. - The magnetic transformation diagram of the Fe-Ni system. Points I and II correspond to the cold state in Fig. 2 and to the hot states in Figs. 2 and 3.

2'2. *Process with nickel.* - The same procedure as for the Invar specimen was carried out for powder of nickel. The double diagram obtained with the cold and the hot specimens is shown in Fig. 5. The ring eccentricity similar to that in Fig. 2 is recognizable in Fig. 5. We obtain  $\Delta I \simeq 200$  G from Fig. 5 according to eq. (1), where  $\Delta Z = 0.20$  mm and  $\lambda = 0.0336 \text{ \AA}$ . The  $\Delta I$ -value agrees with the difference between the known saturation

Fig. 5. - Double diagram of the nickel specimen at 40 °C and at 300 °C. Ring eccentricity. These two states correspond to the points III and IV in Fig. 4.

Wavelength: 0.0336 Å (\*).



<sup>(2)</sup> S. YAMAGUCHI: *Zeits. angew. Phys.*, **8**, 221 (1956).

(\*) Here the rather long wavelength was employed in order to enlarge the weak ring eccentricity.



induction of nickel at 40 °C and that at 300 °C <sup>(3)</sup>. The points III and IV indicated in the diagram of Fig. 4 correspond to the cold and the hot specimens in Fig. 5, respectively. Here, the temperature rise is not high enough to exceed the Curie point of nickel (360 °C).

It is concluded in this way that the temperatures of the cold and the hot specimens are 40 °C and 300 °C under the present conditions.

### 3. - Thermomagnetic anisotropy of cobalt.

The [100] or the [110] induction in the hexagonal lattice of cobalt increases with the temperature rise. This induction increment amounts to about 200 G for a temperature rise from 40 °C to 300 °C at  $H \simeq 5\,000$  oersted. On the other hand, [001] induction remains constant in this temperature change. This thermomagnetic anisotropy found in the hexagonal lattice of cobalt has been studied by the present procedure.



Fig. 6. - Double diagram from a single crystal of cobalt at 40 °C and at 300 °C. The incident beam is parallel to the (110) and the ( $\bar{1}\bar{1}2$ ) planes. Wavelength: 0.0288 Å. Positive enlarged 3 times.



Fig. 7. - A partial domain of Fig. 6 is 9 times enlarged. The separation of the diffraction spots is similar to the ring eccentricity in Figs. 2 and 5. The strong and the weak spots correspond to 300 °C and 40 °C.

The coarse grains of cobalt (size: about one  $\mu\text{m}$ ) were treated through the same processes as for the Invar and the nickel specimens. A double diagram, in which the diffraction pattern from the cold specimen (40 °C) is superimposed upon that from the hot specimen (300 °C), is shown in Fig. 6. In

(<sup>3</sup>) S. KAYA: *Ferromagnetism* (in Japanese) (Tokyo, 1957), p. 100.

this figure, the electrons run parallel to the (110) and the  $(1\bar{1}2)$  planes, and the magnetic field from the razor edge is perpendicular to the (110) plane.

A small domain in Fig. 6 is further enlarged in Fig. 7 in order to investigate the fine structure of the diffraction spots. It is noticed in Fig. 7 that any

diffraction spot is separated by a constant distance. This phenomenon is quite similar to the ring eccentricity in Fig. 2 and 5. Fig. 7 verifies that the [110]-induction in the cobalt lattice at 40 °C is different from that at 300 °C

It is possible in Fig. 7 to distinguish the « cold » from the « hot » diffraction spots. The « cold » spots were photographed with a very short exposure time (0.5 s), whereas the « hot » spots were photographed with an elongated exposure time (7 s). The former spots, therefore, appear weaker than the latter in Fig. 7. It is recognized according to the relation among the direction of the magnetic field, that of the incident beam and that of the thermomagnetic displacement of the diffraction spots, that the « hot » spots are subjected to a stronger induction than the « cold » spots.

We can calculate the thermal induction increment from Fig. 7 according to eq. (1). We obtain  $\Delta I = 200$  G here, where  $\Delta Z = 0.18$  mm,  $\lambda = 0.0288$  Å, and  $l \approx 2$   $\mu$ m (\*). This  $\Delta I$ -value is in accordance with the known difference between the [110] induction at 40 °C and that at 300 °C at  $H = 5000$  Oe (\*). The points I and II indicated on the two isothermal  $I$ - $H$ -curves in Fig. 8 correspond to the « cold » and the « hot » spots in Fig. 7, respectively.

The orientation of the lattice in relation to the incident electrons is illustrated in Fig. 9. Here, the electrons, the (110) plane and the  $c$ -axis are parallel to the paper face. The (001) and the  $(1\bar{1}2)$  planes and the magnetic field are perpendicular to the paper face.

This termomagnetic anisotropy in the lattice was not observed in an orientation other than that for Fig. 6. *E.g.*, the thermal change of the Lorentz effect was not observed at the diffraction spots under the present conditions when the (001) plane is oriented parallel to the incident beam and perpendicular to the magnetic field.

(\*) See note on p. 2.

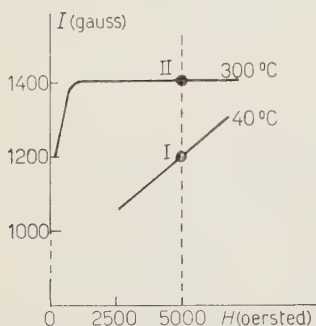


Fig. 8. — The isothermal  $I$ - $H$  curves for [110] induction. I at 40 °C and II at 300 °C correspond to the « cold » and the « hot » spots in Fig. 7.

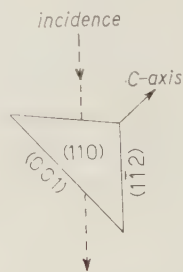


Fig. 9. — Orientation of the lattice in relation to the incident beam. The (110) plane, the  $c$ -axis and the incident beam are parallel to the paper face. The  $(1\bar{1}2)$  and the (001) planes are perpendicular to it. The magnetic field is perpendicular to the (110) plane.

#### 4. - Discussion.

The diffracted electrons run nearly parallel to the corresponding net planes, because the wavelength of the electrons is satisfactorily short. The diffracted electrons give, therefore, directly the information on the induction perpendicular to the corresponding net planes according to the Lorentz effect.

The electrons passing through a material are subjected to the total reflexion<sup>(1)</sup>. The electrons advancing straight through the material are considerably masked by the incoherent electrons. Only the diffracted electrons are, therefore, of use for the study of the induction found in the material.

The above-mentioned two points should be noticed in the present work.

(<sup>1</sup>) Z. G. PINSKER: *Electron Diffraction* (London, 1953), p. 167.

#### RIASSUNTO (\*)

Si misura col metodo magnetico la temperatura di un oggetto bombardato da un fascio di elettroni (150 kV, 0.1 mA). Invar (Ni 36%, Fe 64%, in peso) dal noto punto Curie (250 °C) e nichelio, di cui è nota l'induzione di saturazione in funzione della temperatura, servirono come campioni di riferimento nell'esperimento. L'effetto Lorentz, osservabile nelle figure di diffrazione ottenute dalla sostanza magnetica, venne applicato per questa analisi termomagnetica. Le due temperature di 40 °C e 300 °C vennero riscontrate sugli oggetti nelle condizioni esposte. L'anisotropia termomagnetica, riscontrata nel reticolo esagonale del cobalto, fu messa in luce anche da questo procedimento elettronico. L'induzione [110] di questo cristallo aumentò di circa 200 G quando la sua temperatura passò da 40 °C a 300 °C ed  $H = 5\,000$  Oe.

(\*) Traduzione a cura della Redazione.

## A Redeterminations of the Panofsky Ratio.

V. T. COCCONI (\*), T. FAZZINI, G. FIDECARO, M. LEGROS (\*\*),  
N. H. LIPMAN and A. W. MERRISON (\*\*\*).

CERN - Geneva

(ricevuto il 26 Luglio 1961)

**Summary.** — The Panofsky ratio has been measured using an NaI(Tl)  $\gamma$ -ray spectrometer. The accuracy is limited by the statistical error and not by the resolving power of the spectrometer or by other sources of systematic errors. The final result is  $P = 1.533 \pm 0.021$ .

### 1. — Introduction.

Since ANDERSON and FERMI <sup>(1)</sup> first showed the connection between low-energy pion-proton scattering and pion photoproduction, a great deal of work, both theoretical and experimental, has been done to put this connection on a sound basis. For some time it seemed that quite serious discrepancies existed, which even led to the invention of a new particle <sup>(2)</sup> in order to explain them. However, in the last three years, largely because of the careful theoretical work of BALDIN <sup>(3)</sup>, CINI, GATTO, GOLDWASSER and RUDERMAN <sup>(3)</sup>, and HAMILTON and WOOLCOCK <sup>(4)</sup>, it has become clear that no such drastic remedies are required to remove the disagreements which still exist. On the other

(\*) On leave from Cornell University, Ithaca, N. Y.

(\*\*) Groupe de Physique des Hautes Energies, I.I.S.N.

(\*\*\*) Now at the Nuclear Physics Research Laboratory, Liverpool University, Liverpool.

<sup>(1)</sup> H. L. ANDERSON and E. FERMI: *Phys. Rev.*, **86**, 794 (1952).

<sup>(2)</sup> A. BALDIN: *Nuovo Cimento*, **8**, 569 (1958).

<sup>(3)</sup> M. CINI, R. GATTO, E. L. GOLDWASSER and M. RUDERMAN: *Nuovo Cimento*, **10**, 243 (1958).

<sup>(4)</sup> J. HAMILTON and W. S. WOOLCOCK: *Phys. Rev.*, **118**, 291 (1960).



hand, questions such as the momentum dependence of the  $s$ -wave scattering phase-shift, and the ratio  $\pi^-/\pi^+$  in photoproduction on free nucleons at zero energy require more accurate experimental work in the whole field of low-energy pion physics. With this in mind we have made a careful redetermination of the Panofsky ratio, which forms the connecting link between meson scattering and photoproduction. A preliminary result has been reported at the 1960 Rochester Conference <sup>(5)</sup>.

When a negative pion is absorbed from the  $K$  shell of a mesic hydrogen atom the following reactions occur:

- (1)  $\pi^- + p \rightarrow n + \pi^0$
- (2)  $\pi^- + p \rightarrow n + \gamma$
- (3)  $\pi^- + p \rightarrow n + e^- + e^+.$

Reaction (1), the mesonic capture, produces a neutron of 0.4 MeV and a neutral pion which decays in flight leading to the final channels:

- (1a)  $n + \gamma + \gamma$
- (1b)  $n + \gamma + e^- + e^+$
- (1c)  $n + e^- + e^+ + e^- + e^+.$

where channel (1a) is two orders of magnitude more probable than channel (1b) and four more than channel (1c). The  $\gamma$ -rays produced in channels (1a) and (1b) have energy lying in a continuous spectrum that extends uniformly from 55 to 83 MeV.

Reaction (2), the radiative capture, gives a monoenergetic  $\gamma$ -ray of 129 MeV and a neutron of 8.9 MeV.

Reaction (3) represents the cases in which there is internal  $\gamma$ -ray conversion and has about 1% probability of occurrence, relative to reaction (2).

It has been customary in the literature to define the Panofsky ratio as the branching ratio between mesonic and radiative capture, *i.e.* the ratio (1)/(2), which in practice generally meant the ratio of the two dominant channels, (1a)/(2). However, the number that has the greatest physical meaning is actually the branching ratio between the events involving strong interaction and all those involving electromagnetic interaction. In this paper we thus redefine the Panofsky ratio as follows:

$$P = \frac{(1)}{(2) + (3)},$$

<sup>(5)</sup> *Proc. of the 1960 Rochester Conference* (New York, 1922), pp. 625-26.

which is equivalent to

$$P = \frac{(1a) + (1b) + (1c)}{(2) + (3)}.$$

However (1c) is completely negligible.

This new definition seems necessary, both for semantic reasons, and because the present experimental accuracy warrants consideration of the small effects caused by reactions (1b) and (3).

## 2. - The experimental problem.

In recent years several determinations of the Panofsky ratio have been made by various authors (see Fig. 13, for the bibliography and a summary of the results). The techniques used can be grouped into two classes: a) counters; b)  $H_2$  bubble chambers.

With bubble chambers, one lets the beam of slow pions come to rest in the liquid hydrogen and one identifies reactions (1b) and (3) by observing the electron pairs. One must then use theoretical values for the branching ratios  $\varrho = (1b)/(1a)$  and  $\varrho' = (3)/(2)$  to compute the Panofsky ratio. With our definition, *e.g.*, one has

$$P = \frac{\varrho'}{\varrho} \frac{1 - \varrho}{1 + \varrho'} R,$$

where  $R$  is the experimental ratio (1b)/(3). Obviously one depends heavily on the choice of the values for  $\varrho$  and  $\varrho'$ , whose evaluation suffers from serious theoretical uncertainties.

The usual counter technique consists in defining a beam of pions stopping in a hydrogen target and recording the  $\gamma$ -rays that arise directly from the radiative capture and indirectly, via decay of the neutral pion, from the reaction of mesonic capture. One therefore measures directly the contribution of the two main reactions, (1a) and (2). Reaction (3) goes undetected, and reaction (1b) is in general detected with an efficiency which is half the efficiency for reaction (1a). However, reactions (3) and (1b) can be corrected for later, and even an approximate knowledge of the branching ratios  $\varrho$  and  $\varrho'$  is sufficient, since the total correction is very small. (Actually, the correction for (1b) practically cancels out the correction for (3).) Therefore, the accuracy of the determination of the Panofsky ratio in this case essentially rests only on the accuracy of the experimental procedure.

For these reasons we have chosen a counter technique for a determination of the Panofsky ratio aiming to an accuracy within  $(1 \div 2)\%$ .

The main experimental problems in a counter experiment of this kind are:

- 1) the accurate separation of the two  $\gamma$ -ray spectra typical of the two reactions;
- 2) the subtraction of the background of  $\gamma$ -rays arising from sources other than pions stopping in hydrogen.

For a good separation of the two  $\gamma$ -ray spectra, a spectrometer of particularly good resolution is needed. Preliminary tests indicated that the very large NaI(Tl) crystal already used at CERN in a search for the  $\mu \rightarrow e + \gamma$  mode of decay <sup>(6)</sup> was well suited to this experiment. In fact, though a complete separation of the two spectra could not be obtained, it was found that their overlap was sufficiently small (1.6% of the total area) to be easily unfolded by determining the shape of one of them separately.

In our experiment we chose to separate the radiative capture reaction by selecting those  $\gamma$ -rays (129 MeV) which were associated with 8.9 MeV neutrons emitted in the opposite direction. A careful identification of these neutrons was needed to guard against the possibility of spurious coincidences caused by the two  $\gamma$ -rays produced by the decay of the  $\pi^0$  from the mesonic capture. In fact, if one out of 1000 events of mesonic capture had simulated the coincidence between a  $\gamma$ -ray and a neutron, the Panofsky ratio is lowered by 3%.

The 8.9 MeV neutrons were recorded by a telescope with low sensitivity to  $\gamma$ -rays and besides were identified by their time of flight from the  $H_2$  target to the telescope. With these requirements, all  $\gamma$ -ray contamination was eliminated, except for those few cases in which statistical fluctuations in photo-multiplier transit time and in the light emission in the scintillators have caused a  $\gamma$ -ray pulse to have a delay comparable with that of an 8.9 MeV neutron.

A quantitative verification that this residual contamination was negligible was provided by a subsidiary experiment. A two-dimensional spectrum of the observed time of flight of the particles reaching the neutron telescope and of the pulse-height of the correlated  $\gamma$ -rays in the NaI(Tl) spectrometer was recorded simultaneously with the main experiment. The two-dimensional spectrum provided a better understanding of the background in the neutron telescope and gave us confidence in the method of neutron selection.

The problem of the background of  $\gamma$ -rays in the NaI(Tl) counter arising from sources other than pions stopping in hydrogen turned out to be essentially a shielding problem and a problem of the choice of a suitable geometry, as indicated by a series of preliminary investigations. The shielding

<sup>(6)</sup> J. ASHKIN, T. FAZZINI, G. FIDECARO, N. H. LIPMAN, A. W. MERRISON and H. PAUL: *Nuovo Cimento*, **10**, 1266 (1959).

problem was made easier by the fact that the general background in the CERN SC experimental hall is small.

The design of the experimental layout, that included the construction of a special hydrogen target, is discussed in detail in the next section. Section 3 contains also a description of the electronics. Details of the properties of the NaI(Tl) counter are given in Section 4, and the characteristics of the H<sub>2</sub>-target appendix in Section 5. Section 6 summarizes the results. The analysis and the conclusions are in Section 7.

3. - Experimental arrangement.

3'1. *Layout of the apparatus.* - The experimental layout is shown in Fig. 1.

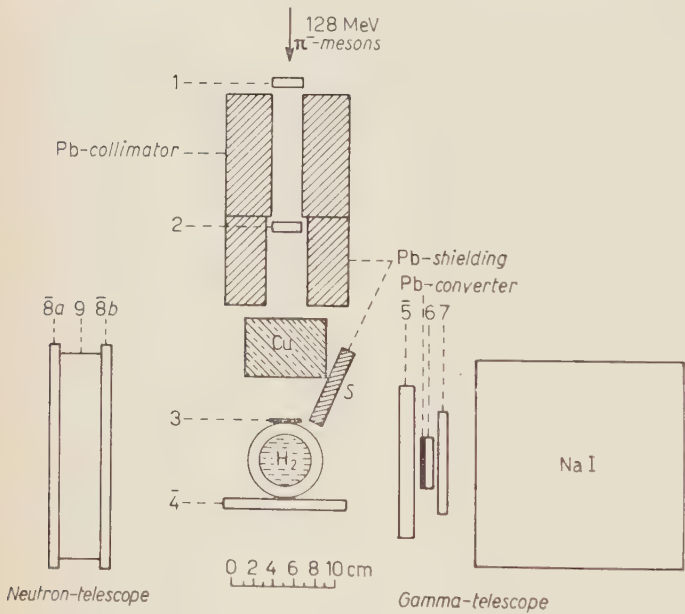


Table I gives details of all counters.

Counter 1 and 2 defined the incoming beam of negative pions produced by the CERN 600 MeV synchro-cyclotron and focused by two quadrupole lenses. The pions were then slowed down in a copper moderator, traversed counter 3

Fig. 1. - General layout of the experiment.

TABLE I.

Counter No. 1	3 × 3 × 1 cm <sup>3</sup>
Counter No. 2	3 × 3 × 1
Counter No. 3	3 × 3 × 0.1
Counter No. 4	10 × 12 × 1
Counter No. 5	15 × 15 × 1.5
Counter No. 6	∅ 5 × 1
Counter No. 7	∅ 9.5 × 1
Counters No. 8, 8'	22 × 22 × 1
Counter No. 9	20 × 20 × 4



and entered the liquid hydrogen target (5 cm in diameter) behind which was located the large anticoincidence counter  $\bar{4}$ .

The  $\gamma$ -rays were selected in the telescope formed by the anticoincidence counter  $\bar{5}$ , a 2 mm thick lead converter, and counters 6 and 7 in coincidence to detect the electrons produced by the  $\gamma$  conversion inside the lead.

The neutron detector consisted of counter 9 (4 cm thick) sandwiched between the two anticoincidence counters  $\bar{8}$  and  $\bar{8}'$ , which were connected by light pipes to the same photomultiplier. The recoil proton made by a neutron in counter 9 would not be detected in  $\bar{8}'$ , but the electron pair from a high-energy  $\gamma$ -ray converting in 9 would also produce a pulse in  $\bar{8}$ , and so be rejected.

The geometry of the apparatus was designed to be as compact as possible. Counter 3 was small and located only 4 cm from the centre of the  $H_2$  target to ensure good definition of the slow meson beam. The  $\gamma$ -telescope was located so as to maximize the solid angle useful for  $\gamma$ -detection. On the other hand, the size of the Pb-converter was chosen so as to guarantee that all conversion electrons, even those at the widest accepted angles ( $\pm 12^\circ$ ), could cross the whole length of the NaI crystal. The geometry of the  $\gamma$ -telescope determined that of the neutron telescope as the latter must subtend an angle not smaller than that entered by the  $\gamma$ -rays, in order to avoid geometrical corrections. This sets a limit on the distance of the neutron counter from the target, *i.e.* on the neutron flight path, and hence on the discrimination against  $\gamma$ -rays that the time-of-flight technique could provide.

To minimize the number of pions stopping in materials other than hydrogen, counter 3 was made only 1 mm thick, the target walls only  $0.07 \text{ g} \cdot \text{cm}^{-2}$  thick, and all other materials in the target were kept well away from the useful region. The protective shielding is not shown in the figure. The whole apparatus was surrounded by 3 to 4 m of baryte-loaded concrete blocks except for an access aperture.

The energy and energy spread of the incoming pion beam were determined on the basis of the range curve of Fig. 2, which was obtained by recording the coincidences 1234567 for different thicknesses of the Cu-moderator.

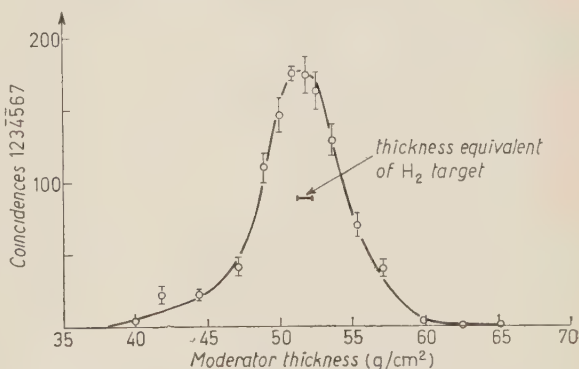


Fig. 2. — Differential range curve for the incoming pions.

The result is  $(128 \pm 4)$  MeV, corresponding to a momentum spread  $\Delta p/p \approx \pm 2\%$ . The equivalent thickness of the hydrogen target is indicated in the figure.

The beam intensity was  $\sim 10\,000$  pions/s over the useful area of  $(3 \times 3)$  cm<sup>2</sup>.

**3.2. Electronics.** – A simplified block diagram of the electronics is shown in Fig. 3. All coincidence circuits used had a resolving time of  $\sim 10$  ns.

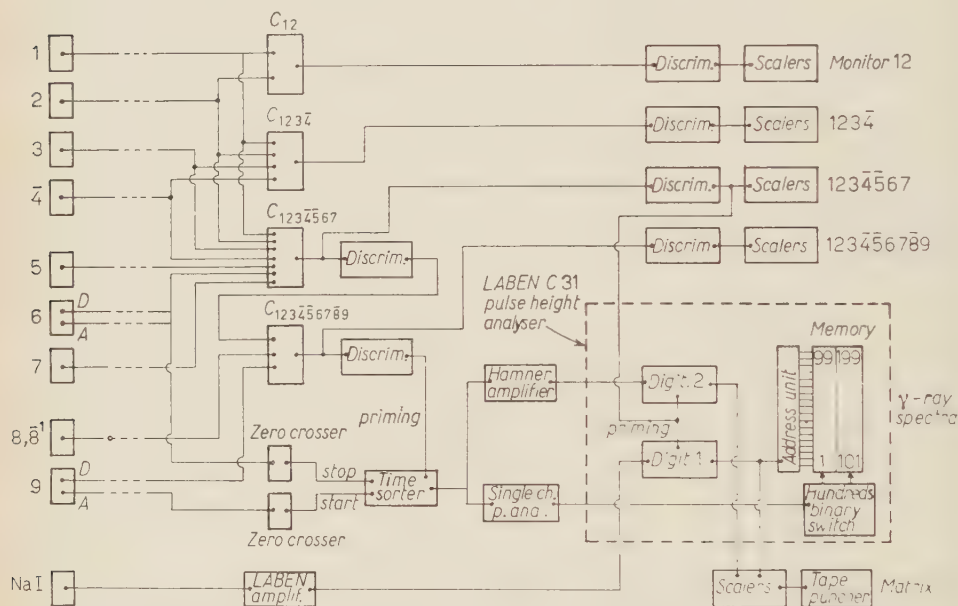


Fig. 3. — Simplified block diagram of the electronics.

Coincidences 12 monitored the incoming beam, coincidences 123 defined the beam of slow pions (\*), coincidences  $123\bar{4}$  selected the pions stopping in the target, while the  $\gamma$ -rays associated with a stopped meson were identified by coincidences  $123\bar{4}567$ .

The pulses from the NaI counter were analysed by a LABEN pulse-height analyser, Mod. C 31, whose 200-channel memory was used here split into two parts of 100 channels each.

The coincidence 1234567 primed the digitizer n. 1 of the LABEN to analyse the response of the NaI counter. The encoded signals were then fed into the address unit of the memory. All  $\gamma$ -ray pulses were addressed to storage in the first part of the memory (channels 1 to 99), except for those that were recognized, by means of the procedure described below, to be 129 MeV

(\*) Coincidences 123 were recorded part of the time by switching off counter  $\bar{4}$ .

$\gamma$ -rays in coincidence with 8.9 MeV neutrons. These events were addressed to the second half of the memory (channels 101 to 199) by a hundreds-binary switch unit primed by a «neutron gate».

Therefore, the second part of the memory recorded the «neutron-gated  $\gamma$ -ray spectrum», i.e., events of radiative capture only. The «total  $\gamma$ -ray spectrum» could then be obtained by summing, channel by channel, the pulses contained in the two halves of the memory. Of course, in the neutron-gated spectrum only a fraction of the events of radiative capture are present, a fraction (11% in our case) that depends on the neutron telescope efficiency and on the number of neutrons scattered in the liquid hydrogen.

The method employed here has the obvious advantage of eliminating the effects of possible drifts in the electronics and in the NaI response. In fact, the total and partial spectra to be compared are not only simultaneously recorded, but indeed have their pulse height measured by the same encoder.

The «neutron gate» was made as follows. The output of the coincidence between a pulse in the  $\gamma$ -telescope and in the neutron telescope, 123456789, was used to prime a time-to-amplitude converter<sup>(7)</sup> which used the pulses from counters 9 and 6 as «start» and «stop» signals respectively<sup>(\*)</sup>. The output of the time converter gives the time-of-flight spectrum of the particles reaching the neutron telescope in slow coincidence with a  $\gamma$  pulse in the NaI counter. An example of such spectrum is shown in the histogram on top of Fig. 9: the peak of the 8.9 MeV neutron is visible as well as the spurious peak of the  $\gamma$ -rays arising from  $\pi^0$ -decay in mesonic capture, as indicated in Section 2. The total width at half height of the  $\gamma$ -ray and neutron peaks are of 1.4 and 2.1 ns respectively, and the two peaks are  $\sim 4$  ns apart. The output of the time converter was connected to a single channel pulse-height analyser, so as to select a given portion of the time-of-flight spectrum. The window was centred on the neutron peak and its width was adjusted so as to cut away the  $\gamma$ -ray contamination. The two thresholds of the window had an indetermination in their position as small as 0.1 ns. The «neutron gate» used to prime the hundreds-binary switch of the LABEN memory was thus available at the output of the single-channel pulse analyser.

The procedure for the choice of the position and width of the window was based on the following experiment. First, the time-of-flight spectrum was recorded on a C.D.C. multi-channel pulse-height analyser gated by the output of the single-channel analyser. Thus only that part of the time-of-flight spectrum which occurs inside the window was displayed and the lower and upper thresholds could be easily set at the sides of the neutron peak. Secondly,

(7) G. CULLIGAN and N. H. LIPMAN: *Rev. Sci. Instr.*, **31**, 1209 (1960).

(\*) The start and stop pulses were reversed from what would seem to be logical, purely for technical reasons.

the neutron telescope was made very sensitive to  $\gamma$ -rays by switching off the anticoincidence counters  $\bar{8}$ ,  $\bar{8}'$  and putting a 3 mm lead converter in front of counter 9. It was thus verified, on the multi-channel pulse-height analyser, that the now large  $\gamma$ -ray peak fell well outside the chosen interval. The two ungated time-of-flight spectra obtained in these auxiliary experiments were similar to those in Figs. 9 and 10.

Fig. 3 also shows the subsidiary recording device used to obtain the two-dimensional spectrum mentioned in Section 2. The output of the time converter was amplified and fed into the digitizer n. 2 contained in the LABEN, primed by the same gating pulse as the digitizer n. 1. The encoded outputs of digitizers nn. 1 and 2 were then fed into scalers and recorded on a tape. This provided a  $100 \times 100$  matrix that recorded *for each event* the height of the pulse produced by the  $\gamma$ -ray in the NaI, and the time delay of the associated pulse, if any, in the neutron telescope. The CERN Mercury-Ferranti computer was instructed to print this information and to sort out those events that *did* have an associated pulse in the neutron telescope.

#### 4. - The NaI (Tl) counter.

The NaI(Tl) counter used in this experiment was supplied to CERN by the Harshaw Chemical Co. of Detroit, Mich., equipped with three 3" Dumont photomultipliers, type 6363. The phosphor is cylindrical in shape, 20 cm in diameter and 20 cm thick, made in two pieces, each half the total thickness, glued together.

The counter was magnetically shielded and also thermally insulated and kept at constant temperature ( $\sim 27^\circ\text{C}$ ) with an accuracy of a few tenths of a degree.

It was used as indicated in the diagram of Fig. 4. The output time constant was of  $\sim 40 \mu\text{s}$  to fit a double delay line differentiating amplifier of the type described by COTTINI *et al.* <sup>(8)</sup>, made by LABEN. The output cathode follower was normally operated with the attenuator indicated in the figure. The attenuator was short-circuited when the counter was calibrated with radioactive sources.

The performance of the counter was studied as follows:

a) Effect of high counting rate: the system counter+amplifier+pulse-height analyser was tested with a  $^{60}\text{Co}$  source at counting rates variable from 1000 to 70 000 pulses/s. No appreciable distortion of the spectrum was observed.

<sup>(8)</sup> C. COTTINI, E. GATTI and E. ZAGLIO: *Energia Nucleare*, **6**, 588 (1959).



b) Long run stability: the position of the  $^{60}\text{Co}$  peaks was checked daily for a period of about one month. No drift was observed. Similarly, no drift was observed in the position of the Panofsky  $\gamma$ -ray peaks during the course of the experiment.

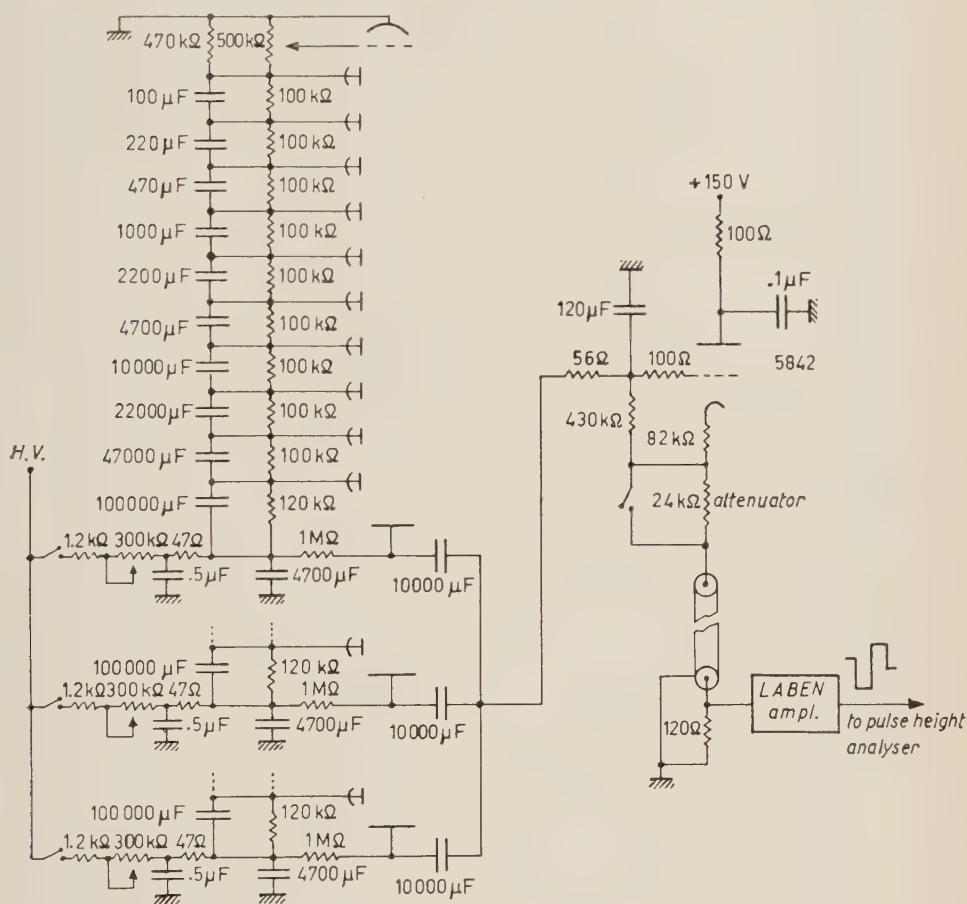


Fig. 4. - Circuit used for the NaI counter.

c) Low-energy resolution: Fig. 5 shows the spectrum obtained with the  $^{60}\text{Co}$  source. The resolution is  $\sim 8\%$ .

d) High-energy resolution: the counter was tested in a beam of positrons from the CERN Synchro-cyclotron, with energies from 25 to 110 MeV, as described by ASHKIN *et al.* (6). It was found that the shape of the resolution curve was completely independent of the positron energy in the range explored. Fig. 6 shows a plot of the results for positrons of 110, 74 and 53 MeV,

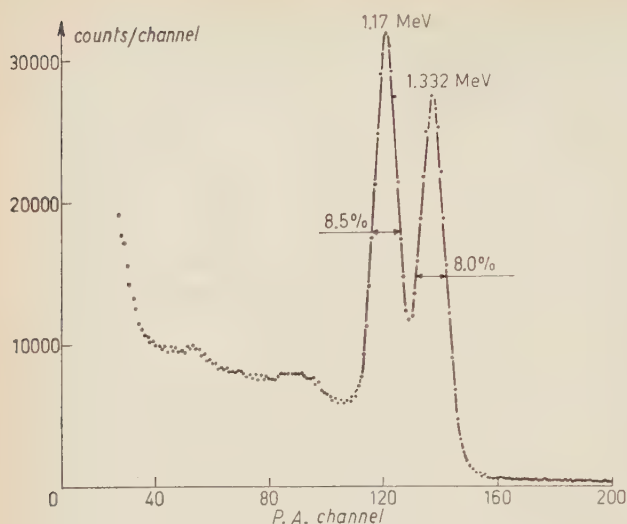


Fig. 5. - Spectrum of  $^{60}\text{Co}$  recorded using the NaI counter.

observed when the useful cross-section of the positron beam was increased from 5 cm to 9.5 cm in diameter.

*i.e.*, in the range that covers the energy interval of interest for the measurements of the Panofsky spectrum. The resolution is of  $\sim 17\%$ . The higher tail of the 110 MeV curve is caused by positrons arising from decay of the  $\pi^+$  and  $\mu^+$  contamination in the beam. No  $\pi^+$  and  $\mu^+$  contamination was present at the lower energies, as these particles could be easily removed by an absorber located in the beam. No difference in resolution was

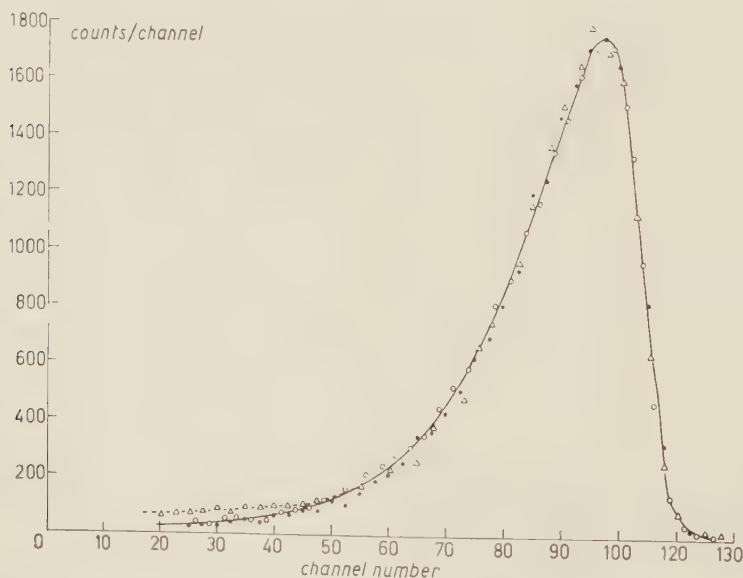


Fig. 6. Normalized resolution curve of the NaI counter obtained using positron beams of 53, 74 and 110 MeV, respectively. The higher tail in the 110 MeV curve is spurious, as it is caused by positrons arising from decay of pions and muons contaminating the beam. [ $\circ$  53 MeV;  $\bullet$  74 MeV;  $\triangle$  110 MeV].

### 5. - The liquid hydrogen target.

The very compact geometry of the experiment and the need of reducing the background of pions stopping in materials other than hydrogen required a target of unconventional design, with  $360^\circ$  thin walls and outer walls very close to the liquid hydrogen.

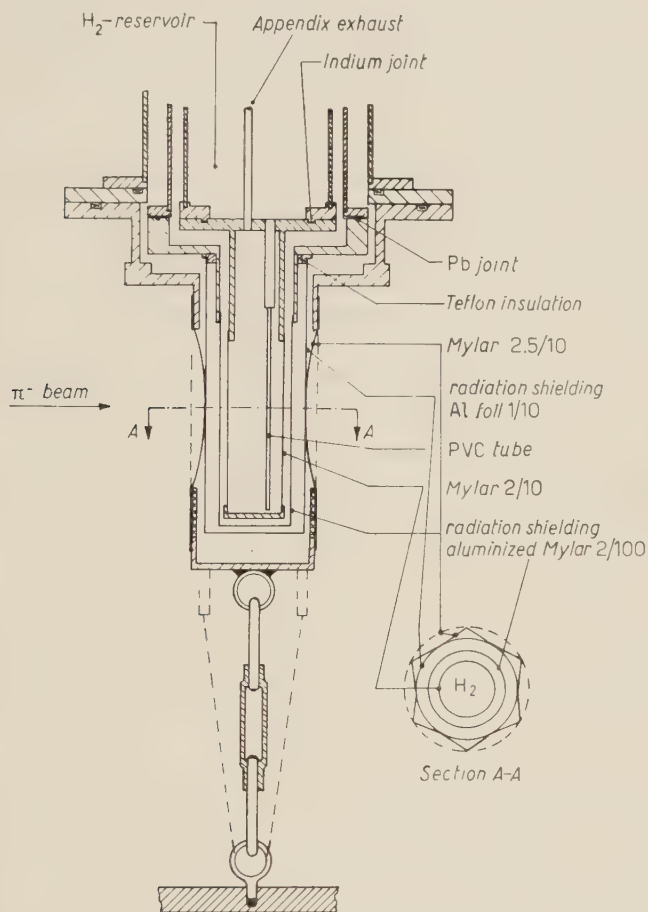


Fig. 7. Sketch of the appendix of the liquid hydrogen target. The dotted lines indicate the configuration of the outer wall when not under vacuum.

The upper part of the target, containing the hydrogen and nitrogen reservoirs was roughly similar in design to that described by WHALIN and REITZ<sup>(9)</sup>. The target proper was contained in an appendix fastened below it and made as sketched in Fig. 7. The liquid hydrogen container was a cylinder made

<sup>(9)</sup> E. A. WHALIN and R. A. REITZ: *Rev. Sci. Instr.*, **26**, 59 (1955).

from mylar foil 0.2 mm thick, 50 mm in diameter, with useful height of 145 mm, glued (\*) at the bottom to a Cu cup and at the top to a Cu flange screwed to the H<sub>2</sub> reservoir and sealed to it by an Indium gasket. A cylindrical radiation shielding 75 mm in diameter surrounded the target, with two walls, one of aluminized mylar (2/100 mm), the other of 1/10 mm Al foil for mechanical strength.

The outer wall, holding the vacuum, was a cylinder, 110 mm in diameter, made from mylar sheet 25/100 mm thick, glued on top to the vacuum chamber and at the bottom to a thick (3 cm) brass plate. This plate was pulled downwards by three adjustable tension cables fastened to the table supporting the whole target. Under vacuum, the outer walls get deformed as indicated in the drawing. The minimum distance at which one could locate a counter was then less than 40 mm from the centre of the hydrogen container.

The total wall thickness of the target was 0.074 g cm<sup>-2</sup>. In the experiment, counter 3 selected in the target a region only 30 mm high and 30 mm wide located at the centre of the thin-walled cylinder 145 mm high. All heavy materials were therefore sufficiently remote, that they produced no background.

Hydrogen gas, and not helium, was always used to help the transfer of the liquid hydrogen from the dewar to the target, to avoid possible contamination due to the solubility of helium in liquid hydrogen.

## 6. - Results.

The data recorded during the experiment are summarized in Table II.

TABLE II.

		12	123	123 $\bar{4}$	Total γ-rays	Neutron-gated γ-rays
series 1	H <sub>2</sub>	2.71 · 10 <sup>9</sup>	2.68 · 10 <sup>8</sup>	7.01 · 10 <sup>7</sup>	51 092	1 469
	no H <sub>2</sub>	4.18 · 10 <sup>8</sup>	4.18 · 10 <sup>7</sup>	7.54 · 10 <sup>6</sup>	404	3
series 2	H <sub>2</sub>	1.39 · 10 <sup>9</sup>	1.40 · 10 <sup>8</sup>	3.60 · 10 <sup>7</sup>	26 476	726
	no H <sub>2</sub>	3.89 · 10 <sup>8</sup>	4.01 · 10 <sup>7</sup>	6.85 · 10 <sup>6</sup>	156	1

(\*) All glueing of mylar with metals and with itself was made with Araldite, supplied by CIBA-BINACA, S.A., Basel.



The «no  $H_2$ » runs were taken after removing the liquid hydrogen from the target (the  $H_2$  gas was left in). The runs with and without hydrogen were alternated during the whole experiment. The data are grouped in two series. The main experimental modification after series 1 was the addition of the Pb shielding  $S$  (see Fig. 1). This reduces strongly the background in the  $\gamma$ -ray spectra due to those events of charge exchange produced by mesons in flight in the Cu-moderator, in which one of the  $\gamma$ -rays from the  $\pi^0$  decay reaches the  $\gamma$  telescope, while the other produces a shower reaching counter 3.

The total «no  $H_2$ » count was 5.1% of the total « $H_2$ » count in series 1, and 2.1% in series 2. About one half of this 2.1% can be explained by meson capture in the  $H_2$  gas left in the target when the liquid hydrogen is removed, and the rest by capture in counter 3 and in the target walls.

From the data of Table II (grouping the two series), as well as from the comparison of the range curve of Fig. 2 with the thickness equivalent of the target and of the other materials around it, one may deduce the information collected in Table III.

TABLE III.

	$H_2$	no $H_2$
123—123 $\bar{4}$	0.74	0.82
Pions stopped in liquid hydrogen	0.08	—
Pions stopped in materials other than liquid hydrogen	0.05	0.05
Pions missing counter $\bar{4}$	0.13	0.13
123	1.00	1.00

The 13% labelled «pions missing counter  $\bar{4}$ » consist mostly of mesons scattered in the Cu-moderator so as to miss that counter, but hitting counter 3. These mesons do not contribute to the  $\gamma$ -ray spectra.

The numbers of  $\gamma$ -rays and neutron-gated  $\gamma$ -rays listed in Table II are respectively the total number of counts recorded in both parts of the LABEN memory, and in the second part only, as explained in Section 3.

Fig. 8 shows examples of these pulse-height spectra, produced by pion capture. The total  $\gamma$ -ray spectrum is shown in Fig. 8a, while Fig. 8b shows the spectrum arising from radiative capture only. The spectrum obtained in the corresponding «no  $H_2$ » run is also indicated in Fig. 8a.

The shape of the neutron-gated spectrum, as well as the shape around its maximum of the high-energy peak of the total spectrum are compared in Fig. 8b with the shape of the resolution curves obtained when the NaI counter

was exposed to positron beams, as described in Section 4. The agreement is surprisingly good.

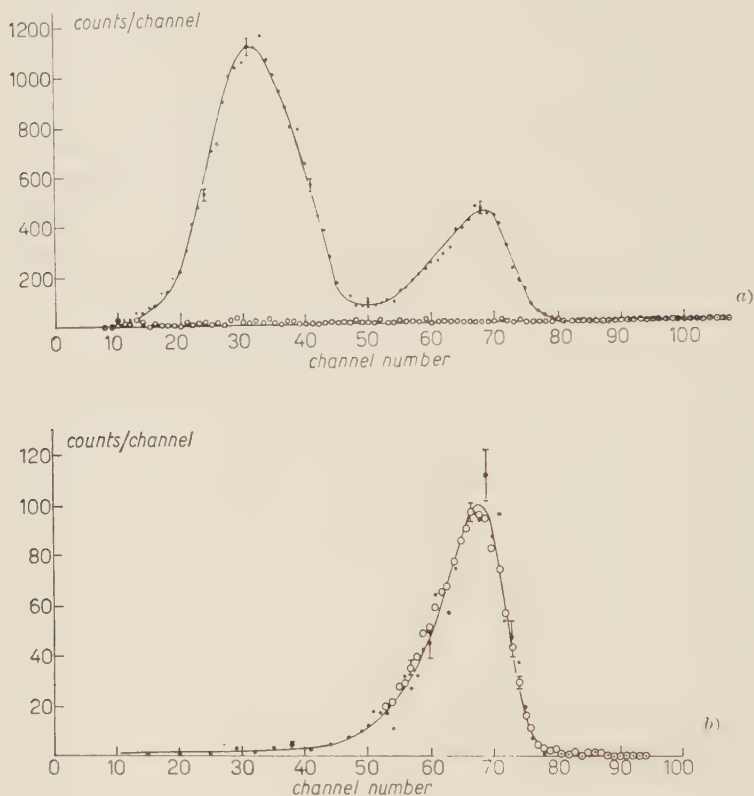


Fig. 8. — Example of a total  $\gamma$ -ray spectrum, as recorded by the NaI counter (Fig. 8a). The first peak arises from the  $\gamma$ -rays produced in mesonic capture, the second peak from the  $\gamma$ -rays produced in radiative capture. The background obtained when the liquid hydrogen was removed from the target is also plotted normalized to the same number of incoming pions. Fig. 8b shows the corresponding neutron-gated  $\gamma$ -ray spectrum that arises from the radiative capture only. This spectrum is compared in the figure with the shape of the high-energy peak of the total spectrum in the region around its maximum, as well as with the resolution curve obtained by calibrating the NaI counter with positron beams. ● Neutron-gated  $\gamma$ -ray spectrum; ○ total  $\gamma$ -ray spectrum; — positron calibration.

Fig. 9 reproduces the matrix described in Section 3, obtained in normal running conditions. The events plotted here are only those in which the NaI pulse produced by a  $\gamma$ -ray was associated with a pulse in the neutron telescope. The NaI pulse height distribution is plotted horizontally (large pulses on the

right), while the time delays from the neutron telescope pulses are plotted vertically (small delays at the bottom). One can see a concentration of large pulses at relatively large delays (several nanoseconds) and a number of small pulses at small delays. The former are the true events of radiative capture,

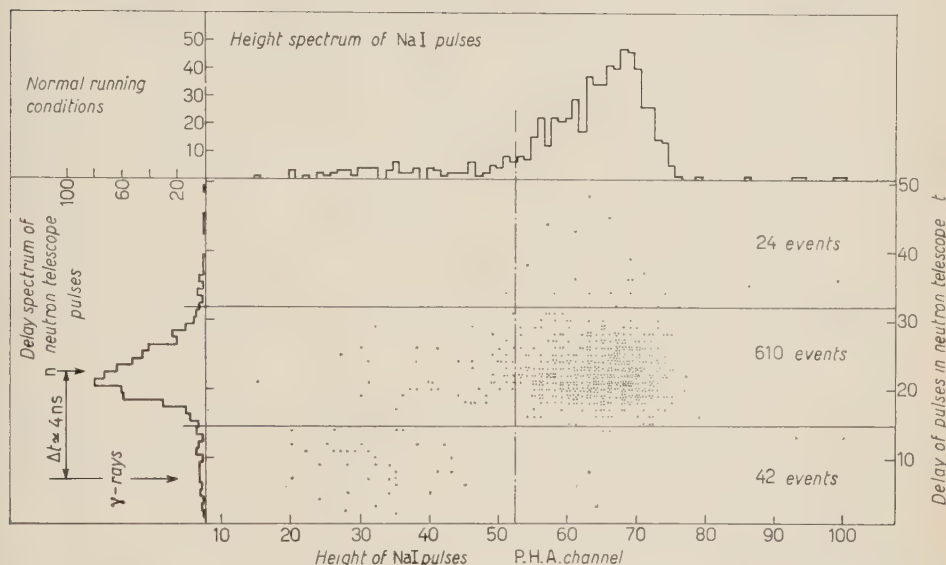


Fig. 9. - Each dot in the matrix corresponds to an event and indicates the pulse height of the NaI pulse caused by the  $\gamma$ -ray produced in the event, and the time delay relative to the velocity of light of the corresponding pulse in the neutron counter. The two horizontal lines show the delay interval used to obtain the neutron-gated spectrum. The dotted vertical line shows the position of the cut chosen for the final analysis. The histogram on top of the matrix is the pulse-height spectrum of all the NaI pulses. The histogram on the side is the time-of-flight spectrum of all the neutron telescope pulses. This matrix contains a sample of 676 events, and was taken in normal running conditions.

while the latter represent the cases in which one of the two gammas from the decay of the  $\pi^0$  from mesonic capture hits the neutron telescope and the other the  $\gamma$  telescope. These events are about 7% of the true events. This interpretation is proved correct by the matrix reproduced in Fig. 10, which was obtained when a 3 mm Pb converter was put in front of the neutron telescope, and the anticoincidence  $\bar{S}$  switched off, thus enhancing detection of  $\gamma$ -rays in the neutron telescope.

The few large pulses at very large delays in Fig. 9 can be interpreted as being caused by those 8.9 MeV neutrons that were scattered in the hydrogen or in the target walls and thus lost energy.

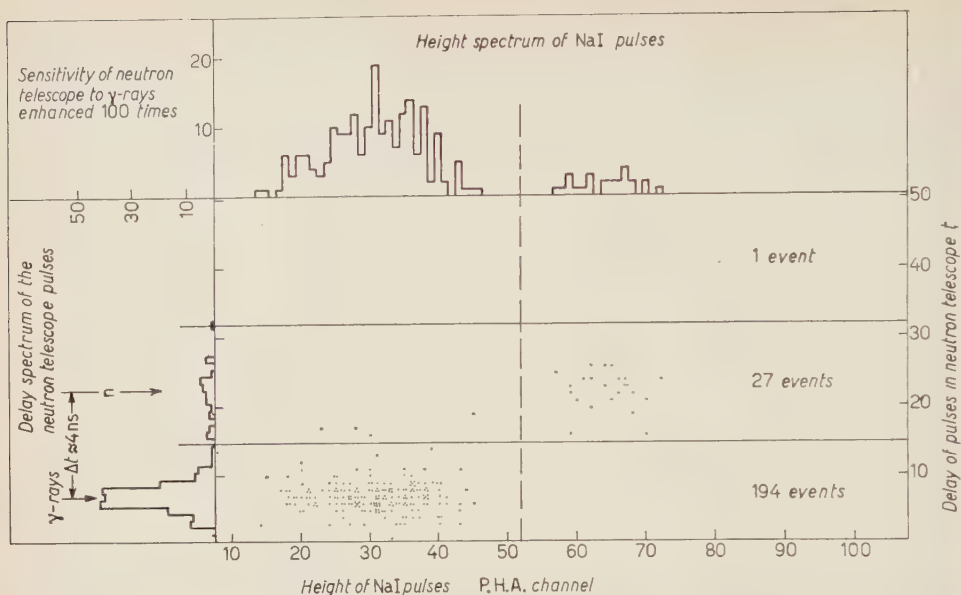


Fig. 10. — Same matrix and histograms as in Fig. 9, but taken when a 3 mm Pb-converter was placed in front of the neutron telescope, and the anticoincidence counters  $\bar{S}$  and  $\bar{S}'$  were turned off. This matrix contains a sample of 222 events.

## 7. — Analysis of the results and conclusions.

For the analysis of the results we have at first assumed, as in all previous counter experiments, that our apparatus detected only reactions (1a) and (2) and have therefore computed the traditional Panofsky ratio, *i.e.*, (1a)/(2). The value directly obtained from the data is called  $P_{\text{uncorr}}$  and that modified to take into account some systematic effects inherent in our determination is called  $P_{\text{corr}}$ .

The final value of the Panofsky ratio according to the definition in Section 1,

$$P = \frac{(1a) + (1b)}{(2) + (3)},$$

is obtained later, by correcting for the occurrence of reactions (1b) and (3).

For the determination of  $P_{\text{uncorr}}$  we have analysed, with the method described below, each of the two series of data summarized in Table II. Their results were then averaged.

The «no  $H_2$ » background normalized to the same number of 12 coincidences was subtracted channel by channel from the  $\gamma$ -ray spectra recorded in the « $H_2$ » runs. The total  $\gamma$ -ray spectrum was then cut into two parts,



$N_1$  and  $N_2$  (see Fig. 11), at an arbitrary channel  $X$ , above which the contribution of mesonic capture is small.  $N_1$  contains the part  $N_{\pi_1}$  due to mesonic capture plus the tail  $N_{\gamma_1}$  of the radiative peak extending below channel  $X$ .  $N_2$  contains the part  $N_{\gamma_2}$  due to radiative capture plus the small tail  $N_{\pi_2}$  of the mesonic peak extending above channel  $X$ .

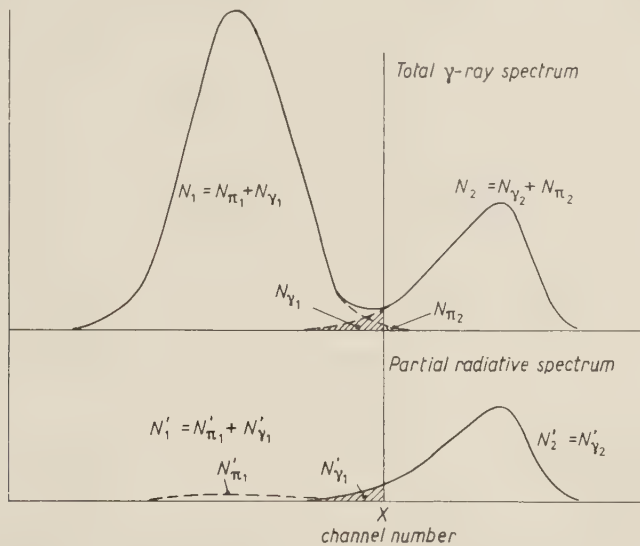


Fig. 11. — Analysis of the results. The mesonic and the radiative capture spectra have been arbitrarily resolved to show the meaning of the symbols used in the analysis.

Similarly, the cut at channel  $X$  splits the neutron-gated spectrum into two parts,  $N'_1$  and  $N'_2$ , where  $N'_1$  contains the tail  $N'_{\gamma_1}$  of the radiative peak plus a small contamination of events of mesonic capture,  $N'_{\pi_1} = \beta N_{\pi_1}$ , with  $\beta \ll 1$  in our case.  $N'_{\pi_2}$  is completely negligible.

If the efficiency for detection of the neutron-gated spectrum is the experimental ratio  $\alpha = N'_2/(N_2 - N_{\pi_2})$ , then the radiative peak is  $(N'_1 + N'_2 - \beta N_{\pi_1})/\alpha$  and the number of mesonic and radiative events are in the ratio

$$(1) \quad P' = \frac{1}{2} \frac{N_1 + N_2 - (N'_1 + N'_2 - \beta N_{\pi_1})/\alpha}{(N'_1 + N'_2 - \beta N_{\pi_1})/\alpha},$$

where the factor  $\frac{1}{2}$  derives from the fact that there are two  $\gamma$ -rays for every  $\pi^0$  from mesonic capture.

For  $N_{\pi_2}/N_2 \ll 1$ , one may write  $\alpha = (N'_2/N_2)(1 + (N_{\pi_2}/N_2))$ , where  $N_{\pi_2} = k(N_{\pi_1} + N_{\pi_2})$ , with  $k \ll 1$ .

Expanding in series for  $\beta N_{\pi_1}/(N_1 + N_2) \ll 1$ , expression (1) becomes:

$$(2) \quad P' = \frac{1}{2} \left\{ \left( 1 + \frac{N_1}{N_2} \right) \frac{N'_2}{N'_1 + N'_2} - 1 \right\} + (2P' + 1)P'k + (2P' + 1)P' \frac{\beta}{\alpha}.$$

The second term represents the correction due to the tail of the low-energy peak extending above channel  $X$ , while the third term represents the correction due to mesonic  $\gamma$ -ray contamination in the neutron-gated spectrum. As these corrections are very small in our case, the Panofsky ratio will be first calculated using only the first term of expression (2). The corrections will be taken into account later, along with other small systematic effects.

The contribution to the error in  $P'$  due to the statistical uncertainties of the experimental values  $N_1, N_2, N'_1$  and  $N'_2$  are

$$\Delta P'(N_1) = \frac{1}{2} \frac{N'_2}{N'_1 + N'_2} \frac{N_1}{N_2} \frac{\Delta N_1}{N_1},$$

$$\Delta P'(N_2) = \frac{1}{2} \frac{N'_2}{N'_1 + N'_2} \frac{N_1}{N_2} \frac{\Delta N_2}{N_2},$$

$$\Delta P'(N'_1) = \frac{1}{2} \frac{N'_2}{N'_1 + N'_2} \left(1 + \frac{N_1}{N_2}\right) \frac{N'_1}{N'_1 + N'_2} \frac{\Delta N'_1}{N'_1},$$

$$\Delta P'(N'_2) = \frac{1}{2} \frac{N'_2}{N'_1 + N'_2} \left(1 + \frac{N_1}{N_2}\right) \frac{N'_1}{N'_1 + N'_2} \frac{\Delta N'_2}{N'_2},$$

and the total error  $\Delta P'$  is the square root of the sum of their squares.

Finally, we calculate  $P_{\text{uncorr}} = \varepsilon P'$ , where  $\varepsilon = \varepsilon_2 \varepsilon_1$  is the ratio of the detection probabilities for a 129 MeV  $\gamma$ -ray and for a  $\gamma$ -ray with energy from 55 to 83 MeV. To compute this ratio we have used the pair production cross

TABLE IV.

	Series 1	Series 2
$N_1$	$36\,687 \pm 228$	$19\,537 \pm 147$
$N_2$	$11\,786 \pm 136$	$6\,372 \pm 82$
$N'_1$	$139 \pm 11.8$	$53 \pm 7.3$
$N'_2$	$1\,330 \pm 36.5$	$673 \pm 25.9$
$P'$	1.3618	1.3846
$\Delta P'(N_1)$	$0.875 \cdot 10^{-2}$	$1.069 \cdot 10^{-2}$
$\Delta P'(N_2)$	$1.626 \cdot 10^{-2}$	$1.829 \cdot 10^{-2}$
$\Delta P'(N'_1)$	$1.496 \cdot 10^{-2}$	$1.895 \cdot 10^{-2}$
$\Delta P'(N'_2)$	$0.483 \cdot 10^{-2}$	$0.529 \cdot 10^{-2}$
$\Delta P'$	$\pm 0.0243$	$\pm 0.0289$
$P_{\text{uncorr}}$	$1.517 \pm 0.027$	$1.542 \pm 0.032$
Average of the two series	$P_{\text{uncorr}} = 1.528 \pm 0.021$	

section given by DAVIS, BETHE and MAXIMON <sup>(10)</sup>, corrected for pair production by electrons and for Compton scattering. The value we adopted is  $\varepsilon = 1.114$ . The uncertainty of this evaluation is discussed later.

Table IV summarizes the results of the analysis of the two series of experimental data, with the cut in the spectra operated at channel  $X=52$ . This channel was chosen not with the criterion of minimizing the statistical error, but rather to achieve a compromise giving a small statistical error together with a small systematic error in the correction for the mesonic peak tail extending above channel  $X$  (see paragraph *b* in the discussion of systematic errors).

As one can see from the table, the main contribution to the final error comes from the statistical uncertainties of  $N_2$  and  $N'_1$ , the two contributions being practically equal in our case. Obviously, if one had a  $\gamma$ -ray spectrometer with resolution high enough to completely separate the two peaks, the limiting factor would be the statistics of the high-energy peak of the total spectrum.

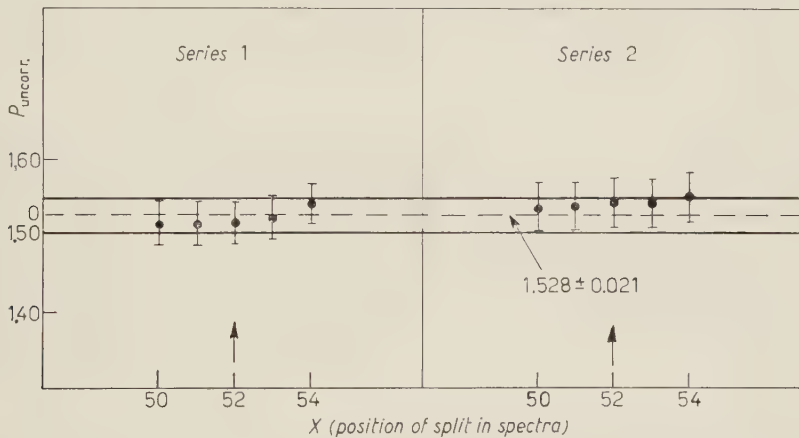


Fig. 12. — Variation of the Panofsky ratio with the channel  $X$  at which the spectra have been split for the analysis. The two horizontal lines define the one standard deviation confidence interval corresponding to the result of the experiment for  $P_{\text{uncorr}}$ .

Fig. 12 shows how the value of  $P_{\text{uncorr}}$  varies with  $X$ , *i.e.*, with the choice of the channel at which the spectra are split for the analysis. Obviously, the choice of  $X$  is not critical.

To arrive at the value of the Panofsky ratio,  $P_{\text{corr}}$ , we have considered the following possible sources of systematic errors:

*a) Effect of the subtraction of the « no  $H_2$  » background.* — The subtraction from the  $\gamma$ -ray spectra of the counts obtained in the « no  $H_2$  » runs cannot

<sup>(10)</sup> H. DAVIES, H. A. BETHE and L. C. MAXIMON: *Phys. Rev.*, **93**, 788 (1954).

introduce significant systematic error in the Panofsky ratio. The procedure should, in fact, correctly eliminate the great majority of the events produced in materials other than hydrogen. Residual spurious events, if any, certainly are a small fraction of the total background. As the total background correction modifies the Panofsky ratio only by about  $-0.6\%$ , their effect is negligible.

*b) Effect of the tail of the mesonic peak extending above channel X.* — The importance of the correction due to the tail  $N_{\pi_2} = k(N_{\pi_1} + N_{\pi_2})$  obviously depends on the choice of the channel  $X$ . This tail can be estimated by folding the shape of the NaI resolution curves (Figs. 6 and 8*b*) with the rectangular spectrum of the  $\gamma$ -rays arising from the  $\pi^0$  decay in the mesonic capture.

With our choice of  $X=52$ , we obtained  $k=7 \cdot 10^{-4}$ . The second term of expression (2) is then

$$(2P' + 1)P'k = 0.0036$$

which modifies the Panofsky ratio by  $+0.26\%$ .

*c) Effect of residual mesonic  $\gamma$ -rays contamination in the neutron-gated spectrum.* — From the matrix shown in Fig. 10, which was obtained when the  $\gamma$ -ray sensitivity of the neutron telescope was enhanced about 100 times, one can deduce that 4 out of 198 events of mesonic capture could have simulated a radiative capture. From this, and from the data in the matrix obtained in normal running conditions (Fig. 9), one concludes that only  $4 \times 42/198 = 0.85$  out of the 610 events classified as radiative captures might have been instead mesonic captures.

The factor  $\beta$  defined at the beginning of this section is then

$$\beta = \frac{N'_{\pi_1}}{N_{\pi_1}} = \frac{0.85}{610 \setminus (1/x) \setminus 2P'}$$

which makes the third term of expression (2)

$$(2P' + 1) \frac{0.85}{610 \times 2} = +2.6 \times 10^{-3}.$$

Therefore, the correction to the Panofsky ratio due to the  $\gamma$ -ray contamination in the neutron-gated spectrum is  $+0.19\%$ .

*d) Effect of small pulses lost in recording the total spectrum.* — In recording the total  $\gamma$ -ray spectrum with the pulse-height analyser, there was a loss of small pulses in the first few channels due to the back-bias of the analyser.



This requires a correction to  $N_1$  that can be evaluated with the same procedure as that used for correction *b*).

It modifies the Panofsky ratio by  $+0.1\%$ .

*e) Effect of meson interaction in flight inside the liquid hydrogen.* — An evaluation has been made of the contribution to the observed  $\gamma$ -ray spectra caused by mesons crossing the target in flight and giving rise to mesonic (charge exchange) and radiative interactions in the liquid hydrogen.

The mesons that were *not* brought to rest were, in our experiment,  $\sim 9$  times more abundant than those stopped in the liquid hydrogen. The range curve in Fig. 2 shows that they have an energy spectrum that extends up to  $\sim 14$  MeV, with median energy at  $\sim 3$  MeV. We estimate that the number of mesons which make a  $(\pi^- \rightarrow \pi^0)$  interaction in flight in the liquid  $H_2$  is  $2.4 \cdot 10^{-3}$  times the number of the stopped mesons which undergo capture. Similarly, the number of reactions  $(\pi^- \rightarrow \gamma)$  in flight is  $1.6 \cdot 10^{-3}$  times the number of stopped mesons which undergo radiative capture. From this it follows that the contribution of the interactions in flight modifies the Panofsky ratio by  $\sim -0.1\%$ .

*f) Systematic effects due to the experimental arrangement.* — Before adopting the final layout described in Section 3, several other geometries have been tried in a series of exploratory experiments that extended over a period of several months. Runs were made with a larger  $H_2$  target (9.5 cm in diameter) and with Pb-converters in the  $\gamma$  telescope of various sizes (5 and 9 cm in diameter) and thickness (2 and 3 mm). Collimations and shieldings were varied to find optimum conditions.

All the values of the Panofsky ratio deduced from these preliminary runs are consistent with the results of the final experiment.

*g) Effect of the uncertainty in the value of  $\varepsilon$ .* — Apart from all experimental errors, the accuracy of the determination of the Panofsky ratio depends on the accuracy of the value used for the ratio  $\varepsilon = \varepsilon_2/\varepsilon_1$  of the detection probability of a 129 MeV  $\gamma$ -ray and of a  $\gamma$ -ray with energy between 55 and 83 MeV.

The errors in  $\varepsilon_1$  and  $\varepsilon_2$ , arise only from the approximations in the DAVIS, BETHE and MAXIMON's calculations<sup>(10)</sup>. As one deals here only with the ratio,  $\varepsilon$ , the error is small. A generous estimate leads to an error  $\Delta\varepsilon = 0.005$ , which has no appreciable effect on our result for the Panofsky ratio.

As conclusion, all the considered systematic errors are small as compared with the  $1.5\%$  statistical error of our result. However, they contribute the corrections summarized in Table V, which are incorporated in our result,  $P_{\text{corr}}$ . This value,  $P_{\text{corr}}$ , is the Panofsky ratio according to the traditional definition, *i.e.*, assuming the existence of reactions (1a) and (2) only.

TABLE V.

$P_{\text{uncorr}}$		$1.528 \pm 0.021$
Corrections	Tail of mesonic peak above ch. $X=52$	+ 0.004
	$\gamma$ -ray contamination in neutron-gated spectrum	+ 0.003
	Loss of small pulses in total spectrum	+ 0.002
	Interaction in flight in the liquid hydrogen	- 0.002
$P_{\text{corr}}$		$1.535 \pm 0.021$

This result can be easily reduced to the new definition of  $P$  as the ratio between mesonic and electromagnetic captures, by correcting for the events lost in channels (1b) and (3). In fact, one has

$$P = \frac{(1a) + (1b)}{(2) + (3)} = \frac{1 + \varrho'}{1 + \varrho} \cdot \frac{P_{\text{corr.}}}{1 + \frac{1}{2} \varrho'},$$

where  $\varrho$  and  $\varrho'$  are the branching ratios (3)/(2) and (1b)/(1a), respectively.

Using for these branching ratios the values calculated by JOSEPH<sup>(11)</sup>,  $\varrho = 0.00710$  and  $\varrho' = 0.01196$ , the correction is  $(1 - 0.0011)$  and the final result is:

$$P = 1.533 \pm 0.021.$$

Fig. 13 presents a comparison of our result with all the results reported by other experimenters. One must be aware of the fact that in general these results are not exactly comparable with one another and with ours. In fact, they are calculated using the definitions  $P = (1)/(2)$  or  $(1a)/(2)$ . Besides, for counter experiments where  $\gamma$ -rays are converted into pairs before the detection, a value  $\varepsilon = 1.12$  has been used, at variance with our  $\varepsilon = 1.114$ . However, these are small points and in all cases their effects are well within the quoted experimental errors. For example, Samios' value 1.62 becomes 1.63 with our definition of  $P$  and JONES *et al.*'s value 1.56 becomes 1.55 with our  $\varepsilon$  and remains 1.55 with our definition of  $P$ . All the previous results can therefore be considered in agreement with our value, within one standard deviation, except for that by FISCHER *et al.* and for Panofsky's original determination. Excluding these two values, the weighted average of all determinations preceding ours, taken as given by the Authors, is:

$$1.538 \pm 0.030.$$

(11) D. W. JOSEPH: *Nuovo Cimento*, **16**, 997 (1960).

Our result is also consistent with the value 1.52 calculated by CINI *et al.* <sup>(3)</sup> on the basis of the photoproduction and pion scattering data available at the beginning of 1958.

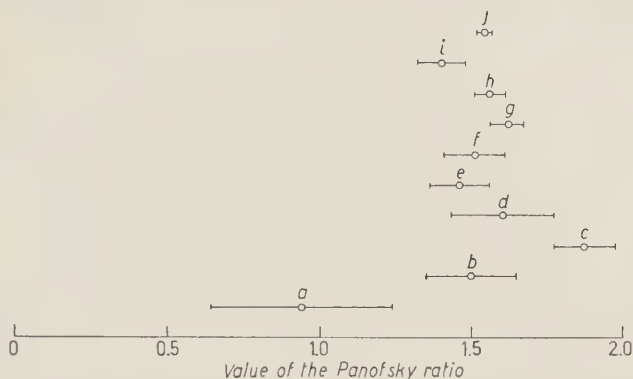


Fig. 13. — Summary of the results of the various determinations of the Panofsky ratio.

a) W. K. H. PANOFSKY, R. L. AAMODT and H. HADLEY: <i>Phys. Rev.</i> , <b>81</b> , 565 (1951)	$0.94 \pm 0.30$
b) J. M. CASSELS, G. FIDECARO, A. M. WETHERELL and J. R. WORMALD: <i>Proc. Phys. Soc. (London)</i> , A <b>70</b> , 405 (1957)	$1.50 \pm 0.15$
c) J. FISCHER, R. MARCH and L. MARSHALL: <i>Phys. Rev.</i> , <b>109</b> , 533 (1958)	$1.87 \pm 0.10$
d) J. A. KUEHNER, A. W. MERRISON and S. TORNABENE: <i>Proc. Phys. Soc. (London)</i> , A <b>73</b> , 545 (1959)	$1.60 \pm 0.17$
e) E. L. KOLLER and A. M. SACHS: <i>Phys. Rev.</i> , <b>116</b> , 760 (1959)	$1.46 \pm 0.10$
f) M. DERRICK, J. FETKOVICH, T. FIELDS and J. DEAHL: <i>Phys. Rev.</i> , <b>120</b> , 1022 (1960)	$1.51 \pm 0.10$
g) N. P. SAMIOS: <i>Phys. Rev. Lett.</i> , <b>4</b> , 470 (1960)	$1.62 \pm 0.06$
h) D. P. JONES, P. G. MURPHY, P. L. O'NEILL and J. R. WORMALD: <i>Proc. Phys. Soc. (London)</i> , A <b>77</b> , 77 (1961)	$1.56 \pm 0.05$
i) A. F. DUNAITSEV, V. S. PANTEUV, YU. D. PROKOSHIKIN, TANG SYOA-WEI and M. N. KHACHATURYAN: <i>Proc. of the Rochester Conference</i> (New York, 1960), p. 181	$1.40 \pm 0.08$
j) This experiment	$1.533 \pm 0.021$

At the moment, the Panofsky ratio is the best determined of the various experimental data that are involved in the analysis of low-energy pion physics.

\* \* \*

We wish to express our appreciation to the crew of the CERN Synchrocyclotron for the efficient operation of the accelerator.

We are very grateful to Mr. M. FELL and to Mr. M. RENEVEY for their continuous help during the preparation and the performance of the experiment. Their skill was particularly valuable in constructing and operating the  $H_2$  target.

Mr. M. DROSI and Mr. E. DEL GIUDICE helped in taking the data.

#### RIASSUNTO

Il rapporto di Panofsky è stato rimisurato con uno spettrometro per raggi  $\gamma$  consistente in un contatore all' NaI(Tl). La precisione è limitata dall'errore statistico, non dal potere risolutivo dello spettrometro o da altre cause di errori sistematici. Il risultato finale è  $P=1.533 \pm 0.021$ .



## Light Diffraction on Slits in Case of Light Sources of Finite Extension.

J. BAKOS and K. KÁNTOR

*Central Research Institute for Physics - Budapest*

(ricevuto il 27 Luglio 1961)

**Summary.** — The diffraction patterns in case of light sources of finite extension have been investigated. Depending on the size of the light source the edges of a slit are illuminated by either coherent or incoherent or partially coherent beams. Considering that according to the Young-Rubinovicz theory the diffraction pattern is produced by secondary waves emerging from the edges of the slit and interfering with each other as well as with the incident waves, it is shown that depending on the degree of coherence, the interference fringes of the diffraction pattern show more or less contrast. The places of the maxima except for the main peak, also depend on the size of the light source. In order to verify the theory the calculated curves were compared with those obtained in the experiments and a good quantitative agreement was found.

### 1. — Introduction.

In the usual treatment of diffraction the spherical waves incident upon the diffracting aperture or obstacle are assumed to be produced by a point-like source. In the experiments, however, which have been performed in order to verify the theory, the light sources were always of finite extension and since the diffraction pattern varies with the dimensions of the source the latter had to be chosen as small as possible. As in optical systems the light source can never be regarded as point-like it seems important from both the practical and the theoretical points of view to eliminate the above restriction. Wolf's theory <sup>(1)</sup> on the partial coherence of light, which may be considered a generalization of the Huygens-Fresnel-Kirchhoff principle, offers a possibility to take

---

<sup>(1)</sup> E. WOLF: *Proc. Roy. Soc., A* **225**, 96 (1954); *Proc. Roy. Soc., A* **230**, 246 (1955).

into account the finite size of the source. However this theory involving the rather wearisome evaluation of multiple surface integrals does not give a clear picture of the true mechanism of diffraction, since contrary to the older conception secondary waves can by no means emerge from the empty space but only from the diffracting obstacle.

In the present paper calculations are given which have been performed to study the dependence of the diffraction pattern on source dimension. For the description of the mechanism of diffraction the conception of YOUNG-RUBINOVICZ<sup>(2)</sup> has been adopted, according to which diffraction arises from interference of the incident wave with the secondary waves emerging from the diffracting edge. As the interfering waves may be coherent, incoherent or partially coherent depending on the size of the light source, the contrast of the interference fringes corresponds to the degree of coherence. The degree of coherence of the waves incident upon the slit edges was computed on the basis of the Zernike-Wolf<sup>(3)</sup> theory assuming the atoms of the light source to radiate independently.

The treatment of the diffraction pattern of light sources of finite extension on the basis of the Rubinovicz theory is presented in Section 2. While the experimental apparatus is described in Section 3. There too the results are given including a comparison of calculated and measured values.

## 2. - Theory.

If a diffracting aperture (Fig. 1) is illuminated by a light source  $L$ , each

point of the area stretched inside the aperture will according to the Huygens-Fresnel-Kirchhoff theory emit spherical waves and the radiation field in a point  $P$  lying in the space  $T$  is given by the sum of these waves:

$$(1) \quad u(P) = \frac{ik}{4\pi} \int_{\sigma} A \exp [ik\xi] df,$$

where

$$A = \frac{\cos(n\rho) - \cos(nr)}{r\rho}$$

and

$$\xi = r + \rho,$$

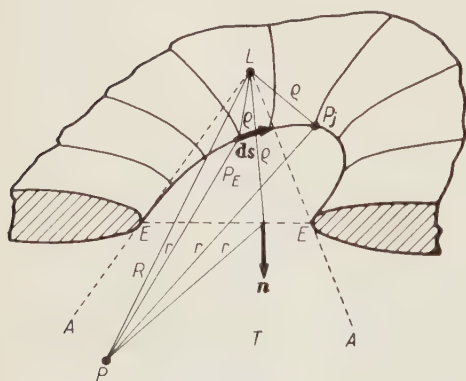


Fig. 1.

<sup>(2)</sup> T. YOUNG: *A course of lectures on natural philosophy mechanical arts* (London, 1807); A. RUBINOVICZ: *Ann. d. Phys.*, (4) 53, 257 (1917).

<sup>(3)</sup> F. ZERNIKE: *Physica*, 8, 785 (1938).

$k$  is the propagation constant,  $n$  the normal of the surface  $f_0$  and the distances from a point on the surface  $f_0$  to the source  $L$  and the point  $P$  are denoted by  $\varrho$  and  $r$ , respectively. The expression (1) can be transformed into an integral taken along the diffracting edge  $E$ , so that the field in the space  $T$  is now given by the superposition of the deflected waves

$$(2) \quad u_B = -\frac{1}{4\pi} \int_E A' \exp[ik\xi] ds,$$

and the incident wave. Each point of the edge emits spherical waves which together form the deflected waves. In expression (2)

$$A' = \frac{\cos(nr) \cdot \sin(\varrho ds)}{r\varrho[1 + \cos(r\varrho)]},$$

is the amplitude factor depending on the direction and  $ds$  is the tangent vector of  $E$  in the point  $P_E$ . In expression (2) the phase along  $E$  changes generally rather quickly ( $k \gg 0$ ) but only such intervals make an appreciable contribution to the integral, where the change is not so rapid or even zero, that is  $d\xi/ds \simeq 0$ . Thus only the integration with respect to these so called stationary points will be of interest. There may be only one, but also several such points, depending on the geometry of the diffracting edge. In the latter case the integrals, of course, have to be summed, that is the field becomes

$$(3) \quad u_B = \sum_j u_B|_j = -\frac{1}{4\pi} \sum_j \int_{s_j - \Delta s_j}^{s_j + \Delta s_j} \frac{A'(\xi)}{d\xi/ds} \exp[ik\xi] d\xi,$$

where  $2\Delta s_j$  is the path of integration taken with respect to the  $j$ -th stationary point.

Considering now a half plane, there is only one stationary point, where  $r + \varrho = \min$ . With an approximate evaluation of the integral (3) the deflected wave front close to the shadow boundary (4) is given by <sup>(5)</sup>

$$(4) \quad u_B = \pm \frac{\exp[i(\pi/4)]}{\sqrt{2}} \cdot \frac{\exp[ikR]}{R} \int_{+\infty}^w \exp\left[i\frac{\pi}{2}v^2\right] dv,$$

where

$$w = \sqrt{\frac{2k}{\pi}(r + \varrho - R)},$$

and  $R$  is the distance from the source to the point  $P$ . In the non-illuminated field the negative sign, in the illuminated one the positive sign is to be applied. In the latter the incident wave, of course, has to be added to the deflected wave.

Using now a slit which may be considered as consisting of two individual half-planes, there will be two stationary points, lying at the edges of the two half-planes, where  $r + \varrho = \min$ , and where the deflected waves are composed of the secondary waves emerging from these points. In the shadow the two waves are of different sign, since any given point  $P$  lies with respect to one of the half-planes in the illuminated field and with respect to the other one in the non-illuminated field. For the deflected wave, therefore, we have

$$(5) \quad u_B = u_{B_1} + u_{B_2} = \frac{\exp [i(\pi/4)]}{\sqrt{2}} \cdot \frac{\exp [ikR]}{R} [H(w_1) - H(w_2)],$$

where the abbreviation

$$H(w) = \int_{+\infty}^w \exp \left[ i \frac{\pi}{2} v^2 \right] dv,$$

has been introduced and

$$w_1 = \sqrt{\frac{2k}{\pi}} (\varrho_1 + r_1 - R), \quad w_2 = \sqrt{\frac{2k}{\pi}} (\varrho_2 + r_2 - R)$$

while the meaning of  $\varrho_1, r_1, \varrho_2, r_2$ , can be read from the Fig. 2. In the non-illuminated field there are but deflected waves emerging from the stationary points on the two edges. In the illuminated field the incident wave has again to be added.

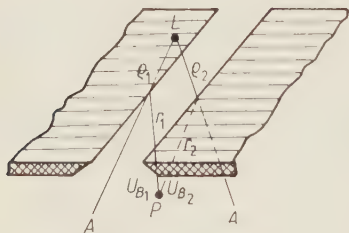


Fig. 2.

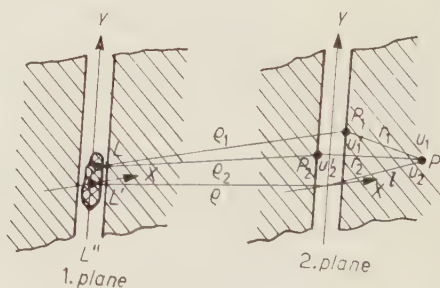


Fig. 3.

Full interference between two waves  $u_1, u_2$  will not take place unless these are coherent. In this case the intensity in point  $P$  (Fig. 3) can be written

$$J = |u_1|^2 + |u_2|^2 + 2 \operatorname{Re} (u_1 u_2^*).$$



This condition, however, cannot be satisfied for waves emerging from two points  $P_1, P_2$  unless the waves arriving in points  $P_1, P_2$  have been emitted by the same point source  $L$ . For a light source  $L'$  of finite extension the two waves are only partially coherent, thus the intensity in point  $P$  will have the form

$$J = |u_1|^2 + |u_2|^2 + 2\gamma_{12} \operatorname{Re} (u_1 u_2^*),$$

where  $\gamma_{12}$  is the degree of coherence of the waves in points  $P_1, P_2$  <sup>(4)</sup>. On the other hand,

$$\gamma_{12} = \frac{u_1' \cdot u_2'^*}{2\sqrt{\mathcal{F}_1' \cdot \mathcal{F}_2'}},$$

where  $u_1', u_2'$  represent the fields and  $\mathcal{F}_1', \mathcal{F}_2'$  the intensities in points  $P_1, P_2$ , respectively. If a light source of finite extension is used, where all points emit spherical waves independently of each other, the degree of coherence will take the form

$$(6) \qquad \gamma_{12} = \frac{u_1' u_2'^*}{2\sqrt{\mathcal{F}_1' \cdot \mathcal{F}_2'}} = \frac{1}{2\sqrt{\mathcal{F}_1' \cdot \mathcal{F}_2'}} \int J(\Sigma) \frac{\exp [ik(\varrho_1 - \varrho_2)]}{\varrho_1 \varrho_2} d\Sigma,$$

where  $\mathcal{F}(\Sigma)$  represents the intensity per unit area of the source. For a slit-like source infinite in the  $Y$ -direction and of a width  $2d$ , lying in the  $X$ - $Y$ -plane (plane 1) which runs parallel to the plane containing points  $P_1, P_2$  (plane 2), the above expression becomes

$$(7) \qquad \gamma_{12} = \frac{\sin [(2\pi/\lambda) \cdot (d/\varrho)(x_1 - x_2)]}{(2\pi/\lambda) \cdot (d/\varrho)(x_1 - x_2)},$$

where  $\lambda$  is the wave length of the illuminating light and  $x_1$  and  $x_2$  are the coordinates of points  $P_1$  and  $P_2$  in the plane 2. This well-known function is shown in Fig. 4, where

$$\eta = \frac{2\pi}{\lambda} \cdot \frac{d}{\varrho} (x_1 - x_2).$$

Diffraction on a slit arises from interference between two waves starting from two

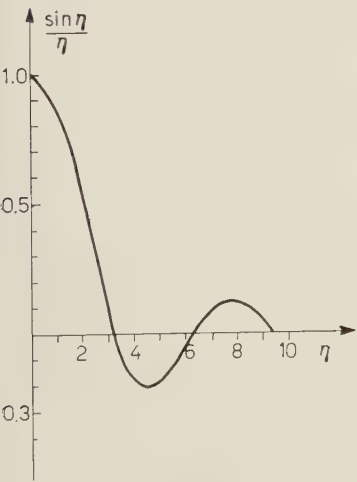


Fig. 4.

(4) M. BORN and E. WOLF: *Principles of Optics* (New York, 1959).

stationary points. Thus for the intensity at the point  $P$  lying in the non-illuminated field we obtain

$$(8) \quad J_B = \frac{1}{2R^2} [ |H(w_1)|^2 + |H(w_2)|^2 - 2\gamma_{12} \operatorname{Re} (H(w_1) \cdot H(w_2)^*) ].$$

Illuminating now the diffracting slit in plane 2 by a slit-like source lying in the  $Y$ -direction parallel to the slit (Fig. 3), the expression (7) for the values of  $\gamma_{12}$  has to be substituted into (8).

In the following the expression (8) will be somewhat transformed and in this way a descriptive model is obtained.  $H(w)$  is a complex integral, since

$$H(w) = \left(\frac{1}{2} - C(w)\right) + i\left(\frac{1}{2} - S(w)\right),$$

where

$$S(w) = \int_0^w \sin \frac{\pi}{2} x^2 dx \quad \text{and} \quad C(w) = \int_0^w \cos \frac{\pi}{2} x^2 dx$$

while

$$H^*(w) = \frac{1}{2} - C(w) - i\left(\frac{1}{2} - S(w)\right).$$

Using these expressions we obtain

$$\operatorname{Re} [H(w_1)H^*(w_2)] = F(w_1)F(w_2) + G(w_1)G(w_2),$$

where

$$F(w) = \frac{1}{2} - S(w), \quad G(w) = \frac{1}{2} - C(w),$$

Hence

$$J = \frac{J_0}{2} \{ F^2(w_1) + G^2(w_1) + F^2(w_2) + G^2(w_2) - 2\gamma_{12} [F(w_1)F(w_2) + G(w_1)G(w_2)] \}$$

where  $J_0 = 1/R^2$ . Let us take now a coordinate system having as horizontal axis  $C(w)$  and as vertical axis  $S(w)$ , the relation between them in this plane is given by the Cornu spiral (Fig. 5).  $F(w)$  and  $G(w)$  are the components of a vector in this plane starting from  $C(w) = \frac{1}{2}$  and  $S(w) = \frac{1}{2}$  respectively, the vector being directed towards a point of the Cornu spiral. Let us take two such vectors,

$$\mathbf{A} [F(w_1)G(w_1)], \quad \mathbf{B} [F(w_2)G(w_2)],$$

then the intensity at point  $P$  is given by

(9) 
$$J = \frac{J_0}{2} (A^2 + B^2 - 2\gamma_{12}AB) .$$

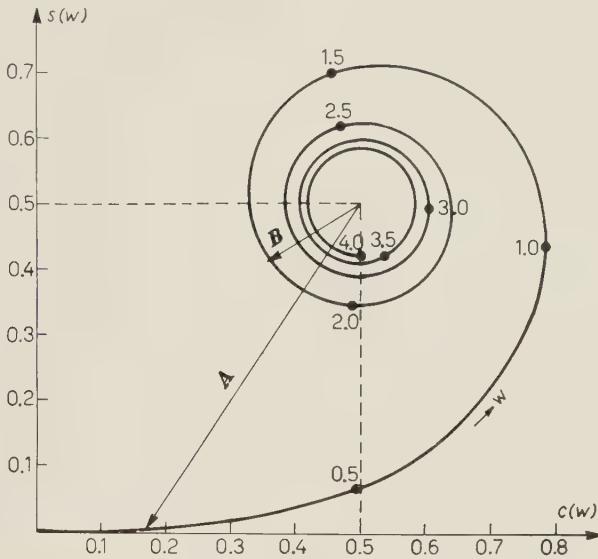


Fig. 5.

The first two terms of the expression in the bracket,  $A^2 + B^2$ , give a monotonic function (Fig. 6), while  $AB$  is a harmonic function (Fig. 7). In the expression (9) the harmonic part depends on  $\gamma_{12}$ , *i.e.* on the width  $2d$  of the slit serving as a light source. The variation of the diffraction pattern with the parameter  $2d$  is

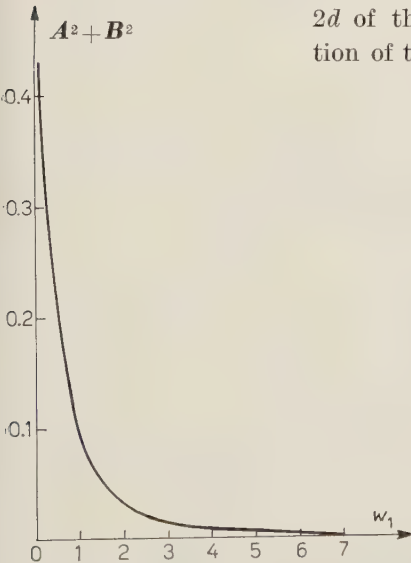


Fig. 6.

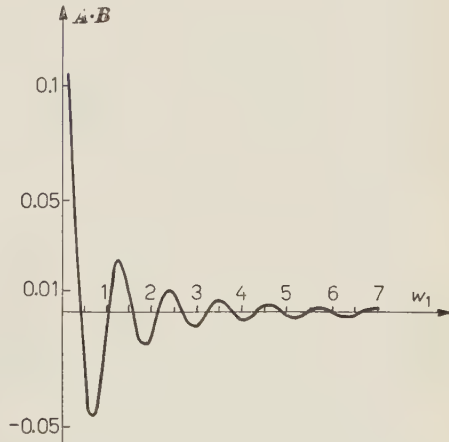
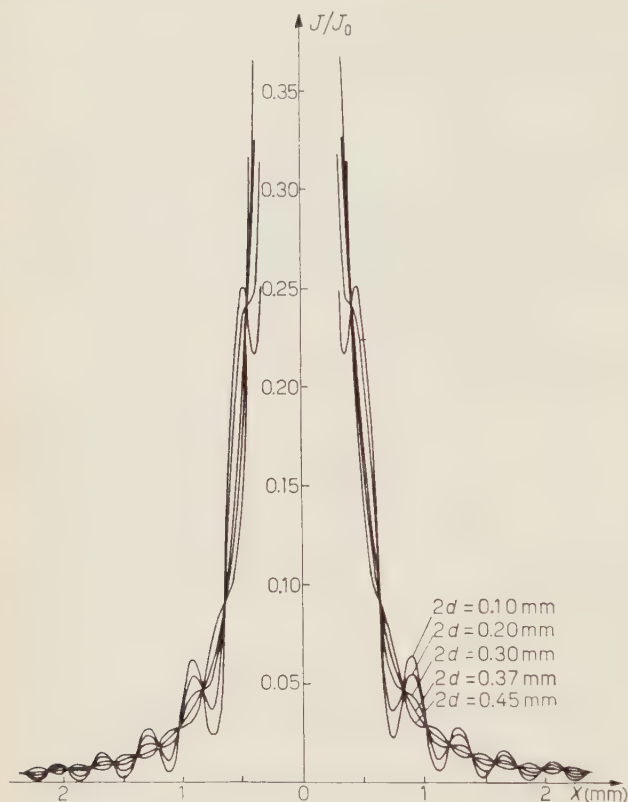


Fig. 7.

shown in Fig. 8. In this case the width of the diffracting slit (in plane 2)



was 0.3 mm and the distances both from the light source and from the observing screen to the diffracting slit were  $\varrho = l = 200$  mm (Fig. 3). It is seen that for a light source of width  $2d = 0.37$  mm, with  $\gamma_{12} = 0$  and  $I = (J_0/2)(A^2 + B^2)$  the monotonic curve of Fig. 6 is obtained. The shape of the curves strongly depends on the slit width  $R_1$  and after the first zero value of  $\gamma_{12}$  the positions of the maxima and minima will be reversed.

Fig. 8. — Calculated relative intensity distribution of the diffraction patterns of slit in case of light sources of different extension ( $2d$ ).

### 3. — Experiment.

In the following the experiment carried out in order to verify the above results will be described. The experimental apparatus (Fig. 9) is quite simple and in principle the same as the arrangement shown in Fig. 3.

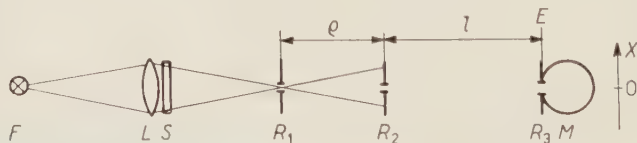


Fig. 9. — Experimental arrangement for measuring the diffraction patterns in the plane  $E$ , of the slit  $R_2$ .  $F$ =light source,  $L$ =condenser lens,  $S$ =interference filter ( $\lambda = 546$  nm),  $R_1$ =the secondary source,  $M$ =photomultiplier.

As light source  $F$  an Osram Hg-Cd spectral lamp was used. It was supplied by an a.c. 220 V, 50 Hz stabilizer. The fluctuation in the light current



was about 1%. The source was imaged by the lens  $L$  having a focal length  $f = 100$  mm with a magnification of about 1:1 on to the surface of the slit  $R_1$ . The interference filter  $S$  (Zeiss type SIF) could be inserted directly behind the lens,  $L$  to select the wavelength  $\lambda = 546$  nm. The line width was about  $0.1 \text{ \AA}$ , thus it did not affect the diffraction process. The diameter of the lens  $L$  being 30 mm, the degree of coherence of the image appearing on  $R_1$  was not being influenced by the diffraction caused by the lens, so that the points of the secondary source could be considered as radiating independently. The light of the secondary source at  $R_1$  was diffracted by the slit  $R_2$ . The calibration of both slits had been checked previously by microscope. The distance between the two slits was adjusted to be  $\varrho = 200$  mm. The measurements were performed with a slit  $R_2$  of 0.3 mm width. The diffraction field in the plane  $E$  was scanned by a multiplier  $M$ . In front of the multiplier a scanning slit  $R_3$  was inserted parallel to slits  $R_1$  and  $R_2$ , its width being so chosen that it was at least the 10-th part of the spacing of the fringes appearing in the diffraction pattern; in this way any appreciable integration could be excluded. The distance from the diffracting to the scanning slit was the same as that between  $R_1$  and  $R_2$ , that is  $\varrho = l = 200$  mm. The slits, including the scanning slit of the multiplier were carefully aligned by means of the telescope of a Zeiss « Richtungs- und Flüchtigkeitsprüfgerät ».

An end-window type multiplier M12FS35 was chosen because the optical conditions are far better in these systems than with a deflected cathode, which may produce the so called « angle-of-incidence effect », as it was observed in fact in the first measurement when the RCA 1P21 multiplier was being used. This effect appeared as asymmetry in the diffraction curve with respect to the centre. In order to prevent the displacement of the image on the photocathode the scanning slit was mounted directly on to the photocathode. For this reason, a slit of very thin material had to be prepared. This was achieved by depositing an aluminium mirror on glass using vacuum evaporation and cutting a slit into the thin metal layer thus formed. The mirror, however, had to be sufficiently thick so as not to affect measurement by its transparency. The use of slits made of very thin material is the more convenient since the intensity strongly increases in the vicinity of the shadow boundary and thus when using conventional slits the light scattered on the back causes a considerable deformation of the measured curve.

The multiplier mounted on a slide could be moved in a direction normal to the optical axis by means of a synchronous motor driving the multiplier at a rate of 0.67 mm/min in the  $x$ -direction (Fig. 9). The signals coming from the multiplier were recorded on a paper tape of 30 cm width by an automatically recording potentiometer. 60 mm spacing on the paper tape corresponded to a multiplier displacement of 1 mm. A d.c. bridge amplifier stage was applied between the multiplier and the potentiometer to obtain the ampli-

fication and impedance transformation required. The sensitivity of the system was  $6 \cdot 10^{-10}$  A/div. The amplifier stability was 1 per cent, the simultaneous

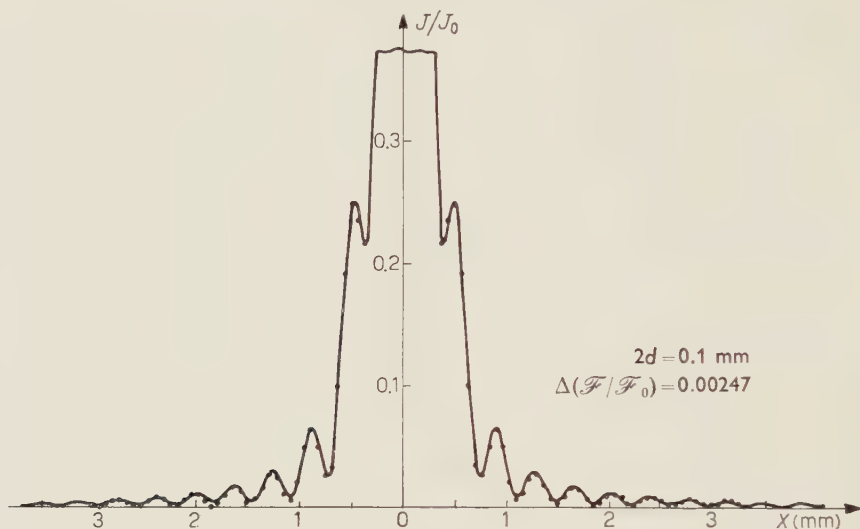


Fig. 10.

run of multiplier and tape displacements can be considered quite satisfactory, since the error in the reproducibility of multiplier displacement was about 0.02 mm.

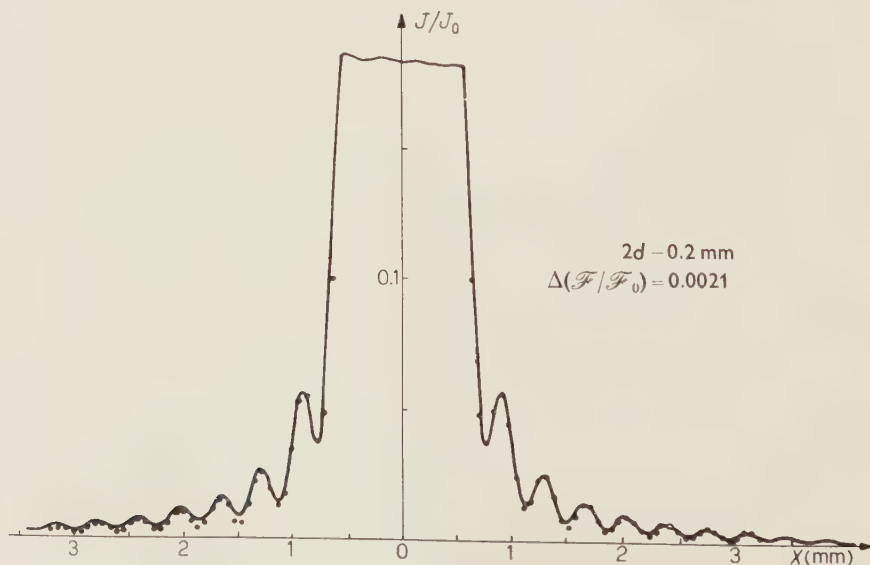


Fig. 11.

Using the above arrangement the diffraction patterns were recorded for various widths of slit  $R_1$ : The result agreed fairly well with the curves shown

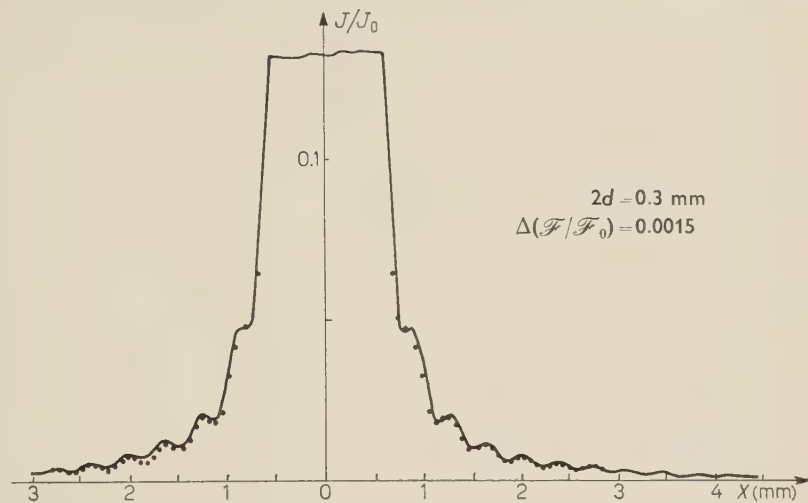


Fig. 12.

in Fig. 8. The experimental curves are to be seen in Figs. 10-15. The solid line was drawn by the recorder, while the points indicate the calculated values

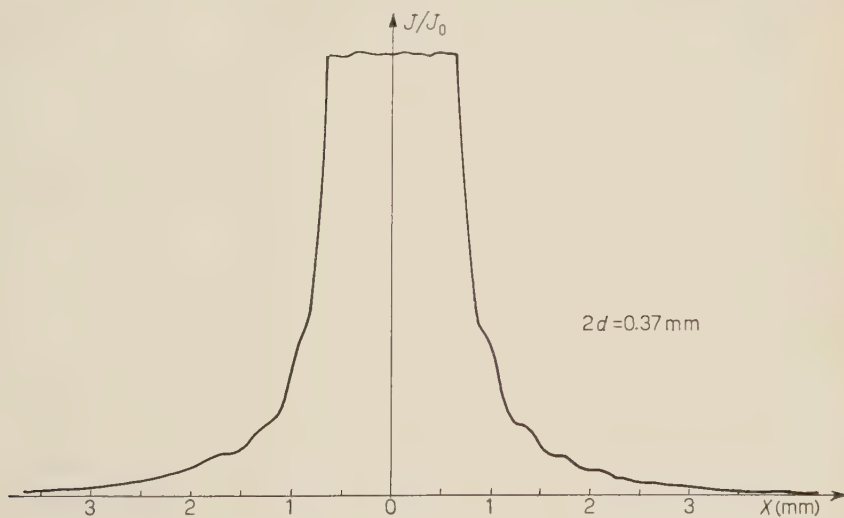


Fig. 13.

and are shown for comparison. The curves are normalized representing the relative intensity distribution  $\mathcal{F}/\mathcal{F}_0$ . Although the scale of the ordinate undergoes

a continuous change, since with increasing size of source the intensity also increases no alternations were made in the experimental arrangement (for

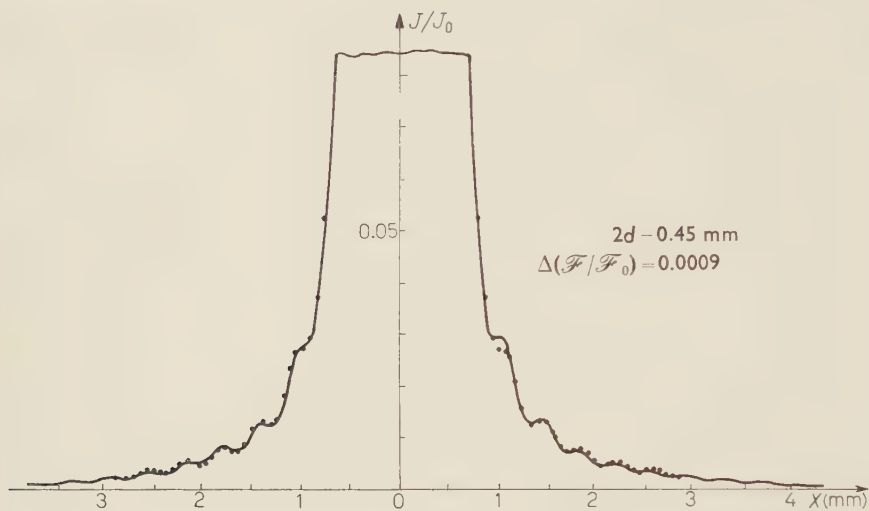


Fig. 14.

instance the plate voltage of the multiplier). Accordingly, the accuracy of measurement also varied during the experiment and this is indicated by the

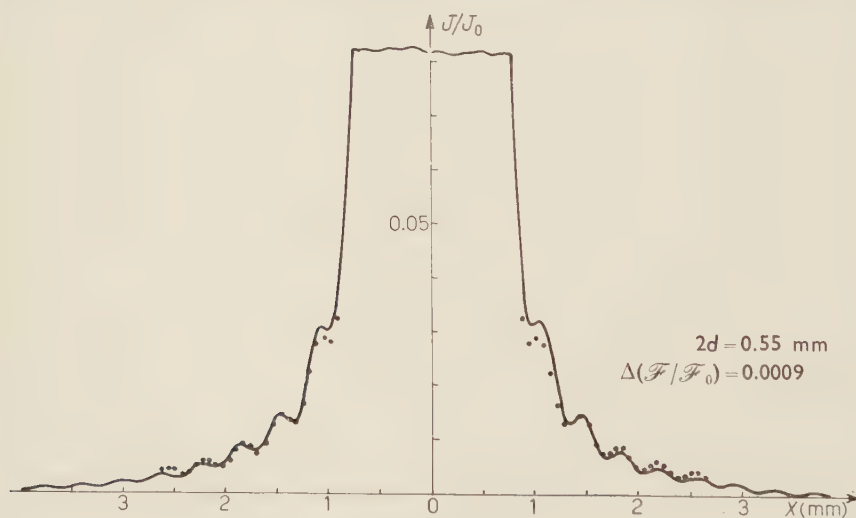


Fig. 15.

symbol  $\mathcal{F}/\mathcal{F}_0$  the value of which is given for each of the curves. The multiplier displacement is given on the abscissa in mm.



The phase shift following the zero value of  $\gamma_{12}$  is shown in Fig. 16, where the experimental curves plotted for slit widths  $2d = 0.2$  mm and  $2d = 0.45$  mm are to be seen. These curves too are normalized.

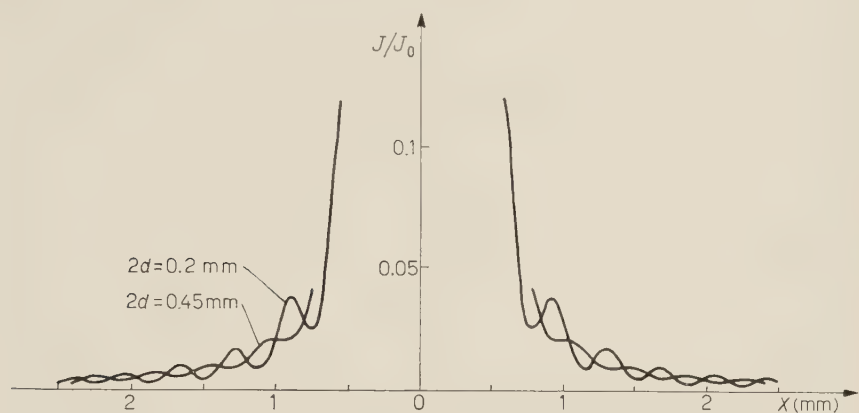


Fig. 16.

From the figures it is apparent that the experimental curves are quantitatively in good agreement with the predicted ones.

Finally, it has to be noted that for the zero values of  $\gamma_{12}$  the contrast does not vanish as it would be expected. Several attempts were made to find an explanation for this phenomenon and although various interpretations might be possible, no sound theory can be formulated on the basis of our experiments.

#### 4. - Conclusions.

From the above considerations and from the result of the experiments the following conclusions may be drawn:

1) A simple procedure has been developed for calculating the diffraction pattern for a light source of finite extension.

2) By supplementing the facts known so far <sup>(5)</sup> additional proof has been obtained showing that the Young-Rubinowicz conception of the diffraction mechanism gives a simpler and more comprehensive representation than the Huygens-Fresnel-Kirchhoff theory.

<sup>(5)</sup> A. RUBINOWICZ: *Die Beugungswelle in der Kirchhoffschen Theorie der Beugung* (Warsawa, 1957).

3) In addition to the qualitative measurements carried out up to now <sup>(6)</sup> the experiment described here leads also to the quantitative confirmation of the Zernike-Wolf theory on partial coherence.

\* \* \*

Thanks are due to Mr. ZS. NÁRAY and to Mr. P. VARGA for valuable advice and helpful discussions in connection with the experiments.

---

<sup>(6)</sup> B. J. THOMSON and E. WOLF: *Journ. Opt. Soc. Am.*, **47**, 895 (1957); B. J. THOMPSON: *Journ. Opt. Soc. Am.*, **48**, 95 (1958).

---

#### RIASSUNTO (\*)

Abbiamo esaminato le figure di diffrazione di sorgenti luminose di estensione finita. A seconda dell'estensione della sorgente luminosa, i margini di una fenditura sono illuminati da fasci coerenti, o incoerenti, o parzialmente coerenti. Considerando che, secondo la teoria di Young-Rubinovicz, la figura di diffrazione è prodotta da onde secondarie emergenti dai margini della fenditura e interferenti sia fra di loro che con le onde incidenti, si dimostra che, a seconda del grado di coerenza, il contrasto delle frange d'interferenza della figura di diffrazione è più o meno marcato. Anche le posizioni dei massimi, eccetto che per il massimo principale, dipende dall'estensione della sorgente luminosa. Per verificare la teoria, le curve calcolate sono state confrontate con quelle ottenute sperimentalmente trovando un buon accordo quantitativo.

---

(\*) Traduzione a cura della Redazione.

## Magneto-Compressional Disturbance in a Tepid Plasma.

P. L. AUER (\*) and J. A. NATION

*Laboratorio Gas Ionizzati (EURATOM - C.N.E.N.)*

*e/o Laboratori Nazionali di Frascati - Roma*

(ricevuto il 3 Agosto 1961)

**Summary.** — The propagation of steady state pulses travelling perpendicular to a magnetic field in a cold plasma was originally discussed by ADLAM and ALLEN <sup>(1)</sup>. It was found that pulses exist when the ratio of the pulse velocity to the Alfvén velocity exceeds unity. An essential feature of the non-linear pulse theory is that the fields rise exponentially in the region of the undisturbed plasma, a result which may be obtained also from the linearized theory. Guided by this we have examined the steady state problem for a tepid plasma in order to establish whether the plasma is capable of supporting exponentially rising fields. In this article a linear and a quasi non-linear analysis of the problem is given and it is shown that pulses exist when the disturbance speed is supersonic. It is also shown that the range of disturbance velocities, for which pulses are formed, is reduced in a highly non analytic manner.

### 1. — Introduction.

We wish to investigate the propagation of plane stationary compressional disturbances, travelling perpendicular to an initially uniform axial magnetic field in an initially uniform quiescent plasma composed of singly charged ions and electrons, using the assumption that interparticle collisions may be neglected. We restrict ourselves to situations where the electron plasma frequency in the undisturbed plasma greatly exceeds the electron gyration frequency; and, consequently the plasma remains macroscopically neutral to

---

(\*) John Simon Guggenheim Fellow 1960-61. Permanent address: General Electric Research Laboratory, Schenectady, N. Y.

<sup>(1)</sup> J. H. ADLAM and J. E. ALLEN: *Phil. Mag.*, **3**, 448 (1958).

a high degree of approximation. Thus

$$(1) \quad n_+(x) = n_-(x),$$

$$(2) \quad n_+(x)u_+(x) = n_-(x)u_-(x),$$

where  $n_{\pm}$ ,  $u_{\pm}$  denote respectively the ion, electron number density and the mean ion, electron velocities in the direction of propagation measured in a reference frame moving with the disturbance. The initial density is  $n_0$  and the disturbance travels with a velocity  $u_0$  in the  $X$  direction. The frequency inequality stated above, which determines macroscopic charge neutrality, may be expressed as  $B_0^2 \ll 4\pi n_0 m_e c^2$ , where  $B_0$  represents the initial magnetic field strength,  $m_e$  the electron mass and  $c$  the velocity of light. It will also be assumed that the disturbance produces only compressional distortions in the original lines of force and consequently that the induced currents will be constrained to flow in a direction mutually perpendicular to the initial magnetic field and direction of propagation.

It is well known <sup>(1-3)</sup> that in the limit of the plasma temperature approaching zero, solutions of the non linear equations exist in the form of isolated symmetric pulses for certain ranges of initial conditions. We term these solutions Adlam-Allen pulses. An important property of these pulses is that the leading and trailing edges decay exponentially in the direction of the undisturbed plasma as  $\exp[-Kx]$  with

$$(3) \quad \begin{cases} K = \frac{\omega_p}{c} \left[ 1 - \frac{u_A^2}{u_0^2} \right]^{\frac{1}{2}} \\ \omega_p^2 = 4\pi n_0 e^2 \left[ \frac{1}{m_e} + \frac{1}{m_i} \right], \\ u_A^2 = \frac{B_0^2}{4\pi n_0 (m_i + m_e)}, \end{cases}$$

where  $m_i$  is the ionic mass and  $e$  the magnitude of the electron charge. It is found that at distances sufficiently removed from the body of the pulse, that is in the wings, a linearized theory correctly predicts the exponential constant  $K$ . Thus one may infer, even from a linearized theory, that the existence of non-undulatory stationary disturbances requires that the disturbance speed exceeds some characteristic velocity, which for an initially cold plasma is  $u_A$ , the Alfvén speed.

(2) L. DAVIS, R. LÜST and A. SCHLÜTER: *Zeits. Naturfor.*, **13a**, 916 (1958).

(3) C. S. GARDNER *et al.*: *Proc. Geneva Conf.*, **31**, 230 (1958).

In this article we wish to ascertain the influence of an initial temperature in the undisturbed plasma on the formation and propagation of such pulses. Whereas a full non-linear treatment with non zero temperature is beyond the scope of the present analysis, certain features may be inferred on the basis of linear or quasi-linear analysis.

In the following section we review briefly some results of cold plasma calculations which will be used in the subsequent sections discussing thermal effects.

## 2. - Cold plasma results.

In this section we assume the plasma temperature is zero and consider initially the results of linear analysis. Instead of eq. (1), (2) we define, in a frame moving with the disturbance

$$(4) \quad \begin{cases} n_{\pm}(x) \equiv n_0[1 + \delta n_{\pm}(x)], \\ u_{\pm}(x) \equiv u_0[1 - \delta u_{\pm}(x)], \\ v_{\pm}(x) \equiv u_0 \delta v_{\pm}(x), \end{cases}$$

where  $v$  is the velocity in the  $y$  direction.

As a result of conservation of particle flux (eq. (2)) we have to lowest order in small quantities

$$(5) \quad \delta n_{\pm}(x) = \delta u_{\pm}(x).$$

The axial magnetic field is taken in the positive  $z$  direction and we write

$$(6) \quad B_z(x) \equiv B_0[1 + \delta B(x)].$$

The electric field has two components and must have zero curl.

$$(7) \quad \begin{cases} E_x \equiv -B_0 \delta \varphi'(x), \\ E_y = E_0 = \text{constant}, \end{cases}$$

where the prime denotes differentiation with respect to the argument and  $\varphi$  the scalar electric potential. The requirement that all first order quantities, denoted by  $\delta$ , and also all derivatives, vanish in the undisturbed plasma provides

$$(8) \quad E_0 = \frac{n_0 B_0}{c}.$$



Using the above notation the equations of motion and field equations required to determine the six unknown first order quantities take the form

$$(9) \quad \begin{cases} u \delta u'_{\pm}(x) = \mp \omega_{\pm} \left[ \delta v_{\pm} - \frac{c}{u_0} \delta \varphi' \right], \\ u \delta v'_{\pm}(x) = \pm \omega_{\pm} [\delta u_{\pm} - \delta B], \\ \delta B'(x) = \left( \frac{4\pi n_0 u_0 e}{e B_0} \right) [\delta v_- - \delta v_+], \\ \delta \varphi''(x) = \left( \frac{4\pi n_0 e}{B_0} \right) [\delta u_- - \delta u_+], \end{cases}$$

where

$$\omega_{\pm} = \frac{e B_0}{c m_{i,e}}.$$

On the basis of the above set of equations one can readily establish that the basic assumption of charge neutrality (eq. (1)) is equivalent to the disturbance velocity being highly non-relativistic.

Accordingly we write

$$(10) \quad \delta u(x) = \delta u_-(x) = \delta u_+(x) = \left( \frac{u_A}{u_0} \right)^2 \delta B(x),$$

where the second equality results from a single integration of eqs. (9). We have then by elimination of  $\delta u$  from eqs. (9) and (10) the relation

$$(11) \quad \delta B''(x) = \frac{\omega_p^2}{c^2} \left[ 1 - \frac{u_A^2}{u_0^2} \right] \delta B(x),$$

which establishes the validity of eq. (3).

The magnetic field and electric potential are related by

$$(12) \quad \left( \frac{m_i - m_e}{m_i + m_e} \right) \delta B = \left( \frac{4\pi n_0 e}{B_0} \right) \delta \varphi,$$

and we find for the current components

$$(13) \quad \begin{cases} \delta v_- = \frac{m_i}{m_i - m_e} \frac{c}{u_0} \delta \varphi' = \frac{u_A^2}{u_0^2} \frac{u_0}{\omega_+} \delta B', \\ \delta v_+ = -\frac{m_e}{m_i - m_e} \frac{c}{u_0} \delta \varphi' = -\frac{u_A^2}{u_0^2} \frac{u_0}{\omega_-} \delta B'. \end{cases}$$

The non linear analogue of eqs. (10) and (12) may be found from the exact solution of the Adlam-Allen pulse. We write this in the form

$$(14) \quad 2 \left[ 1 - \frac{u}{u_0} \right] = \frac{u_A^2}{u_0^2} \left[ \frac{B^2}{B_0^2} - 1 \right], \quad e\varphi = \frac{(m_i - m_e)}{2} u_0^2 \left[ 1 - \frac{u^2}{u_0^2} \right].$$

Combining these two equations one finds

$$(15) \quad \frac{m_i - m_e}{m_i + m_e} \left[ \frac{B}{B_0} - 1 \right] = \frac{4\pi n_0 e\varphi}{B_0^2} \left[ \frac{4}{(1 + u/u_0)(1 + B/B_0)} \right].$$

The quantity in the square bracket on the right hand side of eq. (15) is identically unity in the undisturbed plasma and at the peak of the pulse, while at the inflection point it varies from unity for  $u_0 = u_A$  to approximately 0.95 for  $u_0 = 2u_A$ . Thus, the approximation of eq. (12) is remarkably good throughout the entire non linear region of the pulse and will be used in the discussion of temperature effects.

It should be noted that certain features of the Adlam-Allen pulse appear insensitive to the electron to ion mass ratio. For example if the distance is scaled according to the magnetic skin depth ( $c/\omega_p$ ) and the velocities scaled according to  $u_A$ , the magnetic profiles form a one parameter set of curves where the Alfvén-Mach number  $u_0/u_A$  is the parameter of variation. On the other hand the electrostatic potential and the partial electron and ion currents are sensitive functions of the mass ratio.

In general the compressional mode of the Adlam-Allen pulse is a complicated mixture of effects due to the transverse electric field  $E_y$  and the longitudinal electric field  $E_x$ . Some simplification results in the two limits where the electron to ion mass ratio is very small or unity. In the former case one finds to zero order in the mass ratio that the electrons carry all the current and make large excursions in the  $y$  direction in order to stay in phase with the rectilinear motion of the heavy ions. In this instance the ions provide the entire inertial resistance to compression and the work of compression lodges in the electrostatic field  $E_x$ .

Of course, in the limit the electron mass vanishes, the system of equations leading to the Adlam-Allen pulse become singular and no proper limit point exists. If the electron to ion mass ratio becomes unity, the partial currents become equal in magnitude and the particle motions are appreciably different. The longitudinal  $E_x$  field vanishes identically and the work of compression arises from the transverse  $E_y$  field.

The orbital equations, in the linear approximation follow readily from eqs. (10), (11) and (13)

$$(16) \quad \left( \frac{\partial y}{\partial x} \right)_{\pm} = \left( \frac{\partial v}{\partial u} \right)_{\pm} = \mp \left[ \frac{u_0^2}{u_A^2} - 1 \right]^{\frac{1}{2}}.$$

The initial angle of the orbit with the direction of propagation varies from zero degrees for  $u_0 = u_A$  to  $\mp 60$  degrees for  $u_0 = 2u_A$ .

We shall refer to these two extreme modes as the light and heavy electron models, respectively. In the following section the effect of plasma temperature on these two modes will be discussed.

### 3. - The effect of plasma temperature.

In this section we shall discuss some aspects of the linearized Vlasov equation corresponding to the geometry described in the previous two sections. In a frame moving with the stationary disturbance we look for non undulatory solutions which decay exponentially into the undisturbed plasma where the particle distribution has a mean drift velocity  $u_0$  in the  $x$  direction and carries no current. It is not at all obvious that the problem so stated is self-consistent since an exponentially rising (decaying) solution of the linearized equations may grow into non linear disturbances which cannot be fitted to the assumed initial conditions. For the moment we proceed without noting this objection and postpone a discussion of it to the subsequent portions of the section. We begin by discussing the equal mass case in which  $E_x = 0$ .

3.1. *Heavy electrons.* - We introduce circular coordinates in velocity space

$$(16a) \quad \begin{cases} u = u_0 - w \cos \varphi, \\ v = w \sin \varphi, \end{cases}$$

and expand the particle distribution function, assuming equal electron-ion temperature

$$(17) \quad \begin{cases} f_{\pm}(x, w, \varphi) \equiv f_0(w) + \delta f_{\pm}(x, w, \varphi), \\ n_0 \equiv \int_0^{\infty} 2\pi f_0 w dw. \end{cases}$$

The linearized Vlasov equation for equal mass electrons and ions becomes

$$(18) \quad \left[ \frac{\partial}{\partial \varphi} \pm \left( \frac{u_0 - w \cos \varphi}{\omega_0} \right) \frac{\partial}{\partial x} \right] \delta f_{\pm} = u_0 \delta B \sin \varphi f'_0(w),$$

where

$$\omega_0 = \omega_+ = \omega_-.$$

The above is readily integrated in the form

$$(19) \quad \delta f_{\pm} = u_0 f'_0(w) \int_{-\infty}^q \delta B \left[ x \mp \frac{u_0}{\omega_0} (q - q_0) \pm \frac{w}{\omega_0} (\sin q - \sin q_0) \right] \sin q_0 dq_0,$$

and it is understood that  $\delta f_{\pm}(q) = \delta f_{\pm}(q + 2\pi)$ . (For a given  $\delta B(x)$ , the latter condition is met by adding to the above a suitable function of  $[x \mp ((u_0 - w \sin q)/\omega_0)]$ ). The electric current obtained from eq. (19) is

$$(20) \quad j_z = e \int_0^{\infty} \int_0^{2\pi} [\delta f_+ - \delta f_-] w^2 \sin q dq dw = \\ = 2eu_0 \int_0^{\infty} dw \int_0^{\infty} dw w^2 f'_0(w) \int_0^{2\pi} d\alpha [\cos 2\beta - \cos 2\alpha] \left\{ \delta B \left[ x - \frac{2u_0}{\omega_0} \beta + \frac{2w}{\omega_0} \sin \beta \cos \alpha \right] \right\},$$

with obvious changes in notation.

In general one proceeds to solve Maxwell's equation involving the current by expanding  $\delta B(x)$  into plane waves, thereby obtaining a dispersion relation which has been treated often in the literature<sup>(4,5)</sup>. For our purpose it will suffice to obtain temperature corrections to lowest significant order in the ratio of the thermal velocity to the Alfvén velocity. This may be accomplished by expanding  $\delta B$ , in the argument of the integral (20), in a formal power series in  $w$ . Stopping with the term in  $w^2$  and substituting the result into Maxwell's equation, we obtain after a simple rearrangement the following integro-differential equation:

$$(21) \quad \delta B'(x) = \frac{\omega_p^2}{c^2} \int_{-\infty}^x dy \left\{ \cos \left[ \frac{\omega_0}{u_0} (x - y) \right] \delta B(y) + \frac{kT}{m\omega_0^2} \left( 3 \cos \left[ \frac{\omega_0}{u_0} (x - y) \right] - \right. \right. \\ \left. \left. - \cos \left[ \frac{2\omega_0}{u_0} (x - y) \right] - 2 \right) \delta B''(y) \right\},$$

where

$$2n_0 kT = 2\pi \int_0^{\infty} m w^2 f_0 w dw \quad \text{and} \quad \omega_p^2 = 4\pi n_0 e^2 \left( \frac{2}{m} \right).$$

We look for solutions to eq. (21) of the form  $\delta B(x) = \delta B(0) \exp[-Kx]$  and

(4) I. BERNSTEIN: *Phys. Rev.*, **109**, 10 (1958).

(5) N. ANDERSON: *Proc. Phys. Soc.*, **75**, 905 (1960).

obtain to the lowest order in the pertinent parameter.

$$(22) \quad K^2 \approx \frac{\omega_p^2}{c^2} \left\{ 1 - \frac{u_A^2}{u_0^2} \left[ 1 + \frac{kT}{mu_A^2} \left( \frac{9u_A^2 - u_0^2}{3u_A^2 + u_0^2} \right) \right] \right\}.$$

We now define a Mach number as

$$(23) \quad M = \frac{u_0}{[u_A^2 + (kT/m)((9u_A^2 - u_0^2)/(3u_A^2 + u_0^2))]^{\frac{1}{2}}},$$

and compare with simple theory where

$$(24) \quad M = \frac{u_0}{[u_A^2 + \gamma(kT/m)]^{\frac{1}{2}}},$$

and  $\gamma$  denotes the ratio of specific heats. We note that according to eq. (22) exponential solutions exist for  $M > 1$  and the effective  $\gamma$  of the plasma varies from 2 for  $u_0 = u_A$  to unity for  $u_0 = \sqrt{3} u_A$ . The effect of an initial plasma temperature is to broaden the disturbance in the wings on account of a plasma contribution to the characteristic sound speed.

**3.2. Light electrons.** — In dealing with physically realistic plasma conditions one may often employ to advantage the existence of sets of small numbers. For example, we have already indicated that when  $u_A^2/c^2 \ll m_e/m_i$  the quasi-neutral plasma approximation is quite accurate. If in addition one assumes  $m_e/m_i \ll 1$ , then it becomes possible to neglect the ionic contribution to the total current and the magnetic force on the ions in, at least, certain regions in space. (We shall amplify this remark subsequently.) The tepid plasma approximation consists of assuming that the mean square of the ion thermal speed is much less than  $u_A^2$  and use of this approximation results in considerable simplification in the dispersion relations.

An important consequence of the small electron mass is that we may introduce an adiabatic approximation<sup>(6,7)</sup> (in which the invariant is not the usual magnetic moment). We write

$$(25) \quad \begin{cases} v_-(x) = -\frac{cE_x(x)}{B_z(x)}, \\ \frac{dv_-(x)}{dx} = -\omega_- \left[ \frac{n_-(x)}{n_0} - \frac{B_z(x)}{B_0} \right]. \end{cases}$$

<sup>(6)</sup> C. S. MORAWETZ: New York University Report no. NYO-2885 (1960).

<sup>(7)</sup> P. L. AUER, H. HURWITZ JR. and R. KILB: *Proc. Salzburg Conf.*, Abstract no. 127/A (1961).



Whereas the above set of equations correctly describe the electron motion in the cold plasma is the limit  $m_e/m_i \ll 1$ , it continues to describe the average electron motion to the same degree of approximation when the initial electron temperature is finite. This follows from the fact that the non-adiabatic corrections in lowest order are proportional to the ratio of gyration length to the characteristic length squared. (Cf. eq. (22) or ref. (6)) and for comparable electron and ion temperatures the electron correction terms are correspondingly smaller than the ion correction terms by a factor of  $m_e/m_i$ .

Not only does eq. (25) allow us to relate the electron variables to the field variables; but if we neglect the ion contribution to the total current, then the above equations in combination with Maxwell's equation provide a relation between the field variables in the form

$$(26) \quad \left( \frac{B}{B_0} - 1 \right) = \frac{4\pi n_0 e}{B_0^2} \varphi - \frac{2\pi n_0 m_e c^2}{B_0^2} \left( \frac{E_x}{B} \right)^2.$$

We note that eqs. (12) and (15) result from the above providing we neglect the last non linear term. Presumably this approximation has considerable validity beyond the strictly linear regime.

In what follows we shall use the set of approximate relations

$$(27) \quad \begin{cases} \left( \frac{B}{B_0} - 1 \right) = \frac{4\pi n_0 e}{B_0^2} \varphi, \\ \frac{n_-}{n_0} - 1 = \frac{n_+}{n_0} - 1 = \frac{4\pi n_0 e}{B_0^2} \left[ \varphi - \frac{c^2}{\omega_p^2} \varphi'' \right]. \end{cases}$$

Given the ion density as a function of the field variables, the problem becomes completely specified.

We continue to neglect the magnetic force on the ion, assuming its motion to be rectilinear. The linearized Vlasov equation and its solution take the form

$$(28) \quad \begin{cases} u \frac{\partial}{\partial x} \delta f_+(x, u) = \frac{e}{m_i} \frac{d\varphi}{dx} \frac{dF(u - u_0)}{du}, \\ \delta f_+(x, u) = \frac{e}{m_i} \varphi(x) \frac{1}{u} \frac{dF(u - u_0)}{du}, \end{cases}$$

where

$$F(u - u_0) = \int_{-\infty}^{\infty} f_0(u - u_0, v) dv.$$

The second of eqs. (27) together with the above leads to the relation

$$(29) \quad \varphi''(x) = \frac{\omega_p^2}{c^2} \left\{ 1 - u_A^2 \int_{-\infty}^{\infty} \frac{F'(u)}{n_0} \frac{du}{u + u_0} \right\} \varphi(x).$$

Eq. (29) constitutes a dispersion relation quite familiar in connection with the theory of Landau damping. As stated it has no solution, but the difficulty is artificial. Indeed, had we included the small but finite ion current, we would find that the Landau damping disappears in the linear theory. This is a consequence of the fact that the resonance between particle motion and wave motion cannot exist when the particles have pure gyrating orbits. Rather than introducing the correction terms of order  $m_e/m_i$  we prefer to remove the above difficulty by a quasi non-linear treatment to follow. For present purposes, however, we treat the integral in eq. (29) as a principal value integral without further justification. The tepid plasma approximation is obtained from a formal expression of the integrand in inverse powers of  $u_0$ . Retaining terms to lowest significant order we obtain

$$(30) \quad \begin{cases} \varphi''(x) = \frac{\omega_p^2}{c^2} \left[ 1 - \frac{u_A^2}{u_0^2} \left( 1 + \frac{3kT}{m_i u_0^2} \right) \right] \varphi(x), \\ n_0 kT = \int_{-\infty}^{\infty} m_i (u - u_0)^2 F(u - u_0) du. \end{cases}$$

Denoting the Mach number as

$$M = \frac{u_0}{[u_A^2 + 3(u_A^2/u_0^2)(kT/m_i)]^{\frac{1}{2}}},$$

we observe that exponential solutions exist when  $M > 1$ .

The effect of initial plasma temperature is once again to broaden the disturbance in the wings and is equivalent to stating the plasma has an effective  $\gamma$  which varies from 3 when  $u_0 = u_A$  to unity when  $u_0 = \sqrt{3}u_A$ . Comparing with eq. (22) we note that for  $u_0 = u_A$  there is a difference due to the effective number of degrees of freedom involved in the motion but that the difference diminishes as  $u_0/u_A$  grows.

3.3. *Quasi non-linear approximation.* — As long as we limit ourselves to situations where the magnetic force on the ions may be neglected, the non-linear Vlasov equation for the ion distribution is readily solved. A new feature arises, however, since it is necessary to classify orbits in order to specify the solution to the non linear problem. We note that in the case of a symmetric

Adlam-Allen pulse a unique situation exists in that all particles upstream of the disturbance are able to surmount the barrier provided by the disturbance at the first encounter. The pulse solution breaks down when the barrier height is such that the particles come to rest at the top of the pulse.

Indeed it may be argued that any symmetric stationary pulse solution must have the property that all particles upstream successfully surmount the barrier at the first encounter. If groups of particles exist upstream which become reflected once or more often before they can successfully negotiate the barrier, then in general an asymmetry will develop between the leading and trailing edges of the disturbance. This argument seems to rule out the possibility that stationary symmetric pulses can traverse a plasma containing a continuous distribution of particle velocities from plus to minus infinity, in particular a Maxwellian distribution; for in this case there will always be particles present which are initially reflected by the barrier.

It also seems evident that in regions where particles are reflected; that is orbit looping occurs, the magnetic force on the ions cannot be neglected. In the course of multiple looping and weaving back and forth near the barrier an ion can provide arbitrarily large contributions to the total current irrespective of its mass. This is readily inferred from the Hamiltonian describing the dynamics of the ion motion:

$$(31) \quad \begin{cases} H = \frac{1}{2m_i} \left[ p_x^2 + \left( p_y - \frac{e}{c} A_y \right)^2 \right] + e\varphi(x) - eE_0 y, \\ B(x) = A'_y(x). \end{cases}$$

The  $y$  component of velocity is proportional to  $p_y$  which grows linearly in time, where time varies parametrically along the orbit. Thus  $p_y$  grows as the particle zig-zags in space and this growth need not be compensated by the vector potential, which may be a single valued function of space.

An apparently self consistent formulation of the problem may be made by requiring that the initial distribution in the undisturbed plasma contains only ions capable of surmounting the barrier on the first encounter. For such a class of particles the magnetic force may be made vanishingly small everywhere and the rectilinear approximation becomes valid. This, however, forces us to treat physically unrealistic distributions. A somewhat similar treatment, but in the opposite approximation that  $B_0^2 \gg 4\pi n_0 m_e c^2$  has been given recently<sup>(8)</sup>.

We now consider a symmetric potential pulse whose leading and trailing edges decay exponentially to zero into the undisturbed plasma and which has

<sup>(8)</sup> A. A. VEDENOV, E. P. VELIKHOV and R. Z. SAGDEEV: *Nuclear Fusion*, **1**, 82 (1961).

a peak value denoted by  $\varphi_m$ . Whereas a number of distributions might be tailored to suit such a pulse, we wish to examine in some sense the effect of « temperature » on an Adlam-Allen pulse. Accordingly we choose a distribution containing a single stream of particles, all of which are capable of surmounting the potential barrier at the first attempt. In the undisturbed plasma upstream of the disturbance

$$(32) \quad \begin{cases} f_+(\infty, u) = F(u - u_0); & u > u_m, \\ = 0; & u \leq u_m, \end{cases}$$

where

$$u_m = \sqrt{\frac{2e\varphi_m}{m_i}}.$$

The non linear Vlasov equation for the ions is satisfied in the rectilinear approximation providing the distribution is a function of the total energy; the distribution in regions of the disturbance becomes

$$(33) \quad \begin{cases} f_+(x, u) = F\left[\sqrt{u^2 + \frac{2e\varphi(x)}{m_i}} - u_0\right]; & u > u_c(x), \\ = 0; & u \leq u_c(x), \end{cases}$$

where

$$u_c(x) = \left[\frac{2e}{m_i}(\varphi_m - \varphi(x))\right]^{\frac{1}{2}}.$$

The distribution is normalized to a constant particle flux

$$(34) \quad n_0 u_0 = \int_{u_c(x)}^{\infty} f_+(x, u) u \, du = \int_{u_c(x)}^{\infty} u F\left[\sqrt{u^2 + \frac{2e\varphi}{m_i}} - u_0\right] \, du = \int_{u_m - u_0}^{\infty} (z + u_0) F(z) \, dz.$$

In order to effect a close resemblance to the original cold plasma situation we try to choose an initial distribution bell shaped about  $u_0$ . Consequently the distribution has an upper cut off at

$$u \geq \left[(2u_0 - u_m)^2 - \frac{2e\varphi(x)}{m_i}\right]^{\frac{1}{2}},$$

and for consistency  $u_0 > u_m$ .

Eq. (34) then assume the form

$$(35) \quad n_0 = \oint F(z) \, dz; \quad 0 = \oint z F(z) \, dz,$$

where

$$\oint = \int_{-(u_0 - u_m)}^{(u_0 - u_m)}$$

The ion density in the region of the disturbance is given by

$$(36) \quad n_+(x) = \oint \frac{(z + u_0) F(z) dz}{[(z + u_0)^2 - (2e\varphi(x)/m_i)]^{\frac{1}{2}}}.$$

For small values of  $\varphi(x)$  a Taylor's series expansion yields

$$(37) \quad n_+(x) = n_0 + \frac{e\varphi(x)}{m_i} \oint \frac{F(z) dz}{(z + u_0)^2} = n_0 + \frac{e\varphi(x)}{m_i} \oint \frac{F'(z) dz}{(z + u_0)}.$$

Substitution of the above result into eq. (27) immediately leads to eq. (29) with the important modification that the integral is now properly defined. The problem associated with Landau damping no longer exists since the particles responsible for the damping through resonant interaction with the disturbance are not contained in the self consistent distribution. It is in this sense that the foregoing linear analogue may be justified.

The existence of the pulse in the quasi non-linear theory is demonstrated using eq. (27) for the electrons rather than the full non-linear set provided by eqs. (25) and (26). Combining with eq. (36) we have

$$(38) \quad \varphi''(x) = \frac{\omega_p^2}{c^2} \left\{ \varphi + \frac{B_0^2}{4\pi n_0 e} \left[ 1 - \frac{1}{n_0} \oint \frac{F(z)(z + u_0) dz}{[(z + u_0)^2 - (2e\varphi(x)/m_i)]^{\frac{1}{2}}} \right] \right\}.$$

A single integration of this subject to the boundary condition that  $\varphi'(x)$  vanish as  $\varphi(x)$  vanishes gives

$$(39) \quad \frac{1}{2} [\varphi'(x)]^2 = \frac{\omega_p^2}{c^2} \left\{ \frac{1}{2} \varphi^2 + \frac{B_0^2}{4\pi n_0 e} \left[ \varphi - \frac{m_i}{n_0 e} \oint (z + u_0) F(z) \cdot \left( z + u_0 - \sqrt{(z + u_0)^2 - \frac{2e\varphi(x)}{m_i}} \right) dz \right] \right\}.$$

In order to have a pulse the right hand side of the above equation must vanish for  $\varphi = \varphi_m$

$$(40) \quad 1 + \frac{1}{4} \left( \frac{u_m}{u_A} \right)^2 = \frac{2}{n_0 u_m^2} \oint (z + u_0)^2 \left[ 1 - \sqrt{1 - \frac{u_m^2}{(u_0 + z)^2}} \right] F(z) dz.$$

If we place  $F(z)$  equal to  $n_0 \delta z$ , we recover, with the aid of eq. (27), the cold



plasma result

$$(41) \quad \frac{u_0}{u_A} = \frac{B_0 + B_m}{2B_0},$$

which is the well known relation for Adlam-Allen pulses with  $B_m$  corresponding to  $\varphi_m$ .

The tepid plasma approximation results, as previously, from a formal expansion of the integrand in powers of  $z$ . To lowest significant order eq. (40) provides

$$(42) \quad 1 + \frac{1}{4} \left( \frac{u_m}{u_A} \right)^2 = \frac{2}{u_m^2} \left[ u_0^2 - u_0 \sqrt{u_0^2 - u_m^2} + u_T^2 \left( 1 - \frac{3}{2} \frac{u_0}{\sqrt{u_0^2 - u_m^2}} \right) \right],$$

where

$$u_T^2 \equiv \frac{1}{n_0} \oint z^2 F(z) dz,$$

and we have made use of eq. (35) and tacitly assumed  $u_T^2 \ll u_0^2 - u_m^2$ . To lowest significant order we obtain with the aid of eq. (27)

$$(43) \quad \frac{u_0^2}{u_A^2} = \frac{(B_0 + B_m)^2}{4B_0^2} - \frac{u_T^2}{u_A^2} \left( \frac{B_m + B_0}{B_m - B_0} \right) \left[ 1 + \frac{1}{4} \left( \frac{B_m + B_0}{B_m - B_0} \right) \right].$$

For very weak pulses an expansion of eq. (40) in powers of  $u_m^2$  yields

$$(44) \quad \begin{cases} \frac{u_m^2}{2n_0} \oint \frac{F(z) dz}{(z + u_0)^4} = \frac{1}{u_A^2} - \frac{1}{n_0} \oint \frac{F(z) dz}{(z + u_0)^2}, \\ \frac{u_m^2}{2u_0^4} \approx \frac{1}{u_A^2} - \frac{1}{u_0^2} \left[ 1 - \frac{3u_T^2}{u_0^2} \right], \\ \frac{u_0^2}{u_A^2} \approx \frac{B_m}{B_0} + \frac{3u_T^2}{u_A^2}, \end{cases}$$

and the above is consistent with our previously obtained linear result.

Strictly speaking the above self consistent solution does not provide for any limitation on the pulse velocity beyond the relation of eq. (40) since all particles incapable of passing over the barrier are absent. Nevertheless, we may inquire what value  $u_0$  reaches when some of the particles are brought to rest at the top of the barrier. At this point  $u_0 = u_m$  and in the cold plasma the corresponding value of  $u_0$  is  $2u_A$ . To lowest significant order eq. (40) provides

$$(45) \quad \frac{u_0^2}{u_A^2} = 4 \left| 1 - \left( \frac{8}{u_0} \right)^{\frac{1}{2}} \oint \sqrt{z} \frac{F(z)}{n_0} dz \right|.$$

We note that a finite spread in initial velocities decreases the value of the critical pulse velocity in a highly non analytic manner. As an order of magnitude approximation the above states  $u_0 \sim 2u_A[1 - \sqrt{u_T/u_A}]$  at the critical point in a tepid plasma.

#### 4. - Discussion.

The analysis of the preceeding sections indicates that an initial distribution of particle velocities affects a magneto-compressional disturbance in the following manner.

The criterion for the formation of a pulse becomes modified by the initial temperature due essentially to a plasma contribution to the sound speed. Furthermore the initial temperature broadens the disturbance in the wings in both the heavy electron and the more realistic light electron models. For  $u_0 = u_A$  these two cases may be described by an effective  $\gamma = 2$  and 3 respectively. These values correspond, not unsuprisingly to systems with two and one degree of freedom respectively.

We have argued on the basis of certain non-linear considerations that if the initial particle velocity distribution extends everywhere in velocity space, a symmetric stationary solution may not exist. In this case orbit looping becomes important and the rectilinear approximation for the ions fails. The answer to the interesting question of whether such asymmetric solutions can give rise to something resembling a collision-free shock is beyond the scope of the present analysis.

#### RIASSUNTO

La propagazione di impulsi stazionari in direzione perpendicolare ad un campo magnetico in un plasma freddo fu originariamente discussa da ADLAM e ALLEN <sup>(1)</sup>. Fu trovato che gli impulsi esistono quando il rapporto tra le velocità dell'impulso e la velocità di Alfvén è maggiore di uno. Una caratteristica essenziale della teoria non lineare è che i campi crescono esponenzialmente nella regione del plasma indisturbato, risultato che si può ottenere anche dalla teoria linearizzata. Guidati da ciò abbiamo esaminato il problema stazionario per un plasma tiepido per stabilire se il plasma è capace di sopportare campi crescenti esponenzialmente. In questo articolo si dà un'analisi lineare e quasi non-lineare del problema e si dimostra che gli impulsi esistono quando la velocità della perturbazione è supersonica. Si dimostra anche che il range di velocità per cui si formano impulsi è ridotto in maniera fortemente non analitica.

## The Role of Ion Currents in the Formation of Space Charge Sheaths in a Low Pressure Arc.

P. L. AUER (\*)

*Laboratorio Gas Ionizzati (EURATOM - C.N.E.N.)  
c/o Laboratori Nazionali di Frascati - Roma*

(ricevuto l'11 Agosto 1961)

**Summary.** — It is shown that conditions leading to the establishment of a space charge sheath in the positive column of low pressure arcs provide for a minimal requirement in the positive ion current delivered to the sheath. The minimum required current for a given ion is a function of only the electron density and temperature and is independent of the specific mechanism of ion production for the special case of a plane symmetric discharge. These conclusions are used to shed light on the familiar Bohm criterion, which is found to be misleading. The effect of magnetic fields and possible plasma instabilities is briefly examined.

### 1. — Introduction.

We wish to re-examine an old problem which is concerned with the nature of a plasma-sheath transition in the positive column of a low pressure arc. In this context a low pressure arc is any discharge system with physical dimensions small compared to the ion collision mean free path. The positive column defines that region which is positive ion-rich. Assuming, for the sake of simplicity, that there is only a single ionic species present and that it is singly charged, then the plasma is that region where

$$(1a) \quad (N_p - N_e)/N_e \ll 1 ;$$

(\*) John Simon Guggenheim Fellow 1960-61. Permanent address: General Electric Research Laboratory, Schenectady, N. Y.

while the space charge sheath is that region where

$$(1b) \quad (N_p - N_e)/N_e \gg 1;$$

and  $N_p$ ,  $N_e$  denote, respectively the ion and electron particle densities.

It will be noted that we are dealing with ion-rich space charge sheaths exclusively. This is the situation which arises naturally when an insulating wall is in equilibrium with the positive column. Electrons arriving at the wall charge it negatively until a sufficiently large negative potential is produced at the wall with respect to the plasma. The magnitude of this potential is determined by the requirement that the electron flux,  $J_e$ , just balance the ion flux,  $J_p$ , at the wall. On account of the large disparity in ion and electron masses, the above requirement leads to the establishment of a region in the vicinity of the wall which must be heavily ion-rich. A similar situation is to be expected whenever a highly biased negative probe is introduced in the positive column in order to collect ion current.

Historically there have been two approaches to the description of the positive column, these two approaches being concerned with either one or the other of the regions defined by eq. (1). In their classic paper on the subject TONKS and LANGMUIR <sup>(1)</sup> showed that the potential distribution in the plasma corresponding to a given model of ion generation could be readily obtained providing space charge is neglected. That is, inequality in eq. (1a) is obeyed to a high degree. Subsequently HARRISON and THOMPSON <sup>(2)</sup> showed that the analysis is greatly simplified for plasmas with planar symmetry. A common property of these solutions is that for some given value of the potential infinite electric fields obtain and the physical validity of the solution breaks down. Assuming that the electrons are in thermal equilibrium in the plasma at a temperature  $T$ , HARRISON and THOMPSON show that this blow-up point occurs at  $-eV/kT = 0.8539$  for a plane plasma and the point is independent of the specific ion generation scheme. It is assumed, however, that all ions are born at rest. In the above  $V$  is the local potential,  $e$  the magnitude of the electronic charge, and  $k$  is Boltzmann's constant.

Alternatively one can adopt the point of view that the plasma is a region of large extent in comparison with the sheath, and that in the plasma the electric fields are vanishingly small in view of eq. (1a). Nevertheless, an appreciable potential may develop across the plasma on account of its extent. Furthermore, the space charge sheath is a region essentially devoid of electrons or of ion generation and the variation of potential is quite large over distances small compared with the plasma's dimension. Assuming that it is meaningful

(1) L. TONKS and I. LANGMUIR: *Phys. Rev.*, **34**, 876 (1929).

(2) E. R. HARRISON and W. B. THOMPSON: *Proc. Phys. Soc.*, **74**, Pt. 2, 145 (1959).

to speak of a potential which serves to demarcate plasma and sheath, BOHM<sup>(3)</sup> showed that the continuity of potential across the demarcation requires that  $-eV_s/kT \geq 0.5$ ; where  $V_s$  is the potential at the plasma-sheath boundary and electrons are once more assumed to be in thermal equilibrium. Subsequently ALLEN and THONEMANN<sup>(4)</sup> showed that some of Bohm's assumptions could be relaxed in arriving at the plasma sheath potential criterion. Both analyses have in common the assumptions that the inequality of eq. (1a) is strongly obeyed up to  $V_s$  and that the cold ion stream arriving at the sheath from the plasma is monoenergetic. In the current literature the Bohm criterion is commonly interpreted to mean that the formation of a stable sheath requires ions to enter it with velocities of the order of  $(kT/M)^{1/2}$  or greater, where  $M$  is the ion's mass and  $T$  the electron temperature.

In what follows we shall treat positive columns of planar symmetry in which the electrons are assumed to be in thermal equilibrium and the singly charged positive ions are born at rest. The extension of our arguments to more complicated systems follows readily but will not be given here. In our model the ions are treated as free particles falling to the wall under the influence of mutually generated space charge fields. It will be shown that the Bohm criterion for such a system is essentially incorrect. Instead we find that the existence of a space charge sheath requires that the ion current flowing to the sheath exceed a certain minimum value which, in turn, is independent of the specific mechanism of ion production. Furthermore, in so far as it is possible to speak of a plasma region as one where the inequality of eq. (1a) is obeyed to a high degree, then the potential which marks the extent of this region must be less than the blow-up potential referred to previously; that is,  $-eV_s/kT \leq 0.8539$ . This, of course, places an *upper* bound on the velocity, with which ions arrive at the terminus of the plasma. A brief discussion will also be given of the effect of magnetic fields on the above criteria as well as the problem of plasma stability which may arise on account of ionic currents flowing from plasma to sheath.

## 2. - Integral relations.

We consider a positive column of planar symmetry extending from  $-x_L$  to  $+x_L$  with surfaces at  $\pm x_L$  held at some negative potential  $-V_L$  with respect to the origin. In particular we shall be interested in conditions where  $|eV_L| \gg kT$ . The main discharge current carried by electrons flows in the  $y$  direction and the accompanying magnetic field in the  $z$  direction will be neg-

<sup>(3)</sup> D. BOHM: *Characteristics of Electrical Discharges in Magnetic Fields*, chap. 3, ed. by A. GUTHRIE and R. K. WAKERLING (New York, 1949).

<sup>(4)</sup> J. E. ALLEN and P. C. THONEMANN: *Proc. Phys. Soc.*, B **67**, 769 (1954).



lected initially. The system is assumed to be uniform in the  $y$ - $z$  plane.

Let  $x$ ,  $u$  denote the position and speed of ions in the  $x$  direction and assume that the ions are produced by some unspecified mechanism throughout space. We shall assume that the ions are created at rest and there are no sinks for ion flux in the column itself; thus

$$(2) \quad J'_v(x) \geq 0;$$

and the prime denotes differentiation with respect to argument.

In regions where the potential is a monotonic function of distance the probability distribution of ions in  $x$ - $u$  may be written as

$$(3) \quad f(x, u) = \int_0^x J'_v(x_0) \delta \left[ u^2 + \frac{2e}{M} \{ V(x_0) - V(x) \} \right] dx_0;$$

where  $\delta$  is the usual delta function of Dirac.

In terms of  $f$  the ion density and flux become

$$(4) \quad \begin{cases} N_v(x) = 2 \int_0^\infty f(x, u) du, \\ J_v(x) = 2 \int_0^\infty u f(x, u) du. \end{cases}$$

The following reduced variables will be used

$$(5) \quad \begin{cases} \eta = -\frac{eV}{kT}, \\ \xi = x \left( 8\pi N_0 \frac{e^2}{kT} \right)^{\frac{1}{2}}, \\ n = \frac{N}{N_0}, \\ j = \frac{J}{N_0} \left( \frac{2kT}{M} \right)^{\frac{1}{2}}, \end{cases}$$

where  $N_0$  is the electron density at the origin.

From eq. (2) and (3) we find

$$(6) \quad n_v(\eta) = \int_0^\eta \frac{j'_v(\eta_0) d\eta_0}{\sqrt{\eta - \eta_0}}.$$

Assuming  $j_v$  has a continuous derivative, the above integral relation is readily inverted (it is Abel's integral equation) to yield

$$(7) \quad j'_v(\eta) = \frac{1}{\pi} \frac{d}{d\eta} \int_0^\eta \frac{n_v(\eta_0) d\eta_0}{\sqrt{\eta - \eta_0}}.$$

With the ion current at the origin taken as zero, the above may be integrated in the form

$$(8) \quad j_v(\eta) = \frac{1}{\pi} \int_0^\eta \frac{n_v(\eta_0) d\eta_0}{\sqrt{\eta - \eta_0}}.$$

The relations of eq. (6) to (8) are, of course, exact. The first of these leads to the « plasma equation » of TONKS and LANGMUIR. The inverted form of it given by eq. (7) leads to the analysis of HARRISON and THOMPSON. For our purposes eq. (8) is the fundamental equation.

We write the reduced electric field and Laplacian of the potential as

$$(9) \quad \begin{cases} F(\eta) = \left( \frac{d\eta}{d\xi} \right)^2, \\ F'(\eta) = 2 \frac{d^2\eta}{d\xi^2}. \end{cases}$$

Poisson's equation now takes the form

$$(10) \quad n_v(\eta) = n_e(\eta) + F'(\eta)$$

and with the assumption that the electrons are in thermal equilibrium we have

$$(11) \quad n_e(\eta) = \exp[-\eta].$$

Substitution of eq. (10) and (11) into (8) yields the following expression for the ion flux

$$(12) \quad \begin{cases} j_v(\eta) = I_1(\eta) + I_2(\eta), \\ I_1(\eta) = \frac{1}{\pi} \int_0^\eta \frac{\exp[-\eta_0] d\eta_0}{\sqrt{\eta - \eta_0}}, \\ I_2(\eta) = \frac{1}{\pi} \int_0^\eta \frac{F'(\eta_0) d\eta_0}{\sqrt{\eta - \eta_0}}. \end{cases}$$

By definition the positive column is a region where the ion density always exceeds the electron density, although one may still speak of an essentially neutral region, which is the plasma. In either case we require, on the basis of eq. (10)

$$(13) \quad F'(\eta) \geq 0 ;$$

and that this condition be obeyed throughout the region under consideration. The above condition with the additional requirement that the potential be monotonic defines the nature of the plasma-sheath transitions allowed in a positive column according to our model.

It readily follows from eq. (13) and the definition of  $I_2$  that

$$(14) \quad I_2(\eta) \geq 0 ;$$

consequently we are led to the fundamental relation

$$(15) \quad j_v(\eta) \geq I_1(\eta) ;$$

the quantity  $I_1(\eta)$  is a double valued function of  $\eta$  with a maximum at  $\eta = \eta^*$ , which is found by requiring the derivative

$$(16a) \quad I_1'(\eta) = \frac{1}{\pi\sqrt{\eta}} - I_1(\eta) ,$$

to vanish for  $\eta = \eta^*$ . According to HARRISON and THOMPSON

$$(16b) \quad \begin{cases} \eta^* = 0.854 , \\ I_1(\eta^*) = 0.345 . \end{cases}$$

In the sheath the potential rapidly approaches the wall potential which has been assumed large compared with unity and we are led to the following theorem.

*Theorem I.* — Assuming a sheath to exist with regions of  $\eta > \eta^*$  and assuming the potential distribution to be monotonic from plasma to sheath in the positive column, it becomes necessary to require that a minimal ion flux enter the sheath such that in the sheath

$$\begin{aligned} j_v &\geq I_1(\eta^*) = 0.345 , \\ J_v &\geq 0.488 N_0 (kT/M)^{\frac{1}{2}} . \end{aligned}$$

The point of demarcation between plasma and sheath is, after all, a smooth

one. Nevertheless, we may define the plasma region, in accordance with eq. (1a), as that region where

$$(17) \quad \begin{cases} F'(\eta) = [n_v(\eta) - n_e(\eta)] \ll \exp[-\eta], \\ |F''(\eta)| = \frac{d}{d\eta} [n_v(\eta) - n_e(\eta)] \ll \exp[-\eta]. \end{cases}$$

The condition of continuity of ion production given by eq. (2) states

$$(18) \quad j_v'(\eta) = \frac{1}{\pi\sqrt{\eta}} - I_1(\eta) + I_2'(\eta) \geq 0;$$

where we made use of eq. (12) and (16). According to our definition of the plasma region given by eq. (17), the quantity  $I_2'(\eta)$  does not contribute to the inequality of eq. (18) inside the plasma. Since the sum of the first two terms on the r.h.s. above becomes negative for  $\eta > \eta^*$ , we are led to the following theorem.

*Theorem II.* — If the plasma region of the positive column is to extend from  $0 \leq \eta \leq \eta_s$  and if the plasma region is defined to be the region in which net space charge and the rate of the net space charge production is insignificant, as prescribed by eq. (17), then this region is restricted to values of the potential such that

$$\eta_s \leq \eta^* = 0.854.$$

Should one consider  $\eta > \eta_s$  to be the sheath region, then the above theorem places an upper limit on the speed with which ions can enter the sheath. The arbitrary nature of this requirement may be improved upon if we consider the root mean square speed at arbitrary points in the positive column. By definition the mean square speed can be written as

$$(19) \quad N_v(x) U_v^2(x) = \frac{2N_0 kT}{M} n_v(\eta) u_v^2(\eta) = 2 \int_0^\infty u^2 f(x, u) du.$$

Substituting from eq. (3) we obtain

$$(20) \quad n_v(\eta) u_v^2(\eta) = \int_0^\eta \sqrt{\eta - \eta_0} j_v'(\eta_0) d\eta_0 = n_v(\eta) \eta - \int_0^\eta \frac{\eta_0}{\sqrt{\eta - \eta_0}} j_v'(\eta_0) d\eta_0,$$

where we have used eq. (6) in obtaining the second relation above. Since the second term on the r.h.s. of the last relation is positive definite by virtue of eq. (2), we may state the following.

*Theorem III.* — The root mean square speed of ions in the positive column has an upper bound at any given point, such that

$$u_p(\eta) \leq \sqrt{\bar{\eta}},$$

$$U_p(x) \leq \sqrt{-2_e V(x)/M}.$$

The above theorem is somewhat trivial since it follows obviously from our model of ion production and acceleration.

### 3. — Influence of the sheath.

We define the sheath to be that region where the inequality of eq. (1b) is well obeyed. Since ultimately ion production must be related to electron density, the sheath is a region where ion production is essentially non existent. At this stage we may compare our above results with those of BOHM, who considered a single velocity group of ions in the sheath. With this assumption the ion density becomes

$$(21) \quad n_p(\eta) = j_0/\sqrt{\bar{\eta}};$$

where  $j_0$  is the constant ion flux in the sheath. It is not wise to extend the above expression to the plasma region since it implies infinite density at the origin. The validity of eq. (21) will be discussed subsequently. Combining eq. (21) with eq. (10) and (11) we obtain

$$(22) \quad \begin{cases} F'(\eta) = j_0/\sqrt{\bar{\eta}} - \exp[-\eta], \\ F''(\eta) = \exp[-\eta] - \frac{1}{2} j_0/\eta^{\frac{3}{2}}. \end{cases}$$

The plasma-sheath boundary is defined to be the point

$$(23) \quad \begin{cases} F'(\eta_s) = 0, \\ F''(\eta_s) > 0, \end{cases}$$

the second inequality following from the requirement that the potential be continuous for arbitrary, small, electric fields. From eq. (22) and (23) we obtain

$$(24a) \quad \begin{cases} j_0 = \sqrt{\bar{\eta}_s} \exp[-\eta_s], \\ \eta_s > \frac{1}{2}. \end{cases}$$

We note that the function  $\sqrt{\eta}e^{-\eta}$  has its maximum at  $\eta = \frac{1}{2}$ ; therefore, eq. (24a) implies an upper limit to the current

$$(24b) \quad j_0 < 0.5 \exp[-0.5] = 0.429.$$



There is no obvious physical reason to expect an arbitrary upper bound to the current in the sheath since the actual value of the current must be tied to the specific mechanism of ion generation. Thus, eq. (24b) certainly can't be true in general. The criterion of  $\eta_s > \frac{1}{2}$  is of no particular significance, either, since the definition of  $\eta_s$  is rather arbitrary. All this has been touched upon in the previous discussion.

The concept of the sheath can be made somewhat more precise if we assume that ion production vanishes for all  $\eta < \eta_c$ , where the relationships of the cut-off  $\eta_c$  to  $\eta_s$  or  $\eta^*$  is left unspecified for the time being. Eq. (6) takes the form

$$(25) \quad n_p(\eta) = \int_0^{\eta_c} \frac{j'_b(\eta_0) d\eta_0}{\sqrt{\eta - \eta_0}}; \quad \eta > \eta_c.$$

Substituting the above and eq. (11) into eq. (10), we integrate to obtain

$$(26) \quad F(\eta) = 2 \int_0^{\eta_c} \sqrt{\eta - \eta_0} j'_b(\eta_0) d\eta_0 - [1 - \exp[\eta]]; \quad \eta > \eta_c.$$

Assuming  $\eta$  to be large compared to both  $\eta_c$  and unity, eq. (25) and (26) may be integrated by parts to yield

$$(27) \quad \begin{cases} F(\eta) = 2j_b(\eta_c)\sqrt{\eta - \eta_c} - 1 + 0(1/\sqrt{\eta}), \\ n_p(\eta) = j_b(\eta_c)/\sqrt{\eta - \eta_c} - 0(1/\eta^{\frac{3}{2}}). \end{cases}$$

Therefore, in the sheath the ion current behaves essentially as a single velocity stream once the local potential appreciably exceeds the cut-off value and unity. But in this region the space charge is in general large and Bohm's analysis is inapplicable.

In the sheath the ion current flow will be essentially space charge limited by a modified Langmuir-Childs law, which can be obtained from eq. (27) and (9) in the form

$$(28) \quad j_b(\eta_c) \approx \frac{8}{9}[(\eta_1 - \eta_c)^{\frac{3}{2}} - (\eta_2 - \eta_c)^{\frac{3}{2}}]/(\xi_1 - \xi_2)^2,$$

where the subscripts 1 and 2 label two points within the sheath in the sense of the above discussion. From the above we infer that there need be no limitation to the maximum ion current entering the sheath beyond that given by the specific nature of ion generation. Should some agency act within the plasma to change the ion flux for given fixed wall potential, the width of the space charge sheath simply changes in accordance with eq. (28).

It is conceivable that in some instances the cut-off potential  $\eta_c$  and sheath potential  $\eta_s$  though quite different in magnitude, occur at nearly the same point in space. This is to be expected whenever the plasma is of very large extent in comparison to the Debye length ( $\lambda_D^2 = kT/4\pi N_0 e^2$ ). In the transition from plasma to sheath the potential will vary almost exponentially since  $F'$  and  $F$  are both quite small. The electron density will, in turn, decrease super-exponentially over distances comparable with the Debye length, that is, over distances insignificant with the plasma's extent. Under these circumstances we expect the inequality of Theorem I to approach an equality, independent of the specific mechanism of ion production.

Alternatively, one might say that as

$$j_v(\eta_c) \rightarrow I_1(\eta^*) = 0.345,$$

the Debye length becomes vanishingly small in comparison with other physical dimensions and the positive column has a well defined plasma-sheath structure. The converse also follows, in the sense that when the Debye length becomes comparable with other physical dimensions the cut-off potential will actually approach the wall potential and

$$j_v(\eta_c) \gg I_1(\eta^*) = 0.345$$

assuming  $\eta$  at the wall is still large compared with unity. Of course, under these circumstances eq. (28) is not valid and the distinction between plasma and sheath loses significance.

#### 4. - Effect of magnetic field.

Until now the magnetic field has not entered into our discussion. In general there is a self-magnetic field transverse to the main discharge current and lateral ion flux. In addition there may also be present an externally imposed magnetic field in the same or opposite direction. We shall not consider fields parallel to the discharge current, since their effect is of a higher order than that considered presently. Thus, the geometry is the same as before with ion flux in the  $x$  direction, main electron discharge current in the  $y$  direction, and magnetic field in the  $z$  direction. We continue to assume the positive column to be uniform in the  $y$ - $z$  plane. Although the symmetry about the origin is destroyed by the presence of an external magnetic field, we do not take this into explicit consideration and shall continue to assume that in both  $-X_L < X < 0$  and  $0 < X < X_L$  the potential is monotonic.

We shall assume the magnetic field is so weak that the gyration radius of ions is very large in comparison with other physical dimensions. Therefore,

the curvature of ion trajectories is to be neglected and any effect obtained because of the magnetic field's presence will arise from its action on electrons. Assuming the electrons are in hydrostatic equilibrium with the electric and magnetic fields we have instead of eq. (11)

$$(29) \quad \begin{cases} n_e(\eta) = -\frac{d}{d\eta}(p_e + b^2), \\ p_e(\eta) = P_e(x)/N_0 kT, \\ b^2(\eta) = B^2(x)/8\pi N_0 kT, \end{cases}$$

where  $P_e$  is the electronic pressure and  $B$  is the magnitude of the magnetic field. The expression for the ion density in this approximation remains the same as given by eq. (6). Combining eq. (6), (29) and (10) followed by an integration leads to a statement of stress balance in the form

$$(30) \quad F(\eta) + [b^2(0) - b^2(\eta)] + [p_e(0) - p_e(\eta)] = \\ = 2 \int_0^\eta \sqrt{\eta - \eta_0} j'_v(\eta_0) d\eta_0 = \int_0^\eta \frac{j_v(\eta_0)}{\sqrt{\eta - \eta_0}} d\eta_0.$$

In the above form it becomes apparent that the requirement of minimal ion flux in the sheath is related to the requirement of stress balance across the plasma, where the electric field stress is vanishingly small. In the absence of a magnetic field the ions are only required to balance the electron pressure drop in the plasma; whereas with the magnetic field present the ions will balance the combined pressure. Thus, to determine whether the magnetic field increases or decreases the minimal ionic current it is only necessary to compare the total pressure drop across the plasma in comparison to its nominal value of  $(1 - \exp[-\eta^*])$  in the absence of magnetic fields.

As long as  $b^2$  remains appreciably less than unity everywhere, it is reasonable to assume that the electron velocity distribution continues to be isotropic in the  $x$  direction and we can write an isothermal equation of state in the form

$$(31) \quad p_e(\eta) = n_e(\eta).$$

Inserting the above into eq. (29) we obtain

$$(32) \quad \begin{cases} \frac{dn_e}{d\eta} + n_e(\eta) = -\frac{db^2}{d\eta}, \\ n_e(\eta) = \exp[-\eta] \left[ 1 - \int_0^\eta \exp[\eta_0] \frac{db^2}{d\eta_0} d\eta_0 \right]. \end{cases}$$

By the arguments leading up to eq. (12) and (15) we obtain their counterparts in the form

$$(33) \quad \begin{cases} j_v(\eta) = I_3(\eta) + I_2(\eta), \\ j_v(\eta) \geq I_3(\eta), \end{cases}$$

where

$$(23) \quad I_3(\eta) = \frac{1}{\pi} \int_0^\eta \frac{d\eta_1}{\sqrt{\eta - \eta_1}} \left\{ \exp[-\eta_1] - \int_0^{\eta_1} \exp[-\eta_1 + \eta_0] \frac{db^2}{d\eta_0} d\eta_0 \right\} - \\ = I_1(\eta) - \int_0^\eta I_1(\eta - \eta_0) \frac{db^2}{d\eta_0} d\eta_0;$$

and  $I_1, I_2$  are given by eq. (12).

According to the above relation the effect of the magnetic field on the minimal ion flux depends on the sign of the magnetic pressure gradient, which in our model is proportional to  $db^2(\eta)/d\eta$ .

It is evident that the magnetic pressure gradient of the self-field, *i.e.* due to the discharge current, is always positive; consequently the effect of the self-field is always in the direction of decreasing the minimal ion flux required for the existence of a sheath from the value specified by Theorem I. In the event the external magnetic field is in the same direction as the self-field, the above effect can only be enhanced. However, where the external and self magnetic fields have the opposite sense, there may occur a partial cancellation or overcancellation in gradients and the sign of the total magnetic effect is no longer self-evident.

In order to obtain a semi-quantitative estimate of the magnetic field effect we wish to evaluate approximately the maximum value of  $I_3(\eta^\dagger)$ . Should this occur for some  $\eta = \eta^\dagger \leq 1$ , we can say with some assurance that in the sheath  $j_v$  will exceed  $I_3(\eta^\dagger)$ . We differentiate eq. (34) to find

$$(35) \quad I_3'(\eta) = 0 \quad \text{for } \eta = \eta^\dagger,$$

$$(36) \quad I_3(\eta^\dagger) = \frac{1}{\pi\sqrt{\eta^\dagger}} - \frac{1}{\pi} \int_0^{\eta^\dagger} \frac{d\eta_0}{\sqrt{\eta^\dagger - \eta_0}} \frac{db^2}{d\eta_0},$$

$$(37) \quad I_1'(\eta^\dagger) = \int_0^{\eta^\dagger} I_1'(\eta^\dagger - \eta_0) \frac{db^2}{d\eta_0} d\eta_0.$$

We note that as  $b^2$  or its gradient vanishes eq. (37) reduces to  $\eta^\dagger = \eta^*$ . For small, but not vanishing, values of  $b^2$  we expect  $\eta^\dagger$  to be close to  $\eta^*$ . Developing both sides of eq. (36) and (37) in a Taylor's series about  $\eta^*$  we find

to lowest order

$$(38) \quad \left\{ \begin{aligned} I_3(\eta^\dagger) &\approx 1/\pi \sqrt{\eta^*} - \int_0^{\eta^*} I_1(\eta^* - \eta_0) \frac{db^2}{d\eta_0} d\eta_0, \\ \eta^\dagger - \eta^* &\approx 2\pi (\eta^*)^{\frac{3}{2}} \int_0^{\eta^*} I_1'(\eta^* - \eta_0) \frac{db^2}{d\eta_0} d\eta_0. \end{aligned} \right.$$

Any further estimate of magnetic field effect requires some information about the variation of magnetic pressure with electric potential. For example, it may be argued that the currents responsible for the magnetic gradient are concentrated largely within the plasma, where the electric potential is essentially flat. In this case the major contribution to the integrals in eq. (38) comes from the neighborhood of  $\eta = 0$ , and we find approximately

$$(39) \quad I_3(\eta^\dagger) \approx [1 - \Delta b^2] I_1(\eta^*), \quad \eta^\dagger \approx \eta^*,$$

where  $\Delta b^2$  is the magnetic pressure difference across the plasma.

The analysis of this section could have been based on the idea of an effective potential  $\varphi(\eta)$ , where

$$(40a) \quad \varphi(\eta) = \eta + \frac{1}{c} \int_0^{\xi(\eta)} v b \, d\xi_0,$$

and  $v$  is the electron drift velocity in the  $y$  direction,  $c$  is the velocity of light. Instead of eq. (32) one obtains

$$(40b) \quad n_e(\eta) = \exp[-\varphi(\eta)].$$

This was the procedure adopted by ALLEN and MAGISTRELLI<sup>(5)</sup> who considered an isothermal electron distribution with constant drift velocity and a single velocity group of ions. They find by arguments previously given<sup>(4)</sup> that Bohm's concept of a sheath potential takes the form

$$(41) \quad \left\{ \begin{aligned} \eta_s &= \frac{1}{2}(1 + \alpha_s), \\ \alpha_s &= [vb/c \sqrt{E}]_{\eta=\eta_s} = \left[ v / \left( \frac{cE}{B} \right) \right]_{\eta=\eta_s}; \end{aligned} \right.$$

where  $E$  is the electric field in the  $x$ -direction. The same objection voiced in Section 3 in connection with the original Bohm criterion may be repeated in

<sup>(5)</sup> J. E. ALLEN and F. MAGISTRELLI: *Nuovo Cimento*, **18**, 1138 (1960).



this instance in that the sheath potential concept is somewhat vague and the single velocity group approximation is only valid in the sheath proper, where the electric field no longer makes vanishing contributions to stress balance.

We note that if we write the effective potential  $\varphi(\eta)$  in the form

$$(42) \quad \varphi(\eta) = \eta + \int_0^\eta \alpha(\eta_0) d\eta_0,$$

and if we treat  $\alpha$  as if it were a constant in the plasma region, we obtain rigorously

$$(43) \quad I_3(\eta^\dagger) = \frac{1}{\sqrt{1+\alpha}} I_1([1+\alpha]\eta^\dagger), \quad \eta^\dagger = \eta^*/(1+\alpha).$$

The above relation is of the same form as the one derived by ALLEN and MAGISTRELLI and given by eq. (41). However, there appears to be no particular reason why the quantity  $\alpha$ , which is the ratio of the electron drift velocity to the  $E \cdot B$  drift produced by uniform fields, should remain constant in the plasma of a positive column.

In conclusion we find that the results of Section 2 are modified by the presence of a magnetic field through its contribution to overall stress balance. If the electron gas remains in isothermal equilibrium, Theorems I and II are changed in that  $I_3(\eta^\dagger)$  and  $\eta^\dagger$  must be substituted for  $I_1(\eta^*)$  and  $\eta^*$ , respectively. Theorem III, as stated, remains unaffected.

However, it should be stressed that there are many other equilibrium states besides the isothermal one conforming to eq. (31). For example, it is conceivable that the electron gas be in equilibrium but at zero pressure. Thus its drift velocity will be proportional to the ratio of electric to magnetic field strengths, and the electric field will have to adjust itself to requirements dictated largely by the conditions of ion production.

## 5. - Instabilities.

We wish to discuss briefly whether the stationary equilibrium described in the preceding sections is stable or unstable to small amplitude electrostatic perturbations. For purposes of this discussion we idealize matters by considering the plasma and sheath to be separate entities which may be treated independently. Dealing with the sheath first, we note that this is essentially a region in which a constant ion flux flows under its own space charge forces, the role of electrons being negligible. It is relatively easy to show that there are no inherent instabilities to be ascribed to this situation.

Consider the general one-dimensional problem of a single charged fluid in stationary equilibrium with a force field. We write for the density  $n(x) + \delta n(x, t)$  and for the velocity  $u(x) + \delta u(x, t)$  where the time dependent terms are small perturbations about the equilibrium state. Since in equilibrium the flux is constant, we have in general

$$(44) \quad n(x) u(x) = \text{constant}.$$

From the equations of continuity, motion and the Poisson equation we obtain the following equation for the perturbation

$$(45) \quad \left[ \left( \frac{\partial}{\partial t} + u(x) \frac{\partial}{\partial x} \right) \left( \frac{\partial}{\partial t} + u(x) \frac{\partial}{\partial x} + \left( \frac{du}{dx} \right) \right) + \omega_0^2(x) \right] \delta u = 0,$$

$$\omega_0^2(x) = 4\pi e^2 n(x)/m,$$

where  $e/m$  is the charge to mass ratio of the fluid particles. The co-ordinate transformation

$$(46) \quad \tau = t - \int^x \frac{dx_0}{u(x_0)},$$

transforms eq. (45) to the form

$$(47) \quad \left[ \frac{d^2}{d\tau^2} + k^2(x) \right] [u(x) \delta u(x, \tau)] = 0, \quad k^2(x) u^2(x) = \omega_0^2(x);$$

which will be recognized as the one dimensional wave equation with real propagation vector. The solutions of eq. (47) are, of course, stable.

The situation in the plasma is quite different from that of the sheath. In the plasma electrons and positive ions of nearly equal densities are in relative motion with respect to each other.

As is well known, under these conditions, it is possible to excite two stream instabilities. Neglecting for the moment the effect of non-uniformity, the necessary condition for instability is that the arithmetic mean of the individual particle distributions, weighted according to their respective plasma frequencies squared, possess a minimum<sup>(6)</sup>. It is to be expected that in general this criterion can be met in the plasma in spite of the fact that there

<sup>(6)</sup> P. L. AUER: *Phys. Rev. Lett.*, **1**, 514 (1958).

is no net current under equilibrium conditions. The reason is that in the absence of collisions the electron distribution will tend to resemble a truncated Maxwellian distribution, their contribution to the net current arising from the energetic electrons escaping over the potential barrier, whereas the ion distribution will resemble a  $\delta$ -function.

More detailed considerations lead to estimates of a sufficient criterion for instability. Assuming cold ions and electrons in thermal equilibrium at the same density, there exist low frequency ion oscillations according to the relation

$$\omega^2 = \frac{\omega_{pi}^2}{1 + (k\lambda_D)^{-2}},$$

where  $\omega$  is the frequency,  $k$  the propagation constant,  $\omega_{pi}$  the ion plasma frequency and  $\lambda_D$  the Debye length corresponding to the electron temperature. The short wave length oscillations at the ion plasma frequency have a large Landau damping coefficient, the long wavelength oscillations travel at a constant phase velocity

$$\omega/k = \pm \sqrt{kT/M},$$

and are virtually undamped. The approximate sufficient condition for instability is that the relative directed velocity of ions and electrons exceed the above phase velocity (?).

According to our previous discussion in Section 2, the above criterion is either closely approached or actually met somewhere in the plasma in view of the fact that on the average the electrons are nearly at rest while the directed motion of ions is nearly one-half, if no greater, than the above phase velocity. Although there are several mitigating factors present in a real discharge system which may eliminate the onset of instability—for example, collisions, damping due to density gradients, finite interaction space between ion current and plasma—it is nevertheless quite conceivable that in the ideal plasma with extent very large compared to the Debye length but very small compared to the collision-mean-free path the possible existence of two-stream instability acts as a velocity, and thereby current, limitation on the ion stream within the plasma.

Once again the effect of such a current limitation is to move the inequality of Theorem I in the direction of an equality. It should be possible to investigate experimentally whether two-stream instability plays a dominant role

(?) I. B. BERNESTEIN, E. A. FRIEMAN, R. M. KULSRUD and M. N. ROSENBLUTH: *Phys. of Fluids*, **3**, 136 (1960).

in establishing the ion current requirements of the positive column since a plasma on the verge of instability should give rise to density fluctuations well above the thermal equilibrium value.

\* \* \*

It is a pleasure to acknowledge a number of illuminating conversations with Dr. J. E. ALLEN from which the present investigation benefited at all stages. The generous hospitality of the Laboratorio Gas Ionizzati is also gratefully acknowledged.

#### RIASSUNTO

Si dimostra che le condizioni che portano alla formazione di una guaina di carica spaziale nella colonna positiva degli archi a bassa pressione, impongono un minimo alla corrente di ioni positivi alla guaina. Questa corrente per un dato tipo di ioni è funzione soltanto della densità e della temperatura elettronica ed è indipendente dal meccanismo specifico della produzione di ioni nel caso particolare di una scarica a simmetria piana. Queste conclusioni sono impiegate per meglio illustrare il noto criterio di Bohm che, come qui è dimostrato, può condurre a false interpretazioni. È studiato anche, brevemente, l'effetto di campi magnetici e di possibili instabilità di plasma.

## Uniqueness of the Electron Polarization Operator.

M. E. ROSE

*Physics Department, University of Virginia - Charlottesville, Va.*

R. H. GOOD, Jr. (\*)

*Institute for Advanced Study - Princeton, N. J.*

(ricevuto il 17 Agosto 1961)

**Summary.** — The most general three-vector polarization operator, that commutes with the Hamiltonian and has the algebra of spin one-half, is constructed for a free Dirac particle. The non-uniqueness inherent in this operator may be resolved by imposing either of the following two conditions: 1) the operator should be well-defined in the rest system; 2) it should correspond to the space part of a four-vector operator evaluated in the rest system. In either case the operator obtained is the Foldy-Wouthuysen transform of  $\beta\boldsymbol{\sigma}$ .

There are several operators that can be used to describe the polarization of a free electron: CALOGERO <sup>(1)</sup> has listed many of them and discussed some of their properties. However, among all the possibilities, the operator  $\mathbf{O}_1$ , defined by

$$(1) \quad \mathbf{O}_1 = \boldsymbol{\sigma} \cdot \hat{\mathbf{p}} (H/|H|) \hat{\mathbf{p}} + \hat{\mathbf{p}} \times (\beta \boldsymbol{\sigma} \times \hat{\mathbf{p}})$$

and first introduced by STECH <sup>(2)</sup>, is to be preferred for the reasons presented below. Here  $\hat{\mathbf{p}}$  is  $\mathbf{p}/p$ , the unit momentum operator, and the Hamiltonian is

$$(2) \quad H = \boldsymbol{\alpha} \cdot \mathbf{p} + \beta.$$

(\*) National Science Foundation Senior Postdoctoral Fellow 1960-61, on leave from Institute for Atomic Research and Department of Physics, Iowa State University, Ames, Iowa.

<sup>(1)</sup> F. CALOGERO: *Nuovo Cimento*, **20**, 280 (1961).

<sup>(2)</sup> B. STECH: *Zeits. Phys.*, **144**, 214 (1956).



The reasons for considering  $\mathbf{O}_1$  especially are: 1) It has the algebra

$$(3) \quad \mathbf{O}_i \mathbf{O}_j = \delta_{ij} + i\epsilon_{ijk} \mathbf{O}_k (H/|H|),$$

2) It commutes with the Hamiltonian, as well as with  $\mathbf{p}$ ,

$$(4) \quad [\mathbf{O}, H]_- = 0.$$

3) It corresponds to the definition of polarization used in many earlier papers. That is, if  $\hat{\mathbf{s}}$  is the direction of polarization of a state in the sense of DARWIN<sup>(3)</sup>, MOTT<sup>(4)</sup>, and TOLHOEK<sup>(5)</sup>, then the system is in an eigenstate of  $\mathbf{O}_1 \cdot \hat{\mathbf{s}}$  with eigenvalue  $+1$ . The properties of the operator  $\mathbf{O}_1$  and its relations to some of the other polarization operators have been worked out by FRADKIN and GOOD<sup>(6)</sup> and their notation is used in the present paper also.

In view of the usefulness of this operator it is interesting to inquire into its uniqueness. We have therefore considered the problem of finding the most general Hermitian vector operator  $\mathbf{O}$  that satisfies eqs. (3) and (4). It is known to begin with that  $\mathbf{O}_1$  as given by eq. (1) is a particular solution; the general solution is given in eq. (14) below.

The problem is simpler in the Foldy-Wouthuysen representation<sup>(7)</sup>. For any operator  $A$  the transformed operator  $A_{FW}$  is defined by

$$(5) \quad A_{FW} = \exp[iS] A \exp[-iS],$$

where

$$(6) \quad \exp[\pm iS] = [2|H|(|H|+1)]^{-\frac{1}{2}} \beta [\beta(|H|+1) \pm \boldsymbol{\alpha} \cdot \mathbf{p}].$$

It is known that  $H_{FW}$  is  $\beta|H|$  and that  $\mathbf{O}_{1FW}$  is  $\beta\boldsymbol{\sigma}$ . Eqs. (3) and (4) become

$$(7) \quad \mathbf{O}_{iFW} \mathbf{O}_{jFW} = \delta_{ij} + i\epsilon_{ijk} \mathbf{O}_{kFW} \beta,$$

$$(8) \quad [\mathbf{O}_{FW}, \beta]_- = 0,$$

and the problem is to find the most general operator that satisfies these equations.

Eq. (8) implies that  $\mathbf{O}_{FW}$  depends linearly only on the matrices  $1$ ,  $\beta$ ,  $\boldsymbol{\sigma}$ , and  $\beta\boldsymbol{\sigma}$ . Eq. (7) implies that  $\mathbf{O}_{FW}$  is a similarity transformation from  $\beta\boldsymbol{\sigma}$ . Since  $\mathbf{O}$  is to be Hermitian the transformation must be unitary and since  $\mathbf{O}$

(3) C. G. DARWIN: *Proc. Roy. Soc. London*, A **120**, 621 (1928).

(4) N. F. MOTT: *Proc. Roy. Soc. London*, A **124**, 425 (1929).

(5) H. A. TOLHOEK: *Rev. Mod. Phys.*, **28**, 277 (1956).

(6) D. M. FRADKIN and R. H. GOOD JR.: *Rev. Mod. Phys.*, **33**, 343 (1961).

(7) L. L. FOLDY and S. A. WOUTHUYSEN: *Phys. Rev.*, **78**, 29 (1950).

is to be a vector  $\sigma$  and  $\beta\sigma$  must enter in the form  $\sigma \cdot \hat{p}$  and  $\beta\sigma \cdot \hat{p}$ . One concludes that

$$(9) \quad O_{FW} = \exp[-iR_{FW}]\beta\sigma \exp[iR_{FW}],$$

where

$$(10) \quad R_{FW} = \frac{1}{2}[\theta_1 + \theta_2\beta + \theta_3\sigma \cdot \hat{p} + \theta_4\beta\sigma \cdot \hat{p}]$$

and the  $\theta_i$  are real parameters. This means that, in the original representation

$$(11) \quad O = \exp[-iR]O_1 \exp[iR],$$

where

$$(12) \quad R = \frac{1}{2}[\theta_1 + \theta_2(H/|H|) + \theta_3\sigma \cdot \hat{p} + \theta_4(H/|H|)\sigma \cdot \hat{p}].$$

It is clear that  $R$  is the most general operator that commutes with  $H$  and has properties 1) it is Hermitian, 2) it is constructed from the momentum operator and the Dirac matrices only, 3) it is a scalar under space rotations. The first two terms in  $R$  do not contribute and one can simplify by writing

$$(13) \quad \exp[\frac{1}{2}i\theta_3\sigma \cdot \hat{p}] = \cos \frac{1}{2}\theta_3 + i\sigma \cdot \hat{p} \sin \frac{1}{2}\theta_3$$

and similar for the  $\theta_4$  term. The final result is

$$(14) \quad O = \sigma \cdot \hat{p}(H/|H|)\hat{p} + [\cos \theta_3 \cos \theta_4 - (H/|H|) \sin \theta_3 \sin \theta_4]\hat{p} \times (\beta\sigma \times \hat{p}) + \\ + [\sin \theta_3 \cos \theta_4 + (H/|H|) \cos \theta_3 \sin \theta_4]\beta\sigma \times \hat{p}.$$

One sees that  $O$  is produced by rotating  $O_1$  about the  $\hat{p}$  direction.

It is seen that eqs. (3) and (4) leave considerable freedom in the choice of the operator  $O$ . The first term in eq. (14) must always be present but then, by choosing the  $\theta$ 's to be multiples of  $\pi/2$ , one finds four other possible terms which may be added or subtracted. The first term is axial under the parity transformation,  $\hat{p} \times (\beta\sigma \times \hat{p})$  is axial and  $\beta\sigma \times \hat{p}$  is polar. The first term,  $\hat{p} \times (\beta\sigma \times \hat{p})$ , and  $(H/|H|)\beta\sigma \times \hat{p}$  are unchanged by charge conjugation whereas the other two types of terms change sign. Therefore in processes that conserve parity and that are charge-conjugation invariant only the operators

$$(15) \quad O_{1,2} = \sigma \cdot \hat{p}(H/|H|)\hat{p} \pm \hat{p} \times (\beta\sigma \times \hat{p})$$

would be appropriate. However, for the processes which do not conserve parity but which are covariant by combined inversion the operators

$$(16) \quad O_{3,4} = \sigma \cdot \hat{p}(H/|H|)\hat{p} \pm \beta\sigma \times \hat{p}$$

could be used, since both terms here are axial under combined inversion. Perhaps the most important consideration is that the operator should be well-defined in the rest system of the particle. Only  $\mathbf{O}_1$  satisfies this requirement and it reduces to  $\beta\sigma$ .

There is another criterion which may be imposed on the polarization operator. It is known <sup>(6)</sup> that, if  $(\mathbf{O}_1, 0)$  are the components of a four-vector in the rest system, on Lorentz transforming to the laboratory system one obtains the covariant Bargmann-Wigner <sup>(8)</sup> operator

$$(17) \quad T_\mu = \gamma_5(i\gamma_\mu - p_\mu),$$

where  $p_4$  is  $iH$ . If the same Lorentz transformation is applied to  $(\mathbf{O}, 0)$ , with  $\mathbf{O}$  as given in eq. (14), a covariant result is not obtained in general. The only circumstance under which the transformed operator is covariant is the case in which  $\mathbf{O} = \mathbf{O}_1$ . The reason for this result is apparent when one considers that the unitary transformation of eq. (11) will not commute with the Lorentz transformation of the wave function.

It is concluded that, despite the non-uniqueness which one first notices in  $R$  (and which is also in the Foldy-Wouthuysen transformation), one can, by the imposition of reasonable requirements, eliminate the ambiguity in the definition of the polarization operator.

\* \* \*

One of us (R.H.G.) is grateful to Professor J. ROBERT OPPENHEIMER for the hospitality of the Institute for Advanced Study.

<sup>(8)</sup> V. BARGMANN and E. P. WIGNER: *Proc. Nat. Acad. Sci. U. S.*, **34**, 211 (1948).

#### RIASSUNTO (\*)

Si costruisce il più generale operatore trivettoriale di polarizzazione, che commuta con l'Hamiltoniano ed ha un'algebra di spin  $\frac{1}{2}$ , per una particella libera di Dirac. La non-unicità inerente a questo operatore può essere risolta imponendo una delle due seguenti condizioni: 1) l'operatore deve essere ben definito nel sistema in quiete; 2) deve corrispondere alla parte spaziale di un operatore quadrivettoriale valutato nel sistema in quiete. In entrambi i casi l'operatore ottenuto è la trasformata di Foldy-Wouthuysen di  $\beta\sigma$ .

(\*) Traduzione a cura della Redazione.

## A Theoretical Approach to High-Energy Pion Phenomena.

D. AMATI

*CERN - Geneva*

S. FUBINI

*Istituto di Fisica dell'Università - Padova*  
*CERN - Geneva*

A. STANGHELLINI (\*)

*Istituto di Fisica dell'Università - Bologna*

M. TONIN

*Istituto di Fisica dell'Università - Padova*

(ricevuto il 18 Agosto 1961)

**Summary.** — A theoretical analysis of the main features of high-energy strong interactions is performed. First of all, by applying dispersion theory to the elastic scattering amplitude for high-energy and low-momentum transfer we have obtained expressions for the shape of diffraction scattering and for the total cross-sections. The form of those results has suggested a definite model for the most important inelastic processes. In this model a well-defined group of Feynman graphs, the « most peripheral » ones, gives the dominating effect in high-energy collisions.

### 1. — Introduction.

A great effort, both experimental and theoretical, has recently been devoted to the study of strong interactions at high energy.

The theoretical investigations have followed many different directions.

First of all, several estimates of cross-sections, multiplicities, etc., have been carried out on the basis of the statistical model <sup>(1)</sup> which is essentially

(\*) Now at CERN - Geneva.

<sup>(1)</sup> F. CERULUS and R. HAGEDORN: CERN Report 59-3. Cf. also *Proc. of the Intern. Conf. on Theoretical Aspects of Very High-Energy Phenomena* (CERN, 1961), Section 4.

based on the idea that a very complicated interaction takes place in a certain volume  $V$  and that the probabilities for the different final states are determined by the available phase space.

A different and complementary approach is the peripheral one <sup>(2)</sup> which studies those events in which only one pion is exchanged between the two colliding particles.

A very interesting point of view has recently been developed by CHEW and FRAUTSCHI <sup>(3)</sup>: if one considers the elastic scattering amplitudes at high energy it is possible to make use of the MANDELSTAM <sup>(4)</sup> representation which gives an unambiguous prescription to locate the singularities of the amplitude.

In addition to that, it is possible by using unitarity to obtain explicit formulae for the singularities located near the physical region in the so-called « strips ». The « strip approximation » approach tries to evaluate the effect of peripheral collisions on elastic scattering. It has the advantage on the Drell-Salzman method that, due to the possibility of writing down a complete spectral representation, a greater control on the different approximations is possible. On the other side, the amount of information on high-energy physics which one obtains from the Chew and Frautschi programme is limited to diffraction scattering and to the total cross-section.

In this paper we wish to propose a general model for high-energy processes suggested by dispersion theory <sup>(\*)</sup>. Let us discuss the a qualitative picture of high-energy scattering. The main experimental features are the following:

I) Total cross-sections tend to reach energy-independent behaviour (constants) satisfying more or less « Pomeranchuk's theorems », with magnitude of the order of the square of the pion Compton wavelength.

II) All elastic cross-sections show the characteristic diffraction pattern consisting of a peak in the forward direction. The width of such a peak when plotted as a function of the momentum transfer is nearly independent of the process and of the energy and of the order of magnitude of the pion mass. Another general indication is that besides the diffraction peak, elastic scattering is substantially small.

<sup>(2)</sup> S. DRELL: *Phys. Rev. Lett.*, **5**, 342 (1960); F. SALZMAN and G. SALZMAN: *Phys. Rev. Lett.*, **5**, 377 (1960).

<sup>(3)</sup> G. F. CHEW and S. C. FRAUTSCHI: *Phys. Rev. Lett.*, **5**, 580 (1960); *Phys. Rev.*, **123**, 1478 (1961).

<sup>(4)</sup> S. MANDELSTAM: *Phys. Rev.*, **112**, 1344 (1958); **115**, 1741, 1752 (1959).

<sup>(\*)</sup> An independent investigation on high-energy diffraction scattering has been recently carried out by C. GOEBEL (see reports of the CERN Conference on Theoretical Aspects of High-Energy Phenomena, p. 353) leading to physical conclusions very similar to ours.



III) At high energies the elastic scattering amplitude is mainly imaginary. In  $\pi N$  scattering this happens already around 1.5 GeV.

IV) If the energy is not too big it seems that peripheral formulae work rather well for total cross-sections <sup>(5)</sup> as well as for many inelastic processes (mainly those for which there is a clear distinction between forward and backward « cones » in the c.m.s., processes that, however, are rather dominant).

These features are not independent from each other; in fact it will be shown that unitarity gives a simple relation between the size of the total cross-section and the width of the elastic diffraction peak.

The general features I) and II) show that the effective radius of the target nucleon from high-energy process is of the order of the pion Compton wavelength  $1/\mu$ .

We can get the following picture of the high-energy collision. The nucleon can be visually divided into two parts: a core with a radius of the order  $1/3\mu$ , and the external meson cloud.

About the core we know very little; its structure is very complicated since it depends on states with several virtual particles. Very probably it will act like a completely absorptive sphere; in any case because of the geometrical limitations on cross-section it can only contribute to a small fraction of the total cross-section. Besides, its contribution to the elastic scattering cross-section is also small because of the smallness of such cross-section outside the narrow diffraction peak.

The outer part of the nucleon, which will be the object of our theoretical investigation, plays a very important role in the process (as shown by the large size of the total cross-section); it acts as a semi-transparent medium whose absorption will decrease with the cloud density <sup>(\*)</sup> and thus with the distance from the centre.

In the following we shall concentrate our attention on the absorptive part of elastic scattering amplitudes. They shall be of particular interest because:

1) The optical theorem relates their value in the forward direction to total cross-sections.

2) Because of III) they shall give the main contribution to elastic scattering at high energies determining therefore its angular distribution.

<sup>(5)</sup> I. M. GRAMENITSKII, I. M. DREMIN, V. M. MAKSIMENKO and D. S. CHERNAUSKII: *Žurn. Éksp. Teor. Fiz.*, **40**, 1093 (1961); *Sov. Phys. JETP*, **13**, 771 (1961); I. M. DREMIN and D. S. CHERNAUSKII: *Žurn. Éksp. Teor. Fiz.*, **40**, 1333 (1961); S. DRELL: *Rev. Mod. Phys.*, **33**, 458 (1961).

<sup>(\*)</sup> This is confirmed experimentally by the fact that  $\sigma_{el}$  is smaller than  $\sigma_{react.}$

3) Their angular dependence is mainly due to the absorption of the incident wave by inelastic processes and it will depend in an essential manner on the way this absorption takes place.

4) And, last but not least, we have a theoretical tool for its investigation *i.e.* the Mandelstam representation.

In Section 2 a general scheme is introduced to study the absorptive part of the scattering amplitude for large energies and small momentum transfer. Using the Mandelstam representation in a manner similar to CHEW and FRAUTSCHL, a non-linear integral for the amplitude is obtained.

In Section 3 a method of solution is discussed. The solution is obtained in the form of a sequence of terms in which the only external parameters are the low-energy scattering cross-sections. In this manner definite expressions are obtained both for the total cross-sections and for the form of the diffraction peak.

As already discussed earlier, the form of the diffraction pattern is determined by the manner in which the absorption mechanism takes place. In this manner our result for diffraction and for the total cross-sections will enable us (Section 4) to construct a general model for all inelastic processes. This model has a very simple physical interpretation in terms of the Feynman graphs implying that all final particles are produced directly either by the two colliding particles or by the pion which is exchanged between the incoming particles. The only parameters entering in the model are low-energy parameters, like the position and width of the pion-nucleon and pion-pion resonances.

## 2. - The integral equation for the absorptive amplitude.

We shall treat the high-energy elastic scattering in which strongly interacting particles are involved.

We shall disregard in the following the spin and isotopic spin indices of the particles in order to manifest in a simpler way the analytic properties of the scattering amplitudes. We shall try to make clear however, in a subsequent note, that spin and isospin shall not change at all our results for what regards total cross-sections and elastic scattering near the forward direction.

We shall denote by  $X$  and  $Y$  the two colliding particles and define as usual

$$(1) \quad \left\{ \begin{array}{l} s = (q_X + q_Y)^2 \\ t = (q_X + p_X)^2 \\ i = (q_X + p_Y)^2. \end{array} \right.$$

$q, p$  are the initial and final X and Y momenta:

$$(1') \quad s + t + \bar{t} = 2M_X^2 + 2M_Y^2.$$

In the forward direction the imaginary part of the scattering amplitude <sup>(6)</sup>  $A_{XY}(s, t)$  is related to the total cross-section by the optical theorem <sup>(5)</sup>

$$(2) \quad A(s, 0) = 2qW\sigma_T(s).$$

As a consequence of the optical theorem we want to show that, at high energy,  $A(s, t)$  must have a strong and narrow peak in the forward direction, whose width is roughly inversely proportional to the total cross-section. The total elastic cross-section satisfies the obvious inequality

$$(3) \quad \sigma_{el}(s) = \frac{1}{s} \int \left| \frac{F(s, t)}{8\pi} \right|^2 d\Omega \geq \frac{1}{\pi s} \int_{t_{\max}}^0 \left( \frac{A(s, t)}{8q} \right)^2 dt,$$

where  $t_{\max} = -4q^2$ .

On the other hand, using the optical theorem we can write

$$(4) \quad A(s, t) = 2qW\sigma_T(s)U(s, t),$$

where the form factor  $U(s, t)$  is normalized to

$$U(s, 0) = 1.$$

Substituting eq. (4) into eq. (3) we get

$$(5) \quad \langle t \rangle \leq 16\pi \frac{\sigma_{el}}{(\sigma_T)^2},$$

where

$$(5') \quad \langle t \rangle = \int_{t_{\max}}^0 |U(s, t)|^2 dt,$$

is the width of the forward diffraction peak. Eq. (5) gives a very strong limitation on  $\langle t \rangle$ .

<sup>(6)</sup> Our amplitudes  $F(s, t)$  correspond to the Feynman ones multiplied by a factor  $\sqrt{2M}$  for each external nucleon line.

The relation (5) is roughly satisfied with the equality sign. In fact, taking as an example the  $\pi N$  scattering in the two GeV regions we have

$$\sigma_T \sim \frac{1.5}{\mu^2}, \quad \sigma_{el} \sim \frac{1}{3} \sigma_T,$$

and so  $t \sim 10\mu^2$  which is of the same order of the width of the diffraction peak. This means that the low momentum transfer scattering is so important to saturate the unitarity condition, and to leave very little place for the rest.

Let us discuss now the information one can get on  $A(s, t)$  from dispersion theory. The Mandelstam representation allows us to write the following fixed energy spectral representation:

$$(6) \quad A(s, t) = \frac{1}{\pi} \int_{a_1}^{\infty} dt' \frac{\varrho_1(s, t')}{t' - t} + \frac{1}{\pi} \int_{a_2}^{\infty} dt' \frac{\varrho_2(s, t')}{t' - \bar{t}}.$$

The real functions  $\varrho_1$  and  $\varrho_2$  are the two-dimensional spectral functions introduced by MANDELSTAM. The lower limits  $a_1$  and  $a_2$  depend on the nature of the particles exchanged in the  $(X, Y)$  scattering:  $a_1$  is always of the order of  $4\mu^2$ ;  $a_2$  is  $\sim 4\mu^2$  for  $(\pi\pi)$  and  $(N N)$  scattering and is  $M^2$  for  $(\pi N)$  scattering.

Here we are interested in the features of the forward diffraction peak: this will lead us to study the amplitude only for small ( $< 9\mu^2$ ) positive or negative values of  $t$ . Because of eq. (1') for energy high enough, the singularities in  $\bar{t}$  are very far from the values of  $t$  in which we are interested and will have a very small influence on the amplitude  $A$ .

We shall therefore only take into account the effect of  $\varrho_1(s, t)$ . Let us discuss now the different contributions to  $\varrho$ . Using unitarity in the channel  $X + \bar{X} \rightarrow Y + \bar{Y}$  (see Appendix) we can decompose  $\varrho(s, t)$  as a sum of contributions coming from the different groups of particles which can be exchanged between  $X$  and  $Y$ . The variable  $t$  represents the square of the « mass » (*i.e.*, the total c.m. energy) of each group of particles.

Therefore the larger the number of exchanged particles, the more distant from the physical region will be the singularities of  $A(s, t)$ . On the other hand, we have already seen that  $A(s, t)$  has a very large peak of width  $\sim 10\mu^2$  in the forward direction and is almost zero everywhere else. This strongly suggests that the region of singularities for  $4\mu^2 < t < 16\mu^2$  (the so-called « strip ») gives the dominating contribution to the integral (6).

In other words, we known experimentally that the contribution from outside the strip to (6) must be small. This doesn't imply however the smallness of

$q(s, t)$  for big  $t$ : it is well possible (\*) that big cancellations due to oscillations of  $q(s, t)$  as function of  $t$  outside the strip are responsible for the small contribution of such region.

Therefore the contribution of the two-pion states will be the most important since it gives the only contribution to  $q(s, t)$  for  $4\mu^2 < t < 16\mu^2$  for  $\pi\pi$  and  $\pi\mathcal{N}$  and  $4\mu^2 \leq t \leq 9\mu^2$  for  $\mathcal{N}\mathcal{N}$ .

This result is the dispersive analogue of the geometrical argument which had led us to believe that the external part of the nucleon structure gives the largest effect to the high-energy cross-sections. Let us now consider in detail the two-pion term. In the Appendix it is shown that  $q_{\pi\pi}(s, t)$  can be written in the form:

$$(7) \quad q_{\pi\pi}(s, t) = \frac{1}{\pi^2} \iint ds_1 ds_2 K_0(st; s_1 s_2) A_{X\pi}^*(s_1, t) A_{Y\pi}(s_2, t),$$

where

$$(8) \quad \begin{cases} K_0(st; s_1 s_2) = 0, & \text{for } t_0 > t \text{ and } \sqrt{s} < \sqrt{s_1} + \sqrt{s_2}, \\ \text{and} \\ K_0(st; s_1 s_2) = \frac{1}{8\sqrt{f(s, s_1 s_2)}} \frac{1}{\sqrt{t[t - t_0(s, s_1 s_2)]}}, & \text{for } t \geq t_0 \text{ and } \sqrt{s} \geq \sqrt{s_1} + \sqrt{s_2}, \end{cases}$$

where

$$(8') \quad \begin{cases} t_0 = \frac{g(s, s_1 s_2)}{f(s, s_1 s_2)}; & f(s, s_1 s_2) = [s - (\sqrt{s_1} + \sqrt{s_2})^2][s - (\sqrt{s_1} - \sqrt{s_2})^2], \\ g_{\pi\pi}(s, s_1 s_2) = 4\{\mu^2 s^2 + s[s_1 s_2 - 2\mu^2(s_1 + s_2)] + \mu^2(s_1 - s_2)^2\}, \\ g_{\mathcal{N}\pi}(s, s_1 s_2) = 4\{\mu^2 s^2 + s[s_1 s_2 - 2s_1 \mu^2 - s_2(M^2 + \mu^2)] + \mu^2(s_1 - s_2)^2 + \\ \quad + [(s_1 - s_2)(\mu^2 - M^2) + (\mu^2 - M^2)^2]s_2\}, \\ g_{\mathcal{N}\mathcal{N}}(s, s_1 s_2) = 4\{\mu^2 s^2 + s[s_1 s_2 + (M^2 - \mu^2)^2 - (M^2 + \mu^2)(s_1 - s_2)] + \\ \quad + M^2(s_1 - s_2)^2\}, \end{cases}$$

and  $A_{X\pi}(s, t)$  and  $A_{Y\pi}(s, t)$  are the absorptive parts of the  $(X\pi)$  and  $(Y\pi)$  scattering amplitudes (\*\*). The physical meaning of eq. (7) is illustrated in Fig. 1.  $q_{\pi\pi}(s, t)$  is related to all inelastic processes in which only one pion is exchanged between X and Y.  $\sqrt{s_1}$  and  $\sqrt{s_2}$  are the energies of the two groups of particles produced in such a collision.  $A_{X\pi}$  and  $A_{Y\pi}$  are

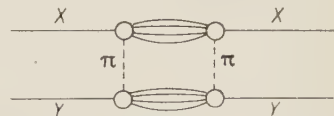


Fig. 1. — Graphs contributing to eq. (7).

(\*) Cf. C. GOEBEL: *Reports of the Intern. Conf. on Theoretical Aspects of Very High-Energy Phenomena*, CERN, p. 353.

(\*\*) In eq. (8') for the  $\pi\mathcal{N}$  case,  $s_1$  corresponds to  $\pi\mathcal{N}$  and  $s_2$  to  $\pi\pi$ .



the elastic amplitudes for the two subprocesses contained in the two black boxes. The function  $K(s, t; s_1 s_2)$  is the Mandelstam spectral function of the

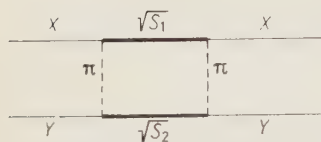


Fig. 2. — The perturbation graph corresponding to  $K_0(s, t; s_1 s_2)$ .

perturbation graph in Fig. 2, and represents the weight with which the different groups of particles in Fig. 1 contribute to the elastic diffraction scattering. Eq. (8) and (8') show that the spectral function is different from zero only for  $t \geq t_0(s; s_1 s_2)$ ; in particular, we must always have  $\sqrt{s} \leq \sqrt{s_1} + \sqrt{s_2}$ . The boundary curves  $t = t_0$  are called the Landau's curves; it is easy to verify that we can have  $t_0 < 16\mu^2$  only when  $\sqrt{s_1} + \sqrt{s_2} \ll s$ . In other words, all values of  $s_1, s_2$  for which  $\sqrt{s_1} + \sqrt{s_2} \leq \sqrt{s}$  are kinematically possible, but  $\sqrt{s_1}$  and  $\sqrt{s_2}$  must both be rather small as compared to  $\sqrt{s}$  in order to have contributions from the strip.

We understand here that the process of diffraction begins at energies for which some Landau's curves have already entered into the strip. It is easy to verify that for  $\pi N$  scattering the forward peak appears near 900 MeV which is just the energy for which the first Landau's curve has entered into the strip. This fact shows, for example, that the pion-pion scattering must be of some importance near its Landau's curve (characterized by  $s = 4\mu^2$ ), *i.e.*, that  $(\pi\pi)$  scattering must have its importance even at low energies (far before the region around  $s = (20 \div 30)\mu^2$  at which the  $T = J = 1$  resonance is expected to appear).

Eq. (7) is the starting point for our investigation of diffraction scattering. It gives a relation between the absorptive part at an energy  $s$  and those at the lower energies  $s_1$  and  $s_2$ . In the next section we shall take advantage of the fact that  $s_1$  and  $s_2$  must be smaller than  $s$  in order to obtain an approximate solution of eq. (7).

### 3. — Expressions for the absorptive amplitudes.

In order to solve the self-consistent problem given by eq. (6) and (7), we want first to write down an explicit expression for the absorption amplitude valid at all energies.

Of course, at low energy in the resonance region the important contribution will not come from the two-pion singularities which become important only in the diffraction region.

We shall therefore write

$$(9) \quad A_{XY}(s, t) = A_{XY}^R(s, t) + \frac{1}{\pi^3} \iiint dt' ds_1 ds_2 \frac{K(s, t'; s_1 s_2)}{t' - t} A_{X\pi}^*(s_1, t') A_{Y\pi}(s_2, t'),$$

where  $A_{\pi\pi}^R(s, t)$  is the contribution to the absorptive part of the amplitude coming from the  $(\pi\pi)$  or  $(\pi N)$  resonances and bound states. Therefore it will be very important at low energy and then drop to zero very rapidly.

Since for low energy the singularities in  $t$  are far, both from the physical region and from the strip, one can safely write (7)

$$(10) \quad A_{\pi\pi}^R(s, t) \approx A_{\pi\pi}^R(s, 0) = 2q \sqrt{s} \sigma_{\pi\pi}^R(s).$$

Let us now consider the meaning of eq. (9) for the different scattering processes. In the case of  $(\pi\pi)$  scattering, eq. (9) is a non-linear equation involving only the  $(\pi\pi)$  amplitude. The  $\pi N$  equation is a linear equation whose kernel contains  $(\pi\pi)$  amplitude. Finally the  $(N, N)$  amplitude can be obtained directly once the  $(\pi N)$  amplitude is known.

This corresponds to the usual classification of the different processes given by the Mandelstam representation.

We see that the only inputs one has to insert in eq. (9) are the values of low-energy pion-pion and pion-nucleon cross-sections.

Let us now solve eq. (9) by iteration: we obtain

$$(11) \quad A_{\pi\pi}(s, t) = A_{\pi\pi}^R(s) + \frac{1}{\pi^3} \iint \int dt' ds_1 ds_2 \frac{K_0(s, t'; s_1 s_2)}{t' - t} A_{\pi\pi}^R(s_1) A_{\pi\pi}^R(s_2) + \\ + \frac{1}{\pi^4} \iiint \int dt' ds_1 ds_2 ds_3 \frac{K_1(s, t'; s_1 s_2 s_3)}{t' - t} A_{\pi\pi}^R(s_1) A_{\pi\pi}^R(s_2) A_{\pi\pi}^R(s_3) + \dots,$$

where

$$(12) \quad K_1(s, t'; s_1 s_2 s_3) = \frac{1}{\pi^2} \iint \frac{dt'' ds_A}{t'' - t'} \{ K_0(s, t'; s_1 s_A) K_0(s_A, t''; s_2 s_3) + \\ + K_0(s, t'; s_A s_3) K_0(s_A, t''; s_1 s_2) \}, \quad \text{etc.}$$

(7) The reasoning leading to eq. (9) and (10) can also be understood in the following manner. Consider for sake of definiteness the case of  $\pi\pi$  scattering. We can separate the  $T$  matrix into four parts,  $T = T_1 + T_2 + T_3 + T_0$ , where  $T_1, T_2, T_3$  have the two-pion singularities between  $4\mu^2$  and  $t_{\text{max}}$  (which may be as usual larger than the inelastic singularities at  $16\mu^2$ ) in the variables  $s, t, \bar{t}$ , respectively, and  $T_0$  has no low singularities in any variables. In the spirit of the strip approximation one can disregard the effect of  $T_0$ ;  $T_1, T_2, T_3$  can be computed once the singularities in the strip are known. Taking the imaginary part (in the  $s$  channel) of  $T$  we get

$$A = A_1 + A_2 + A_3.$$

$A_2$  and  $A_3$  are the contributions to  $A$  given in eq. (6),  $A_1$  corresponds to  $A^R$  of eq. (9) which has to vanish for  $s$  outside the elastic region.

We see that it is in principle possible in terms of elastic scattering to compute the  $t$  dependence of  $A^R(s, t)$  through a Legendre polynomial expansion (whose analytic continuation converges in the strip) and therefore to improve on the simple approximation (10).

It can immediately be seen that

$$(13) \quad K_{i-2}(s, t; s_1, s_2 \dots s_i) \neq 0 \quad \text{only for } \sqrt{s} > \sum_{j=1}^i \sqrt{s_j}.$$

This implies that since  $|s_j| > 4\mu^2$  for each finite value of  $s$  the iteration sequence will only have a finite number of terms, so that eq. (11) will indeed represent a solution of eq. (10).

We have, however, still to verify that the solution (11) is a physically acceptable one in which the maximum contribution comes from the integration range inside the strip.

This is clear for the first term since only small values of  $s_1, s_2$  appear in the sum and the integral in  $t'$  is rapidly convergent.

On the other hand, it is very difficult to obtain a direct estimate of the higher order terms since the different kernels  $K_i$  are oscillating functions.

Therefore in order to be able to study the form and the consistency of the expansion (11) we shall transform the different terms of this sum into integrals of a positive definite function.

Let us first of all recall that  $K_0(s, t; s_1 s_2)$  is the Mandelstam spectral function of the perturbation graph of Fig. 2. Now it is shown in Appendix II that the functions  $K_{i-2}(s, t; s_1 s_2 \dots s_i)$  are the Mandelstam spectral functions of the perturbation graphs of Fig. 3.

Let us now rewrite eq. (11) in the form

$$(14) \quad A(s, t) = A^R(s) + \frac{1}{\pi^2} \iint ds_1 ds_2 I_0(s, t; s_1 s_2) A^R(s_1) A^R(s_2) + \\ + \frac{1}{\pi^3} \iiint ds_1 ds_2 ds_3 I_1(s, t; s_1 s_2 s_3) A^R(s_1) A^R(s_2) A^R(s_3) + \dots,$$

where

$$(15) \quad I_{i-2}(s, t; s_1 s_2 \dots s_i) = \frac{1}{\pi} \int_{4\mu^2}^{\infty} dt' \frac{K_{i-2}(s, t'; s_1 s_2 \dots s_i)}{t' - t}.$$

The new functions  $I_{i-2}(s, t; s_i)$  are the absorptive parts in the  $s$  channel of the elastic amplitudes given by the graphs in Fig. 3.

Those quantities can be computed directly by using unitarity in the

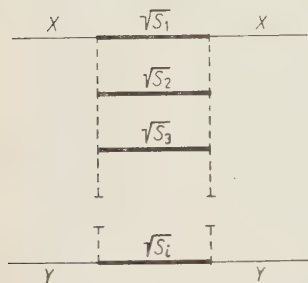


Fig. 3. — The perturbation graphs corresponding to  $K_i(s, t; s_1 s_2 \dots s_n)$ .

channel  $s$ , *i.e.*, by cutting vertically the graphs of Fig. 3. Thus we can write <sup>(8)</sup>

$$(16) \quad I_{i-2}(s, t; s_1 s_2 \dots s_i) = \frac{1}{2(2\pi)^{3i-4}} \int \frac{\delta(k_1^2 - s_1) d^4 k_1 \delta(k_2^2 - s_2) d^4 k_2 \dots}{(u_{x_1} - \mu^2)(v_{x_1} - \mu^2) \dots} \cdot$$

$$\frac{\delta(k_i^2 - s_i) d^4 k_i \delta^4(q_x + q_y - \sum_{j=1}^i k_j)}{(u_{x_{i-1}} - \mu^2)(v_{x_{i-1}} - \mu^2)},$$

$$(17) \quad \begin{cases} u_{x_1} = (q_x - k_1)^2; & v_{x_1} = (p_x - k_1)^2, \\ u_{x_r} = (q_x - \sum_{j=1}^r k_j)^2 & v_{x_r} = (p_x - \sum_{j=1}^r k_j)^2. \end{cases}$$

Let us now discuss the properties of the integral (16). The integrand is always positive definite and the largest contribution will come from those integration regions for which all  $u_{x_j}$  and  $v_{x_j}$  are small. We remark here that:

- 1) all denominators can be simultaneously small only for  $\sum \sqrt{s_j} \ll s$ ;
- 2) the integral  $I$  is a rapidly decreasing function of the momentum transfer  $t$ ; this means that the most important contributions to the spectral integrals in eq. (11) do indeed come from the strip.

Let us now analyse in more detail eq. (14) for scattering in the GeV region.

To be more specific, let us work at energies for which the resonant behaviour of particular partial waves has already disappeared and which are not too high, on the other side, so that only the first integral in (14) contributes. In the case of  $\pi N$  scattering, this means a pion laboratory energy in the interval from 1 GeV to  $(3 \div 4)$  GeV. Then, making use of (10),

$$(18) \quad A_{XY}(s, t) = \frac{1}{\pi^2} \iint ds_1 ds_2 I_0(s, t; s_1 s_2) 2q_1 \sqrt{s_1} \sigma_{\pi X}^R(s_1) 2q_2 \sqrt{s_2} \sigma_{\pi Y}^R(s_2),$$

<sup>(8)</sup> Here we are making use of the important fact that a perturbation Feynman graph can always be computed by using unitarity both in the  $s$  and in the  $t$  channel.

For the ladder graphs of Fig. 3 the use of unitarity in channel  $t$  allows us to consider only graphs with only four external lines and therefore to use at each step the Mandelstam representation. From the computational point of view, however, one has the big disadvantage of the possibility of many energy denominators which can have both signs giving rise to oscillations.

On the other hand, unitarity in the  $s$  channel introduces immediately the amplitudes for the inelastic processes. So its use is at the moment impossible in the framework of a general theory of strong interaction since we have not yet any general representation (like the Mandelstam one) for inelastic amplitudes. However, if we are able, as in our case, to reduce the whole problem to the computation of the *well-defined perturbation graphs* of Fig. 3, then the unitarity in the  $s$  channel has an enormous advantage since it has to be used *only once* and gives rise to well convergent integrals on a positive definite integrand.

where

$$(19) \quad I_0(s, t; s_1 s_2) = \frac{1}{4\pi} \frac{1}{\sqrt{f(s, s_1 s_2)}} \frac{1}{t_0(s, s_1 s_2)} F\left(\frac{|t|}{t_0}\right),$$

where

$$(20) \quad F\left(\frac{|t|}{t_0} \equiv x^2\right) = \frac{1}{x\sqrt{1+x^2}} \log(x + \sqrt{1+x^2}).$$

For  $\sqrt{s} \ll \sqrt{s_1} + \sqrt{s_2}$ ,  $t_0$  will be very near to its lowest value  $4\mu^2$ . Therefore we can get approximately

$$(21) \quad A_{XY}(s, t) \simeq A_{XY}(s, 0) F\left(\frac{t}{4\mu^2}\right).$$

This shows that, at least at intermediate energies, the shape of the diffraction pattern depends weakly both on the process and on the incident energy.

This is very reasonable from the physical point of view and in good agreement with experiment.

In Fig. 4a) and 4b) a comparison with  $\pi N$  experimental data at 1.8<sup>(5)</sup> and 5 GeV<sup>(6)</sup> is reported. At 5 GeV the theoretical curve is less peaked than the

experimental one; the dotted curve represents the result of an estimate of the higher order terms.

Eq. (18) give us also a definite expression for  $A(s, 0)$  and therefore for total cross-sections at intermediate energies. Inserting (19) in (18) for  $t=0$  we obtain

$$(22) \quad \sigma_{XY}(s) = \frac{1}{2\pi^2 q \sqrt{s}} \cdot \iint \frac{ds_1 ds_2 q_1 \sqrt{s_1} \sigma_{\pi X}(s_1) q_2 \sqrt{s_2} \sigma_{\pi Y}(s_2)}{\sqrt{f(s; s_1, s_2)} t_0(s; s_1, s_2)}.$$

Eq. (22) corresponds to what one would obtain by integrating over energies and angles the peripheral formula of Salzman and Salzman<sup>(2)</sup>. We see therefore that this theoretic approach justifies the peripheral model for interme-

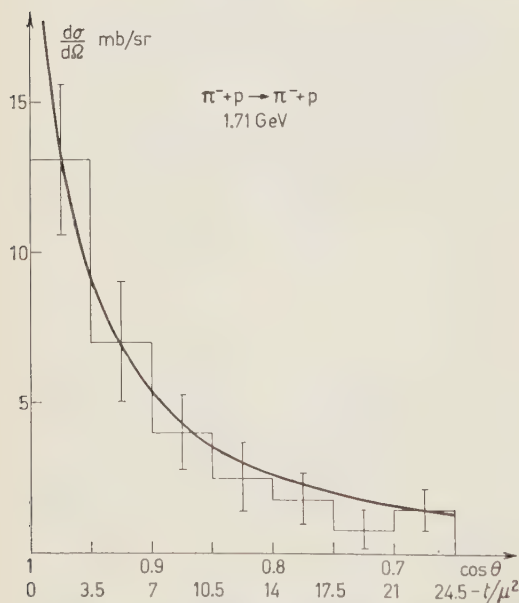


Fig. 4a. -  $\pi N$  scattering angular distribution taken from ref. (5) compared with the theoretical diffraction curve [eq. (21) of Section 3].

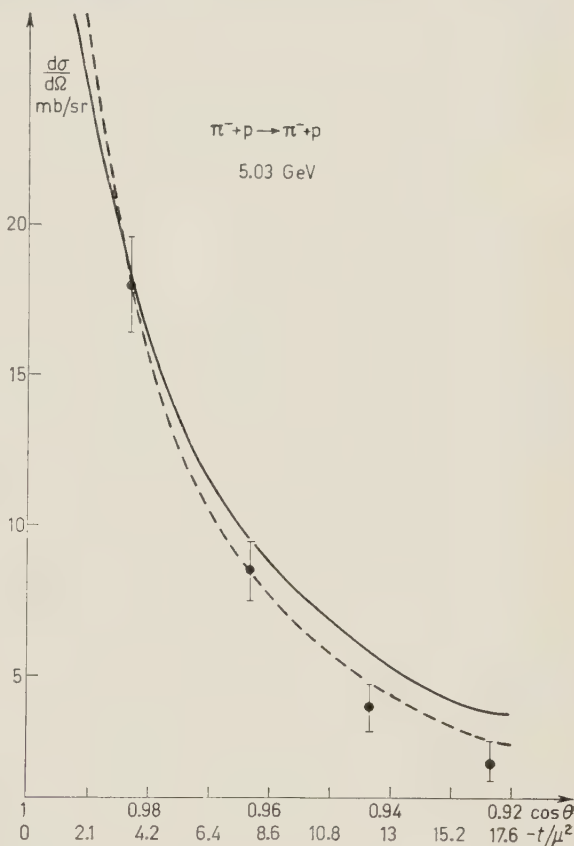
(5) R. C. WHITTEN and M. M. BLOCK: *Phys. Rev.*, **111**, 1676 (1958).



diate energies, but it allows also to understand that it breaks down for very high energies as some cosmic ray experimental analysis already indicates <sup>(5)</sup>.

In fact, when  $s$  is too big other integrals beside the first shall count in (14) so no simple formula as (22) can be obtained. Or, in other words, for too high energies,  $s_1$  and  $s_2$  can be at their turn sufficiently big so that it would be a very bad approximation to neglect the  $t'$ -dependence of  $A_{\pi X}(s_1 t')$  and  $A_{\pi Y}(s_2 t')$  in (9) by using for them the approximation (10), with which (9) would give us back (22). We see that this procedure would grossly overestimate  $A_{\pi\pi}(s_1 t')$  and  $A_{\pi\pi}(s_2 t')$  meaning therefore that (22)—or the simple peripheral model—would give too big cross-sections at very high energies.

Fig. 4b. —  $\pi N^0$  scattering angular distribution taken from ref. <sup>(10)</sup> compared with the theoretical diffraction curve [eq. (21) of Section 3] and with the improved theory (broken curve). The theoretical curves are normalized to the first point.



#### 4. — A model for high-energy interaction.

In the preceding section we have obtained expressions for the absorptive part of the scattering amplitude. This is all that one can obtain directly on the basis of a dispersion theory of elastic scattering. We want now to show that the form of our result strongly suggests a definite model about the inelastic processes responsible for the absorption process. Let us write explicitly the expression for the total cross-section given by eq. (14) and (16):

$$(23) \quad \sigma(s) = \sum_i \sigma_i(s),$$

<sup>(10)</sup> R. G. THOMAS JR.: *Phys. Rev.*, **120**, 1015 (1960).

where

$$(24) \quad \sigma_i(s) = \frac{1}{2q\sqrt{s}} \frac{1}{\pi^i} \int \dots \int ds_1 ds_2 \dots ds_i \cdot \\ \cdot 2q_1\sqrt{s_1}\sigma^R(s_1) 2q_2\sqrt{s_2}\sigma^R(s_2) \dots 2q_i\sqrt{s_i}\sigma^R(s_i) I_{i-2}(s; s_i),$$

where

$$(25) \quad I_{i-2}(s; s_i) = \frac{1}{2(2\pi)^2} \int \dots \int F(q_X, q_Y; k_i, s_i) \cdot \\ \cdot \delta(k_1^2 - s_1) d^4k_1 \delta(k_2^2 - s_2) d^4k_2 \dots \delta(k_i^2 - s_i) d^4k_i \delta^4(q_X + q_Y - \sum k_i),$$

$$(26) \quad F(q_X, q_Y; k_i, s_i) = \frac{1}{(2\pi)^{3(i-2)}}$$

$$\cdot \frac{1}{[(q_X - k_1)^2 - \mu^2]^2 [(q_X - k_1 - k_2)^2 - \mu^2]^3 \dots [(q_X - k_1 \dots k_{i-1})^2 - \mu^2]^2}.$$

It is very reasonable to consider the different terms  $\sigma_i$  in the sum (23) as different partial cross-sections corresponding to the production of  $i$  groups of particles.

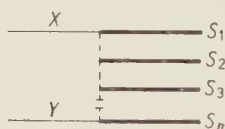


Fig. 5. - Diagrammatic representation of the production process in: a)  $\pi\pi$  interaction; the masses  $s_1, \dots, s_i$  will be of the order of  $30\mu^2$  corresponding to the  $\pi\pi$  resonance in the  $J=T=1$  state or  $\sim 4\mu^2$ , if there is a strong  $s$ -wave interaction at threshold. b)  $\pi N^*$  interaction; the mass  $s_i$  connected with the nucleon will likely be or the nucleon mass squared or of the order of  $W_R^2$  corresponding to the  $(3, 3)$  resonance. The other masses will be similar to those of the  $\pi\pi$  case. c)  $N^*N^*$  interaction; the two masses  $s_1$  and  $s_i$  connected with the nucleon will be  $\approx m^2$  or  $W_R^2$ , the others like the  $\pi\pi$  case.

The important contributions to the integral (24) come from the energies of the different groups of particles corresponding to a large scattering cross-section. In other words the dominating effect will be the production of several  $(\pi\pi)$  or  $(\pi N^*)$  isobars. Let us now examine the form for  $\sigma_i$  given by eq. (24), (25) and (26). Also in this case one can reasonably interpret the integrand  $F(q_X, q_Y; k_i)$  as the angular distribution of the different isobars in the high-energy collisions <sup>(11)</sup>.

We are therefore led to the model illustrated in Fig. 5.

<sup>(11)</sup> An important feature of the model is that all integrations on  $s_i$  are limited to the resonance region. This automatically ensures [see eq. (25)] that the important contribution comes from small values of the different pion momentum transfers  $t_i$ . This is not equivalent to the procedure of cutting off the integrations to small values. Using that procedure and choosing a sufficiently high value of the initial energy, one would still have integrations on large values of  $s_i$ .

- 1) The incoming particles exchange a single pion.
- 2) The produced particles are emitted either by the initial particles or by the intermediate pion. In other words the emission must take place either from one of the two vertices or by the meson propagator.
- 3) In each single act of emission either one particle or a group of low-energy particles will be produced.
- 4) The differential cross-section for production is given by

$$(27) \quad d\sigma = \frac{1}{16q\sqrt{s}} \frac{1}{\pi^{i+2}} F(q_x q_y; k_1, s_i) 2q_1 \sqrt{s_1} \sigma^R(s_1) \delta(k_1^2 - s_1) d^4 k_1 \dots \cdot \\ \cdot 2q_i \sqrt{s_i} \sigma^R(s_i) \delta(k_i^2 - s_i) d^4 k_i \delta^4(q_x + q_y - \sum k_i).$$

Of course, eqs. (25) and (26) could have been derived more directly by summing the series of Feynman graphs shown in Fig. 5<sup>(12)</sup>. However, it would have been difficult in that case to have any estimate of the order of magnitude of the neglected graphs and of the error introduced in the different extrapolation in the mass variable.

The dispersion analysis gives very strong arguments implying that the graphs selected in Fig. 5 are the dominating effect in high-energy collisions.

We want to discuss now some qualitative features of the model. Let us consider a fixed incident energy. For each pair of pions one wants to produce, one has to add one extra propagator  $1/(t - \mu^2)^2$ . The average multiplicity will be therefore determined by the competition of the graphs with different number of denominators. For a small number of mesons produced it will be possible kinematically to make all denominators of the order of a few  $\mu^2$ . For a larger number it will no longer be possible to have all small denominators; those terms will become therefore less and less important. We have thus to expect an average multiplicity much lower than that predicted by the statistical model.

About the angular distributions in a particular production process, the most probable configurations will be those corresponding to the lowest value for the product of all denominators. This happens first of all when all transverse momenta are very small. In the c.m. system we have to expect jets of particles collimated in the forward and in the backward direction. An approximate calculation shows that the different groups of particles in the two beams will have different energies decreasing rapidly from the maximum available energy to zero.

<sup>(12)</sup> Multijet graphs of the kind shown in Fig. 5 have been first considered by V. B. BERESTETSKY and YA. POMERANCHUK: *Nucl. Phys.*, **22**, 629 (1961).

The first very qualitative indications of such a model for multiplicities, nature of secondary particles and spectra of them, seem to point in a good direction. So, it is perhaps reasonable to expect that from such a description of inelastic processes it would be possible to understand some characteristic features pointed out by high energy accelerators and cosmic rays; for instance, the large amount of pions among the secondaries, as compared to K-mesons and baryons, their multiplicity as function of the incident primary energy, the small and rather constant mean transverse momentum, as well as the spectra of secondary pions showing a reasonable high energy tail.

## 5. - Conclusions.

Let us review briefly the different points which have been raised in this paper.

The empirical basis for the model proposed here comes from the fact that the high-energy total cross-section has a constant and rather large value. This implies that the collisions with large impact parameters give the most important effect. This fact is expressed in a more precise form by showing (see eq. (4)) that a large cross-section implies a very narrow peak in  $A(s, t)$  and therefore the two-pion singularities give the dominating effect.

An evaluation of the two-pion exchange effect to elastic scattering amplitudes in terms of the low-energy ( $\pi\pi$ ) and ( $\pi N$ ) cross-sections has allowed us to obtain definite expressions for the total cross-sections and for the absorptive part of the scattering amplitude.

This last gives us a definite prediction for the shape of the diffraction peak. Its form at intermediate energies is given by the square of  $F$  given in eq. (21), independently of the process and the energy, and fit very well present experimental data.

On the other hand our results for the total cross-section reproduce the peripheral one for intermediate energies and show that as the energy increases too much the simple peripheral model breaks down and must be supplemented by the «superperipheral» processes of Fig. 5. These results for the total cross-sections suggest that this «superperipheral» model can be suitable to calculate all high energy processes (inelastic collisions).

Work is now in progress to evaluate numerically the consequences of the model, but it seems already that the qualitative features give reasonable predictions for extremely high energy processes.

A detailed comparison between theory and experiment will be most interesting.

One point which might look somewhat surprising is the fact that the model contains only low-energy parameters. Thus, by looking at the general features of high-energy collisions, one does not learn anything essentially new as com-



pared to low-energy physics. The following example might be useful to clarify the situation. Consider the elastic scattering of high-energy electrons by protons and suppose one asks very general questions such as: in what direction is the majority of the electrons scattered and with what cross-section? The answer is that the cross-section is dominated by a Rutherford denominator and that the great majority of the electrons are scattered around the forward direction with a cross-section which depends only on the renormalized charge which is certainly a low-energy parameter (of course much better known than low-energy ( $\pi\pi$ ) interaction!). If one wants to get new and interesting information about the nucleon form factors one has to lose a large factor in intensity and to look for the rare events which take place at large angles. In the same manner if one wants to test the internal part of the nucleon by means of strong interactions one has to look for those collisions with large momentum transfer which lie outside the range of our model. But also in this case one has probably to lose an appreciable factor in intensity.

One other important point is that, as pointed out by CHEW and FRAUTSCHI, our understanding of high-energy phenomena might improve the status of our theories of low-energy scattering. One can get important information about low-energy scattering by means of the customary dispersion relations at fixed momentum transfer. Our model allows to obtain the imaginary part of the scattering amplitudes at high energy and one will not be obliged, as in the past, to cut the dispersion integrals above the (3, 3) resonance energy. This will probably lead to a reduction of the number of independent parameters one had to introduce in order to explain the main features of low-energy scattering.

\* \* \*

We want to express our most sincere thanks to Dr. LUCIANO BERTOCCHI for very useful discussions and much help in the experimental comparison of the diffraction formulae. We wish to thank Profs. B. FERRETTI and L. VAN HOVE for very illuminating discussions and criticism.

## APPENDIX

Let us consider the absorptive part of the scattering amplitude in the channel  $X + \bar{X} \rightarrow Y + \bar{Y}$ .

Using the unitarity condition and taking as intermediate states the two pions only we have

$$(A.1) \quad A_{X\bar{X}}(s, t) = \frac{1}{2(2\pi)^2} \int d^4d F_{X\pi}^*[(q - q_X)^2, t] F_{Y\pi}[(q + q_Y)^2, t] \delta(q^2 - \mu^2) \cdot \\ \cdot \delta(q_X + p_X - q)^2 - \mu^2].$$



Using the fixed momentum transfer dispersion relation we have

$$(A.2) \quad F_{\pi\pi}(s, t) = \frac{1}{\pi} \int \frac{A_{\pi\pi}^1(s', t)}{s' - s} ds' + \frac{1}{\pi} \int \frac{A_{\pi\pi}^2(\bar{t}', t)}{\bar{t}' - \bar{t}} d\bar{t}',$$

and substituting in eq. (A.1) we shall obtain four terms. We are only interested in the singularity of the absorptive part in the  $s$  variable as explained in the text, *i.e.*,

$$(A.3) \quad A_{\pi\pi}^-(s, t) = \frac{1}{\pi} \int \frac{\varrho_{\pi\pi}(s', t)}{s' - s} ds',$$

and we can drop the crossed terms which gives singularity in  $\bar{t}$ .

The two remaining terms give contribution to  $\varrho_{\pi\pi}(s, t)$ . In our case in which we neglect isotopic dependence, the two intermediate pions are identical and also the two terms give identical contribution. Therefore we shall insert in eq. (A.1) only the first term of eq. (A.2). The factor 2 is compensated by the normalization of the two identical particle phase spaces. We obtain

$$(A.4) \quad A_{\pi\pi}^-(s, t) = \frac{1}{\pi^2} \iint ds_1 ds_2 A_{\pi\pi}^*(s_1, t) A_{\pi\pi}(s_2, t) I_{\pi\pi}^-(s, t; s_1 s_2),$$

where

$$(A.5) \quad I_{\pi\pi}^-(s, t; s_1 s_2) = \frac{1}{\pi} \int \frac{K_0(s', t; s_1 s_2)}{s' - s} ds',$$

and

$$(A.6) \quad K(s, t; s_1 s_2) = \frac{1}{2} \int d^4q \delta(q^2 - \mu^2) \delta[(q_x + p_x - q)^2 - \mu^2] \cdot \\ \cdot \delta[s_1 - (q - q_x)^2] \delta[s_2 - (q + q_x)^2].$$

From eq. (A.3), (A.4) and (A.5) we get

$$(A.7) \quad \varrho_{\pi\pi}(s, t) = \frac{1}{\pi^2} \iint ds_1 ds_2 A_{\pi\pi}^*(s_1, t) A_{\pi\pi}(s_2, t) K(s, t; s_1 s_2).$$

We note that  $K$  is the Mandelstam spectral function of the 4-th order graph. This can be seen by direct inspection of eq. (A.6) or simply by using the general formula (A.7) and substituting for  $A(s, t) = \pi \delta(s - \bar{s})$  which is the 2-nd order absorptive part.

This iteration procedure to construct the spectral function of the 4-th order graph using the unitarity condition and the analyticity properties (which was first worked out by Mandelstam) can be used in order to obtain the spectral functions of higher-order graphs. For the 6-th order diagram in which we are interested, substituting in eq. (A.7) the absorptive part of the amplitude up to the 4-th order.

$$A(s, t) = A_2(s, t) + A_4(s, t) = \pi \delta(s - \bar{s}) + \frac{1}{\pi} \int \frac{K_0(\bar{s}, t')}{t' - t},$$

and collecting the crossed terms  $A_2^* A_4 + A_4^* A_2$  we get

$$\varrho_6(s, t) = \frac{1}{\pi^2} \iint \frac{ds_A dt'}{t' - t} \{K_0(s, t; s_1 S_A) \bar{K}_0(s'; s_1 s_2 s_3) + \bar{K}_0(s, t; s s_3) K_0(s'; s_1 s_2)\}.$$

In this manner we have verified the  $K_1$  in the text is the 6-th order spectral function. In a similar way it is possible to prove that the  $K_n$  are the Mandelstam spectral functions of the  $(2n+4)$ -th order graphs.

### RIASSUNTO

Le caratteristiche essenziali delle interazioni forti di alta energia vengono discusse teoricamente. Applicando la teoria dispersiva agli elementi di matrice dell'urto per energie elevate e piccoli momenti trasferiti, otteniamo espressioni esplicite per la forma del picco di diffrazione e per le sezioni d'urto totali. Questi risultati suggeriscono fortemente un modello per i fenomeni anelastici. In questo modello gli effetti dominanti alle alte energie vengono dati da un ben definito gruppo di diagrammi di Feynman in termini di sezioni d'urto di basse energie.

## Quasi-Elastic Nucleon-Nucleus Scattering at High Energy (\*).

R. KARPLUS (\*\*) and Y. YAMAGUCHI (\*\*\*)

*CERN - Geneva*

(ricevuto il 21 Agosto 1961)

**Summary.** — The angular distribution for elastic nucleon-nucleon scattering at high energy is sharply peaked in the forward direction. As a consequence, there is an angular interval in nucleon-nucleus scattering to which successive small-angle elastic nucleon-bound nucleon scatterings are more likely to contribute than a single nucleon-bound nucleon scattering through the angle of observation. Such « plural » collisions result in outgoing nucleons which have suffered a smaller energy loss than nucleons that are scattered from hydrogen at the same angle. The Fermi motion of the bound nucleons produces a broadening in the energy distribution of the scattered nucleons, but displaces the centre of the distribution only negligibly. The results of calculations with a simple model are in satisfactory agreement with the observations on proton-carbon scattering.

### 1. — Introduction.

In the scattering of a nucleon by a nucleus, above an incident energy of about 300 MeV, an easily identifiable group of the scattered nucleons satisfies the kinematic requirements of nucleon-nucleon collisions. The expression « quasi-elastic scattering » is used to describe this process, which is attributed to the elastic scattering of the incident particles by single nucleons within

---

(\*) This work was supported in part under contract no. AF 49(638)-327 administered by the Office of Scientific Research of the Air Research and Development Command.

(\*\*) Permanent address: University of California, Berkeley.

(\*\*\*) On leave of absence from Osaka City University, Osaka.

the target nucleus <sup>(1)</sup>; the energy transfer to the struck nucleon, of course, is somewhat larger than the energy transfer to the carbon nucleus in genuine elastic scattering from the latter, but it is not as large as it is in processes involving meson production <sup>(2)</sup>.

Experimental work with very high-energy ( $15 \div 26$  GeV) incident protons being scattered at small angles by carbon, tantalum, and beryllium has revealed a structure near the upper limit of the energy spectrum of the scattered protons that appeared to confirm the usefulness of the model in which a single bound nucleon acts as the target <sup>(3)</sup>. More precise measurements of the secondary energy, however, showed that the group of most energetic scattered protons had suffered an average energy loss only two-thirds that calculated for elastic scattering from single target nucleons <sup>(4)</sup>. Accordingly, it appeared likely that the effective target consisted of more than one nucleon. Because the effective target acquires a large momentum near 1 GeV/c, it seemed implausible to postulate that it consists of a bound fragment such as a deuteron; instead, we investigated the possibility that the scattering took place successively on two uncorrelated nucleons in the nucleus. It is our purpose to show that the observations can be accounted for in this way. As a matter of fact, such plural interaction had been considered as a possible mechanism for producing many mesons in high-energy nuclear stars <sup>(5)</sup>, but they have never been studied in connection with quasi-elastic scattering in the absence of particle production.

At first thought it seems implausible that the probability for two elastic collisions should compete favorably with the probability for one collision in a small, strongly absorbing object such as a carbon nucleus (or a deuteron <sup>(6)</sup>).

---

<sup>(1)</sup> The term «quasi-elastic» has been introduced by J. B. CLADIS, W. N. HESS and B. J. MOYER: *Phys. Rev.*, **87**, 425 (1952). For earlier theoretical work devoted to the development of the concept see R. SERBER: *Phys. Rev.*, **72**, 1114 (1947).

<sup>(2)</sup> B. T. FELD and C. ISO: *Nuovo Cimento*, **21**, 59 (1961). These authors, and those in ref. <sup>(3)</sup>, have extended the meaning of the term «quasi-elastic» to include meson-production phenomena. We consider this an unfortunate change and shall adhere to the more conventional and appropriate definition given in the text.

<sup>(3)</sup> G. COCCONI, A. N. DIDDENS, E. LILLETHUN and A. W. WETHERELL: *Phys. Rev. Lett.*, **6**, 231 (1961).

<sup>(4)</sup> G. COCCONI *et al.*: *Proc. of International Conference on Theoretical Aspects of Very High Energy Phenomena*, CERN 61-22 (1961) and private communication of very preliminary data.

<sup>(5)</sup> W. HEITLER and L. JÁNOSSY: *Proc. Phys. Soc. (London)*, A **62**, 669 (1949); *Helv. Phys. Acta*, **23**, 417 (1950).

<sup>(6)</sup> R. J. GLAUBER: *Phys. Rev.*, **100**, 242 (1955) has discussed the non-additivity of the elementary cross-section in the deuteron because of the shadowing of one nucleon by the other. This correction to the total cross-section (*i.e.* forward scattering amplitude) is just a double-scattering effect, but one in which the waves singly and

While the total probabilities unquestionably favor the single collision, the comparison becomes more difficult when we focus our attention on a fixed scattering angle, for then one must have information about the angular distribution in single scattering. In particular, if the angular distribution is sharply peaked in the forward direction, the relative probabilities may be inverted: one scattering at a substantial angle may be less probable than two successive scatterings, each at an angle only one-half as great.

In this article, we shall calculate the importance of the plural scattering for a simple model of the nucleus and the elementary cross-sections. The nucleus of mass number  $A$  is treated as a spherical region of radius ( $\hbar = c = 1$ )

$$(1) \quad R(A) = r_0 A^{\frac{1}{3}}, \quad (r_0 \simeq 1.17 f)$$

filled with uncorrelated nucleons with a momentum distribution

$$(2) \quad P(\mathbf{p}) = \left( \frac{2M\varepsilon}{\pi} \right)^{\frac{3}{2}} \exp \left[ -\frac{\mathbf{p}^2}{2M\varepsilon} \right], \quad (M = \text{nucleon mass, } \varepsilon/M = 1.70).$$

The elementary nucleon-nucleon cross-section  $[d\sigma(p, \theta)/d\Omega]_{\text{lab.}}$  at incident momentum  $p$  and scattering angle  $\theta$  (in the «lab. system», where the target nucleon is at rest) we take as

$$(3) \quad \left[ \frac{1}{p^2} \frac{d\sigma(p, \theta)}{d\Omega} \right]_{\text{lab}} \simeq \left( \frac{\sigma_{\text{tot}}}{4\pi} \right)^2 \exp[-\alpha p^2 \theta^2],$$

$$(4) \quad \sigma_{\text{tot}} = 40 \text{ mb}, \quad \alpha \simeq 7/M^2, \quad \sigma_e = \sigma_{\text{tot}}^2/16\pi\alpha \simeq 10 \text{ mb},$$

independent of spin and charge. There is very little experimental information about these quantities except  $\sigma_{\text{tot}}$ . It seems reasonable in the light of present theoretical views to assume that the angular variation eq. (3) depends on the square of the invariant momentum transfer

$$(5) \quad t \simeq p^2 \theta^2$$

at small angles; then a combination of measurements at different energies yields the form we have chosen for  $t \sim M^2$  (4). For larger  $t$  the cross-section drops less steeply. The integrated value obtained for the elastic cross-section also is reasonable in the light of data at lower energies. We neglect the effect

doubly scattered in the forward direction interfere destructively (hence the word «shadow») and give a reduction in the cross-section. For scattering at a finite angle with a momentum loss, the plurally scattered waves are incoherent with one-another, so that the cross-sections rather than the wave amplitudes must be added.



of nuclear binding on the cross-sections except to the extent to which the Pauli principle (and coherent effects) reduce the quasi-elastic scattering at very small angles and give  $\sigma_{qe} \simeq 7$  mb for the quasi-elastic cross-section and 37 mb for the «total» cross-section.

The calculation now proceeds in three steps. First, we evaluate the cross-section  $\sigma_n(A)$  for a high-energy nucleon to undergo  $n$  elastic collisions within a nucleus of mass number  $A$ . Second, we calculate the angular distribution for the outgoing nucleon in the hypothetical case in which the bound nucleons are stationary. Third, we take into account the motion of the bound nucleons and evaluate the energy spectrum of the nucleons scattered at the angle of observation. The effects of the exclusion principle are estimated before, in conclusion, we apply the results to the scattering from nuclei of mass numbers 12 and 189 to obtain a possible comparison with experiment.

## 2. - The plural scattering cross-section.

For the purposes of this section, we shall treat the nucleus as an absorbing medium rather as a collection of discrete scatterers. The complications that the latter more consistent description would entail are not justified. As a matter of fact, the high-energy cross-section of nucleons is such that the nucleon may be thought of as a gray region with radius 1.2 fermi. The nucleus is, therefore, filled about uniformly with this nuclear medium (7).

In terms of the mean-free-paths  $\lambda_e$  and  $\lambda_t$  for elastic and total scattering in the nuclear medium, the probability  $P_n(z)$  that a nucleon suffers  $n$  elastic collisions after traversing a thickness of material  $z$  is

$$(6) \quad P_n(z) = \frac{1}{n!} \left( \frac{z}{\lambda_e} \right)^n \exp[-z/\lambda_t].$$

Since the particle wave-length is small and the deflection and momentum loss in a single scattering are negligible, we calculate the cross-section  $\sigma_n(A)$  for  $n$  elastic collisions in a sphere of radius  $R(A)$  by using geometrical optics and straight rays in the sphere,

$$(7) \quad \sigma_n(A) = \int_0^R 2\pi b db P_n(2\sqrt{R^2 - b^2}) = \frac{\pi \lambda_t^2}{2n!} \left( \frac{\lambda_t}{\lambda_e} \right)^n \int_0^{2R/\lambda_t} x^{n+1} \exp[-x] dx = \\ = \frac{\pi}{2} (n+1) \lambda_t^2 \left( \frac{\sigma_{qe}}{\sigma_{tot}} \right)^n [I_{2R/\lambda_t}(n+2)/I(n+2)].$$

(7) Of course, one must not make the mistake of using our procedure to calculate plural scattering from protons.

The quantity in brackets is obtainable from tables of the incomplete  $\Gamma$ -function<sup>(8)</sup>, where it is denoted by the symbol  $I(2R/\lambda_t, n+1)$ . When numerical values are inserted into eq. (7), we obtain

$$(8) \quad \sigma_n(A) = 54 \left( \frac{\sigma_{qe}}{\sigma_{tot}} \right)^n (n+1) I\left(\frac{2R}{\lambda_t}, n+1\right) \text{ mb.}$$

### 3. - The differential cross-section.

For single quasi-elastic scattering, we write the relative differential cross-section  $r_1(p, \theta)$  at the incident momentum  $p$  and angle  $\theta$

$$(9) \quad r_1(p, \theta) = \frac{1}{\sigma_{qe}} \cdot \frac{d\sigma_{qe}}{d\Omega} = \left( \frac{\sigma_e}{\sigma_{qe}} \right) \cdot \frac{\alpha p^2}{\pi} \exp[-\alpha p^2 \theta^2],$$

where we neglect the effects of the exclusion principle and coherence that become important at momentum transfers  $p\theta \ll p_F = 250 \text{ MeV}/c$ . The angular distribution of double scattering is then given by the integral

$$(10) \quad r_2(p, \theta) = \frac{1}{2\pi} \int r_1(p, \theta) r_1(p, \theta_2) d \cos \theta_1 d \cos \theta_2 \cdot \\ \cdot d\varphi_1 d\varphi_2 \delta(\cos \theta - \cos \theta_1 \cos \theta_2 - \sin \theta_1 \sin \theta_2 \cos(\varphi_1 - \varphi_2)),$$

since the energy loss in each collision is so small that the decrease in incident momentum may be neglected. After the azimuthal integrations are carried out, it is helpful to approximate the trigonometric functions by their small-angle expansions to second order and to extend the range of integration to infinity. The angular distribution function now becomes

$$(11) \quad r_2(p, \theta) = \left( \frac{\sigma_e}{\sigma_{qe}} \right) \int_0^\infty d(\theta_1^2) \int_0^\infty d(\theta_2^2) \left( \frac{\alpha p^2}{\pi} \right)^2 \exp[-\alpha p^2 (\theta_1^2 + \theta_2^2)] \cdot \\ \cdot \frac{\Theta(4\theta_1^2\theta_2^2 - (\theta - \theta_1^2 - \theta_2^2)^2)}{\sqrt{4\theta_1^2\theta_2^2 - (\theta - \theta_1^2 - \theta_2^2)^2}}.$$

The main contribution comes from the smallest values of  $\theta_1^2 + \theta_2^2 \simeq \frac{1}{2}\theta^2$  permitted by the step function  $\Theta$ . An exact evaluation of the integral is possible because of the form we have chosen for the angular dependence. All the integrals can

<sup>(8)</sup> K. PEARSON: *Tables of the Incomplete  $\Gamma$ -Function* (London, 1922).

be found with the help of the integral formula

$$(12) \quad \int_0^\infty dx_1 \int_0^\infty dx_2 f\left(\frac{x_1}{a_1} + \frac{x_2}{a_2}\right) \left\{ \frac{\Theta(4x_1x_2 - (y - x_1 - x_2)^2)}{\sqrt{4x_1x_2 - (y - x_1 - x_2)^2}} \right\} - \frac{\pi a_1 a_2}{a_1 + a_2} \int_{y/(a_1+a_2)}^\infty dz f(z) .$$

By the use of this formula we obtain from eq. (11) the result

$$(13) \quad r_2(p, \theta) = \left(\frac{\sigma_e}{\sigma_{qe}}\right)^2 \frac{\alpha p^2}{2\pi} \exp[-\alpha p^2 \theta^2 / 2] .$$

The obvious iteration of this expression according to eq. (10) leads to the further values

$$(14) \quad r_n(p, \theta) = \left(\frac{\sigma_e}{\sigma_{qe}}\right)^n \frac{\alpha p^2}{n\pi} \exp[-\alpha p^2 \theta^2 / n] .$$

for  $n$  fold scattering. We must remember, however, that the effects of the exclusion principle become more severe, since the higher order scattering depends on contributions from smaller and smaller angles. Hence  $n$  should not exceed  $\sim p\theta/p_F$ .

The differential cross-section for plural scattering is

$$(15) \quad \frac{d\sigma_n(A)}{d\Omega} = \sigma_n(A) r_n(p, \theta) .$$

By comparing eqs. (9) and (13), we see that double scattering becomes comparable to single scattering when

$$(16) \quad \frac{1}{2} \left(\frac{\sigma_{qe}}{\sigma_{tot}}\right) \exp[\alpha p^2 \theta^2 / 2] \sim 1 \quad \text{or} \quad p\theta \sim 0.8M ,$$

a value of momentum transfer within the range of the recent experiments. We see that the quasi-elastic cross-section  $\sigma_{qe}$  cancels in eq. (15); obviously, when the exclusion principle can be ignored, the free elastic cross-section determines the relative contributions. Further numerical conclusions are postponed until the final section of the paper.

#### 4. - The energy spectrum - single scattering.

The spectrum of quasi-elastically scattered nucleons is not mono-energetic because of the motion of the bound nucleons. This effect gives to the secon-

dary nucleons at the angle  $\theta$  a momentum distribution of a width

$$\sim \frac{p\theta}{M} \cdot p_F,$$

as we shall show below. The centre of this spectrum is displaced by a negligible amount from the secondary momentum  $p'_0$  resulting in free nucleon-nucleon collisions at small angles

$$(17) \quad p'_0 \simeq p - \frac{p^2 \theta^2}{2M}.$$

The plural scattering we have described also affects the spectrum of the nucleons scattered at an angle  $\theta$ , because the momentum loss  $\Delta p(\theta)$  depends on the scattering angle in each of the quasi-elastic processes that took place. By using eq. (17) several times, we obtain

$$(18) \quad \Delta p(\theta) = \frac{p^2}{2M} \sum_{i=1}^n \theta_i^2 \sim \frac{p^2}{2M} \frac{\theta^2}{n}.$$

according to the properties of the plural scattering noted after eq. (11). As expected the momentum loss for plural scattering is smaller than for single quasi-elastic scattering, and corresponds approximately to that evaluated for scattering from a more massive target with mass  $\sim nM$ .

It is now our task to combine the two effects we have described. First, we obtain the energy spectrum of single quasi-elastic scattering. Accordingly, we consider the scattering of two nucleons with energy-momentum vectors  $(\mathbf{p}_1, E_1)$  and  $(\mathbf{p}_2, E_2)$  into a final state with  $(\mathbf{p}'_1, E'_1)$  and  $(\mathbf{p}'_2, E'_2)$ . We use the invariant form for the differential scattering rate <sup>(9)</sup>

$$(19) \quad B_0(s) d\sigma = |I(s, t)|^2 \cdot \frac{d^3 p'_1}{E'_1} \frac{d^3 p'_2}{E'_2} \delta(\mathbf{p}'_1 + \mathbf{p}'_2 - \mathbf{p}_1 - \mathbf{p}_2) \delta(E'_1 + E'_2 - E_1 - E_2),$$

where  $s$  is the mass invariant of the two-particle system

$$(20) \quad s = (E_1 + E_2)^2 - (\mathbf{p}_1 + \mathbf{p}_2)^2.$$

$t$  is the invariant momentum transfer squared,

$$(21) \quad t = -(E'_1 - E_1)^2 + (\mathbf{p}'_1 - \mathbf{p}_1)^2,$$

<sup>(9)</sup> C. MØLLER: *Kgl. Dan. Vid. Selskab.*, **22**, no. 19 (1946).

$B_0(s)$  is the invariant flux,

$$(22) \quad B_0(s) = \frac{1}{2} \sqrt{s(s - 4M^2)},$$

and  $I(s, t)$  is the invariant matrix element of the interaction. The assumed form eq. (3) implies that

$$(23) \quad |I(s, t)|^2 = \frac{1}{4\pi} s(s - 4M^2) \alpha \sigma_e \exp[-\alpha t],$$

at high energy and small angles. For the nucleus, the target momenta must be averaged over the distribution  $P(\mathbf{p}_2)$  given in eq. (2). We then obtain the differential cross-section for quasi-elastic scattering

$$(24) \quad \frac{d^2\sigma}{dp'_1 d\Omega'_1} = \frac{1}{B_0} \frac{p'_1}{E'_1} \int \frac{d^3p_2}{E'_2} |I(s, t)|^2 P(\mathbf{p}_2) \delta(E'_1 + E'_2 - E_1 - E_2),$$

which neglects the effects of the exclusion principle. The momentum  $\mathbf{p}'_2$  is to be expressed by means of the other three momenta,  $\mathbf{p}'_2 = \mathbf{p}_1 + \mathbf{p}_2 - \mathbf{p}'_1$ . In carrying out the evaluation of eq. (24), it is wise to make approximations based on the high-incident energy, the small scattering angles, and the non-relativistic nature of the target nucleons where possible. The errors are characteristically of the order of  $M/E_1$ , or smaller. Thus we have <sup>(10)</sup>

$$(25) \quad \left\{ \begin{array}{l} E_1 \simeq E'_1 \simeq p_1 \simeq p'_1, \quad s \simeq 2Mp_1, \quad t \simeq p_1^2 \theta^2, \\ B_0 \simeq Mp_1, \\ |I(s, t)|^2 \simeq \frac{1}{\pi} M^2 p_1^2 \alpha \sigma_e \exp[-\alpha p_1^2 \theta^2], \\ |\mathbf{p}_1 - \mathbf{p}'_1| \simeq p_1^2 \theta^2 + (p_1 - p'_1)^2. \end{array} \right.$$

It is useful to define the momentum loss

$$(26) \quad \Delta p = p_1 - p'_1 \simeq p_1^2 \theta^2 / 2M,$$

which is an experimentally controlled variable.

<sup>(10)</sup> In making these approximations, we neglect a small Doppler shift in the momentum-loss spectrum. This small effect comes from the dependence of  $|I(s, t)|^2$  on the momentum-loss and is of the order of  $\epsilon$ .



We now proceed to carry out the average over the Fermi momentum. The energy conserving  $\delta$ -function, of course, selects certain values of  $\mathbf{p}_2$  that make possible a particular outgoing momentum  $p'_1$ . If we introduce a co-ordinate system with the  $z$ -axis along  $\mathbf{p}_1 - \mathbf{p}'_1$ , then we find  $p_{2z}$  is fixed,

$$(27) \quad p_{2z} \simeq \frac{-\frac{1}{2}p_1^2\theta^2 + M\Delta p}{\sqrt{p_1^2\theta^2 + (\Delta p)^2}},$$

but the other two components of  $\mathbf{p}_2$  are arbitrary. The integral over  $p_{2z}$  is

$$(28) \quad \frac{1}{E'_2} \int dp_{2z} \delta(E'_1 + E'_2 - E_1 - E_2) = \frac{2}{\partial(E'_2)^2 / \partial p_{2z}} = \\ = \frac{1}{p_1 - p'_1} \simeq \frac{1}{\sqrt{p_1^2\theta^2 + (\Delta p)^2}} \approx \frac{1}{p_1\theta}.$$

We shall make an approximation in eq. (27) and (28) by neglecting  $(\Delta p)^2$  compared to  $(p_1\theta)^2$ ,

$$(27') \quad p_{2z} \approx -\frac{1}{2}p_1\theta + \frac{M\Delta p}{p_1\theta}.$$

This depends on the fact that  $\Delta p, p_1\theta \sim p_1\theta/2M < \frac{1}{2}$  in the range of interest. Eq. (27') gives a much more manageable result than eq. (27). The remaining integrations can be carried out with no difficulty to yield a shape function  $G(\Delta p, p\theta)$

$$(29) \quad G(\Delta p, p_1\theta) = \frac{M}{p_1\theta} \int [P(\mathbf{p}_2)]_{p_{2z} = -\frac{1}{2}p_1\theta + M\Delta p/p_1\theta} dp_{2x} dp_{2y} \simeq \\ \simeq \frac{M}{p_1\theta} \frac{\Theta(\Delta p)}{\sqrt{2\pi\epsilon}M} \exp \left[ -\frac{M}{2\epsilon p_1^2\theta^2} \left( \Delta p - \frac{p_1^2\theta^2}{2M} \right)^2 \right].$$

The differential cross-section for quasi-elastic scattering with momentum loss  $\Delta p$  is, therefore,

$$(30) \quad \frac{d^2\sigma_{qe}}{d\Delta p d\Omega'_1} \simeq \frac{\alpha p_1^2 \sigma_e}{\pi} G(\Delta p, p_1\theta) \exp[-\alpha p_1^2\theta^2].$$

As expected, the most likely momentum loss is  $p_1^2\theta^2/2M$ , the value for scattering on free nucleons. The half width of the secondary momentum distribution is  $(p_1\theta/M) \sqrt{2\epsilon M}$ .

### 5. - The energy spectrum - plural scattering.

We repeat now the discussion of Section 2 with the differential cross-section eq. (30) rather than with the free cross-section eq. (3) for the elementary process. We again introduce a relative cross-section

$$(31) \quad r_1(\Delta p, p_1\theta) = \frac{1}{\sigma_{qe}} \frac{d^2\sigma_{qe}}{d\Delta p d\Omega},$$

which is iterated according to the relation

$$(32) \quad r_n(\Delta p, p_1\theta) = \frac{1}{2\pi} \int r_1(\Delta p_1, \theta p_1) r_{n-1}(\Delta p - \Delta p_1, p\theta_2) \cdot \\ \cdot d\cos\theta_1 d\cos\theta_2 d\varphi_1 d\varphi_2 d(\Delta p_1) \delta(\cos\theta - \cos\theta_1 \cos\theta_2 - \sin\theta_1 \sin\theta_2 \cos(\varphi_1 - \varphi_2)),$$

analogous to eq. (10). We extend the range of the  $\Delta p$  integration over the entire real axis. Then we can use the simple property of Gaussian distributions that

$$(33) \quad \int_{-\infty}^{\infty} d(\Delta p_1) G(\Delta p_1, p\theta_1) G(\Delta p - \Delta p_1, p\theta_2) = G(\Delta p, p\sqrt{\theta_1^2 + \theta_2^2}).$$

With the use of the formula (12), the double scattering relative cross-section  $r_2$  can now be written as a single integral over the variable  $u = \alpha p^2(\theta_1^2 + \theta_2^2)$ ,

$$(34a) \quad r_2(\Delta p, p_1\theta) = \frac{\alpha p^2}{2\pi} \left( \frac{\sigma_e}{\sigma_{qe}} \right)^2 \int_{\alpha p^2 \theta^2 / 2}^{\infty} du \exp[-u] G\left(\Delta p, \sqrt{\frac{u}{\alpha}}\right),$$

$$(34b) \quad = \frac{\alpha p^2}{2\pi} \left( \frac{\sigma_e}{\sigma_{qe}} \right)^2 \exp[-\alpha p^2 \theta^2 / 2] \int_0^{\infty} du' \exp[-u'] G\left(\Delta p, \sqrt{\frac{u'}{\alpha} + \frac{p^2 \theta^2}{2}}\right).$$

The integral in eq. (34b) is shown in Fig. 1 as function of  $\Delta p$  for some values of momentum transfer  $p\theta$ . It is seen that the most likely momentum loss is about two-thirds of the value of the momentum loss in nucleon-nucleon scattering. By iteration one can again obtain the formula for  $n$  fold scattering.

$$(35) \quad r_n(\Delta p, p\theta) = \frac{\alpha p^2}{n\pi} \left( \frac{\sigma_e}{\sigma_{qe}} \right)^n \frac{1}{(n-2)!} \int_{\alpha p^2 \theta^2 / n}^{\infty} du \exp[-u] G\left(\Delta p, \sqrt{\frac{u}{\alpha}}\right) \left(u - \frac{\alpha p^2 \theta^2}{n}\right)^{n-2}, \\ (n \geq 2),$$

but again it is not very meaningful for large  $n$  because the neglected exclusion principle severely affects the cross-section at the small momentum transfers



Fig. 1. - The momentum-loss spectrum (normalized) in double scattering. The exclusion principle has not been taken into account.

and momentum losses that contribute heavily. After integration over  $\Delta p$ , eq. (35) reduces to eq. (14).

## 6. - The exclusion principle.

We have referred already several times to the fact that the exclusion principle reduces the cross-section for quasi-elastic scattering at extremely small angles. In this section we shall attempt to reach an estimate of the effect without, however, pretending to make a complete, consistent theory of the « one-particle states » in a nucleus.

First, we may ask for the reduction in the elastic cross-section and the plural scattering angular distribution. To this end we make a Gaussian ap-

proximation to the average fraction  $f$  of states not available to a nucleon in a degenerate Fermi distribution (rather than the distribution (2)) when this nucleon receives an impulse,  $p\theta$ ,

$$(36) \quad f = \left(1 - \frac{p\theta}{2p_F}\right)^2 \left(1 + \frac{1}{4} \frac{p\theta}{p_F}\right) \approx \exp \left[ -1.25 \frac{p^2 \theta^2}{p_F^2} \right] \exp \left[ -\frac{5}{2} \alpha p^2 \theta^2 \right].$$

The quasi-elastic differential cross-section then becomes

$$(37) \quad r'_1 = \frac{\alpha p^2}{\pi} \left( \frac{\sigma_e}{\sigma_{qe}} \right) \exp[-\alpha p^2 \theta^2] \left( 1 - \exp \left[ -\frac{5}{2} \alpha p^2 \theta^2 \right] \right),$$

whose integral determines  $\sigma_{qe}$ ,

$$(38) \quad \sigma_{qe} = \frac{5}{7} \sigma_e \simeq 7 \text{ mb},$$

as stated earlier. We see also that scattering at angles such that  $p\theta \simeq 2p_F$  is only slightly reduced. The Gaussian form of the correction makes it possible to calculate the modified  $r'_n(p, \theta)$  by repeated use of eq. (12). Thus we have

$$(39) \quad r'_2(p, \theta) = \frac{\alpha p^2}{2\pi} \left( \frac{\sigma_e}{\sigma_{qe}} \right)^2 \exp \left[ -\frac{1}{2} \alpha p^2 \theta^2 \right] \cdot (1 - 0.89 \exp[-0.278 \alpha p^2 \theta^2] + 0.28 \exp[-1.25 \alpha p^2 \theta^2]),$$

$$(40) \quad r'_3(p, \theta) = \frac{\alpha p^2}{3\pi} \left( \frac{\sigma_e}{\sigma_{qe}} \right)^3 \exp \left[ -\frac{1}{3} \alpha p^2 \theta^2 \right] \cdot (1 - 1.125 \exp[-0.104 \alpha p^2 \theta^2] + 0.468 \exp[-0.303 \alpha p^2 \theta^2] - 0.082 \exp[-0.833 \alpha p^2 \theta^2]), \text{ etc.}$$

We see here the transition from the larger angle plural scattering described by eq. (15), which is determined by the free elastic cross-section, to the plural scattering at smaller angles, whose magnitude is essentially determined by the quasi-elastic cross-section. Thus we have

$$(41) \quad \frac{r'_n}{r_n} \simeq \left( \frac{\sigma_{qe}}{\sigma_e} \right)^n, \quad \text{for } n = \frac{p\theta}{p_F},$$

while the exclusion effects are small for  $n \ll p\theta/2p_F$ . Because of the crudeness of our one-parameter model, one must not push the use of eq. (39) and (40) to very small angles. It seems reasonable to go as far as is done in eq. (41).

More difficult to determine is the modification in the momentum spectrum. We may proceed as above with a degenerate Fermi distribution and calcu-

late a modified spectral function from eq. (29) with a correction factor for the occupied states. Rather than trying to find a usable analytic form for this function, we shall take advantage of the fact that the width of the secondary spectrum becomes very small for small momentum transfer. The changes in the shape of this narrow spectrum are relatively less important than the reduction in its amplitude, a reduction that can be represented by the factor calculated in eq. (36). We therefore introduce the new function

$$(42) \quad G'(\Delta p, p\theta) = G(\Delta p, p\theta)(1 - \exp[-\frac{5}{2}\alpha p^2\theta^2])$$

which is to be used instead of  $G$  in the plural scattering calculation. The relative differential cross-sections then become

$$(43) \quad r'_1(\Delta p, p, \theta) = \frac{\alpha p^2}{\pi} \left( \frac{\sigma_e}{\sigma_{qe}} \right) G(\Delta p, p\theta) \exp[-\alpha p^2\theta^2] (1 - \exp[-\frac{5}{2}\alpha p^2\theta^2]),$$

$$(44) \quad r'_2(\Delta p, p, \theta) = \frac{\alpha p^2}{2\pi} \left( \frac{\sigma_e}{\sigma_{qe}} \right)^2 \int_{\frac{1}{2}\sqrt{p^2\theta^2}}^{\infty} du G\left(\Delta p, \sqrt{\frac{u}{\alpha}}\right) \cdot \\ \cdot \left\{ \exp[-u] + \exp\left[-\frac{7}{2}u\right] - 2 \exp\left[-\frac{9}{4}u\right] I_0\left(\frac{5}{2}\right) \frac{\alpha p^2\theta^2}{2} \left(u - \frac{\alpha p^2\theta^2}{2}\right) \right\}.$$

and similar, more complicated expressions for the higher orders. The expression (44) has the reasonable properties that almost the entire spectrum is reduced in scale for severely affected scattering conditions ( $p\theta/p_F \sim 2$ ), while for larger momentum transfer there is a suppression of the spectrum near  $\Delta p \sim p^2\theta^2/2M$ , the momentum loss suffered in single collisions. Our naive model does not justify a more detailed investigation of the modifications in the spectrum.

## 7. - Conclusions.

We begin this section by collecting the results of our calculation for the quasi-elastic plural scattering cross-sections. The angular distributions are eq. (7), (37), (39) and (40)

$$(45) \quad \frac{d\sigma_{qe}^{(n)}}{d\Omega} = \sigma_n(A) r'_n(p, \theta),$$

while the distribution in angle and momentum loss  $\Delta p$  is given by eq. (7),



(43) and (44),

$$(46) \quad \frac{d^2\sigma_{qe}^{(n)}}{d\Delta p d\Omega} = \sigma_n(A) r_n'(\Delta p, p, \theta) .$$

For numerical evaluation, we tabulate  $\sigma_n(A)$  for two mass numbers (12, 189) in Table I and  $(M^2/p^2)r_n'(p, \theta)$ , which depends only on  $p\theta$ , for several values

TABLE I. — *The plural scattering cross-sections.*

A	12	189
$\sigma_1$	11.2 mb	19.8 mb
$\sigma_2$	1.92	5.40
$\sigma_3$	0.248	1.24
$\sigma_4$	—	0.25

of this argument, in Table II. The predicted angular distributions based on these values are shown in Fig. 2 and 3 for the two cases. As expected, there is a range of momentum transfer from 0.75 GeV/c to 1.5 GeV/c in which plural scattering dominates over single quasi-elastic scattering. At smaller momentum transfer the Pauli principle and the greater normalization of the single scattering make the plural scattering relatively less likely. At larger momentum transfers the nucleon-nucleon cross-section no longer decreases so rapidly and eventually remains larger than the still decreasing plural scattering cross-sections. The overall effect on the angular distribution is to broaden it compared to the nucleon-nucleon cross-section, as though

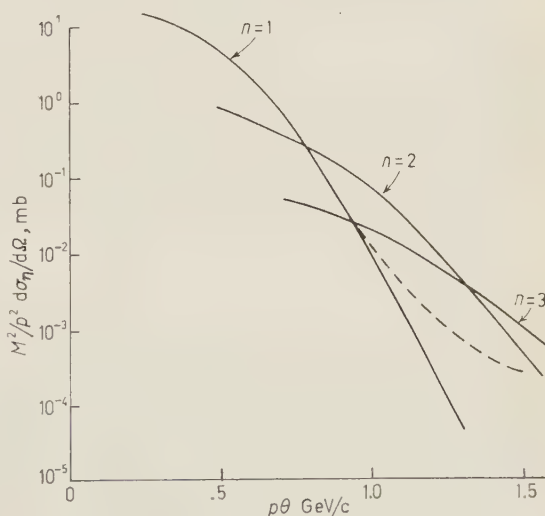


Fig. 2. — The angular distribution for plural quasi-elastic scattering from carbon. The dashed part of the curve for  $n=1$  is based on the measured p-p cross-section (4) rather than on our fit eq. (3).

TABLE II. — *The relative angular distributions for plural scattering.*

$p\theta =$	.25	.50	.75	1.00	1.25	1.50 GeV/c
$(M^2/p^2)r'_1$	1.39	0.436	0.0347	0.00104	$1.15 \cdot 10^{-5}$	
$(M^2/p^2)r'_2$	—	0.436	0.177	$3.79 \cdot 10^{-2}$	$4.2 \cdot 10^{-3}$	$2.8 \cdot 10^{-4}$
$(M^2/p^2)r'_3$	—	—	0.20	0.083	$2.4 \cdot 10^{-2}$	$4.5 \cdot 10^{-3}$

the bound nucleons were « smaller » scatterers than the free nucleons. A rough Gaussian fit of the form

$$(47) \quad \exp[-\alpha' p^2 \theta^2]$$

is obtained with  $\alpha' \simeq 5/M^2$ . From Fig. 2 we can also see that the carbon cross-section will be about of an order of magnitude greater than the hydrogen

cross-section for  $p\theta \sim 1$  GeV/c (plural scattering), but will exceed it only by a factor of 2 at small momentum transfer (single quasi-elastic scattering).

The momentum-loss spectra are capable of giving more convincing evidence for the occurrence of plural scattering. As we have seen, the mean energy loss depends on the number of collisions. If we expect that the spectra from single and plural collisions are not resolved, we predict an observed mean momentum loss that is a weighted average of the momentum losses of the various processes. This quantity  $\langle \Delta p \rangle_A$  for the nuclei with  $A=12$  and 189 is plotted in Fig. 4. The experimental points are also

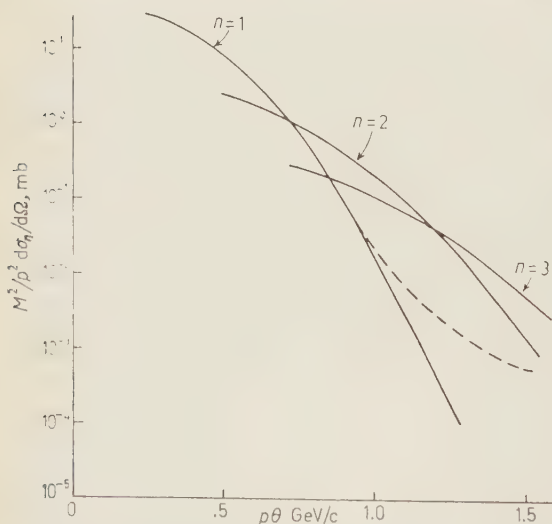


Fig. 3. — The angular distribution for plural quasi-elastic scattering from a heavy nucleus ( $A=189$ ). The dashed part of the curve for  $n=1$  is based on the measured p-p cross-section<sup>(4)</sup> rather than on our fit eq. (3).

indicated. We consider the agreement satisfactory. Whether triple collisions also contribute to scattering from carbon is not clear. Blind acceptance of

the results of our calculation would suggest that they do. Still, carbon is such a small nucleus that treating it as a « medium », as we have done, is not a very accurate procedure.

In larger nuclei, triple collisions are likely to play a role at momentum transfers from 1.3 to 1.7 GeV/c, and will broaden the momentum-loss spectrum. When our considerations are applied to the deuteron, then it turns out that single and double collisions with total momentum transfer of 1 GeV/c are about equally likely, if the density parameter is chosen so as to give the correct « shadowing »<sup>(6)</sup>. Because of the smaller momenta of the target nucleons, one expects to observe two well-resolved maxima at  $\Delta p = p^2\theta^2/2M$  and at  $\Delta p = p^2\theta^2/4M$  in the momentum-loss spectrum.

Finally, we shall point out that the study of quasi-elastic collisions up to momentum transfers of about 2 GeV/c cannot give as direct information about the elementary nucleon-nucleon cross-section as one might have hoped.

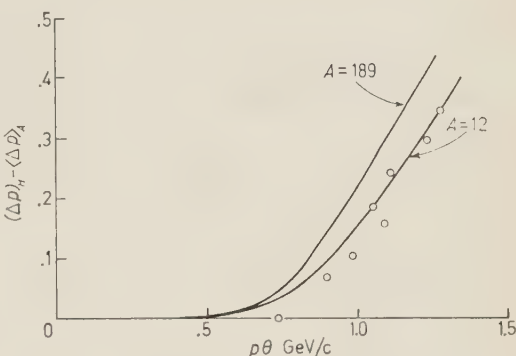


Fig. 4. — The mean momentum loss for nuclear scattering compared with the momentum loss in p-p scattering at the same incident energy and scattering angle. For  $A=12$ , single and double scattering have been used, for  $A=189$ , single, double and triple scattering have been used. The circles represent the measurements<sup>(4)</sup> but do not indicate probable errors.

\*\*\*

We are grateful to Drs. DIDDENS, LILLETHUN, MANNING, TAYLOR, WALKER and WHETHERELL for making available their results before publication and for stimulating conversations. We have enjoyed the hospitality of CERN, and numerous discussions with members of the Theoretical Division.

#### RIASSUNTO (\*)

La distribuzione angolare dello scattering nucleone-nucleone alle alte energie è fortemente accentuata in avanti. Per conseguenza, nello scattering nucleone-nucleo, esiste un intervallo angolare al quale è molto più probabile che contribuiscano successivi scattering elastici nucleone-nucleone legato di piccola apertura anziché un solo scattering nucleone-nucleone legato di apertura uguale all'angolo di osservazione. Una tale collisione « plurale » produce nucleoni uscenti che sono dispersi dall'idrogeno secondo lo stesso angolo. Il moto di Fermi dei nucleoni legati è causa di un allargamento della distribuzione di energia dei nucleoni sparpagliati, ma sposta solo trascurabilmente il centro della distribuzione. I risultati dei calcoli con un semplice modello sono in soddisfacente accordo con le osservazioni sullo scattering protone-carbonio.

(\*) Traduzione a cura della Redazione.

## Some Consequences of Spin $\frac{3}{2}$ for $\Xi$ .

ALLADI RAMAKRISHNAN, G. BHAMATHI (\*), S. INDUMATHI (\*\*),  
T. K. RADHA (\*\*\*) and R. THUNGA (\*\*\*)

*Department of Theoretical Physics, University of Madras - Madras*

(ricevuto il 24 Agosto 1961)

**Summary.** — Consequences of the assignment of spin  $\frac{3}{2}$  for the cascade are investigated. The  $\Xi$ -p and  $\bar{\Xi}$ -p interactions are analysed for both even and odd  $\Xi$ -N parity. The binding energies of double hyperfragments by the capture of  $\Xi$  by nuclei are also calculated. The decay systematics of the  $\Xi$  is also given.

It is normally assumed that all the baryons have spin  $\frac{1}{2}$  but the possibility of  $\Xi$  having spin  $\frac{3}{2}$  is not ruled out. There is no clear cut experimental evidence for spin  $\frac{1}{2}$  for  $\Xi$  unlike in the case of  $\Lambda$  and  $\Sigma$ . We wish to investigate some of the consequences of the assignment of spin  $\frac{3}{2}$  for  $\Xi$  in strong and weak interactions. We expect these considerations to become relevant when more data on  $\Xi$ -particles will be available. If this assignment proves to be true it is quite probable that  $\Xi$  is not elementary.

### 1. — Consider the reaction

$$\Xi + p \rightarrow \Lambda + \Lambda.$$

This interaction has been analysed in great detail <sup>(1)</sup> for the case of spin  $\frac{1}{2}$  for  $\Xi$ . For spin  $\frac{3}{2}$  the allowed final states are respectively  $^3P_1$  and  $^1D_2$  for odd and even  $\Xi$ -N parity for initial S-state.

(\*) Council of Scientific and Industrial Research (Junior) Research Fellow.

(\*\*) University Grants Commission (Junior) Research Fellow.

(\*\*\*) Atomic Energy Commission (Junior) Research Fellow.

(1) S. B. TREIMAN: *Phys. Rev.*, **113**, 355 (1959); see also L. B. OKUN and YA. POME-RANCHUK: *Soviet Physics J.E.T.P.*, **7**, 862 (1959).

It is quite reasonable to assume an initial  $S$ -state for  $\Xi^-p$  as the interaction is subsequent to the stopping of  $\Xi$  in the hydrogen bubble chamber. If in the final state we rule out all orbital angular momenta higher than  $l = 1$ , we see that in the case of even parity this reaction cannot occur. Of course, the initial state should have  $l = 0$  and this suggests the possibility of a bound system of  $\Xi^-p$  corresponding to the deuteron in a metastable state since it has no allowed final state into which it can decay. But it can decay by the emission of a hard  $\gamma$ -ray, *i.e.*

$$\Xi^- + p \rightarrow \Lambda + \Lambda + \gamma.$$

It is also possible that  $\Xi^0$  is heavier than  $\Xi^-$  in which case the charge exchange reaction will have a threshold, while of course, the  $\Lambda$ - $\Lambda$  system has no threshold. We thus expect a cusp in the production cross-section at about 9 MeV. The angular distribution of the  $\Lambda$ - $\Lambda$  system at the  $\Xi^0n$  threshold will fix the relative  $\Xi\Lambda$  parity. To determine the exact behaviour of the cross-section and polarization at the cusp we require the matrix elements for the processes

$$\Xi^- + p \rightarrow \Xi^0 + n$$

and

$$\Lambda + \Lambda \rightarrow \Xi^0 + n$$

which of course are not known. In the case of odd  $\Xi\Lambda$  parity we cannot distinguish between spin  $\frac{1}{2}$  and  $\frac{3}{2}$  as the cusps in both cases involve mainly an interference of  $^3S_1$  and  $^3P_1$ . On the other hand if the  $\Xi\Lambda$  parity is even we have to allow  $D$ -waves also and an unambiguous analysis becomes complicated. The main point is that the existence of the cusp fixes the sign of the mass difference of  $\Xi^-$  and  $\Xi^0$ .

2. — BARSHAY <sup>(2)</sup> has considered

$$\Xi^+ + p \rightarrow K^+ + K^+$$

for spin  $\frac{1}{2}$  of  $\Xi$ . Extending this to the case of spin  $\frac{3}{2}$  we find that the angular distribution of the final pair of bosons is sensitive to the spin as well as the relative  $\Xi\Lambda$  parity. As before, restricting the initial state to  $S$ -waves only we find from Table I that the reaction occurs only for odd parity and a final isotropic distribution does not distinguish between spin  $\frac{1}{2}$  and  $\frac{3}{2}$ .

<sup>(2)</sup> S. BARSHAY: *Phys. Rev.*, **120**, 265 (1960).



TABLE I. — Possible transitions and angular distributions for  $\Xi^+ + p \rightarrow K^+ + K^+$ .

Spin	Relative $\Xi$ -p parity	Initial state	Final orbital ang. momentum	Amplitude for transition	Centre-of-mass angular distribution ( $x = \cos \theta$ )
$\frac{1}{2}$	---	$^1S_0$	0	$A$	1
		$^1D_2$	2	$B$	$1 - 6x^2 + 9x^4$
		$^3D_2$	2	$C$	$x^2 - x^4$
		$^3P_0$	0	$A''$	1
		$^3P_2$	2	$B''$	$1 + 3x^2$
$\frac{3}{2}$	---	$^3S_2$	2	$A'$	1
		$^3D_0$	0	$B'$	1
		$^3D_2$	2	$C'$	$x^2 - x^4$
		$^5D_2$	2	$D'$	$4 - 9x^2 + 9x^4$
		$^5D_4$	4	$E'$	$45x^4 - 10x^2 + 13$
	+	$^3P_0$	0	$A''$	1
		$^3P_2$	2	$B''$	$1 + 3x^2$
		$^5P_2$	2	$C''$	$1 - x^2$

If we allow  $P$ -states (for even parity) the distribution has the form

$$F(x) = a' + b'x^2,$$

where

$$a' = 18|A|^2 + |B|^2 + 3|C|^2 + 6\sqrt{2} \operatorname{Re} A^*B,$$

$$b' = 3|B|^2 - 3|C|^2 - 18\sqrt{2} \operatorname{Re} A^*B.$$

It is to be noted that the coefficients  $a'$  and  $b'$  are distinct from  $a$  and  $b$  of spin half distribution. Including  $D$ -waves also in the initial state the distribution (for odd parity) when  $^3S_2$ ,  $^3D_0$ ,  $^3D_2$ ,  $^5D_2$  and  $^5D_4$  participate is found to be quite different from that corresponding to spin  $\frac{1}{2}$ . For spin  $\frac{3}{2}$  we have

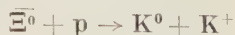
$$F(x) = c' + d'x^2 + e'x^4 + f'x^6$$

while for spin  $\frac{1}{2}$

$$F(x) = c + dx^2 + ex^4.$$

The  $x^6$ -dependence in  $F(x)$  for spin  $\frac{3}{2}$  arises mainly because of the  $^5D_1 \rightarrow ^1G_4$  reaction.

If we consider the reaction



since there is no restriction on the final state orbital angular momentum to be even, from the angular distribution it is possible to distinguish between spin  $\frac{3}{2}$  and  $\frac{1}{2}$  for  $\Xi$  with initial  $S$  and  $P$  waves.

3. — It is well known that  $\Xi$ -capture in nuclei can lead to double hyperfragments. Assuming spin  $\frac{1}{2}$  for  $\Xi$  a detailed analysis of the binding energies of double hyperfragments where the two  $\Lambda$ 's form a single  $S$ -state has been calculated by IWAO <sup>(3)</sup>. When  $\Xi$  has spin  $\frac{3}{2}$  the  $\Lambda$ 's will be in a relative  $P$  or  $D$ -state depending on the odd or even  $\Xi N$  relative parity. It is unlikely that bound light hypernuclei occur with a  $\Lambda$  in a  $D$ -state. We shall therefore consider only the case of  $\Xi N$  odd parity. The  $\Xi$  is assumed to be captured from rest and the excess energy released in the process  $\Xi^- + p \rightarrow \Lambda + \Lambda$  will be shared by all the nucleons present. Under these assumptions the binding energies of the double hyperfragments are given below in Table II.

TABLE II. — *Binding energies for double hyperfragments.*

System	Binding energies in MeV	
	parallel spin favoured	antiparallel spin favoured
$\Lambda\Lambda n, {}^3\text{H}_{\Lambda\Lambda}$	— 12.54	— 10.13
$\Lambda\Lambda nn$	— 8.51	— 8.9
${}^4\text{H}_{\Lambda\Lambda}$	— 9.66	— 6.4
${}^5\text{H}_{\Lambda\Lambda}$	— 8.03	— 6.69
${}^6\text{He}_{\Lambda\Lambda}$	— 1.03	— 1.77
${}^6\text{H}_{\Lambda\Lambda}$	— 1.55	+ 2.82
${}^7\text{He}_{\Lambda\Lambda}, {}^7\text{Li}_{\Lambda\Lambda}$	2.39	4.10
${}^8\text{He}_{\Lambda\Lambda}, {}^8\text{Be}_{\Lambda\Lambda}$	6.47	5.3

The correlation between the charged pions arising from the decay of the 2  $\Lambda$ 's can be calculated using the density matrix in the combined spin space of the 2  $\Lambda$ 's. It is well known that the density matrix <sup>(4)</sup> for the final state is given by

$$\varrho_f = \frac{T\varrho_i T^\dagger}{\text{Tr}(T\varrho_i T^\dagger)},$$

where  $\varrho_i$  is the density matrix of the initial state and  $T$  is the transition operator. Since we have assumed spin  $\frac{3}{2}$  for  $\Xi$  the basic matrices are  $4 \times 4$  and

<sup>(3)</sup> S. IWAO: preprint.

<sup>(4)</sup> L. WOLFENSTEIN: *Ann. Rev. Nucl. Sci.*, **6**, 46 (1956).

we can conveniently choose the sixteen linearly independent  $\gamma$  matrices as our base. The density matrix will be given by

$$\varrho_i = \sum_{\mu} \frac{S_{\mu}^i S_{\mu}^i}{(2 \cdot \frac{3}{2} + 1)(2 \cdot \frac{1}{2} + 1)} = \sum_{\mu} \frac{S_{\mu}^i S_{\mu}^i}{8},$$

where  $S_{\mu}^i$  is the direct product  $S^i \cdot \sigma$ ,  $S^i$  and  $\sigma$  being the corresponding matrices for spin  $\frac{3}{2}$  and  $\frac{1}{2}$  respectively.

The distribution in angle of the pion is given by

$$P(\boldsymbol{\sigma}) d\Omega = (1 + \alpha \boldsymbol{\sigma} \cdot \mathbf{p}) d\Omega,$$

where  $\alpha$  is the asymmetry parameter and  $\mathbf{p}$ , the unit vector in the direction of the pion in the  $\Lambda$  rest frame. In the present case the joint distribution of the two pions is

$$P(\boldsymbol{\sigma}_1, \boldsymbol{\sigma}_2) d\Omega_1 d\Omega_2 = (1 + \alpha \boldsymbol{\sigma}_1 \cdot \mathbf{p}_1)(1 + \alpha \boldsymbol{\sigma}_2 \cdot \mathbf{p}_2).$$

The distribution function in pion angles is

$$P(\theta_1, \theta_2) = \frac{\text{Tr } \varrho_i P(\boldsymbol{\sigma}_1, \boldsymbol{\sigma}_2)}{\text{Tr } \varrho_i} = \frac{\text{Tr } [T \varrho_i T^\dagger P(\boldsymbol{\sigma}_1, \boldsymbol{\sigma}_2)]}{\text{Tr } (T \varrho_i T^\dagger)} = 1 + \frac{39}{14} \alpha^2 \mathbf{p}_1 \cdot \mathbf{p}_2.$$

#### 4. - The decay

$$\Xi^- \rightarrow \Lambda + \pi^-$$

will have an asymmetry parameter  $\alpha_\Lambda$  which will depend on the spin of the  $\Xi$ . Taking  $\Xi$  to decay from rest only  $P$  and  $D$ -waves are possible in the final system. The subsequent decay of  $\Lambda$  to  $p\pi^-$  will show an asymmetry dependent on the polarization of the  $\Lambda$ . Taking the spin-flip and non-spin-flip amplitudes for the first decay separately we can calculate the probability for the proton polarization to be along or opposite that of the  $\Xi$ . We thus have

$$\psi(\Lambda\pi^-) = A_p V^{\frac{1}{2}} Y_1' + A_D \left[ -\frac{1}{\sqrt{5}} V^{\frac{1}{2}} Y_2' + \frac{2}{\sqrt{5}} V^{-\frac{1}{2}} Y_2^2 \right],$$

which gives for the distribution

$$\frac{3}{8\pi} \sin^2 \theta [ |A_p|^2 + |A_D|^2 - 2 \text{Re } A_p^* A_D \cos \theta ],$$

and

$$\alpha = \frac{3}{2} \frac{\text{Re } A_p^* A_D}{|A_p|^2 + |A_D|^2}.$$

The measurement of the correlation between the direction of motion of  $\Lambda$  and the proton, each measured in the rest system of its parent particle determines  $\alpha\alpha_{\Lambda}$  <sup>(5)</sup>.

\* \* \*

We are very grateful to Professor M. GELL-MANN for drawing our attention to the possibility of spin  $\frac{3}{2}$  for the  $\Xi$  and to Professor R. H. DALITZ for helpful discussions. One of the authors (G.B.) wishes to thank the C.S. & I.R. India and the other (S.I.) the University Grants Commission for the award of Research Fellowships. The authors (T.K.R. and R.T.) wish to thank the Atomic Energy Commission, India, for the Research Fellowships awarded to them.

<sup>(5)</sup> W. B. TEUTSCH, S. OKUBO and E. C. G. SUDARSHAN: *Phys. Rev.*, **114**, 1148 (1959).

#### RIASSUNTO (\*)

Si studiano le conseguenze dell'assegnazione dello spin  $\frac{3}{2}$  alla cascata. Si analizzano le interazioni  $\Xi$ -p e  $\bar{\Xi}$ -p per parità  $\Xi$ -N' sia pari che dispari. Si calcolano pure le energie di legami dei doppi iperframmenti per cattura di  $\Xi$  nei nuclei. Si dà anche la sistematica di decadimento del  $\Xi$ .

(\*) Traduzione a cura della Redazione.

## Momentum-Spin Correlations in Photoelectric Effect and in Single Quantum Positron Annihilation.

H. KOLBENSTVEDT and H. OLSEN

*Institute of Theoretical Physics, N.T.H. - Trondheim*

(ricevuto il 26 Agosto 1961)

**Summary.** — The transverse polarization of photoelectrons and the photon emission asymmetry with respect to the polarization plane in single quantum annihilation of transversely polarized positrons is calculated in the lowest non-vanishing order Born approximation. The effects are of the same nature and of the same order of magnitude as the polarization and asymmetry effects in Mott scattering. The momentum spin correlation in quantum theory of radiation is shown to be proportional to the imaginary part of the matrix element integrals. The fact that the correlation only occurs in the second order Born approximation, the first order Born approximation matrix element integrals being real, is closely related to time reversal invariance.

### 1. — Introduction.

The transverse polarization of Coulomb scattered electrons was calculated by MOTT <sup>(1)</sup>. Similarly one expects correlations between electron momentum and spin in electrodynamic processes involving photons, like photoelectric effect, positron annihilation, bremsstrahlung and pair production. As will be shown below, only higher order corrections either in  $e^2/\hbar c$  or in  $Ze^2/\hbar c$  beyond the lowest order Born approximation, contribute to this correlation,  $Z$  being

(1) N. F. MOTT: *Proc. Roy. Soc., A* **124**, 425 (1929).



the atomic number. The correlations expected in processes involving an atom, like photoelectric effect, single quantum positron annihilation, bremsstrahlung and pair production will therefore be of the order  $Z$  times larger than the correlations in the cases in which no atom is involved, like the Compton effect and two quantum positron annihilation.

In this paper we shall consider the simplest processes with large momentum-spin correlations, the photoelectric effect and single quantum annihilation of positrons. The calculation is performed in the lowest non-vanishing Born approximation.

Photoelectrons produced by unpolarized photons may be expected to be polarized transversely to the plane of emission, since the cross-section may contain the quantity  $\boldsymbol{\zeta} \cdot (\mathbf{p} \times \mathbf{k})$ .  $\mathbf{p}$  and  $\mathbf{k}$  are the momenta of the electron and the photon respectively and  $\boldsymbol{\zeta}$  is a unit vector in the direction of the electron spin.  $\boldsymbol{\zeta} \cdot (\mathbf{p} \times \mathbf{k})$  is obviously an invariant under space reversal and also effectively under time reversal when higher order Born approximations are taken into account. This is discussed in some detail below in Section 2 and in Appendix A.

Since single quantum annihilation is related to the photoelectric effect by the substitution law, one expects for this process an asymmetry in the emission of the photon with respect to the  $\mathbf{p}_+ - \boldsymbol{\zeta}$  plane provided the positron is transversely polarized.  $\mathbf{p}_+$  is here the momentum of the positron.

We shall here use the same method as in an earlier paper on polarized photoelectrons produced by polarized photons <sup>(2)</sup>.

The transverse polarization of photoelectrons is calculated in Sections 3-7, and in Section 9 the photon asymmetry in single quantum annihilation of positrons is obtained. In order to illustrate the simplicity of the present method we include (in Section 8) a derivation of the transverse polarization of electrons in Coulomb scattering to lowest non-vanishing order in  $Ze^2/\hbar c$ .

Possible experimental application of the photon asymmetry effect in positron annihilation is discussed elsewhere <sup>(3)</sup>.

While this work was in preparation, we received a paper from NAGEL <sup>(4)</sup> where the problem of transverse polarization of photoelectrons is treated using a method similar to Sauter's method of expanding the final state into spherical waves and retaining only the lowest order in  $Z$  in the angular momentum sums. The numerical results given by NAGEL in his Fig. 4 are in agreement with those of our Fig. 1.

<sup>(2)</sup> H. OLSEN: *Kgl. Norske Vidensk. Selsk. Forh.*, **31**, 61 (1958). See also U. FANO and K. W. McVOY and J. R. ALBERS: *Phys. Rev.*, **116**, 1159 (1959).

<sup>(3)</sup> H. KOLBENSTVEDT and H. OLSEN: to be published.

<sup>(4)</sup> B. C. H. NAGEL: *Ark. f. Fys.*, **18**, 1 (1960).

## 2. - Momentum-spin correlations.

Considerable simplification is obtained by noting that in general the spin-dependent part of the cross-section is proportional to the imaginary part of the matrix element integrals. This follows easily since the matrix element must always be of the form

$$(1) \quad \int d^3x v_2^\dagger (A + \boldsymbol{\sigma} \cdot \mathbf{B} \cdot \boldsymbol{\sigma} \cdot \mathbf{C}) v_1 = v_2^\dagger (J_1 + i \boldsymbol{\sigma} \cdot \mathbf{J}_2) v_1 ,$$

where  $v_1$  and  $v_2$  are the initial and final state Pauli spinors, respectively, and  $\boldsymbol{\sigma}$  the Pauli spin vector.  $J_1$  and  $\mathbf{J}_2$  are the matrix element integrals. We have here used

$$(2) \quad \boldsymbol{\sigma} \cdot \mathbf{B} \boldsymbol{\sigma} \cdot \mathbf{C} = \mathbf{B} \cdot \mathbf{C} + i \boldsymbol{\sigma} \cdot (\mathbf{B} \times \mathbf{C}) .$$

Averaging over the initial spin states, the cross-section is proportional to

$$v_2^\dagger \{ |J_1|^2 + |\mathbf{J}_2|^2 + i J_1^* \boldsymbol{\sigma} \cdot \mathbf{J}_2 - i J_1 \boldsymbol{\sigma} \cdot \mathbf{J}_2^* + i \boldsymbol{\sigma} \cdot (\mathbf{J}_2 \times \mathbf{J}_2^*) \} v_2 .$$

Now it is well known that the first order Born approximation matrix element integrals are always real. Thus  $\text{Im } J_1$  and  $\text{Im } \mathbf{J}_2$  must come from the second order Born approximation. The spin-dependent cross-section to the lowest order in  $Z$  is thus proportional to

$$(3) \quad (\text{Re } J_1)^2 + (\text{Re } \mathbf{J}_2)^2 + 2 \boldsymbol{\zeta} \cdot \{ \text{Re } \mathbf{J}_2 \text{ Im } J_1 - \text{Re } J_1 \text{ Im } \mathbf{J}_2 + \text{Re } \mathbf{J}_2 \times \text{Im } \mathbf{J}_2^* \} ,$$

where  $\boldsymbol{\zeta}$  is a unit vector in the final state spin direction

$$\boldsymbol{\zeta} = v_2^\dagger \boldsymbol{\sigma} v_2 .$$

We shall use formula (3) in Sections 6 and 8.

It may also be interesting to see in a simple way how the invariance of the cross-section under time reversal comes about in the second order Born approximation. The spin-dependent part of eq. (3) in general contains factors  $\boldsymbol{\zeta} \cdot (\mathbf{p}_1 \times \mathbf{p}_2)$  because of invariance with respect to space reversal.  $\mathbf{p}_1$  and  $\mathbf{p}_2$  are the momenta of the particles taking part in the process. This factor is multiplied with the imaginary part of the matrix element integrals. This imaginary part comes from the imaginary part of the Green's function

$$(\boldsymbol{\alpha} \cdot \mathbf{s} + \beta + \varepsilon)^{-1} \text{Im } \mathcal{G}_\pm(\mathbf{r}) = \text{Im} \left\{ \lim_{\eta \rightarrow 0} \left( \frac{1}{2\pi} \right)^3 \int \frac{d^3s \exp[i\mathbf{s} \cdot \mathbf{r}]}{s^2 - p^2 \pm i\eta} \right\} = \\ = \left( \frac{1}{2\pi} \right)^3 (\mp \pi) \int d^3s \delta(s^2 - p^2) \exp[i\mathbf{s} \cdot \mathbf{r}] .$$

where  $+$  and  $-$  denote asymptotically ingoing and outgoing spherical waves, respectively. Thus in time reversal, the change of sign of  $\boldsymbol{\zeta} \cdot (\mathbf{p}_1 \times \mathbf{p}_2)$  due to reversal of all vectors, is compensated by the change of sign of the imaginary parts of the matrix element integrals due to the change of direction of motion of the accompanying spherical waves.

Thus since the first Born approximation matrix element is real and therefore does not depend on the sign of  $\eta$ , the fact that the momentum-spin correlation occurs in the second and not in the first Born approximation is closely connected with the time reversal invariance requirement.

A more detailed discussion of these questions is given in Appendix A.

### 3. - Photoelectric effect.

We follow closely the calculation of reference (<sup>2</sup>). The wave-function of the  $1S_{\frac{1}{2}}$ -state is given by

$$(4) \quad \Psi_1(\mathbf{r}) = \begin{pmatrix} 1 \\ \frac{ia}{2} \boldsymbol{\sigma} \cdot \hat{\mathbf{r}} \end{pmatrix} v_1 \exp[-ar] = u_1 \exp[-ar].$$

$\boldsymbol{\sigma}$  and  $v$  are the Pauli spin-vector and two-component spinor, respectively,  $a = Ze^2/\hbar c = Z/137$  and  $\hat{\mathbf{r}} = \mathbf{r}/r$ . Energy is measured in units of  $mc^2$  and lengths in units of the Compton-wavelength  $\hbar/mc$ .

For the final state of the electron we use the wave-function obtained from the second order Born approximation

$$(5) \quad \Psi_2(\mathbf{r}) = u_2 \exp[i\mathbf{p} \cdot \mathbf{r}] - \int \mathcal{G}_+(\mathbf{r} - \mathbf{r}') V(\mathbf{r}') u_2 \exp[i\mathbf{p} \cdot \mathbf{r}'] d^3r' + \\ + \int \mathcal{G}_+(\mathbf{r} - \mathbf{r}') V(\mathbf{r}') \mathcal{G}_+(\mathbf{r}' - \mathbf{r}'') V(\mathbf{r}'') u_2 \exp[i\mathbf{p} \cdot \mathbf{r}''] d^3r' d^3r''.$$

Here  $u_2$  is the free particle spinor,

$$u_2 = \begin{pmatrix} 1 \\ \boldsymbol{\sigma} \cdot \mathbf{p} \\ \varepsilon + 1 \end{pmatrix} v_2,$$

where  $v_2$  is the Pauli spinor.

$\mathcal{G}_+(\mathbf{r} - \mathbf{r}')$  is the Green's function for the Dirac equation and  $V(\mathbf{r})$  the potential of the nucleus. The Green's function satisfying

$$(\boldsymbol{\alpha} \cdot \mathbf{p} + \beta - \varepsilon) \mathcal{G}(\mathbf{r} - \mathbf{r}') = \delta(\mathbf{r} - \mathbf{r}')$$

is given by

$$(6) \quad \mathcal{G}_{\pm}(\mathbf{r} - \mathbf{r}') = \left(\frac{1}{2\pi}\right)^3 \int \frac{\exp[i\mathbf{s} \cdot (\mathbf{r} - \mathbf{r}')] d^3s}{\boldsymbol{\alpha} \cdot \mathbf{s} + \beta - \varepsilon \pm i\eta},$$

where  $+$  and  $-$  denote asymptotically ingoing and outgoing spherical waves, respectively. The real and imaginary parts are separated by means of the identity

$$(7) \quad (\boldsymbol{\alpha} \cdot \mathbf{s} + \beta - \varepsilon \pm i\eta)^{-1} = (\boldsymbol{\alpha} \cdot \mathbf{s} + \beta - \varepsilon) \left\{ P\left(\frac{1}{s^2 - p^2}\right) \mp i\pi \delta(s^2 - p^2) \right\},$$

where  $P$  denotes the principal value.

For a pure Coulomb field the Fourier transforms of  $V(\mathbf{r})$  that occur in the matrix elements diverge<sup>(5)</sup>. To avoid these divergences, we use a screened potential

$$V(\mathbf{r}) = -\frac{a}{r} \exp[-\Lambda r],$$

and let  $\Lambda \rightarrow 0$  after the integrations have been carried out. The matrix elements then turn out to be logarithmic divergent. The cross-section must of course be finite, and terms containing  $\Lambda$  cancel out as shown in Section 6.

The matrix element for absorption of a photon  $\mathbf{k}$  with polarization vector  $\mathbf{e}$  together with the emission of an electron from the  $K$ -shell with momentum  $\mathbf{p}$ , energy  $\varepsilon$  and spin  $\zeta$  is proportional to

$$M = (\Psi_2, \boldsymbol{\alpha} \cdot \mathbf{e} \exp[i\mathbf{k} \cdot \mathbf{r}] \Psi_1),$$

where  $\boldsymbol{\alpha}$  is the Dirac matrix-vector.

Following reference (2) the matrix element is divided into three parts

$$(8) \quad \left\{ \begin{array}{l} M = M_1 + M_2 + M_3, \\ M_1 = (\Psi_{20}, \boldsymbol{\alpha} \cdot \mathbf{e} \exp[i\mathbf{k} \cdot \mathbf{r}] \Psi_1), \\ M_2 = (\Psi_{21}, \boldsymbol{\alpha} \cdot \mathbf{e} \exp[i\mathbf{k} \cdot \mathbf{r}] \Psi_1), \\ M_3 = (\Psi_{22}, \boldsymbol{\alpha} \cdot \mathbf{e} \exp[i\mathbf{k} \cdot \mathbf{r}] \Psi_1), \end{array} \right.$$

<sup>(5)</sup> This was first noticed by M. GAVRILA: *Phys. Rev.*, **113**, 514 (1959) in calculations of the second Born approximation correction to the photoelectric cross-section.

where the second index in  $\Psi_{2,}$  refers to the power of  $Z$  in the expansion of  $\Psi_2$ , eq. (5).

#### 4. - The real matrix element integrals.

$M_1$  is given by <sup>(6)</sup>

$$(9) \quad M_1 = v_2^\dagger \left\{ \boldsymbol{\sigma} \cdot \mathbf{p} \boldsymbol{\sigma} \cdot \mathbf{e} \frac{I_0}{\varepsilon + 1} + \boldsymbol{\sigma} \cdot \mathbf{e} \boldsymbol{\sigma} \cdot \mathbf{I}_1 \right\} v_1.$$

Here

$$(10) \quad I_0 = \frac{8\pi a}{(q^2 + a^2)^2}, \quad I_1 = -\frac{4\pi a \mathbf{q}}{(q^2 + a^2)^2},$$

where the momentum transfer  $\mathbf{q}$  is

$$\mathbf{q} = \mathbf{k} - \mathbf{p}.$$

The part of  $M_2$  involving the real part of the matrix element integral,  $M_2(\text{Re})$  is found to be given by <sup>(6)</sup>

$$(11) \quad M_2(\text{Re}) = v_2^\dagger \left( \frac{\varepsilon - 1}{\varepsilon + 1} \boldsymbol{\sigma} \cdot \mathbf{p} + \boldsymbol{\sigma} \cdot \mathbf{k} \right) \boldsymbol{\sigma} \cdot \mathbf{e} I_2 v_1,$$

where

$$(12) \quad I_2 = \frac{4\pi a}{(k^2 - p^2)q^2}.$$

The part of the matrix element which is proportional to the real part of the matrix element integrals is thus <sup>(6)</sup>

$$(13) \quad M(\text{Re}) = v_2^\dagger (\mathbf{I}^+ + i \boldsymbol{\sigma} \times \mathbf{I}^-) \cdot \mathbf{e} v_1$$

with

$$(14) \quad \mathbf{I}^\pm = \frac{\mathbf{p}}{\varepsilon + 1} I_0 + \left( \frac{\varepsilon - 1}{\varepsilon + 1} \mathbf{p} + \mathbf{k} \right) I_2 \pm \mathbf{I}_1.$$

This is also the total first order Born approximation matrix element as discussed in the introduction.

<sup>(6)</sup> For details of the calculation see ref. (2).



## 5. - The imaginary matrix element integrals.

In order to obtain the contribution to the matrix element from the imaginary part of the integrals we go back to eq. (4)–(8) and find

$$\begin{aligned}
 M_2(\text{Im}) &= \frac{ia}{2\pi} \int d^3s \, d^3r \frac{\delta(s^2 - p^2)}{(s - p)^2 + A^2} \exp[i(\mathbf{k} - \mathbf{s}) \cdot \mathbf{r} - ar] v_2^\dagger \left( 1 \frac{\boldsymbol{\sigma} \cdot \mathbf{p}}{\varepsilon + 1} \right) \\
 &\quad \cdot (\boldsymbol{\alpha} \cdot \mathbf{s} + \beta + \varepsilon) \boldsymbol{\alpha} \cdot \mathbf{e} \left( \frac{1}{\frac{ia}{2} \boldsymbol{\sigma} \cdot \hat{\mathbf{r}}} \right) v_1 = \frac{ia}{2\pi} \int d^3s \frac{\delta(s^2 - p^2)}{(s - p)^2 + A^2} \\
 &\quad \cdot v_2^\dagger \left\{ \left( \frac{\varepsilon - 1}{\varepsilon + 1} \boldsymbol{\sigma} \cdot \mathbf{p} + \boldsymbol{\sigma} \cdot \mathbf{s} \right) \boldsymbol{\sigma} \cdot \mathbf{e} \int d^3r \exp[i(\mathbf{k} - \mathbf{s}) \cdot \mathbf{r} - ar] \right. \\
 &\quad \left. + \left( \varepsilon + 1 + \frac{1}{\varepsilon + 1} \boldsymbol{\sigma} \cdot \mathbf{p} \boldsymbol{\sigma} \cdot \mathbf{s} \right) \boldsymbol{\sigma} \cdot \mathbf{e} \frac{ia}{2} \int d^3r \boldsymbol{\sigma} \cdot \hat{\mathbf{r}} \exp[i(\mathbf{k} - \mathbf{s}) \cdot \mathbf{r} - ar] \right\} v_1.
 \end{aligned}$$

Performing the  $\mathbf{r}$ -integrations this may be written

$$\begin{aligned}
 (15) \quad M_2(\text{Im}) &= i \cdot 2a^2 v_2^\dagger \left\{ 2 \frac{\varepsilon - 1}{\varepsilon + 1} \boldsymbol{\sigma} \cdot \mathbf{p} \boldsymbol{\sigma} \cdot \mathbf{e} I_3 + 2 \boldsymbol{\sigma} \cdot \mathbf{I}_4 \boldsymbol{\sigma} \cdot \mathbf{e} - (\varepsilon + 1) \boldsymbol{\sigma} \cdot \mathbf{e} \boldsymbol{\sigma} \cdot \mathbf{k} I_3 \right. \\
 &\quad \left. + (\varepsilon + 1) \boldsymbol{\sigma} \cdot \mathbf{e} \boldsymbol{\sigma} \cdot \mathbf{I}_4 - \frac{1}{\varepsilon + 1} \boldsymbol{\sigma} \cdot \mathbf{p} \boldsymbol{\sigma} \cdot \mathbf{I}_4 \boldsymbol{\sigma} \cdot \mathbf{e} \boldsymbol{\sigma} \cdot \mathbf{k} + \frac{1}{\varepsilon + 1} \boldsymbol{\sigma} \cdot \mathbf{p} \boldsymbol{\sigma} \cdot \mathbf{e} \boldsymbol{\sigma} \cdot \mathbf{I}_{lm} \right\} v_1.
 \end{aligned}$$

Here

$$(16) \quad (I_3, \mathbf{I}_4, I_{lm}) = \int \frac{d^3s \delta(s^2 - p^2)}{[(\mathbf{s} - \mathbf{p})^2 + A^2][(\mathbf{s} - \mathbf{k})^2 + a^2]} (1, \mathbf{s}, s_l s_m).$$

These integrals are evaluated in the Appendix.

The contributions to  $M_3$  from the imaginary part integrals are found in a similar manner from eq. (4)–(8). It should be noted that in this case, since the potential acts twice in this matrix element, the  $\mathbf{r}$ -integral may be performed with  $a = 0$ , thus giving simply a  $\delta$ -function

$$\left( \frac{1}{2\pi} \right)^3 \int \exp[i(\mathbf{k} - \mathbf{s}) \cdot \mathbf{r}] d^3r = \delta(\mathbf{k} - \mathbf{s}),$$

which simplifies the calculation considerably.

In this way one finds

$$(17) \quad M_3(\text{Im}) = -ia^2v_2^+ \left\{ \left( \frac{\varepsilon+1}{\varepsilon-1} \boldsymbol{\sigma} \cdot \mathbf{k} \boldsymbol{\sigma} \cdot \mathbf{e} + \frac{\varepsilon-1}{\varepsilon+1} \boldsymbol{\sigma} \cdot \mathbf{p} \boldsymbol{\sigma} \cdot \mathbf{e} \right) I_5 + \right. \\ \left. + \boldsymbol{\sigma} \cdot \mathbf{I}_6 \boldsymbol{\sigma} \cdot \mathbf{e} + \frac{1}{\varepsilon^2-1} \boldsymbol{\sigma} \cdot \mathbf{p} \boldsymbol{\sigma} \cdot \mathbf{I}_6 \boldsymbol{\sigma} \cdot \mathbf{k} \boldsymbol{\sigma} \cdot \mathbf{e} \right\} c_1,$$

where

$$(18) \quad (I_5, I_6) = \int \frac{d^3s \delta(s^2 - p^2)}{[(\mathbf{s} - \mathbf{k})^2 + A^2][(\mathbf{s} - \mathbf{p})^2 + A^2]} (1, \mathbf{s}).$$

These integrals are also given in the Appendix.

## 6. - The cross-section.

The imaginary integrals contributing to  $M$  are given by eq. (15) and (17). Using eq. (2)  $M(\text{Im})$  may be written

$$(19) \quad M(\text{Im}) = 2ia^2v_2^+ \left\{ \mathbf{A} \cdot \mathbf{e} + i \boldsymbol{\sigma} \cdot \mathbf{B} \times \mathbf{e} + \frac{i}{\varepsilon+1} \boldsymbol{\sigma} \times \mathbf{p} \cdot \mathbf{I} \cdot \mathbf{e} + \frac{i}{\varepsilon+1} \boldsymbol{\sigma} \cdot \mathbf{D} \cdot \mathbf{p} \cdot \mathbf{e} \right\} c_1,$$

where we have used the notation

$$e_l I_{lm} = (\mathbf{e} \cdot \mathbf{I})_m; \quad I_{lm} e_m = (\mathbf{I} \cdot \mathbf{e})_l.$$

$\mathbf{A}$ ,  $\mathbf{B}$  and  $\mathbf{D}$  are, from eq. (15) and (17), given by

$$(20a) \quad \mathbf{A} = - \frac{(\varepsilon-1)^2}{\varepsilon+1} I_3 \mathbf{p} + (\varepsilon+3) \mathbf{I}_4 + \frac{1}{\varepsilon+1} \mathbf{I}_4 \cdot \mathbf{k} \mathbf{p} - \frac{1}{\varepsilon+1} \mathbf{p} \cdot \mathbf{k} \mathbf{I}_4 + \\ + \frac{2}{\varepsilon+1} \mathbf{p} \cdot \mathbf{I} - \frac{1}{2(\varepsilon^2-1)} [(\varepsilon-1)^2 I_5 + \mathbf{I}_6 \cdot \mathbf{k}] \mathbf{p} - \frac{1}{2} \left( 1 - \frac{\mathbf{p} \cdot \mathbf{k}}{\varepsilon^2-1} \right) \mathbf{I}_6,$$

$$(20b) \quad \mathbf{B} = 2 \left[ \frac{\varepsilon-1}{\varepsilon+1} \mathbf{p} + (\varepsilon+1) \mathbf{k} \right] I_3 - (\varepsilon-1) \mathbf{I}_4 + \frac{1}{\varepsilon+1} \mathbf{p} \cdot \mathbf{I}_4 \mathbf{k} - \frac{1}{\varepsilon+1} \mathbf{p} \cdot \mathbf{I} - \\ - \frac{1}{2} \left[ \frac{\varepsilon+1}{\varepsilon-1} \mathbf{k} + \frac{\varepsilon-1}{\varepsilon+1} \mathbf{p} \right] I_5 - \frac{1}{2} \mathbf{I}_6 - \frac{1}{2(\varepsilon^2-1)} \mathbf{I}_6 \cdot \mathbf{p} \mathbf{k},$$

and

$$(20c) \quad \mathbf{D}_{lm} = k_l \left( I_{4m} + \frac{1}{2k} \mathbf{I}_{6m} \right) + I_{lm}.$$

We have here neglected the binding energy of the electron which is of the order  $a^2$ , thus

$$k^2 - p^2 = -2k.$$

By comparison with eq. (1) it is easily seen from eq. (13) and (19) that  $J_1$  and  $J_2$  are, to the lowest orders in  $a$ , given by

$$(21) \quad \left\{ \begin{array}{l} \text{Re } J_1 = \mathbf{I}^+ \cdot \mathbf{e}, \\ \text{Im } J_1 = 2a^2 \mathbf{A} \cdot \mathbf{e}, \\ \text{Re } J_2 = \mathbf{I}^- \times \mathbf{e}, \\ \text{Im } J_2 = 2a^2 \left\{ \mathbf{B} \times \mathbf{e} + \frac{1}{\varepsilon + 1} \mathbf{p} \times \mathbf{I} \cdot \mathbf{e} + \frac{1}{\varepsilon + 1} \mathbf{D} \times \mathbf{p} \cdot \mathbf{e} \right\}. \end{array} \right.$$

Dividing the cross-section into spin-independent and spin-dependent parts,  $d\sigma_0/d\Omega$  and  $d\sigma_z/d\Omega$ , respectively,

$$\frac{d\sigma}{d\Omega} = \frac{d\sigma_0}{d\Omega} + \frac{d\sigma_z}{d\Omega},$$

the spin independent part of the photoelectric cross-section for unpolarized photons is thus from eq. (3) for the two  $K$ -shell electrons

$$(22) \quad \frac{d\sigma_0}{d\Omega} = C \{ (\mathbf{I}_\perp^+)^2 + (\mathbf{I}_z^-)^2 \},$$

where  $\perp$  and  $z$  denote vector components perpendicular to and along  $\mathbf{k}$ , respectively, and where we have introduced the factor

$$C = \left( \frac{1}{2\pi} \right)^2 Z^2 \left( \frac{e^2}{k} \right)^2 \left( \frac{e^2}{mc^2} \right)^2 a^2.$$

In the same way the corresponding spin-dependent part of the cross-section is from eq. (3)

$$(23) \quad \frac{d\sigma_z}{d\Omega} = 4a^2 C \left\{ (\boldsymbol{\zeta} \cdot \mathbf{I})_\perp \cdot \mathbf{A}_\perp - (\boldsymbol{\zeta} \times \mathbf{B})_\perp \cdot \mathbf{I}_\perp^+ - \boldsymbol{\zeta}_\perp \cdot (\mathbf{B} \times \mathbf{I})_\perp - \right. \\ \left. \frac{1}{\varepsilon + 1} [(\boldsymbol{\zeta} \cdot \mathbf{p} \times \mathbf{I})_\perp \cdot \mathbf{I}_\perp^+ + \boldsymbol{\zeta} \cdot \mathbf{I} (\mathbf{p} \times \mathbf{I} \cdot \hat{\mathbf{u}})_\perp - (\mathbf{I} \cdot \mathbf{p} \times \mathbf{I})_\perp \cdot \boldsymbol{\zeta}_\perp] - \right. \\ \left. - \frac{1}{\varepsilon + 1} [(\boldsymbol{\zeta} \cdot \mathbf{D} \times \mathbf{p})_\perp \cdot \mathbf{I}_\perp^+ + \boldsymbol{\zeta} \cdot \mathbf{I} (\mathbf{D} \times \mathbf{p} \cdot \hat{\mathbf{u}})_\perp - (\mathbf{I} \cdot \mathbf{D} \times \mathbf{p})_\perp \cdot \boldsymbol{\zeta}_\perp] \right\},$$

where  $\mathbf{u}$  is the component of  $\mathbf{p}$  perpendicular to  $\mathbf{k}$  and  $\hat{\mathbf{u}} = \mathbf{u}/u$ .

Introducing the expressions for the real part of the integrals from eq. (10), (12) and (14) and for the imaginary part of the integrals from eq. (B.2) in the Appendix, one finds after some algebra

$$(24) \quad \frac{d\sigma_z}{d\Omega} = Z \left( \frac{Ze^2}{\hbar c} \right)^5 \left( \frac{e^2}{mc^2} \right)^2 \frac{\beta(k-1)}{2k^4(k+1)^2} \frac{\boldsymbol{\zeta} \cdot \hat{\mathbf{k}} \wedge \hat{\mathbf{p}}}{(1-\beta \cos \theta)^3} \cdot \left\{ 2 + (k+1)(1-\beta \cos \theta) \left[ 2 + \beta \frac{k+1}{k-1} \ln \frac{1-\beta}{1+\beta} + \left( \frac{\beta(k+1)}{2k(k-1)} \operatorname{cosec}^2(\theta/2) - 1 \right) \cdot \ln \frac{1-\beta \cos \theta}{1-\beta} - \left( \frac{\beta(k+1)}{2k(k-1)} \sec^2(\theta/2) + 1 \right) \ln \frac{1-\beta \cos \theta}{1+\beta} \right] \right\},$$

where  $\theta$  is the angle of emission of the electron,  $\hat{\mathbf{k}} = \mathbf{k}/k$  and  $\hat{\mathbf{p}} = \mathbf{p}/p$ . The electron velocity in units of the light velocity,  $\beta$ , is given by  $\beta = \sqrt{2k(k+2)/(k+1)}$ . The terms containing  $\ln A$  in eq. (23) have cancelled out as they should.

The spin-independent cross-section is given by the well-known Sauter cross-section (7) which may also be derived from eq. (22),

$$(25) \quad \frac{d\sigma_0}{d\Omega} = Z \left( \frac{Ze^2}{\hbar c} \right)^4 \left( \frac{e^2}{mc^2} \right)^2 \frac{2\beta(k+2)}{k^4(k+1)^3} \frac{\sin^2 \theta}{(1-\beta \cos \theta)^4} \left[ 1 + \frac{1}{2} k(k^2-1)(1-\beta \cos \theta) \right].$$

It should be noted that the spin-dependent part of the cross-section, eq. (24), contains one extra power of  $(Ze^2/\hbar c)$  as compared to the spin-independent part, eq. (25), which is due to the fact that only the second order Born approximation contributes to the spin-dependent part, as discussed in Section 2.

## 7. - The polarization.

Denoting the cross-section for emission of an electron whose spin  $\boldsymbol{\zeta}$  is parallel to  $\mathbf{k} \times \mathbf{p}$  by  $(d\sigma/d\Omega)_{\text{par}}$  and for the opposite case that  $\boldsymbol{\zeta}$  is antiparallel to  $\mathbf{k} \times \mathbf{p}$  by  $(d\sigma/d\Omega)_{\text{anti}}$ , we define the transverse electron polarization by

$$(26) \quad P_{\perp} = \frac{(d/d\Omega)(\sigma_{\text{par}} - \sigma_{\text{anti}})}{(d/d\Omega)(\sigma_{\text{par}} + \sigma_{\text{anti}})}.$$

(7) F. SAUTER: *Ann. d. Phys.*, **11**, 454 (1931).

Using (24) and (25) one finds

$$(27) \quad P_{\perp} = \left( \frac{Ze^2}{\hbar c} \right) \frac{k^2 - 1}{4(k+2)} \frac{1 - \beta \cos \theta}{\sin \theta} \cdot \frac{2 + (k+1)(1 - \beta \cos \theta) + 2 + \beta \frac{k+1}{k-1} \ln \frac{1-\beta}{1+\beta} + K_- - K_+}{1 + \frac{1}{2}k(k^2 - 1)(1 - \beta \cos \theta)},$$

where

$$K_{\pm} = \left( \frac{\beta(k+1)}{k(k-1)} \frac{1}{1 \pm \cos \theta} \pm 1 \right) \ln \frac{1 - \beta \cos \theta}{1 \pm \beta}.$$

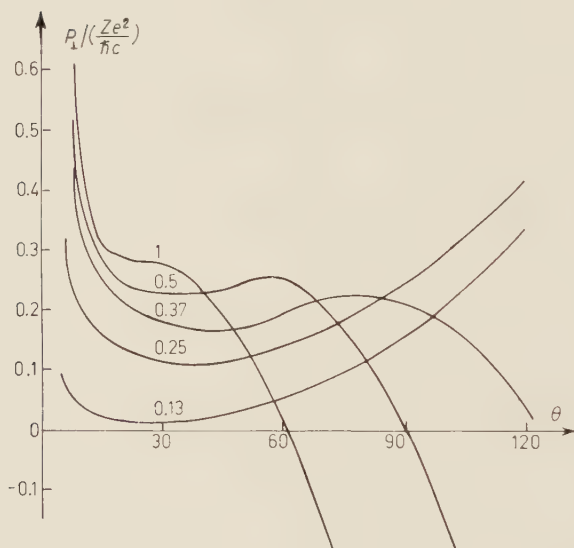


Fig. 1. — Transverse polarization of photoelectrons produced by unpolarized photons as a function of the emission angle  $\theta$ . The numbers affixed to the curves refer to the photon energy in MeV.

Graphs showing the angular dependence of the polarization for several energies are given in Fig. 1.

### 8. — Coulomb scattering.

As mentioned in the introduction we also use the present method to calculate the transverse polarization of Coulomb scattered electrons. The comparison with the exact result of SHERMAN <sup>(8)</sup> is given in Section 8 and in Fig. 2.

<sup>(8)</sup> N. SHERMAN: *Phys. Rev.*, **103**, 1601 (1956).



The scattering matrix  $R$  is given by

$$R = u_2^\dagger \int \exp [-i \mathbf{p}_2 \cdot \mathbf{r}] V(\mathbf{r}) \Psi_1(\mathbf{r}) d^3 r,$$

where  $\Psi_1$  is

$$\Psi_1(\mathbf{r}) = u_1 \exp [i \mathbf{p}_1 \cdot \mathbf{r}] - \int \mathcal{G}_-(\mathbf{r} - \mathbf{r}') V(\mathbf{r}') u_1 \exp [i \mathbf{p}_1 \cdot \mathbf{r}'] d^3 r',$$

which is analogous to eq. (5), but where we now have  $\mathcal{G}_-$  corresponding to outgoing spherical waves.

Again the matrix element is divided into two parts containing the real and imaginary integrals

$$R = R(\text{Re}) + R(\text{Im}).$$

To the lowest order in  $a$  one obtains

$$(28) \quad R(\text{Re}) = -\frac{4\pi a}{q^2} v_2^\dagger \left[ 1 + \frac{\boldsymbol{\sigma} \cdot \mathbf{p}_2 \boldsymbol{\sigma} \cdot \mathbf{p}_1}{(\varepsilon + 1)^2} \right] v_1,$$

and

$$(29) \quad R(\text{Im}) = -\frac{i \cdot 2a^2}{\varepsilon + 1} v_2^\dagger \left\{ \mathbf{r}_2 \cdot (\mathbf{p}_1 + \mathbf{p}_2) + \left[ (\varepsilon + 1)^2 + \frac{\varepsilon - 1}{\varepsilon + 1} \mathbf{p}_1 \cdot \mathbf{p}_2 \right] r_1 - \right. \\ \left. - i \boldsymbol{\sigma} \cdot \left[ \mathbf{q} \times \mathbf{r}_2 + \frac{\varepsilon - 1}{\varepsilon + 1} r_1 (\mathbf{p}_1 \times \mathbf{p}_2) \right] \right\} v_1,$$

where

$$(r_1, \mathbf{r}_2) = \int \frac{d^3 s \delta(s^2 - p^2)}{[(\mathbf{s} - \mathbf{p}_1)^2 + A^2][(\mathbf{s} - \mathbf{p}_2)^2 + A^2]} (1, \mathbf{s}).$$

$r_1$  and  $\mathbf{r}_2$  are found analogously to  $I_5$  and  $\mathbf{I}_6$ ,

$$(30) \quad \begin{cases} r_1 = \frac{2\pi}{pq^2} \ln \frac{q}{A}, \\ \mathbf{r}_2 = \frac{4\pi}{p(\mathbf{p}_1 + \mathbf{p}_2)^2} \left( \frac{p^2}{q^2} \ln \frac{q}{A} + \frac{1}{4} \ln \frac{A}{2p} \right) (\mathbf{p}_1 + \mathbf{p}_2). \end{cases}$$

$J_1$  and  $J_2$  are in this case from eq. (28) and (29)

$$(31) \quad \left\{ \begin{aligned} \operatorname{Re} J_1 &= -\frac{4\pi a}{q^2} \left( 1 + \frac{\mathbf{p}_1 \cdot \mathbf{p}_2}{(\varepsilon + 1)^2} \right), \\ \operatorname{Im} J_1 &= -\frac{2a^2}{\varepsilon + 1} \left\{ \mathbf{r}_2 \cdot (\mathbf{p}_1 + \mathbf{p}_2) + \left[ (\varepsilon + 1)^2 + \frac{\varepsilon - 1}{\varepsilon + 1} \mathbf{p}_1 \cdot \mathbf{p}_2 \right] r_1 \right\}, \\ \operatorname{Re} J_2 &= \frac{4\pi a}{q^2} \frac{\mathbf{p}_1 \times \mathbf{p}_2}{(\varepsilon + 1)^2}, \\ \operatorname{Im} J_2 &= \frac{2a^2}{\varepsilon + 1} \left[ \mathbf{q} \times \mathbf{r}_2 + \frac{\varepsilon - 1}{\varepsilon + 1} r_1 (\mathbf{p}_1 \times \mathbf{p}_2) \right]. \end{aligned} \right.$$

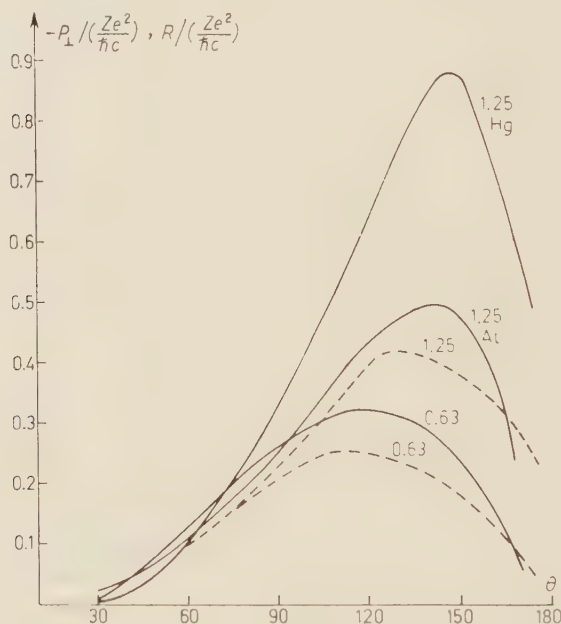


Fig. 2. — Transverse polarization  $P_{\perp}$  of initially unpolarized electrons by Coulomb scattering, as a function of the scattering angle  $\theta$ . Numbers given refer to the kinetic energy of the electrons in MeV. Dashed curve: second Born approximation calculation. Full drawn curve: exact results of ref. (8). The curves also give the scattering asymmetry  $R$  (with opposite sign), eq. (33), of transversely polarized electrons. Corresponding quantities for positron scattering in the second order Born approximation are obtained by reversal of signs of  $P_{\perp}$  and  $R$ .

From formula (3) the spin-dependent cross-section is found to be

$$(32) \quad \frac{d\sigma_z}{d\Omega} = \frac{1}{2} \left( \frac{Ze^2}{\hbar c} \right)^3 \left( \frac{e^2}{mc^2} \right)^2 \frac{\boldsymbol{\zeta} \cdot \hat{\mathbf{p}}_1 \times \hat{\mathbf{p}}_2}{(\beta\varepsilon)^3 \sin^2 \theta} \ln \sin \frac{\theta}{2},$$

which is Mott's result (1) to the lowest order in  $(Ze^2/\hbar c)$ .

The transverse electron polarization, defined according to eq. (26), where now « par » means parallel to  $\mathbf{p}_1 \times \mathbf{p}_2$  is

$$(33) \quad P_{\perp} = \left( \frac{Ze^2}{\hbar c} \right) \frac{2\beta \sin^2(\theta/2) \operatorname{tg}(\theta/2) \ln \sin(\theta/2)}{\varepsilon (1 - \beta^2 \sin^2(\theta/2))}.$$

In Fig. 2 the angular dependence of the polarization is calculated from the second Born approximation eq. (33) and also from the exact results of SHERMAN<sup>(8)</sup>.

## 9. - Single quantum positron annihilation.

Denoting the positron energy, momentum and spin by  $\varepsilon_+$ ,  $\mathbf{p}_+$  and  $\zeta_+$ , respectively, the single quantum positron annihilation cross-section is obtained from the photoelectric cross-section by the substitutions

- 1)  $\varepsilon, \mathbf{p}, \zeta \rightarrow -\varepsilon_+, -\mathbf{p}_+, -\zeta_+$  since the particle in the unbound state now is a positron,
- 2)  $k, \mathbf{k}, \mathbf{e} \rightarrow -k, -\mathbf{k}, \mathbf{e}^*$  since the photon now is emitted,
- 3)  $\eta \rightarrow -\eta$  in the Greens functions

$$\mathcal{G}(\mathbf{r}) = \left( \frac{1}{2\pi} \right)^3 \int \frac{\exp[i\mathbf{s} \cdot \mathbf{r}] d^3s}{\boldsymbol{\alpha} \cdot \mathbf{s} + \beta - \varepsilon + i\eta}, \quad (\eta \rightarrow 0),$$

since the positron is an *incoming* particle and therefore is accompanied by *outgoing* spherical waves. This changes the sign on the imaginary part of the matrix element integrals and thereby on the spin-dependent part of the cross-section as discussed in Section 2 and Appendix A.

- 4) multiplication by the statistical volume factor  $k^2/p_+^2$ .

In this way we find from eq. (24) and (25) the spin-dependent part of the cross-section,

$$(34) \quad \frac{d\sigma_{\zeta}}{d\Omega} = -Z \left( \frac{Ze^2}{\hbar c} \right)^5 \left( \frac{e^2}{mc^2} \right)^2 \frac{\beta_+(\varepsilon_+ + 2)}{\varepsilon_+^2(\varepsilon_+ + 1)^3(\varepsilon_+ - 1)} \frac{\zeta_+ \cdot \hat{\mathbf{k}} \times \hat{\mathbf{p}}_+}{(1 - \beta_+ \cos \theta)^3} \cdot \left\{ 2 - \varepsilon_+(1 - \beta_+ \cos \theta) \left[ 2 + \frac{\beta_+ \varepsilon_+}{\varepsilon_+ + 2} \ln \frac{1 - \beta_+}{1 + \beta_+} + K'_- - K'_+ \right] \right\},$$

where

$$(35) \quad K'_{\pm} = \left( \frac{\beta_+ \varepsilon_+}{(\varepsilon_+ + 1)(\varepsilon_+ + 2)} \frac{1}{1 \mp \cos \theta} \pm 1 \right) \ln \frac{1 - \beta_+ \cos \theta}{1 \mp \beta_+},$$

and the spin-independent part

(36) 
$$\frac{d\sigma_0}{d\Omega} = -Z \left( \frac{Ze^2}{\hbar c} \right)^4 \left( \frac{e^2}{mc^2} \right)^2 \frac{4\beta_+}{\varepsilon_+^3 (\varepsilon_+ + 1)^3} \frac{\sin^2 \theta}{(1 - \beta_+ \cos \theta)^4} \cdot [1 - \tfrac{1}{2} \varepsilon_+ (\varepsilon_+ + 1) (\varepsilon_+ + 2) (1 - \beta_+ \cos \theta)] .$$

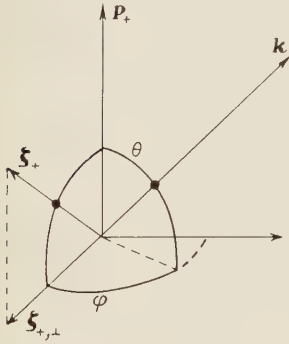


Fig. 3. — Angles occuring in single quantum positron annihilation.

Defining the photon emission asymmetry with respect to the polarization plane as

$$R = \frac{(d/d\Omega)[\sigma(\varphi = \pi/2) - \sigma(\varphi = -\pi/2)]}{(d/d\Omega)[\sigma(\varphi = \pi/2) + \sigma(\varphi = -\pi/2)]} ,$$

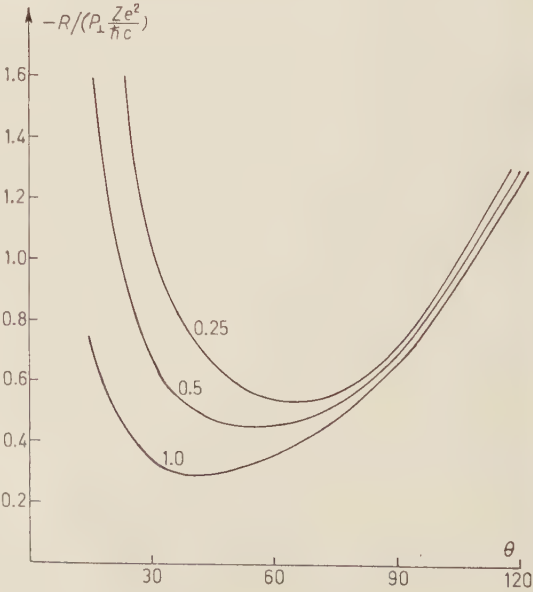
where  $\varphi$  is the azimuthal angle of Fig. 3, measured from the polarization plane, we find

(37) 
$$R = |\zeta_{+, \perp}| \left( \frac{Ze^2}{\hbar c} \right)^2 \frac{\varepsilon_+ (\varepsilon_+ + 2) (1 - \beta_+ \cos \theta)}{4(\varepsilon_+ - 1) \sin \theta} \cdot \frac{2 - \varepsilon_+ (1 - \beta_+ \cos \theta) \left[ 2 + \frac{\beta_+ \varepsilon_+}{\varepsilon_+ - 2} \ln \frac{1 - \beta_+}{1 + \beta_+} - K'_+ - K'_- \right]}{1 - \tfrac{1}{2} \varepsilon_+ (\varepsilon_+ + 1) (\varepsilon_+ + 2) (1 - \beta_+ \cos \theta)} ,$$

where  $K'_+$  is defined in eq. (35), and  $\zeta_{+, \perp}$  is the component of  $\zeta_+$  perpendicular to  $\mathbf{p}_+$ . Graphs of the photon emission asymmetry for various positron energies are given in Fig. 4.

The effect is analogous to the asymmetry of transversely polarized Coulomb scattered electrons or positrons (1). In that case we

Fig. 4. — Photon emission asymmetry in single quantum annihilation of positrons transversely polarized to the degree  $P_\perp$ . The numbers affixed to the curves refer to the kinetic energy of the positron in MeV.



have from eq. (33)

$$(38) \quad R = \zeta_{\pm} \left( \frac{Ze^2}{\hbar c} \right) \frac{2\beta \sin^2(\theta/2) \operatorname{tg}(\theta/2) \ln \sin(\theta/2)}{1 - \beta^2 \sin^2(\theta/2)},$$

where the upper sign refers to electrons and the lower to positrons. Thus Fig. 2 also gives the scattering asymmetry of transversely polarized electrons, and of positrons with the opposite sign.

It is interesting to note that the sign and order of magnitude of the asymmetry is the same in single quantum annihilation as in positron scattering. A transversely polarized positron hitting an atom is preferably scattered in the direction  $\varphi = -\pi/2$  of Fig. 3, and this is also the most probable direction of emission of its annihilation radiation.

## 10. - Discussion.

From Fig. 1 and 2 it is seen that the degrees of polarization of photoelectrons and of Coulomb scattering are of the same order of magnitude and of the order of at most  $(4 \div 6)^\circ$  in the case of Aluminium. The photon emission asymmetry, Fig. 4, is of the same order of magnitude. Since  $P_{\perp}$  and  $R$  are proportional to  $Ze^2/\hbar c$  one might expect sizable effects for heavy elements, provided the Coulomb correction due to higher order Born approximations does not lower the effects.

From Fig. 2 it follows that the Coulomb correction to the polarization of scattered electrons is reasonably small for light elements when the electrons are not too slow. For heavy elements the Coulomb correction increases the polarization. From the analogy of the processes one might conclude that for the cases of photoelectric effect and positron annihilation the Coulomb correction should be of the same order of magnitude as for scattering. Thus even for fairly heavy elements Fig. 1 and 4 should represent the correct order of magnitude of  $P_{\perp}$  and  $R$ .

The photoelectrons are polarized parallel to the vector product of the momentum of the initial particle with the momentum of the final particle while the Coulomb scattered electrons are polarized in the opposite direction. The asymmetries in Coulomb scattering of positrons and in positron annihilation are on the other hand of the same sign as discussed in Section 9.

Formula (27) for the polarization of photoelectrons cannot be used for angles close to  $\theta = 0$ , since it is based on the Born approximation cross-section, eq. (25). The latter predicts zero intensity in the forward direction, while it



is well known both from experiments <sup>(9)</sup> and theory <sup>(10)</sup> that the current is finite in this direction. Similarly eq. (37) for the photon asymmetry in positron annihilation is not reliable for very small angles.

For small angles also higher order Born approximations should be added to  $d\sigma_0/d\Omega$ , eq. (25), replacing  $\sin^2\theta$  by  $\sin^2\theta + \alpha^2$ , where  $\alpha$  is a constant for small angles. The polarization  $P_\perp$ , eq. (27), and the asymmetry  $R$ , eq. (37), are thus for small angles to be multiplied by

$$(39) \quad \frac{\sin^2\theta}{\sin^2\theta + \alpha^2}.$$

Thus both  $P_\perp$  and  $R$  are equal to zero when the secondary particle is emitted in the forward or in the backward directions. From Reitan's work <sup>(11)</sup>, one finds

$$(40) \quad \alpha = \left( \frac{Ze^2}{\hbar c} \right) \beta/\varepsilon.$$

Our formulae eq. (27) and (37) and the curves of Fig. 1 and 4 are thus valid for angles larger than

$$(41) \quad \theta_0 \approx \left( \frac{Ze^2}{\hbar c} \right) \beta/\varepsilon.$$

For Aluminium  $\theta_0$  is always less than  $3^\circ$  and even for lead  $\theta_0$  never exceed  $18^\circ$ . Our present results are therefore always valid in the region of angles in which the cross-section is largest.

For high energies the degree of polarization of photoelectrons is small of the order  $1/\varepsilon$ , but still much larger than that of Coulomb scattered electrons for the most important angles of emission,  $\theta \sim 1/\varepsilon$ . For scattering one finds when  $\varepsilon \gg 1$  and  $u \approx \varepsilon\theta \sim O(1)$

$$(42) \quad P_\perp = \left( \frac{Ze^2}{\hbar c} \right) \frac{u^3}{4\varepsilon^4} \ln \frac{\theta}{2}.$$

while for the photoelectric effect

$$(43) \quad P_\perp = \left( \frac{Ze^2}{\hbar c} \right) \frac{1}{\varepsilon u} \left[ 1 + \frac{1+u^2}{2u^2} \ln(1+u^2) \right].$$

<sup>(9)</sup> S. HULTBERG: *Ark. f. Fys.*, **15**, 307 (1959).

<sup>(10)</sup> B. C. H. NAGEL: ref. <sup>(4)</sup>; K. MØRK and H. OLSEN: *Proc. Phys. Sem. Trondheim*, no. 4 (1960); A. REITAN: to be published.

<sup>(11)</sup> A. REITAN: ref. <sup>(10)</sup>.

The asymmetry in positron annihilation is correspondingly at high energies

$$(44) \quad R = - \left( \frac{Ze^2}{\hbar c} \right) \frac{|\zeta_{+, \perp}|}{\varepsilon_+ u} \left[ 1 + \frac{1+u^2}{2u^2} \ln(1+u^2) \right].$$

That the momentum-spin correlations in quantum theory of radiation vanish at high energies is as might have been expected from calculations of high energy bremsstrahlung and pair production<sup>(12)</sup>, where to all orders in  $Ze^2/\hbar c$  no correlation of the form  $\zeta \cdot (\mathbf{p} \times \mathbf{k})$  was found.

## APPENDIX A

Consider the matrix element occurring in quantum theory of radiation for an absorption process

$$\mathcal{M} = \int \Psi_2^\dagger(\mathbf{p}_2, \zeta_2, \eta_2) \exp[i\varepsilon_2 t] \boldsymbol{\alpha} \cdot \mathbf{e} \exp[i(\mathbf{k} \cdot \mathbf{r} - \omega t)] \Psi_1(\mathbf{p}_1, \zeta_1, \eta_1) \exp[-i\varepsilon_1 t] d^3x dt.$$

Applying the time reversal operator  $T = i\sigma_y \times (\text{complex conjugation})$  we have

$$\mathcal{M}_T = \int (T\Psi_2)^\dagger \exp[-i\varepsilon_2 t] \boldsymbol{\alpha} \cdot \mathbf{e}^* \exp[-i(\mathbf{k} \cdot \mathbf{r} - \omega t)] (T\Psi_1) \exp[i\varepsilon_1 t] d^3x dt,$$

since now the photon is emitted.

Writing  $\Psi$  as a Born series

$$\Psi = \left\{ \exp[i\mathbf{p} \cdot \mathbf{r}] - \int \mathcal{G}_\eta(\mathbf{r} - \mathbf{r}') V(\mathbf{r}') \exp[i\mathbf{p} \cdot \mathbf{r}'] d^3x' + \dots \right\} u(\mathbf{p}, \zeta),$$

it is easy to show that

$$T\Psi = \left\{ \exp[-i\mathbf{p} \cdot \mathbf{r}] - \int \mathcal{G}_{-\eta}(\mathbf{r} - \mathbf{r}') V(\mathbf{r}') \exp[-i\mathbf{p} \cdot \mathbf{r}'] d^3x' + \dots \right\} u(-\mathbf{p}, -\zeta),$$

noting that if  $u$  is a spinor with spin in the direction  $\zeta$ ,

$$u = \begin{pmatrix} 1 \\ \boldsymbol{\sigma} \cdot \mathbf{p} \\ \varepsilon + 1 \end{pmatrix} v, \quad \zeta \cdot \boldsymbol{\sigma} v = v,$$

(12) H. OLSEN and L. C. MAXIMON: *Phys. Rev.*, **114**, 887 (1959).

then  $i\sigma_y u^*$  is a spinor with spin in the opposite direction,

$$i\sigma_y u^* = \begin{pmatrix} 1 \\ -\boldsymbol{\sigma} \cdot \mathbf{p} \\ \varepsilon - 1 \end{pmatrix} (i\sigma_y v^*), \quad \boldsymbol{\zeta} \cdot \boldsymbol{\sigma} (i\sigma_y v^*) = (i\sigma_y v^*).$$

Thus

$$T\Psi(\mathbf{p}, \boldsymbol{\zeta}, \eta) = \Psi(-\mathbf{p}, -\boldsymbol{\zeta}, -\eta),$$

and invariance of the cross-section under time reversal is equivalent to invariance under the substitution

$$(\mathbf{p}_1, \mathbf{p}_2, \boldsymbol{\zeta}_1, \boldsymbol{\zeta}_2, \mathbf{k}, \mathbf{e}, \eta) \rightarrow (-\mathbf{p}_1, -\mathbf{p}_2, -\boldsymbol{\zeta}_1, -\boldsymbol{\zeta}_2, -\mathbf{k}, \mathbf{e}^*, -\eta).$$

In particular then since the first Born approximation does not depend on the sign of  $\eta$ , spin-dependent terms like

$$\boldsymbol{\zeta}_1 \cdot \mathbf{e} \times \mathbf{e}^*, \quad \boldsymbol{\zeta}_1 \cdot \boldsymbol{\zeta}_2, \quad \boldsymbol{\zeta}_1 \cdot \mathbf{p}_1 \times \mathbf{p}_2 \boldsymbol{\zeta}_2 \cdot \mathbf{p}_1 \times \mathbf{p}_2,$$

etc. may occur in the first Born approximation, while  $\boldsymbol{\zeta}_1 \cdot \mathbf{p}_1 + \mathbf{p}_2$  may only occur in higher Born approximations.

## APPENDIX B

It is only necessary to calculate the two integrals

$$P(a^2) = \int \frac{d^3s \delta(s^2 - p^2)}{[(\mathbf{s} - \mathbf{p})^2 + A^2][(\mathbf{s} - \mathbf{k})^2 + a^2]},$$

and

$$Q(a^2) = \int \frac{d^3s \delta(s^2 - p^2) \mathbf{s}}{[(\mathbf{s} - \mathbf{p})^2 + A^2][(\mathbf{s} - \mathbf{k})^2 + a^2]}.$$

The desired integrals follow from these by the rules

$$(B.1) \quad \begin{cases} I_3 = \frac{\partial}{\partial a^2} P(a^2), \\ I_1 = \frac{1}{2} \nabla_k P(a^2) \cdot \mathbf{k} I_3, \\ I_5 = P(A^2), \end{cases}$$

$$(B.1) \quad \begin{cases} I_6 = Q(\Lambda^2), \\ I_{lm} = \frac{1}{2} \frac{\partial}{\partial k_l} Q_m + I_{4l} k_m. \end{cases}$$

We shall only need the integrals in the limit  $a=0$ . It should be noted that in this limit  $P(a^2)=P(\Lambda^2)=P(0)$ , since there is no divergency from the denominator  $(\mathbf{s}-\mathbf{k})^2+a^2$  when  $a=0$ . This follows since when  $s=p$ , then  $\mathbf{s}-\mathbf{k}$  is never zero.

Using a method due to Feynman<sup>(13)</sup>,  $P$  may be written

$$P = \int d^3s \int_0^1 \frac{dx \delta(s^2 - p^2)}{[s^2 + k^2 + a^2 + (p^2 - k^2 + \Lambda^2 - a^2)x - 2\mathbf{s}(\mathbf{k} - \mathbf{q}x)]^2}.$$

The angular integrations are now easily performed giving

$$P = 2\pi p \int_0^1 dx \{ [p^2 + k^2 + a^2 + (p^2 - k^2 + \Lambda^2 - a^2)x]^2 - 4p^2(\mathbf{k} - \mathbf{q}x)^2 \}^{-1},$$

which may be integrated by standard methods. The result is

$$P = \frac{\pi}{2p(q^2 + a^2)} \left| \ln \frac{(q^2 + a^2)^2}{(k^2 + p^2 + a^2)^2 - 4k^2p^2} - 2 \ln \frac{\Lambda^2}{2p} \right|.$$

In a similar way one finds, as  $Q$  depends on the two vectors  $\mathbf{p}$  and  $\mathbf{k}$  only

$$Q = A\mathbf{p} + B\mathbf{k}.$$

In this case we may take immediately  $a=0$ , thus

$$A = P - \frac{\pi}{2k^2p^2} (p \ln L_2 + p_z \ln L_1),$$

$$B = \frac{\pi}{2k^2p^2} (p \ln L_1 + p_z \ln L_2),$$

where

$$L_1 = \varepsilon(1 - \beta \cos \theta), \quad L_2 = \varepsilon(1 + \beta).$$

(13) R. P. FEYNMAN: *Phys. Rev.*, **76**, 769 (1949).

From the rules Eq. (A.1) we finally find for  $a = 0$ ,

$$(B.2) \quad \left\{ \begin{aligned} I_3 &= \frac{\pi}{pq^2} \left[ \frac{p}{\pi} I_5 - \frac{\varepsilon}{2(\varepsilon-1)} - \frac{1}{q^2} \right], \\ I_4 &= \frac{\pi}{pq^2} \left[ \left( \frac{p}{\pi} I_3 - \frac{1}{q^2} \right) \mathbf{p} + \frac{1}{2} \frac{\varepsilon-1}{\varepsilon} \mathbf{k} \right], \\ I_5 &= \frac{\pi}{pq^2} \left[ \ln L_1 - \ln \frac{1}{2p} \right] \\ I_6 &= \left[ I_5 - \frac{\pi}{2kp u^2} (p \ln L_2 + p_z \ln L_1) \right] \mathbf{p} + \frac{\pi}{2k^2 u^2} (p \ln L_1 + p_z \ln L_2) \mathbf{k} \\ \mathbf{k} \cdot \mathbf{I} &= k\varepsilon I_4 - \frac{1}{2} I_6, \\ \mathbf{p} \cdot \mathbf{I} \times \mathbf{p} &= \frac{\pi}{2k^2} \left[ \frac{p^3}{q^2} - \frac{p\varepsilon}{2k} - \frac{1}{4k} \ln L_2 \right]. \end{aligned} \right.$$

#### RIASSUNTO (\*)

Calcoliamo nel più basso ordine non nullo, dell'approssimazione di Born la polarizzazione trasversa dei fotoelettroni e l'asimmetria, rispetto al piano di polarizzazione, dei fotoni emessi nella annichilazione ad un solo quanto dei positoni polarizzati trasversalmente. Gli effetti sono della stessa natura e dello stesso ordine di grandezza degli effetti di polarizzazione e di asimmetria nello scattering di Mott. Mostriamo che, nella teoria quantistica della radiazione, la correlazione fra momento e spin è proporzionale alla parte immaginaria degli integrali degli elementi di matrice. Il fatto che la correlazione abbia luogo solo nella approssimazione di Born del secondo ordine, mentre gli integrali degli elementi di matrice nella approssimazione di Born del primo ordine sono reali, ha una stretta relazione con l'invarianza rispetto all'inversione del tempo.

(\*) Traduzione a cura della Redazione.



## The Automatic Collection and Reduction of Data for Nuclear Spark Chambers (\*).

H. GELERENTER (\*\*)

*CERN - Geneva*

(ricevuto il 30 Agosto 1961)

**Summary.** — A system is described which dispenses with the traditional use of photographic film for recording the data contained in the discharge of a nuclear spark chamber. Instead, the chamber itself is directly viewed by a television vidicon camera, whose output is digitized for direct input to a computer or for recording on magnetic tape. Preliminary experiments indicate that a measurement precision of 0.1% (*i.e.*, to locate the center of a spark to 1 mm in a meter-wide chamber) will be easy to achieve with ordinary industrial vidicon tubes. The existence of currently available high resolution vidicons makes it likely that this figure can be substantially improved. By coupling the video system directly to an IBM 7090 computer, it is shown that the automatic collection and on-line analysis of 100 000 spark chamber events per day is probably feasible.

### 1. — Introduction.

The development of the nuclear spark chamber as a particle trace detector is currently being pursued with increasing interest at many high energy accelerator laboratories. As a visual particle detecting device, the spark chamber possesses a number of characteristics which, taken together, differentiate it sharply from all other such instruments and, indeed, make it uniquely suitable for certain kinds of experiments <sup>(1)</sup>. We enumerate the most important of these properties as follows:

(\*) This work has been jointly supported by the Ford Foundation and IBM Research.

(\*\*) On leave from: IBM Research Center, Yorktown Heights, N. Y., U.S.A.

<sup>(1)</sup> a) 1960 *Intern. Conf. on Instrumentation for High-Energy Physics* (Berkeley, Sept. 1960); b) 1961 *Argonne Symposium on Nuclear Spark Chambers*, in *Rev. of Sci. Inst.*, vol. **32**, pp. 480-531 (May 1961).

- 1) Extremely short sensitive time (of the order  $1\ \mu\text{s}$ ).
- 2) May be triggered by a system of counters to display a selected interaction.
- 3) Very short recovery time (of the order  $10\ \text{ms}$ ).
- 4) Extremely high signal-to-noise ratio of output.
- 5) Simplicity and low cost of construction and operation, even for large chamber assemblies.

The first two of the listed properties make it possible to place the chamber in a relatively intense particle flux so that interactions occurring with very low cross-sections may be detected and recorded at high rates. Because the chamber is sensitive for so short a time, the triggering event will, in general be all that is displayed. Consequently, the signal-to-noise ratio is favorable in the sense of information content as well as detectability of the trace.

The ten millisecond recovery time, of course, makes it possible to acquire large amounts of data during a short run. For example, using the  $100\ \text{ms}$  long pulse produced by the CERN proton synchrotron every three seconds, one could expect to record about 10 events/pulse, or about 100 000 events during eight hours of running time!

While the newly-developed scintillation and filament chambers share the first three advantages with the spark chamber, they fall far short on the points of signal output and simplicity and low cost of fabrication of large detecting assemblies. As we shall point out below, the intense spark signal eases greatly the potentially difficult problem of high-speed data collection, while the last-mentioned point needs no elaboration.

So silvery a lining must have its concomitant cloud, and, in fact, the spark chamber has several, which assure the continued importance of the bubble chamber as a visual particle detector. The most important of these failings are the limited precision of trace reconstruction attainable with a system where the track element is a spark discharge between two plates, and the fact that the mass of the chamber is heavily concentrated in the chamber plates, so that the point of origin of interactions occurring within the volume of the spark chamber can be determined only by extrapolation. A somewhat less important disadvantage is the fact that the precision of trace reconstruction falls off sharply for tracks more than  $45^\circ$  off the plate normals. To state the limitation in precision of energy and momentum determination is, of course, merely to reiterate the first three points.

Despite the gloomy prognosis of the last paragraph, spark chambers do, in fact, make possible whole new classes of high energy physics experiments that would be difficult or impossible to perform by any other technique. We address this paper, in particular, to an interesting subclass of these experiments

described by ROBERTS <sup>(2)</sup>. These experiments are characterized by the requirement that extremely large numbers of events must be collected and *measured*, either because of statistical demands, or because the desired event occurs rarely, but can be distinguished from an unwanted case only by performing the measurement and analysis of all events releasing the trigger.

As an example of the first kind, ROBERTS cites the determination of angular distributions where visual detection is required to identify the event, and where one might, for example, be searching for a small peak superimposed on a smooth angular distribution.

As a representative of the second class, ROBERTS mentions the extremely interesting problem of the scattering of hyperons by protons. Because of the short hyperon lifetimes, the compound probability for the production of a hyperon and its subsequent scattering before decay is extremely low, making the hydrogen bubble chamber an impractical instrument for collecting scattering data. One can, however, devise triggering systems which will detect the production of a hyperon by, for example, an intense K beam through a liquid hydrogen target. Almost every spark chamber discharge will, then, record the production of a hyperon, but only a small fraction of these will have scattered before decay. Since the scattering occurs in an interaction medium placed inside the spark chamber, it is «in the dark» with respect to our visual detection system, and can be detected only by kinematical reconstruction of each production event.

One might point out that in the experiments described above, the spark chamber may be realistically considered as a very high resolution, close-packed, three dimensional array of very fast counters. Our proposal, then, is for a high-speed, automatic, real time system for determining which of the counters in such an array has fired at a given time. From the latter point of view, a spark chamber is no longer a cheap, but blurry bubble chamber, but rather a significant improvement in high-speed particle counter technology.

## 2. — The problem.

In order that our discussion may be concretely based, we shall develop our system requirements for a particular spark chamber configuration and a particular mode of operation. While the generalization will be, for the most part, obvious, we shall, in summarizing, indicate the limitations of the technique and the conditions under which certain critical specifications may be relaxed.

(2) A. ROBERTS: unpublished report.

We assume, then, the following:

- 1) one-meter wide spark chamber;
- 2) 100 spark gaps in the assembly;
- 3) position of each spark to be determined to 1 mm (1 part in 1000);
- 4) data collection at rate of 100 000 events/day;
- 5) spark chamber recovery time of 10 ms;
- 6) one 100 ms long proton synchrotron pulse every 3 s;
- 7) on the average, each gap will display 5 sparks;
- 8) sparks about 1 mm wide.

The specification for co-ordinate precision of 1 mm in a meter may, of course, be replaced by any equivalent ratio; for example,  $\frac{1}{2}$  mm in a 50 cm wide chamber might possibly represent a more useful configuration

A goal of 100 000 events/day is attractive for an on-line real-time 7090 coupled system, since, as we have already pointed out, these could be collected in about eight hours. This arrangement would allow one to assign the second shift of computer time to the spark chamber production run, leaving the full daytime shift to the more traditional uses of the computer.

The low information content (in the information-theoretic sense) of a single spark chamber discharge is a well-publicized fact. For our representative configuration, 7 bits are required to specify the plate co-ordinate (*i.e.*, which one of 100 gaps contains the spark), 10 bits to specify the gap co-ordinate (the position of the spark within the gap) to 1 part in 1000. We may choose to allow 3 bits to specify an additional useful quantity, the intensity of the spark (allowing for eight distinguishable levels). The latter quantity should significantly simplify the problem of reconstructing the event automatically. A single «view» of the chamber, then, will contain, at an average of 5 sparks/gap, 500 spark co-ordinates of 20 bits each, or about 10 000 bits/view. Again for the purpose of simplifying automatic reconstruction, we allow for 3 «views» of the discharge, making a grand total of 30 000 bits/discharge, or fewer than 1000 thirty-six bit computer words. We hasten to point out that for most experiments, our estimate is, without doubt, generous. Clearly, different interactions will produce different numbers of secondary particles to be recorded.

### 3. - The direct digitization of spark chamber «pictures».

Thus far, we have tacitly assumed that any large scale spark chamber data-reduction system will entail the completely automatic reconstruction and recognition of the events of interest, as well as automatic measurement and



interpretation. There is nothing particularly bold about the foregoing presumption: the properties of a spark chamber and the nature of the data produced by it lead one quickly to the latter conclusion (\*). We shall not dwell upon this point, except to mention briefly the most important factors favorable to a completely automatic system. These are: *a*) the relatively low maximum precision of the primary data; *b*) the almost complete absence of noise and extraneous information; *c*) the event displayed will have been preselected by the triggering system; *d*) triviality of the stereo reconstruction due to the fact that the same point is measured in all views; and *e*) sparks in a given gap belonging to different tracks are often of different intensity.

Accepting the foregoing as a point of departure, we propose to eliminate the introduction of photographic film as an intermediate data storage medium. Instead, the spark chamber is viewed by commercially available vidicon-type television camera tubes, whose output is immediately digitized for input to a high-speed digital computer. Alternatively, the information may be stored on magnetic tape, for later processing.

The advantages of dispensing with the film are easy to see. For each of the experiments mentioned above, one might collect perhaps  $10^6$  to  $10^7$  3-view «pictures». Under such conditions, film and processing costs, bookkeeping procedures, and storage space requirements become serious problems. But by far the most important advantage lies in the elimination (for the computer-coupled system) or drastic reduction (for magnetic tape) of the time lag between the collection and the analysis of the data. Since magnetic tape may be erased and reused, the advantages of cost and space reduction are not lost in the latter case.

We must emphasize the fact that it is quite possible to store *all* of the information produced by the spark discharge in digital form, including an intensity figure for each spark. If a daily magnetic tape of the raw data is also produced by the directly-coupled system, one could visually scan at will any doubtful event merely by having a computer program reconstruct the picture on a cathode ray output tube, *with no loss of useful information*. In fact, the event could easily be reconstructed in slowly rotating perspective on the screen, for the amusement of the physicist, if not as an aid in recognition and interpretation. Such doubtful events would lie compactly assembled on a special tape, the daily tapes being returned to service.

Granting the desirability of eliminating the film, the feasibility of doing so has been demonstrated in a preliminary experiment performed at CERN. An ordinary off-the-shelf 1" commercial vidicon in an inexpensive industrial

(\*) KOESTER and ROBERTS both consider the automatic scanning and interpretation of spark chamber photographs in ref. (1) *b*).



television camera was used to examine the problem of securing adequate precision of measurement.

A vidicon-type camera tube has much to recommend it for our purposes in preference to the more highly-developed image orthicon. Both are storage-type tubes, in which the optical image is converted into a distribution of charges on a target plate, and subsequently read by scanning with an electron beam. Charge images may be preserved for a significant fraction of a second without serious degradation. In the orthicon, the image is produced by photoemission; in the vidicon, by photoconduction. Vidicons are considerably simpler and more stable in operation than image orthicons. They are, consequently, much less expensive, and require simpler operating circuits.

For spark chamber data collection, vidicons possess a further critical advantage. The formation of the image charge distribution in a vidicon is a passive process; electrons leak through a charged photoconductor where the target has been exposed to light. Image formation is, therefore, unaffected by the intense electrical noise produced by discharging the spark chamber. The process of converting the image into a time-varying current by scanning with an electron beam can wait for complete quiescence in the high-powered transmitter that a spark chamber, in fact, is. The image orthicon, on the other hand, includes an electron image intensification section before the target, which will probably be highly susceptible to the electrical noise produced by the spark discharge. Our preliminary experiment has confirmed the insensitivity of the vidicon to the latter condition.

All tubes employing electron beam scanning are, of course, disturbed by varying magnetic fields. However, unless a spark chamber is to be used in conjunction with a pulsed magnetic field, the latter are not expected to be especially intense in the vicinity of the chamber, so that one may successfully resort to magnetic shielding of the vidicon cameras. If a pulsed magnetic field is indeed to be used, the rate at which the chamber may be operated will be determined by the decay time of the field rather than the recovery time of the chamber or the information transfer rate of the vidicon system.

In order to examine the requirements for the video section of the data collection system, we assume the following plan of operation. During the ten milliseconds available between « pictures », we allow perhaps the first millisecond for all noise transients to die out. The next five milliseconds are used for scanning the data from the tube, and the remaining four milliseconds are used to erase the after-image from the target by flooding it with electrons.

In the five milliseconds allotted to scanning, the beam must make 100 sweeps of the image target; one for each gap. Dividing each 50  $\mu$ s sweep into 1000 units, the electron beam must be able to detect the image of a line approximately 1 unit in width to a precision of 1 unit (0.1%).

One will readily note that the term « resolution » has thus far been stu-

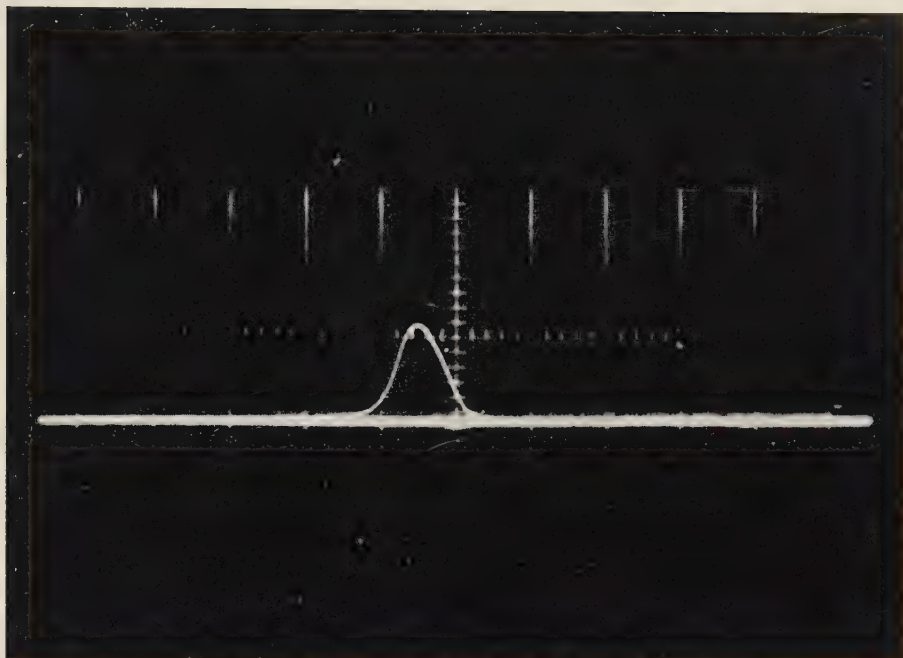


Fig. 1. — Video signal obtained from 10 kV spark in alcohol-saturated argon. Each square represents  $\frac{1}{50}$  of a full vidicon sweep horizontal scale; 1 V vertical scale.

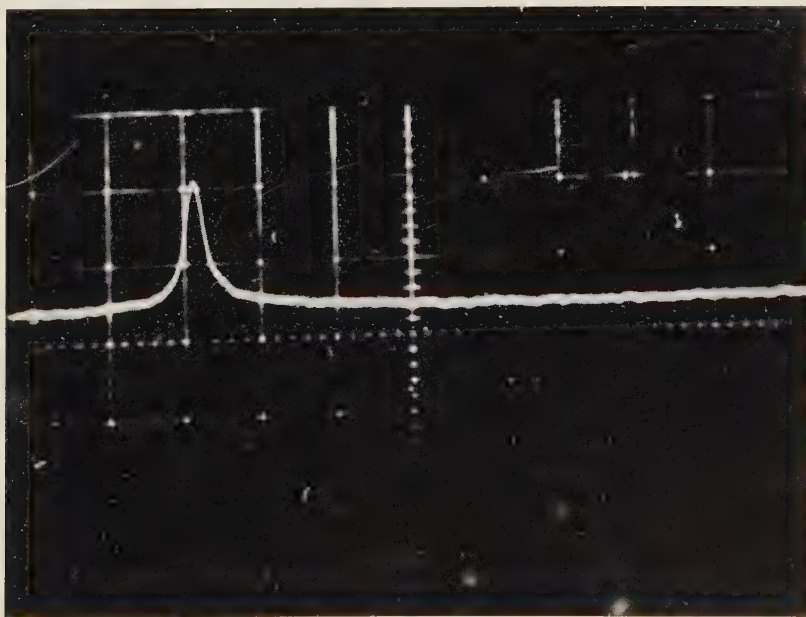


Fig. 2. — Video signal obtained from mercury-arc illuminated slit 0.47 mm wide. Each square represents  $\frac{1}{50}$  of a full vidicon sweep horizontal scale; 1 V vertical scale.



diously avoided in specifying vidicon requirements. The resolving power of an optical system (for photons or electrons) is a well-defined concept. It refers to the ability of the system to form two separate and distinguishable images of two separate objects. Thus, when a vidicon tube is represented as being able to resolve, let us say, 400 TV lines (or 200 optical line pairs) at 45% modulation, the following is implied. If an object consisting of 200 pairs of alternating black and white stripes is imaged on the full width of the target, the periodic signal current one measures when sweeping across the pattern will be, at its minimum, 45% less than at maximum, after allowing for the constant dark current. Since, for our purpose, we do not demand that two lines one unit apart be separated, but merely that one line one unit wide be detected, a vidicon of considerably less than 500 optical line pair resolution will suffice for a precision of one part in a thousand, providing that the signal is sufficiently intense to bring it well out of the noise. Such a tube will, of course, produce a signal broader than the line being scanned, but because of the low noise level, the center of the signal will accurately represent the center of the line.

The oscillograms below are Tektronix displays of the video signal obtained with an ACEC industrial closed circuit TV camera fitted with a one-inch PTW 255 IND vidicon tube. The scanning speed of the unit, about 60  $\mu$ s/sweep, is within 20% of the sweep speed requirement for our representative system. Fig. 1 is a single sweep display of the signal produced by a 10 kV spark in an alcohol-argon filled single gap spark chamber triggered by cosmic rays passing through the chamber. The chamber was positioned so that its 12 cm width took up about one eighth of the full vidicon sweep (*i.e.*, a full sweep to scan a meter-wide chamber). The oscilloscope setting (1  $\mu$ s/cm sweep speed; 1 V/cm sensitivity) was such that a square on the face plate scale represents about 2 cm of spark chamber gap. Our requirement for one part per thousand precision, then, or one mm in a meter, translates into the requirement that the center of the pulse displayed in Fig. 1 be determined to 1/20 of a square. Despite the makeshift experimental conditions, and the fact that no attempt was made to optimize either the vidicon operating conditions or the behavior of the spark chamber, the spark signal obtained is certainly adequate for our purposes.

Fig. 2 is a display of the video signal obtained by replacing the spark chamber with a 0.47 mm slit at the same distance. Oscilloscope settings were identical with those obtaining for Fig. 1. The center of the slit signal could easily be determined to 1/2 000 of the sweep (*i.e.*,  $\frac{1}{2}$  mm in a meter). Further narrowing of the slit produced no corresponding narrowing of the signal pulse, indicating that Fig. 2 represents the effective scanning spot «cross-section» for the present experimental set-up (including amplifier rise time).

#### 4. - Digitization of the video signal.

A more serious problem than that of securing the required precision of spark position measurement is that of accuracy in digitizing the sweep position along the image of the gap. It is unlikely that a sufficiently well-regulated power supply can be designed to do this in purely analogue mode without going to great expense. Fig. 3 illustrates our proposed solution to the problem.

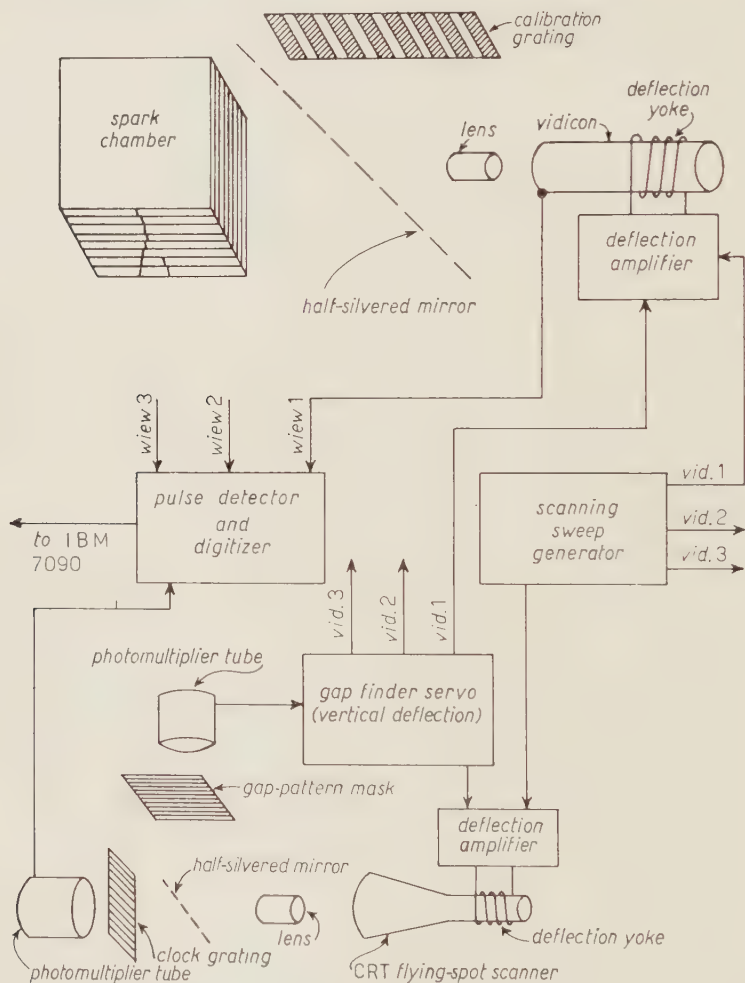


Fig. 3. - Digitizing and gap-finding system.

As is the case for a number of photographic image processing systems currently being developed, we introduce precisely ruled gratings to link our electronics to a physical standard of length.



Since we cannot use our vidicon electron beam to simultaneously scan the image and supply grating signals, a slaved high resolution cathode ray tube flying spot scanner, driven by the same deflection voltage that sweeps the vidicon image, is used to produce the required clock pulses. The CRT spot is imaged on a grating, and the signal from the photomultiplier behind the grating is used to supply timing pulses to the digitizer.

The digitizing circuitry will accept the timing pulses and insert uniformly spaced interpolation pulses to give the required precision of measurement. If the CRT grating is designed to give 64 timing pulses during the  $50\ \mu\text{s}$  sweep, and the digitizer inserts 16 interpolation pulses between adjacent timing pulses to give our specified 1024 units, the scaler will be almost identical to one currently under development at Brookhaven National Laboratories for the high-speed HPD bubble chamber data reduction system <sup>(3)</sup>. Assuming that the center of the signal pulse from the vidicon is defined as that abscissa which divides the signal into two equal areas, the signal integrating circuits, too, will be similar to those designed for the latter system.

As often as necessary, between accelerator pulses, the vidicons are calibrated against the scanner to correct for drift in the vidicon and CRT characteristics. Calibration may easily be accomplished while the spark chamber is dark by illuminating a calibration grating properly positioned behind a half-silvered mirror (every accelerator pulse, if necessary). Our experiment indicates that one can well afford the spark image light loss due to the interposed half-silvered glass. Note that each vidicon is to be separately calibrated over its entire face with respect to the flying spot scanner.

Although one may resort to other schemes than the above to ensure accuracy of digitization, the availability of the slaved spot on the CRT offers an additional dividend. By splitting the image of the spot, it may be used, in

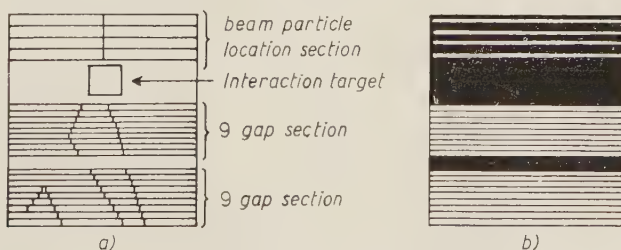


Fig. 4. - Gap-finder. The mask (b) corresponds to the spark chamber configuration (a).

conjunction with a mask supplied for the particular experiment, to guide the vidicon sweep in scanning any arbitrary (but parallel) spark chamber gap configuration. The mask (Fig. 4) is prepared so that each gap to be scanned

<sup>(3)</sup> P. W. HOUGH: private communication.

is represented to scale by a clear stripe on a transparent base. The remainder of the mask is opaque. A photomultiplier behind the mask indicates whether the electron beam is in the gap (to the accuracy of voltage regulation: perhaps  $\frac{1}{4}\%$ ). In operation, the beam is positioned in the first gap and swept its length. At the end of the sweep, the vertical deflection voltage is switched on until the photomultiplier signal indicates that the beam has found the next gap. The beam is swept in alternate directions in adjacent gaps; the sign of the horizontal deflection voltage determining whether the digitizing scaler is to count up or down. Periodically, the «gap finder» would be checked against the spark chamber gaps themselves.

## 5. - Reduction of the digital data.

Assuming a direct link to the IBM 7090, we examine now the data processing problem which we have brought upon ourselves. During the 10 ms recovery time of the chamber, we have indicated that we must expect to extract about 1000 36-bit words of information from the ensemble of three viewing cameras. This information, then, must be transferred to the computer at an average rate of one word every 10  $\mu$ s. Since the 7090 Direct Data Connection is able to accept information at a maximum rate of one word every 6  $\mu$ s, no difficulty is anticipated here, although a small buffer storage will be necessary to smooth out the data flow rate. Since the IBM 729 IV tape unit will require a full second to record the 10 000 words of data (10 events) accumulated during a machine pulse, all of the raw data will have to be kept in core storage between accelerator pulses.

Information is stored on tape at a density of 1000 words/foot, so that a 2 400 foot tape reel will contain about 2 500 events, or the output of 12 minutes of running time. The 40 reels of tape containing an 8-hour day's run will be reused, after their contents have been reviewed, and unusual and doubtful events have been recopied on a small fraction of a single reel (\*).

All ten events collected from a single pulse are to be processed during the three seconds available between accelerator pulses, allowing 300 ms/event processing time. Assuming that the average 7090 instruction consumes 3 cycles of machine time, 50 000 instructions are available for processing an event of about 500 points in space, or 100 instructions/point. It is, of course, impossible to predict with certainty that the instruction allowance is adequate, but we might make the following points. First, the events recorded will all fall

(\*) It is only the anticipated resistance of the spark chamber physicist that prevents the author from suggesting that one might dispense with the daily tape, and record only the «special events».

into the narrowly circumscribed class permitted by the spark chamber triggering system, so that interpretation is greatly simplified. Second, the rare events that threaten to require much more than the allotted time can be put off for later off-line consideration on the special-events tape. Finally, the time allowed per point compares very favorably with that available for bubble-chamber event reconstruction in the HPD system currently under development at CERN, Brookhaven, and Berkeley <sup>(4)</sup>, whereas the precision required in our case is an order of magnitude lower.

## 6. - Conclusion.

Most of the specifications for our representative system have been quite arbitrary; they are certainly not inviolable. Thus, if 100 000 events/day were impossible to attain, 50 000 events/day would be likely to satisfy even the most statistics-crazed physicist. A chamber narrower than the allowed 1 m could be measured with correspondingly-increased precision. On the other hand, to maintain the specified 1 mm precision in a two-meter wide chamber, one would probably have to take advantage of currently available high-resolution  $1\frac{1}{2}$  in. vidicons operated under special high-resolution conditions. One such tube, soon to be distributed as a standard commercial component by RCA, could be expected to at least double the resolution (and hence the measuring precision) of the system using a 1 inch vidicon.

Increasing the number of chamber gaps will, of course, increase the data collection and processing time per event, as well as severely tax the beam positioning deflection voltage regulating circuitry. Decreasing the number of plates is not, however, likely to increase substantially the possible number of events/pulse, despite the shorter time required for data collection and processing, for the latter quantity is limited not only by the recovery time of the spark chamber, but also by the characteristics of the vidicon tube (\*).

\* \* \*

The work reported in this paper stems from a remark made by L. KOWARSKI to the effect that the introduction of photographic film in the spark chamber experimental procedure was probably superfluous. Dr. KOWARSKI, too, was the author's gracious and effective host during his stay at CERN, which was supported by the Ford Foundation and the IBM Research Center.

(<sup>4</sup>) H. WHITE: private communication.

(\*) In particular, the rate at which new information can replace the old on the target plate of a vidicon depends on the photoconductive and capacitive lag of the tube at the prevailing operating conditions.

D. WISCOTT, N. H. LIPPMAN, G. CULLIGAN and H. KUHN were most helpful in the author's effort to get genuine spark chamber sparks for the vidicon tests, and J. RICHEZ made the necessary modifications of the ACEC television camera to make it suitable for our purposes. The measurements were performed with the competent assistance of Mr. RICHEZ.

#### RIASSUNTO (\*)

Si descrive un sistema che dispensa dall'usare la tradizionale pellicola fotografica per registrare i dati contenuti nella scarica della camera a scintille. Invece la camera stessa viene osservata direttamente da una camera vidicon televisiva, la cui uscita viene digitizzata per l'alimentazione diretta in un calcolatore o per la registrazione su nastro magnetico. Esperimenti preliminari indicano che una precisione dello 0.1% nelle misure (cioè la localizzazione entro 1 mm del centro di una scintilla in una camera larga un metro) si può ottenere facilmente con gli ordinari tubi vidicon industriali. L'esistenza di vidicon ad alta risoluzione, correntemente reperibili, rende verosimile un miglioramento sostanziale di questa percentuale. Si mostra che, accoppiando direttamente il sistema video ad un calcolatore IBM 7090, si può probabilmente effettuare la raccolta automatica e l'elaborazione in linea di 100 000 eventi della camera a scintille al giorno.

(\*) *Traduzione a cura della Redazione.*

# Tensor Operator for Electron Polarization (\*).

D. M. FRADKIN

*Institute for Atomic Research and Department of Physics,  
Iowa State University - Ames, Iowa*

R. H. GOOD, JR. (\*\*)

*Institute for Advanced Study - Princeton, N. J.*

(ricevuto il 1<sup>o</sup> Settembre 1961)

**Summary.** — In this paper it is shown that the polarization of a free Dirac particle can be treated in a covariant way in terms of an anti-symmetric second-rank tensor operator which commutes with the Hamiltonian. The operator has the interpretation that in the rest system of the particle the space-space part is the spin and the space-time part is zero. In the quantized theory the second-rank tensor description of the polarization is a more appropriate notion than the four-vector description. The converse holds for the Foldy-Wouthuysen mean spin.

## 1. - Introduction.

Recently it was shown <sup>(1)</sup> that the operator

$$(1) \quad O = (H/|H|)\boldsymbol{\sigma} \cdot \hat{\mathbf{p}}\hat{\mathbf{p}} + \hat{\mathbf{p}} \times (\beta \boldsymbol{\sigma} \times \hat{\mathbf{p}}),$$

which was first used by STECH <sup>(2)</sup> to describe the polarization of a free Dirac

(\*) This research was partially done in the Ames Laboratory of the U. S. Atomic Energy Commission.

(\*\*) National Science Foundation Senior Postdoctoral Fellow 1960-61, on leave from Institute for Atomic Research and Department of Physics, Iowa State University, Ames, Iowa.

<sup>(1)</sup> D. M. FRADKIN and R. H. GOOD jr.: *Rev. Mod. Phys.*, **33**, 343 (1961).

<sup>(2)</sup> B. STECH: *Zeits. Phys.*, **144**, 214 (1956).



particle, is to be interpreted as the laboratory-system operator for the spin of the particle in its own rest frame. Here  $H$  is the Hamiltonian,

$$(2) \quad H = \alpha \cdot \mathbf{p} + \beta,$$

$\hat{\mathbf{p}}$  is the operator  $\mathbf{p}/p$ , where  $\mathbf{p}$  is  $-i\hbar\nabla$ , and the notation is mostly the same as in reference (1). Also it was shown that the four-vector operator of BARGMANN and WIGNER (3), which may be written in either of the forms

$$(3) \quad T_\mu = \gamma_5(i\gamma_\mu - \bar{p}_\mu),$$

$$(4) \quad T_\mu = -\frac{1}{2}\epsilon_{\mu\nu\sigma\tau}\gamma_\nu\gamma_\sigma\bar{p}_\tau,$$

may be interpreted as the Lorentz transform of  $(\mathbf{O}, 0)$  from the rest to the laboratory system. Here  $p_\mu$  is  $(\mathbf{p}, iH)$ . Both  $\mathbf{O}$  and  $T_\mu$  commute with  $H$ .

In the classical theory which develops equations of motion for a polarized particle in an external field, there are two equivalent ways to treat the polarization of the particle. Given the polarization  $\mathbf{O}$  in the instantaneous rest system, one may, following BARGMANN, MICHEL, and TELEGGI (4), define a four-vector  $T_\mu$  by assigning it the components  $(\mathbf{O}, 0)$  in the rest system. The other possibility is to define an antisymmetric tensor  $R_{\mu\nu}$  by letting the components  $R_{ij}$ ,  $R_{i4}$  be  $\epsilon_{ijk}O_k$ , 0 in the rest system; this was done by FRENKEL (5) and KRAMERS (6). The two approaches are equivalent, as has been shown recently in detail by FORD and HIRT (7).

This raises the question: Is it possible to introduce in a similar way an antisymmetric tensor Dirac operator  $R_{\mu\nu}$  which also commutes with the Hamiltonian and gives a description of the electron polarization? The purpose of this paper is to show that this program can indeed be carried out and to exhibit some of the properties of the tensor operator.

The existence of a tensor operator treatment of electron polarization was foreseen by ROSE (8). CALOGERO (9) and FRONSDAL and ÜBERALL (10) have considered operators related to those introduced here, but without defining them in such a way that they are constants of the motion.

(3) V. BARGMANN and E. P. WIGNER: *Proc. Nat. Acad. Sci. U. S.*, **34**, 211 (1948).

(4) V. BARGMANN, L. MICHEL and V. L. TELEGGI: *Phys. Rev. Lett.*, **2**, 435 (1959).

(5) J. FRENKEL: *Zeits. Phys.*, **37**, 243 (1926).

(6) H. A. KRAMERS: *Quantum Mechanics* (Amsterdam, 1957), Sec. 57.

(7) G. W. FORD and C. W. HIRT: to be published.

(8) M. E. ROSE: *Relativistic Electron Theory* (New York, 1961), p. 105.

(9) F. CALOGERO: *Nuovo Cimento*, **20**, 280 (1961).

(10) C. FRONSDAL and H. ÜBERALL: *Phys. Rev.*, **111**, 580 (1958).

## 2. - Definitions of the operators.

For a particle in a state with definite momentum  $\mathbf{q}$  and energy  $E = (q^2 + 1)^{\frac{1}{2}}$  the Lorentz transformation from the rest to the laboratory system is given by

$$\begin{aligned} (5a) \quad x_{lab\mu} &= a_{\mu\nu} x_{rest\nu}, \\ (5b) \quad a_{ij} &= \delta_{ij} + (E + 1)^{-1} q_i q_j, \\ (5c) \quad a_{4i} &= -a_{i4} = i q_i, \\ (5d) \quad a_{44} &= E. \end{aligned}$$

Corresponding to a polarization direction  $\hat{\mathbf{s}}$ , one may define a four-vector  $n_\mu$  by assigning its components to be  $(\hat{\mathbf{s}}, 0)$  in the rest system; eq. (5) then give

$$\begin{aligned} (6a) \quad \mathbf{n} &= \hat{\mathbf{s}} + (E + 1)^{-1} \mathbf{q} \cdot \hat{\mathbf{s}} \mathbf{q}, \\ (6b) \quad n_4 &= i \mathbf{q} \cdot \hat{\mathbf{s}}. \end{aligned}$$

Similarly one may define an antisymmetric second-rank tensor  $m_{\mu\nu}$  by assigning the components  $m_{ij}$ ,  $m_{i4}$  to be  $\varepsilon_{ijk} s_k$ , 0 in the rest system. In detail, the components turn out to be

$$\begin{aligned} (7a) \quad m_{ij} &= \varepsilon_{ijk} [E \hat{\mathbf{s}} - (E + 1)^{-1} \mathbf{q} \cdot \hat{\mathbf{s}} \mathbf{q}]_k, \\ (7b) \quad m_{i4} &= i (\mathbf{q} \times \hat{\mathbf{s}})_i. \end{aligned}$$

Here  $n_\mu$  and  $m_{\mu\nu}$  are defined for a specific polarization direction, momentum, and energy. One may generalize these quantities into operators, which are defined for a specific polarization direction, by replacing  $\mathbf{q}$  and  $E$  by the momentum and energy operators,  $(H/|H|)\mathbf{p}$  and  $|H|$ . Thus the operators  $n_{\mu op}$  and  $m_{\mu\nu op}$  are given by

$$\begin{aligned} (8a) \quad \mathbf{n}_{op} &= \hat{\mathbf{s}} + (|H| + 1)^{-1} \mathbf{p} \cdot \hat{\mathbf{s}} \mathbf{p}, \\ (8b) \quad n_{4 op} &= i (H/|H|) \mathbf{p} \cdot \hat{\mathbf{s}}, \\ (9a) \quad m_{ij op} &= \varepsilon_{ijk} [(H/|H|) \hat{\mathbf{s}} - (|H| + 1)^{-1} \mathbf{p} \cdot \hat{\mathbf{s}} \mathbf{p}]_k, \\ (9b) \quad m_{i4 op} &= i (H/|H|) (\mathbf{p} \times \hat{\mathbf{s}})_i. \end{aligned}$$

The operator  $(H/|H|)p_\mu$  is generated in a parallel way from the value  $(0, i)$  in the rest system. Since everything commutes, the validity of tensor equations relating  $\bar{p}_\mu$ ,  $n_{\mu op}$ , and  $m_{\mu\nu op}$  is easily tested by specializing to the rest system.

In this way the relations

$$\begin{aligned}\bar{p}_\mu \bar{p}_\mu &= -1, \\ n_{\mu \circ \mathfrak{D}} n_{\mu \circ \mathfrak{D}} &= 1, \\ m_{\mu \nu \circ \mathfrak{D}} m_{\mu \nu \circ \mathfrak{D}} &= 2, \\ \bar{p}_\mu n_{\mu \circ \mathfrak{D}} &= 0, \\ \bar{p}_\mu m_{\mu \nu \circ \mathfrak{D}} &= 0, \\ m_{\mu \nu \circ \mathfrak{D}} &= i \varepsilon_{\mu \nu \varrho \sigma} (H/|H|) \bar{p}_\varrho n_{\sigma \circ \mathfrak{D}}, \\ n_{\sigma \circ \mathfrak{D}} &= \frac{1}{2} i \varepsilon_{\mu \nu \varrho \sigma} (H/|H|) \bar{p}_\varrho m_{\mu \nu \circ \mathfrak{D}}\end{aligned}$$

are easily established.

The operators  $T_\mu$  and  $R_{\mu\nu}$  are defined in such a way that they bear the same relation to  $\mathbf{O}$  as  $n_{\mu \circ \mathfrak{D}}$  and  $m_{\mu \nu \circ \mathfrak{D}}$  bear to  $\hat{\mathbf{s}}$ , that is,

$$(10a) \quad \mathbf{T} = \mathbf{O} + (|H| + 1)^{-1} \mathbf{p} \cdot \mathbf{O} \mathbf{p},$$

$$(10b) \quad T_4 = i(H/|H|) \mathbf{p} \cdot \mathbf{O},$$

$$(11a) \quad R_{ij} = \varepsilon_{ijk} [ |H| \mathbf{O} - (|H| + 1)^{-1} \mathbf{p} \cdot \mathbf{O} \mathbf{p} ]_k,$$

$$(11b) \quad R_{i4} = i(H/|H|) (\mathbf{p} \times \mathbf{O})_i,$$

and where  $R_{\mu\nu}$  is to be antisymmetric. It is known that this definition of  $T_\mu$  coincides with that of eq. (3) or eq. (4). Since  $\mathbf{O}$  commutes with  $H$ , it is clear from the beginning that  $R_{\mu\nu}$  commutes also,

$$[R_{\mu\nu}, H] = 0.$$

When eqs. (1) and (2) are used to express  $R_{\mu\nu}$  in terms of the primitive matrices the results are

$$R_{ij} = \varepsilon_{ijk} |H|^{-1} [\beta \boldsymbol{\sigma} - \gamma_5 \mathbf{p} + \mathbf{p} \times (\beta \boldsymbol{\sigma} \times \mathbf{p})]_k,$$

$$R_{i4} = i |H|^{-1} [\mathbf{p} \times (\boldsymbol{\sigma} - i \beta \boldsymbol{\alpha} \times \mathbf{p})]_i.$$

Although the different components of  $\mathbf{O}$  do not commute, one may nevertheless still take advantage of the formal correspondence to a Lorentz transformation by writing down tensor-type equations which are valid in the rest system, as long the order of the  $\mathbf{O}$  factors is not disturbed. The components of  $T_\mu$  in the rest system must be assigned to be  $(\mathbf{O}, 0)$  and the components  $R_{ij}$ ,  $R_{i4}$

must be assigned to be  $\varepsilon_{ijk}O_k$ , 0. In this way the relations

$$T_\mu T_\mu = \mathbf{O} \cdot \mathbf{O} = 3,$$

$$R_{\mu\nu} R_{\mu\nu} = 6,$$

$$\bar{p}_\mu T_\mu = 0,$$

$$\bar{p}_\mu R_{\mu\nu} = 0,$$

$$(12) \quad R_{\mu\nu} = i\varepsilon_{\mu\nu\rho\sigma}(H|H|)\bar{p}_\rho T_\sigma,$$

$$T_\sigma = \frac{1}{2}i\varepsilon_{\mu\nu\rho\sigma}(H|H|)\bar{p}_\rho R_{\mu\nu},$$

$$(13) \quad T_\mu n_{\mu\text{op}} = \mathbf{O} \cdot \hat{\mathbf{s}},$$

$$(14) \quad R_{\mu\nu} m_{\mu\nu\text{op}} = 2\mathbf{O} \cdot \hat{\mathbf{s}}$$

are easily established.

### 3. - Discussion.

Eq. (12) is a convenient form for  $R_{\mu\nu}$  because all the factors on the right commute. However, by combining eqs. (3) and (12), one sees that  $R_{\mu\nu}$  may also be written in the form

$$(15) \quad R_{\mu\nu} = \varepsilon_{\mu\nu\rho\sigma}(H|H|)\gamma_5\gamma_\rho\bar{p}_\sigma.$$

This is close to an operator which has been discussed by CALOGERO <sup>(9)</sup>.

A system is said to be polarized in the  $\hat{\mathbf{s}}$  direction if it is in an eigenstate of  $\mathbf{O} \cdot \hat{\mathbf{s}}$  with eigenvalue  $+1$ . It is seen that the operator  $\mathbf{O} \cdot \hat{\mathbf{s}}$  may be written as  $T_\mu n_{\mu\text{op}}$  or as  $\frac{1}{2}R_{\mu\nu} m_{\mu\nu\text{op}}$ . Other forms are found by combining eqs. (13) and (3) to obtain

$$\mathbf{O} \cdot \hat{\mathbf{s}} = i\gamma_5\gamma_\mu n_{\mu\text{op}}$$

and by combining eqs. (14), (12), and (4) to obtain

$$\mathbf{O} \cdot \hat{\mathbf{s}} = -\frac{1}{2}i(H|H|)\gamma_\mu\gamma_\nu m_{\mu\nu\text{op}}.$$

When the operators are applied to the wave function of a state with definite energy and momentum,  $n_{\mu\text{op}}$  and  $m_{\mu\nu\text{op}}$  may be replaced by  $n_\mu$  and  $m_{\mu\nu}$ . In this case the operator  $\mathbf{O} \cdot \hat{\mathbf{s}}$  may be replaced by  $i\gamma_5\gamma_\mu n_\mu$ , the MICHEL and WIGHTMANN <sup>(11)</sup> covariant description of the spin, or by  $-\frac{1}{2}i(H|H|)\gamma_\mu\gamma_\nu m_{\mu\nu}$ .

<sup>(11)</sup> L. MICHEL and A. S. WIGHTMAN: *Phys. Rev.*, **98**, 1190 (1955).

The equivalence of these last two operators was shown by FRONSDAL and ÜBERALL <sup>(10)</sup>.

The Foldy-Wouthuysen <sup>(12)</sup> transform of  $\mathcal{O}$  is  $\beta\sigma$ , whereas the transform of their mean spin operator is  $\sigma$ . Therefore in the present notation the Foldy-Wouthuysen mean spin operator is  $(H/|H|)\mathcal{O}$ . It is clear that the same process as used above to generate  $T_\mu$  and  $R_{\mu\nu}$  from the polarization  $\mathcal{O}$  could also be used to infer operators appropriate to the mean spin and that the results would differ from  $T_\mu$  and  $R_{\mu\nu}$  only by the factor  $H/|H|$ . Thus, in contrast to the operators of eqs. (4) and (15) for the polarization, one would obtain the operators

$$\begin{aligned}\tilde{T}_\mu &= -\frac{1}{2}\varepsilon_{\mu\nu\varrho\sigma}(H/|H|)\gamma_\nu\gamma_\varrho\bar{p}_\sigma, \\ \tilde{R}_{\mu\nu} &= \varepsilon_{\mu\nu\varrho\sigma}\gamma_5\gamma_\varrho\bar{p}_\sigma,\end{aligned}$$

for the mean spin.

It is known that it is appropriate to use the operator  $T_\mu$  in extending the theory of polarization to the case of a single Dirac particle in an external electromagnetic field <sup>(1)</sup>. The operator  $R_{\mu\nu}$  would not be appropriate for this purpose because of the  $H/|H|$  factor. It is difficult to generalize  $H/|H|$  to the case where there are electromagnetic fields present.

In making the transition to the quantized theory an additional factor of  $H/|H|$  comes in because of the anticommuting of the basic operators. For example, in the  $c$ -number theory the expectation values of the energy and momentum are

$$\int \psi^+ |H| \psi \, d^3x \quad \text{and} \quad \int \psi^+ (H/|H|) \mathbf{p} \psi \, d^3x,$$

but in the  $q$ -number theory the operators for the energy and momentum are

$$\int \psi^+ H \psi \, d^3x \quad \text{and} \quad \int \psi^+ \mathbf{p} \psi \, d^3x.$$

Avoiding the occurrence of the  $H/|H|$  factor, one defines a tensor operator for polarization,

$$\mathcal{R}_{\mu\nu} = \int \psi^+ \varepsilon_{\mu\nu\varrho\sigma} \gamma_5 \gamma_\varrho \bar{p}_\sigma \psi \, d^3x,$$

and a vector operator for mean spin,

$$\tilde{\mathcal{T}}_\mu = - \int \psi^+ \frac{1}{2} \varepsilon_{\mu\nu\varrho\sigma} \gamma_\nu \gamma_\varrho \bar{p}_\sigma \psi \, d^3x.$$

<sup>(12)</sup> L. L. FOLDY and S. A. WOUTHUYSEN: *Phys. Rev.*, **78**, 29 (1950).



For non-interacting particles these are conserved Lorentz tensors with the reflection properties expected from the fact that  $\mathbf{O}$  is an angular momentum. The proof for  $\mathcal{R}_{\mu\nu}$  and the continuous group, for example, is as follows. The operator  $\psi(\mathbf{x}, t)$  satisfies the Dirac equation

$$H\psi = i\hbar \partial\psi/\partial t.$$

Since  $\varepsilon_{\mu\nu\rho\sigma}\gamma_5\gamma_\rho\bar{p}_\sigma$  is time-independent and commutes with  $H$ , the operator  $\psi'$  defined by

$$\psi' = \varepsilon_{\mu\nu\rho\sigma}\gamma_5\gamma_\rho\bar{p}_\sigma\psi$$

also satisfies the Dirac equation

$$H\psi' = i\hbar \partial\psi'/\partial t.$$

These facts imply the continuity equation

$$\partial(\psi^+\psi')/\partial t + \nabla \cdot (\psi^+\alpha\psi') = 0,$$

which may be written in the form

$$\partial(\psi^+\gamma_4\gamma_\lambda\varepsilon_{\mu\nu\rho\sigma}\gamma_5\gamma_\rho\bar{p}_\sigma\psi)/\partial x_\lambda = 0.$$

The left-hand side is in the form of a four-divergence of a tensor function of position. It follows that the space integral of the fourth component of the function,  $\mathcal{R}_{\mu\nu}$ , is constant in time and is a Lorentz tensor.

\* \* \*

It is a pleasure for the second author to thank Professor J. ROBERT OPPENHEIMER for the hospitality of the Institute for Advanced Study.

# RIASSUNTO (\*)

In questo lavoro si mostra che la polarizzazione di una particella di Dirac libera può essere trattata in maniera covariante in termini di un operatore tensoriale antisimmetrico del second'ordine che commuta con l'hamiltoniano. L'interpretazione dell'operatore è che, nel sistema di riposo della particella, la parte spazio-spazio è lo spin e la parte spazio-tempo è nulla. Nella teoria quantizzata la descrizione della polarizzazione a mezzo di un tensore del second'ordine è un concetto più appropriato della descrizione a mezzo di un quadrivettore. L'inverso vale per lo spin medio di Foldy-Wouthuysen.

(\*) Traduzione a cura della Redazione.

## LETTERE ALLA REDAZIONE

(La responsabilità scientifica degli scritti inseriti in questa rubrica è completamente lasciata dalla Direzione del periodico ai singoli autori)

### The Fracture of Liquids under Stress Due to Ionizing Particles.

B. HAHN

*Department of Physics, University of Fribourg, Fribourg*

(ricevuto il 9 Settembre 1961)

Several liquids, *e.g.* water <sup>(1)</sup>, benzene, carbon tetrachloride <sup>(2)</sup>, and other are known to withstand large negative pressures (hydrostatic tensile strength) up to several hundred atmospheres before « breaking ». A stressed liquid with strong adhesion to its container wall will only break inside the body of the liquid if by some mechanism a hole of radius  $r$  larger than a critical radius  $r_c = 2\sigma/p_n$  is produced [ $\sigma$ =surface tension of the liquid,  $p_n$ =negative pressure; vapor pressure assumed to be  $\ll p_n$ ]. According to the nucleation theory of bubbles in liquids <sup>(3)</sup> subcritical holes are always present in a liquid due to statistical density variations. The calculated negative pressures <sup>(4)</sup> required for rendering such holes supercritical are large [*e.g.*  $p_n$  (water 27 °C) = -1320 atm,  $p_n$  (ethyl ether 27 °C) = -138 atm], and seem to be difficult to reach experimentally. Pre-existing vapor or gas bubbles, micro-

scopic dust particles, and weak adhesion of the liquid to the container wall, can cause the liquid to rupture prematurely at small negative pressures.

A mechanism capable of producing holes of supercritical size at moderately high negative pressures is provided, as presented in this paper, by ionizing particles. The rupture of several stressed liquids due to  $\alpha$ -decay inside the liquid, and due to neutron and  $\gamma$ -ray irradiation has been experimentally observed.

An easy method for producing negative pressures inside a liquid is by centrifugal forces <sup>(1)</sup>. A 24 cm long pyrex glass capillary tube of 1 mm inner

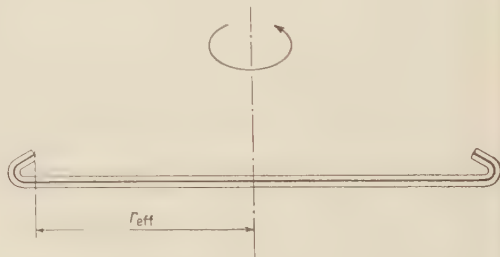


Fig. 1. — Rotating pyrex glass capillary tube.

diameter with back bent open ends, and filled with a liquid has been rotated about an axis as indicated in Fig. 1 up

<sup>(1)</sup> L. J. BRIGGS: *Journ. Appl. Phys.*, **24**, 721 (1950).

<sup>(2)</sup> L. J. BRIGGS: *Journ. Chem. Phys.*, **49**, 970 (1951).

<sup>(3)</sup> See *e.g.* M. VOLMER: *Kinetik der Phasenbildung* (Dresden und Leipzig, 1939).

<sup>(4)</sup> J. C. FISHER: *Journ. Appl. Phys.*, **49**, 1062 (1948).

to speeds of 180 revolutions per second. The negative pressure created by the centrifugal force in the middle of the capillary is

$$p_n = 2\pi^2 \rho v^2 r_{\text{eff}}^2 - p_b,$$

( $\rho$ =density of the liquid,  $v$ =number of revolutions per second,  $r_{\text{eff}}$ =effective radius,  $p_b$ =outer barometric pressure; vapor pressure of the liquid neglected). When the liquid breaks it is thrown out.

20 °C are shown. The reciprocal average breaking time is plotted versus the applied negative pressure and versus the rotation frequency. Each point corresponds to 30 measurements. Without radioactive sources in the liquid the waiting times were 10 to 100 times longer. The average waiting time at a fixed frequency for the Th-source increased as was expected from the disappearance of the source with the half life for ThB of 10.6 h. The absolute

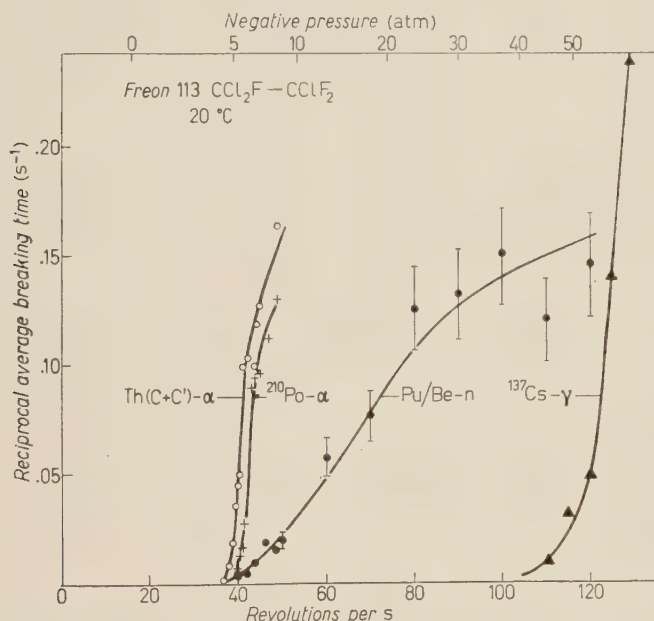


Fig. 2. — Reciprocal average breaking time negative pressure and vs. rotation frequency for  $\alpha$ -decay, neutron and  $\gamma$ -irradiation.

In a first experiment small traces of the  $\alpha$ -emitter  $^{210}\text{Po}$ , and later on of ThB in equilibrium with the  $\alpha$ -emitters ThC and ThC' have been dissolved in the liquids under investigation, and filled into a capillary tube with a widened central volume of 0.6 cm<sup>3</sup>. The average waiting time for breaking of the liquid has been measured at various rotation frequencies. In Fig. 2 curves for the  $\alpha$ -decay of  $^{210}\text{Po}$  and of Th(C+C') in the liquid Freon 113 (CCl<sub>2</sub>F-CClF<sub>2</sub>) at

and relative frequency measurements, done with a stroboscope, are accurate to  $\pm 2\%$ . The observed shift between the Th(C+C') and the  $^{210}\text{Po}$  curve is believed to be real. In this laboratory a similar shift has been found for the same sources under «normal» bubble chamber operation conditions at positive pressures<sup>(5)</sup>, and the conclusion has

(5) G. RIEPE and B. HAIN: *Helv. Phys. Acta* (in press).

been drawn that the bubbles are due to the recoil nucleus of the  $\alpha$ -decay, rather than to the  $\alpha$ -particle itself.

A survey of the  $\alpha$ -decay sensitivity of 28 liquids has been made. The breaking pressure, the surface tension, and the viscosity are given for some liquids in Table I. No well defined

TABLE I. — *Negative breaking pressure for various liquids at 20 °C due to  $\alpha$ -decay.*

	$p_n$ atm	$\sigma$ dyn./cm	$\eta$ cp
Isopentane	3.3	13.7	.22
n-Hexane	6.8	18.4	.33
Acetone	8.2	23.7	.32
Trychlorethylene	11.6	29.7	.58
Cyclohexanol	48.1	32.4	68.0
Ethylenbromide	21.9	38.4	1.7
Acetophenone	32.8	39.8	1.8

second) has been used at a distance of 50 cm from the « spinner ». The rupture of the liquid is due to fast neutrons (nuclear recoils and interactions). The breaking for Freon 113 sets in approximately at the same negative pressure as for the  $\alpha$ -decay; however, the neutron curve in Fig. 2 is much less steep than the  $\alpha$ -decay curves. No detailed interpretation of the neutron curve can be given at the moment.

In a third experiment sensitivity to  $\gamma$ -rays has been found. A weak  $^{137}\text{Cs}$   $\gamma$ -ray source held near the spinner was capable of breaking Freon 113 at 20 °C at approximately minus 52 atm as indicated in Fig. 2. The liquids isopentane (— 40), methylodide (— 49), and Freon 11 ( $\text{CCl}_3\text{F}$ ) (— 56) broke at the negative pressures given in parentheses.

Without the presence of a radioactive source Freon 113 has been brought

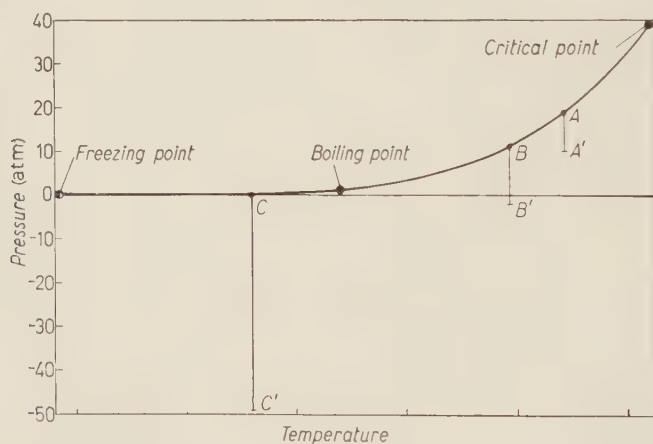


Fig. 3. — Pressure-temperature diagram with operating points for normal bubble chamber operation ( $A-A'$ ), partly negative pressure operation ( $B-B'$ ) according to PLESS and PLANO (<sup>3</sup>), and « pure » negative pressure operation ( $C-C'$ ).

dependence of the breaking pressure on the surface tension has been found. Liquids of high viscosity (e.g. cyclohexanol) have especially high breaking pressures.

In a second experiment an external Pu/Be neutron source ( $10^6$  neutrons per

for short waiting times of the order of 1 s to a pressure of minus 120 atm.

The effect of liquid fracture due to ionizing particles might be compared to the process of bubble formation in a superheated liquid at positive pressure by ionizing particles as discovered by

GLASER<sup>(6)</sup>. For comparison of the operating conditions, the operating pressure intervals and the relative operating temperatures for normal bubble chamber operation (*A-A'*), and for «pure» negative pressure operation (*C-C'*) are shown qualitatively in Fig. 3. PLESS and PLANO<sup>(7)</sup> have expanded a small isopentane bubble chamber into the negative pressure region to minus two atmospheres (*B-B'*).

A pure negative pressure operation of a bubble chamber seems to be impractical because of the high negative pressures ( $\sim -50$  atm) required and because of very fast hole growth.

Another possible application of the effect might be the study of very small  $\alpha$ -activities using a spinner with a large central volume and returning arms to prevent the liquid to spill out after breaking. For a central volume of 150 cm<sup>3</sup> filled with pure Freon 113 at 20 °C an average waiting time of 20 s at 50 Hz as zero effect has been observed. A similar method has been proposed by BRAUTTI *et al.*<sup>(8)</sup> at positive pressures.

\* \* \*

The author wishes to thank Professor O. HUBER, Dr. N. PEACOCK and Dr. G. RIEPE for highly valuable discussions and help.

<sup>(6)</sup> D. GLASER: *Phys. Rev.*, **87**, 665 (1952).

<sup>(7)</sup> I. A. PLESS and R. J. PLANO: *Rev. Sci. Instr.*, **27**, 935 (1956).

<sup>(8)</sup> G. BRAUTTI, M. CESCHIA and P. BASSI: *Nuovo Cimento*, **10**, 1148 (1959).



**$Y^*$  and Two-Nucleon  $K^-$ -Captures.**

N. N. BISWAS

*Max-Planck-Institut für Physik und Astrophysik - München*

(ricevuto il 18 Settembre 1961)

1. — It is well known from the  $K^-$ -meson captures at rest by complex nuclei that the reactions sometimes involve two nucleons leading to two fast baryons. Since the  $K^-$ -interactions with nucleon or nucleons are rather strong, the conventional phenomenological approach in terms of isotopic spin formalism is very useful. In this approach, the channels involving one nucleon and two nucleons are treated independently and two independent sets of matrix elements then describe the  $K^-$ -interactions. It may, however, be worth-while to be able to understand the two phenomena — at least qualitatively — as interrelated.

The existence of a pion-hyperon resonant state as experimentally established by various groups <sup>(1)</sup> is of great help in this instance. The important role of this resonant state designated by  $Y^*$  has been experimentally observed by DAHL *et al.* <sup>(2)</sup> in deuterium capture and by

BLOCK *et al.* <sup>(3)</sup> in helium capture. EISENBERG *et al.* <sup>(4)</sup> have conjectured that it may be important in two-nucleon capture process. The resonance of the pion-hyperon system in the isotopic spin state  $T=1$  is well established and another resonance in  $T=0$  state seems to be present. Possibly, the  $T=0$  state is as important as the  $T=1$  state <sup>(5)</sup>.

2. — In deuterium, for example, the reactions are as follows,

- $$\begin{aligned} (1) \quad & K^- + d \rightarrow Y + \pi + N, \\ (2) \quad & \rightarrow Y^* + N, \quad Y^* \rightarrow Y + \pi, \\ (3) \quad & K^- + d \rightarrow Y + N. \end{aligned}$$

To interrelate one- and two-nucleon reactions, one may consider the reactions (2) and (3) to be basically the same: namely, both proceeding through the production of  $Y^*$ . However, in (2)

(<sup>1</sup>) M. ALSTON, L. ALVAREZ, PH. EBERHARD, M. L. GOOD, W. GRAZIANO, H. K. TICHO and S. G. WOJCICKI: *Phys. Rev. Lett.*, **5**, 520 (1960); H. MARTIN, L. B. LEIPUNER, W. CHINOWSKY, F. T. SHIVELY and R. K. ADAIR: *Phys. Rev. Lett.*, **6**, 283 (1961).

(<sup>2</sup>) O. I. DAHL, N. HORWITZ, D. H. MILLER, J. J. MURRAY and P. G. WHITE: *Phys. Rev. Lett.*, **6**, 142 (1961).

(<sup>3</sup>) HELIUM CHAMBER COLLABORATION GROUP: *Nuovo Cimento*, **20**, 724 (1961).

(<sup>4</sup>) G. ALEXANDER, Y. EISENBERG, N. FRIEDMAN and D. KESSLER: *Reports on Proc. Rochester Conf.* (1960).

(<sup>5</sup>) M. ALSTON, L. ALVAREZ, PH. EBERHARD, M. L. GOOD, W. GRAZIANO, H. K. TICHO and S. G. WOJCICKI: *Phys. Rev. Lett.*, **6**, 698 (1961).

Y\* decays in a hyperon and a *real* pion, apparently indistinguishable from (1), and in case of (3) the resonant state decays non mesonically emitting a *virtual* pion which is subsequently absorbed by the other nucleon. The mechanism considered here is analogous to that of  $\Lambda$ -decay in hyperfragments treated by RUDERMAN and KARPLUS<sup>(6)</sup>. The analogy seems to be in accordance with the experimental results. It is known that  $\Lambda$ 's bound in heavy nuclei decay exclusively in the non-mesic mode and the ratio of non-mesic to mesic decay rate of  $\Lambda$  is strongly dependent on the atomic number of the nucleus containing it. Similarly, in the present case, the two-nucleon capture rate analogous to non-mesic decay rises rapidly from light to heavier nuclei:  $\sim 1\%$  in D,  $\sim 17\%$  in He and  $(15 \div 30)\%$  in emulsion nuclei<sup>(7,8)</sup>. Further, the total production rate (\*) of Y\* in K<sup>-</sup>-capture cases in light nucleus such as *deuterium* is of the same order of magnitude as the two-nucleon reaction rate in *heavy nucleus* (e.g. emulsion nucleus). Thus it seems

indicative that the reaction (2) which proceeds in deuterium through the real pion decay of Y\*, is undergoing virtual decay in heavy emulsion nuclei leading to two-nucleon process. These similar behaviours of the two processes may be indicative of their similar mechanisms.

3. - We would then also have the similar graphs as considered by Ruderman and Karplus, namely,

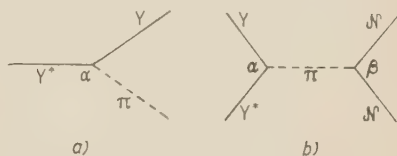


Fig. 1.

where (a) represents mesonic decay of the resonant state which looks similar to a one-nucleon reaction involving a hyperon and a pion, and (b) the virtual absorption of the decay pion giving a hyperon and a nucleon as reaction products. The vertex  $\alpha$  has the same matrix element in both cases and the vertex  $\beta$  can be represented by Yukawa interaction. The ratio  $r$ , of the two-nucleon (non-mesonic) interaction to the reaction involving  $Y^* \rightarrow Y + \pi$  is (\*)

$$(4) \quad r \approx g^2 k^2 M_N / [M_N (M_{Y^*} - M_N) + 1]^2 \cdot \varrho_N (k/q)^{2l+1} P.$$

(\*) From the present experimental data, it is difficult to estimate the total Y\* production rate. In deuterium, only the  $T=1$  state decaying in the  $\Lambda\pi$  mode has been reported ( $\sim 10\%$ ). The decay of this state in  $\Sigma\pi$  mode is rather rare<sup>(9,10)</sup>. However, the contribution from the  $T=0$  state may be considerable. The cross-section for Y\* production in hydrogen near threshold is of the same order of magnitude as that of Y\* production as reported in ref.<sup>(6)</sup>. Thus the total Y\* production in K<sup>-</sup>-captures in deuterium would be as high as  $(20 \div 25)\%$  of the capture events.

(9) P. BASTIEN, M. FERRO-LUZZI and A. H. ROSENFELD: *Phys. Rev. Lett.*, **6**, 702 (1961) and the deuterium results of R. D. LEVINE, J. J. MURRAY, D. H. MILLER and J. SCHWARTZ, quoted in this reference.

Here  $g^2/4\pi = 0.08$  (pion-nucleon coupling constant);  $k, q$  = momenta of the virtual, real pions, respectively, emitted in the Y\*-decay;  $M_N, M_{Y^*}$  are the rest masses of the nucleon and Y\*;  $\varrho_N$  = density of nucleons inside the nucleus;  $l$  = orbital angular momentum of the pion virtually emitted, and is related to the spin  $S$  of Y\* as

$$(5) \quad l = S \pm \frac{1}{2},$$

(\*) All units in  $\hbar = c = \mu_\pi = 1$ .

corresponding to odd, even parity of  $Y^*$  with respect to hyperon. Numerically,

$$k = 3.16 m_{\pi}c, \quad q = 0.885 m_{\pi}c,$$

$$M_{Y^*} = 1385 \text{ MeV},$$

and eq. (4) gives

$$(6) \quad r \approx 0.5 \varrho_N (12.7)^3 P.$$

We should remark that these calculations *a priori* assume the vertex  $\alpha$  to be smaller than the Compton wavelength of the pion; eq. (5) should therefore be taken as a qualitative estimate.

4. — To compare with the experimental data, we assume that the two-nucleon capture proceeds exclusively through the mechanism considered here, *i.e.* virtual decay of  $Y^*$ . The ratio of two nucleon capture events to the total stopped  $K^-$ -mesons is  $\sim 1\%$  in D,  $\sim 17\%$  in He. The reactions involving pions may, however, proceed directly as well through the resonant states. Assuming, as in deuterium, that the  $Y^*$ -production happens in about  $\frac{1}{5}$  of the  $K^-$ -captures, the ratio  $r$  comes out to be  $\sim 5\%$  in D and  $\sim 85\%$  in He.

The theoretical values of  $r$  may be roughly calculated from some simple considerations. We would assume that the probability  $P$  of  $Y^*$  being inside heavy nuclei (*e.g.* emulsion) is about unity and is proportional to  $A^{\frac{1}{3}}$ , where  $A$  is the atomic number of the nucleus containing  $Y^*$ . Using the value of  $A$  for heavy nuclei in normalizing  $P$  to unity, the probabilities in lighter nuclei can be calculated. With appropriate radius for  ${}^3\text{He}$  nucleus for evaluating the nuclear density in  $K^-$  He capture case and the deuterium radius for  $Y^*N$

case, the ratio  $r$  is found as tabulated below for some values of  $l$ .

Nucleus	$l=0$	$l=1$	$l=2$	exp.
D	0.0013	0.0165	0.21	$\sim 0.05$
He	0.053	0.67	8.5	$\sim 0.85$

Comparison of these values with the experimental results favours  $l=1$ . At the momentum involved in the reaction, one would also have expected the pion to be absorbed in the  $p$  wave from the behaviour of the pion nucleon interaction. This consistency gives some support to the validity of the mechanism considered here. Eq. (5) would thus predict odd parity for spin  $\frac{1}{2}$  and even parity for spin  $\frac{3}{2}$  of  $Y^*$  with respect to hyperon. However, these calculations as well as the present experimental data on the spin of  $Y^*$  are uncertain. Therefore, it is not safe to draw any conclusion in this respect and probably it would be more reasonable to look for the compatibility of these results when the spin and parity of  $Y^*$  will be known from some clear cut experiments.

5. — In conclusion, we may remark that the investigation of two-nucleon capture rate and the production rate of  $Y^* \rightarrow Y + \pi$  in  $K^-$ -captures in light nuclei would be of particular interest from the point of view of the mechanism considered here. The  $2N$  capture rate should increase with the atomic number of the capturing nucleus whereas the mesic decay of  $Y^*$  should decrease. A systematic experimental study and a more rigorous calculation may be helpful in extracting some information about the characteristic of the pion-hyperon resonance system.

## Search for Magnetic Monopoles.

M. FIDECARO, G. FINOCCHIARO (\*) and G. GIACOMELLI (\*\*)

CERN - Geneva

(ricevuto il 30 Settembre 1961)

The possible existence of a magnetic monopole is in itself so appealing that it has been thoroughly studied in many theoretical papers <sup>(1,2)</sup>.

On the experimental side, several attempts to discover the monopole resulted in putting lower limits on the mass of such a particle if reasonable assumptions about its interactions are made. At present the available limits are roughly: one pion mass from the Lamb shift <sup>(2)</sup>, three pion masses from the  $g-2$  value for the  $\mu$ -meson <sup>(3)</sup>, one proton mass from direct observation <sup>(2)</sup>. Because the energies available at the CERN Proton Synchrotron make it possible to produce monopole-antimonopole pairs up to a monopole mass of about 2.8 GeV, a few simple counter experiments were planned to push down the previous lower limits. Similar experiments are performed with nuclear emulsions by E. AMALDI, G. BARONI, H. BRAD-

NER, DE CARVALHO, L. HOFFMANN, A. MANFREDINI and G. VANDERHAEGHE and by a Brookhaven group. The experiments were designed to detect isolated magnetic charges of absolute value  $g=137/2e$ , but were also sensitive to charges somewhat different from the above value.

Fast monopoles should produce a strong electric field which heavily ionizes the medium: in the relativistic region the rate of loss should be  $(137/2)^2$  that of a unit electric charge (about 8 GeV per  $g\text{ cm}^{-2}$ ). Thus they should be easily identifiable. Monopoles at thermal energies would be expected to be bound in paramagnetic solids with energies of a few electron volts <sup>(4)</sup> (they would be expelled by diamagnetic materials); a strong magnetic field could remove them. Monopoles in gases could probably attach several paramagnetic molecules (notably oxygen) making a kind of molecular complex. This effect is experimentally undesirable for their observation. Monopoles should be stable, but two poles of opposite magnetic charge should annihilate, presumably into high-energy photons. Assuming (without real justifications) that the classical electron radius would be equal to the «classical

(\*) On leave of absence from the University of Rome.

(\*\*) On leave of absence from the University of Bologna.

<sup>(1)</sup> P. A. M. DIRAC: *Proc. Roy. Soc., A* **133**, 60 (1931); *Phys. Rev.*, **74**, 817 (1948).

<sup>(2)</sup> H. BRADNER and W. M. ISBELL: *Phys. Rev.*, **114**, 603 (1959). This paper contains many references on the monopole subject. See also R. KATZ and O. R. PARNELL: *Phys. Rev.*, **116**, 236 (1959).

<sup>(3)</sup> B. DE TOLLIS: private communication.

<sup>(4)</sup> W. V. R. MALKUS: *Phys. Rev.*, **83**, 899 (1951).



monopole radius», one estimates a probable monopole mass of 2.4 GeV. A first order perturbation calculation assuming *a*) only electromagnetic interactions, and *b*) a nucleon form factor with the core, as suggested by the Cornell results, shows that the production cross-section in nucleon-nucleon collision should be larger than  $10^{-34} \text{ cm}^2$  <sup>(5)</sup>.

Two different kinds of experiments were performed; in both, monopoles were supposed to be produced in nucleon-nucleon collisions. In the first kind of experiments, monopoles should have been directly detected by means of scintillation counters after having been accelerated by solenoids. The monopoles were either *a*) directly bent into the accelerating solenoids or *b*) stopped in a diamagnetic target and immediately extracted by a weak magnetic field, or *c*) stopped, preferentially in a paramagnetic target, assumed to be bound there, and later extracted by a reasonably strong magnetic field.

In the second type of experiments, a counter telescope was used to detect a high-energy induced activity, one possible origin of which being a monopole-antimonopole annihilation.

1. — In the first case we used two solenoids, 165 and 55 cm long, 10 cm inner diameter, 12 cm apart (Fig. 1): they provided a magnetic field of about 2 kG. Three gas (99.99% pure argon) scintillation counters, 10 cm thick and 10 cm diameter, were placed one between the solenoids and two after the shorter coil. The counters were calibrated with the 5 MeV  $\alpha$ -particles from a polonium source. Their usefulness arises from

their good linearity of response to high specific ionizations. Standard transistorized circuitry was used; in particular,

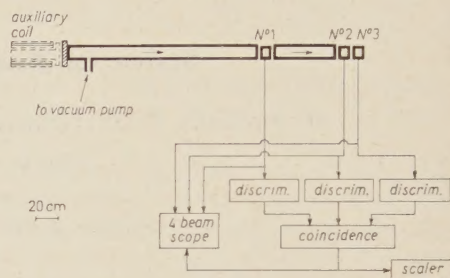


Fig. 1. — Sketch of the apparatus and block diagram of electronics. Solenoid and vacuum pipe shown in dotted lines at left were used only in experiment 1b.

discriminators set a limit on pulse height accepted and the output of a coincidence circuit triggered a 4-beam CERN oscilloscope where the pulses from the three counters were photographed. Monopoles entering the long solenoid should be accelerated to 6 GeV in a  $10^{-5}$  mm Hg vacuum, cross the first counter losing about 135 MeV energy in the scintillator and 400 MeV in the walls of the solenoids and of the counter, gain 2 GeV more in the second solenoid, and be recorded in the last two counters.

The front end of the long solenoid was placed firstly near the PS vacuum chamber, in a straight section. The internal proton beam impinged on a Be target at the entrance of the previous straight section, and a high flux of particles, mainly protons produced by diffraction scattering, impinged on the solenoid front end, which consisted of a 2 cm copper plate. The solenoids made an angle of  $20^\circ$  with respect to beam direction and were pulsed in synchronism with the PS cycle. Most of the monopoles produced in the copper plate should have been slowed down to thermal energies and, since copper is diamagnetic, should have been easily extracted by the field of the solenoids. Monopoles produced at an appropriate thickness

<sup>(5)</sup> E. AMALDI, N. CABIBBO and E. FERRARI: private communication. They point out that the value is extremely rough (though probably underestimated) because perturbation methods fail for large coupling constants as we have here, and moreover, because of the high momentum transfers involved, the cross-section is highly dependent on the nucleon form factors chosen.



should have been slowed down so that the field could bend and collect them. The collection was improved by a series of copper sheets 0.2 mm thick placed 1 cm apart in the direction of the magnetic field. Though the counters were heavily shielded they nevertheless had high single rates, mostly due to particles crossing the glass of the photomultipliers. Effective biases of 35 MeV had to be used, to reduce the random rate to negligible values. No evidence for monopoles was found for an estimated flux of  $6 \cdot 10^{13}$  protons of 19 GeV kinetic energy incident on the copper plate. This corresponds to a cross-section smaller than  $10^{-37}$  cm<sup>2</sup> per nucleon, for the production of monopoles slowed down and extracted, and smaller than  $3 \cdot 10^{-35}$  cm<sup>2</sup> per nucleon, for those bent in the magnetic field<sup>(6)</sup>. The experiment was sensitive to monopoles having a charge between 0.6 and 4 times the predicted value and a mass smaller than 2.2 GeV. Larger magnetic charges would not have been able to cross all the counters, because ionization losses go as the square of the magnetic charge, while the energy gain in a solenoid goes only linearly.

Successively 27.5 GeV kinetic-energy protons were used to bombard, in a PS field free section, a paramagnetic target (10 mm thick aluminium with  $3 \cdot 10^{14}$  protons) and a diamagnetic one (12.5 mm polyethylene with  $1.5 \cdot 10^{14}$  protons). We also used an externally irradiated target of the type used in the emulsion experiments, made of a slightly diamagnetic core (copper  $2.5 \times 2.5 \times 5$  cm<sup>3</sup>) surrounded by a material of higher negative susceptibility (paraffin) exposed to about  $6 \cdot 10^{12}$ , 19 GeV protons, and successively to  $5 \cdot 10^{11}$ , 27.5 GeV protons. The copper plate used before as target for the production of monopoles was removed and an auxiliary coil was connected to the

long solenoid (Fig. 1, dotted lines at left). After irradiation the targets were placed in the  $10^{-5}$  mm Hg vacuum inside the auxiliary coil. This extra coil was pulsed to 7 kG and thus acted as monopole «extractor». The usual two solenoids were continuously on and acted as accelerators and also, providing continuously 100 G at the target position, as helpers for the extraction. From the absence of counts we placed the limits of  $10^{-39}$  in aluminium,  $10^{-39}$  in polyethylene, and  $10^{-36}$  in the Cu+CH<sub>2</sub> target (cross-sections in cm<sup>2</sup> per nucleon)<sup>(6)</sup>. The experiment was sensitive to monopoles having a mass smaller than 2.8 GeV, and a magnetic charge between 0.3 (the counter thresholds were at 10 MeV) and 4 times the Dirac value<sup>(7)</sup>.

2. — To detect the particles originated in a possible monopole-antimonopole annihilation we used a counter telescope consisting of 0.5 cm thick lead converter, three coincidence counters 22 cm diameter, 1 cm thick, and a total absorption lead glass Čerenkov counter 35 cm diameter, 30 cm long<sup>(8)</sup>. The system had an efficiency of about 50% for photons and 100% for electrons. The electronics consisted essentially of a standard coincidence circuit whose output opened a gate letting the pulse from the Čerenkov counter to a 100-channel pulse-height analyser, so that the energy of the particle could be measured.

(<sup>6</sup>) During this experiment the solenoids were part of the time oriented approximately in the direction North-South and the polarity was such that lines of force inside the solenoids were mostly supplied by the earth's magnetic field. Monopoles created by cosmic rays and drifting in the atmosphere should have been collected and accelerated. We estimate an upper limit of  $4 \cdot 10^{-11}$  monopoles cm<sup>-2</sup> s<sup>-1</sup>. This limit would be worse in the case of oxygen molecular complex formation, which we cannot exclude. [See ref. (<sup>4</sup>) for analogous experiment.]

(<sup>8</sup>) M. FIDECARO, G. GATTI, G. GIACOMELLI, W. A. LOVE, W. C. MIDDELKOOP and T. YAMAGATA: *Nuovo Cimento*, **19**, 382 (1961).

(<sup>6</sup>) All limits given correspond to a confidence level of one standard deviation.

The telescope, subtending an angle of  $7.8 \cdot 10^{-4}$  sr, looked at a polyethylene target 12 mm thick while being irradiated by 27.5 GeV protons for a total flux of  $4.5 \cdot 10^{14}$  protons. A gate allowed pulses to be recorded during a period of 1 s, starting either 0.19 s or 1.2 s after each PS burst (the PS repetition rate was of one burst every 5 s, the burst length was 2 ms).

After irradiation, the polyethylene target plus an Al-10 mm thick target irradiated by  $3 \cdot 10^{14}$  protons, and a paraffin-surrounded copper piece irradiated by  $5 \cdot 10^{11}$  protons, were placed immediately in front of the telescope, subtending now  $3.8 \cdot 10^{-2}$  sr. After 2 h of counting, the polyethylene target and the paraffin around the copper one were melted in the hope of speeding up eventual migration processes.

No counts were registered. This result is of difficult interpretation. If there is a high probability for annihilation in the time between 0.1 s and one day after production, then the experiment gives an upper limit of  $(10^{-38} \div 10^{-35}) \text{ cm}^2$  for the production cross-section.

\* \* \*

We would like to express our gratitude to Professors E. AMALDI, G. BERNARDINI, H. BRADNER and L. VAN HOVE, and to Drs. N. CABIBBO, E. FERRARI, L. HOFFMANN, M. MORPURGO, S. RATTI and G. VANDERHAEGHE, for stimulating discussions and suggestions, and to Messrs. G. SICHER and B. SMITH for setting up the equipment.

## ERRATA - CORRIGE

### On the Gauge Invariant Theory of Elementary-Particle Interactions.

P. ROMAN

*Department of Physics, Boston University - Boston, Mass.*

(*Nuovo Cimento*, **21**, 746 (1961))

Owing to an oversight two notes were added at the end of this paper, which do not belong to it.

PROPRIETÀ LETTERARIA RISERVATA

Direttore responsabile: G. POLVANI

Tipografia Compositori - Bologna

Questo fascicolo è stato licenziato dai torchi il 30-X-1961